Fermilab Library
0 1160 0087253 5

E 815 - NuTeV

A Search for Massive Exotic Particles at the NuTeV Neutrino Experiment

Joseph Angelo Formaggio

A SEARCH FOR MASSIVE EXOTIC PARTICLES AT THE NUTEV NEUTRINO EXPERIMENT

Joseph Angelo Formaggio

FERMILAB
LIBRARY

Submitted in partial fulfillment of the
Requirements for the degree
of Doctor of Philosophy
in the Graduate School of Arts and Sciences,

COLUMBIA UNIVERSITY

2001

Gift Thesis AAG 3044

©2001

Joseph A. Formaggio

All Rights Reserved

3 Event Reconstruction **51**

3.1 Track Reconstruction 51

3.2 Vertex Formation 52

3.3 Clustering 54

3.4 Particle Identification 56

3.5 Energy Measurements 62

3.5.1 Muon Energy 62

3.5.2 Pion and Electron Energy 63

3.6 Event Formation 63

3.7 A Note about Variables 64

4 Monte Carlo Simulations **68**

4.1 Neutrino Flux 69

4.2 Neutrino Interactions in the Decay Channel 69

4.2.1 Deep Inelastic Scattering 69

4.2.2 Quasi-elastic and Resonance Neutrino Scattering 71

4.3 Neutrino Interactions in Surrounding Material 76

4.4 Detector Simulation and Response 78

4.5 Cosmic Rays 78

4.6 Noise Simulation 79

4.7 Calibration Beam Contamination 80

4.8 Normalization 80

5 The KARMEN Timing Anomaly **86**

5.1 The KARMEN Experiment 86

5.2 Experimental Searches: PSI 92

5.3 Theoretical Explanations 93

5.3.1 A Conspiracy of Masses 94

5.3.2 Q^0 Interpretation : ν_τ 94
5.3.3 Q^0 Interpretation: Neutral Heavy Lepton 95
5.3.4 Q^0 Interpretation : Supersymmetric Models 98
5.4 Remarks on the KARMEN Result 98

6 Q^0 Event Selection 100
6.1 Q^0 Signal 100
6.2 Q^0 Background 103
6.2.1 Neutrino-Nucleon Interactions 106
6.2.2 Photon Production 106
6.2.3 K_L Production 107
6.2.4 Diffractive π Production 108
6.2.5 Negligible Sources 108
6.3 Event Selection 109
6.3.1 Reconstruction Cuts 109
6.3.2 Kinematic Cuts 111
6.4 Summary of Backgrounds 117

7 Q^0 Sideband Studies 119
7.1 The Low Energy/High Transverse Mass Sideband Study 120
7.2 The $\mu\pi$ Sideband Study 121
7.3 The Multi-Track Sideband Study 122
7.4 Normalization Sideband 122
7.5 Summary of Sideband Studies 124

8 Q^0 Search Results 126
8.1 Transverse Position Dependence 126
8.2 The Signal Region 129

9 Motivation for the High Mass Search **134**

9.1 Neutral Heavy Lepton Production 136

9.1.1 B Production 136

9.1.2 Neutral Current Production 139

9.2 Neutralino Production 139

10 High Mass Event Selection **145**

10.1 N^0 Signature 145

10.2 Sources of Background 149

10.2.1 ν Deep Inelastic Background Events 149

10.2.2 Low-multiplicity Backgrounds 150

10.2.3 Negligible Sources 151

10.3 Event Selection 151

10.3.1 Reconstruction Cuts 152

10.3.2 Clean Cuts 153

10.3.3 Final Background Estimates 158

11 High Mass Sideband Studies **159**

11.1 Longitudinal Vertex Study 159

11.2 Chamber And Intermediate Region Sideband 160

11.3 $\mu\pi$ Sideband 163

11.4 Summary of High Mass Sideband Studies 164

12 High Mass Search Results **166**

12.1 Description of the Three Events 167

13 High Mass Event Analysis **173**

13.1 Considerations under an N^0 Hypothesis 173

13.2 Considerations under a Background Hypothesis 174

13.3 Further Cross-Checks 181
13.4 Null Hypotheses 184
13.4.1 Hypothesis 1: Chamber Interaction 185
13.4.2 Hypothesis 2: Pion Decay 185
13.4.3 Hypothesis 3: Kaon Decay 186
13.5 Limits 189

14 Future Prospects **192**
14.1 Future for the Q^0 192
14.1.1 New Results from KARMEN II 192
14.1.2 The MiniBooNE Experiment 193
14.1.3 Future Detector at ISIS 194
14.2 Future for the N^0 195
14.3 Other Exotic Searches: Muon Storage Ring 197

15 Conclusion **202**

A Paper on the Q^0 Search at NuTeV **204**

B Paper on Helicity Calculations **209**

C Event Catalog **214**

D FORTRAN Code for Helicity Decay Elements **227**

E Convoluted Poisson Probabilities **234**

F Search for Lepton Family Number Violation **236**

G Paper on Lepton Number Violation **239**

List of Tables

1.1 Fermions and their properties. 6

1.2 Bosons and their properties. 6

1.3 Vector and axial vector couplings for fermions. 12

2.1 Breakdown of neutrino beam composition. 28

2.2 Material composition of decay channel drift chambers. 35

2.3 Composition in interaction and radiation length of one unit of the NuTeV calorimeter. 41

2.4 NuTeV data triggers. 46

3.1 Longitudinal and transverse resolution as a function of opening angle. 55

3.2 Particle identification efficiency as a function of energy. 61

3.3 Kinematic variables when event is interpreted as a νN interaction. . . 66

3.4 Kinematic variables when event is interpreted as a decay. 66

4.1 Punch-through rates from earth-berm shielding. 78

4.2 Mass ratio for various components of the NuTeV decay channel relative to the NuTeV calorimeter. 81

4.3 Deep inelastic scattering events occurring in NuTeV decay channel. . 81

6.1 Particle identification efficiency for Q^0 decay events. 103

6.2 Photon production probability in GEANT pion showers. 108

6.3 Reconstruction cut efficiency for Q^0 search. 111
6.4 Q^0 kinematic cuts. 112
6.5 List of Q^0 backgrounds in signal region. 117

7.1 Event rates for low energy/high transverse mass sideband. 121
7.2 Summary of Q^0 sideband studies. 125

10.1 Particle mis-identification probability for a 5 GeV/c^2 N^0 decay. . . . 150
10.2 Origin of DIS background events that pass analysis cuts. 150
10.3 Reconstruction cuts for N^0 search. 154
10.4 Geometric acceptance and reconstruction efficiency for the allowed channels. 157
10.5 Estimated background rates to the $N^0 \to \mu\mu(\nu), \mu e(\nu)$, and $\mu\pi$. . . . 158

11.1 Data and Monte Carlo prediction for high mass chamber and intermediate regions. 164

12.1 Predicted and observed events passing all N^0 signal cuts. 166
12.2 Kinematic and reconstruction quantities for the three candidate $N^0 \to \mu\mu(\nu)$ events. 172

13.1 Vertex probability under signal and background hypotheses. 179
13.2 Observed events and expected background as cuts are sequentially released. 182
13.3 Predicted and observed $\mu\mu$ events as cuts are sequentially released. . 183
13.4 Observed events and expected background for sample with loosened energy and M_T criteria. 184
13.5 Results for fits to kaon decay hypothesis. 187

List of Figures

1.1 Feynman diagrams for charged current and neutral current interactions of neutrinos, anti-neutrinos, and quarks. 13

1.2 L^0 production from π decay via mixing. 18

1.3 L^0 decay to $e^+e^-\nu$ via mixing. 19

2.1 Fermilab Tevatron and Fixed Target Area 26

2.2 Timing structure for NuTeV primary proton beam. 27

2.3 NuTeV's Sign-Selected Quadrupole Train (SSQT) 28

2.4 Event distributions for ν_μ, $\bar{\nu}_\mu$, ν_e, and $\bar{\nu}_e$ in neutrino and anti-neutrino running. 29

2.5 NuTeV decay channel, showing the veto wall, helium bags, six drift chambers, and calorimeter. 31

2.6 Veto wall array. 32

2.7 Logic for veto wall trigger. 33

2.8 Sketch of the decay channel single-wire drift chambers. 35

2.9 Residuals of the decay channel drift chambers. 37

2.10 Residuals between decay channel and calorimeter tracks for muons traversing the NuTeV experiment. 38

2.11 Efficiency of drift chamber across the plane. 39

2.12 The NuTeV target calorimeter. 41

2.13 Schematic of a single calorimeter unit. 42

2.14 The NuTeV toroid spectrometer. 44
2.15 Schematic diagram of the NuTeV calorimeter readout electronics. . . 50

3.1 X and Y residuals for a 33.9 MeV/c^2 decay to $e^+e^-\nu$. 55
3.2 Sample event with deep penetrating muon traversing the NuTeV decay channel and calorimeter. 57
3.3 Sample electron event with short electromagnetic shower in the NuTeV decay channel and calorimeter. 58
3.4 Hit density distribution for 50 GeV electrons, pions, and muons. . . . 59
3.5 Particle identification probabilities. 60
3.6 Kinematic variables used when event is interpreted as a neutrino-nucleon interaction. 65
3.7 Kinematic variables used when event is interpreted as a decay. 67

4.1 Neutrino and anti-neutrino energy distributions for charged current interactions. 70
4.2 The differential cross-section $d\sigma/d\nu$ in the low hadronic energy region. 72
4.3 Data and MC resonance and quasi-elastic distributions of hadronic energy (Rein and Sehgal model). 74
4.4 Data and MC resonance and quasi-elastic distributions of hadronic energy (higher-twist model). 75
4.5 Data and MC resonance and quasi-elastic distributions of transverse momentum. 77
4.6 Number of tracks for data and Monte Carlo normalization sample. . . 83
4.7 Distributions comparing data and Monte Carlo for charged current DIS interactions in the decay channel chambers. 84

5.1 Schematic of the ISIS spallation source and KARMEN neutrino detector. 88
5.2 Timing structure of KARMEN neutrino beam. 89

5.3 Timing distribution of neutrino events in the KARMEN neutrino detector from muon decay. 90
5.4 Energy distribution of Q^0 excess events in the KARMEN detector. . . 91
5.5 Search results from the PSI experiment. 93
5.6 Feynman diagram for Q^0 isosinglet decay to $e^+e^-\nu$. 96
5.7 Feynman diagram for Q^0 isosinglet radiative decay to $\gamma\nu$. 97
5.8 Branching ratio versus lifetime plot for the KARMEN signal. 99

6.1 Relativistic gamma and beta distributions for Q^0 particles. 101
6.2 Energy spectrum of pions created from the 800 GeV protons in the NuTeV neutrino beamline. 102
6.3 Monte Carlo Q^0 decay to $e^+e^-\nu$ within the fiducial volume of the NuTeV decay channel. 104
6.4 Same Monte Carlo Q^0 decay as in Figure 6.3, zoomed in to see the separation of the e^+e^- tracks. 105
6.5 Energy and angle distributions for photons entering the decay channel from the earth-berm shielding. 107
6.6 Transverse mass spectrum for DIS and reconstructed Q^0 decay events. 113
6.7 Blowup of the Q^0 transverse mass spectrum. 114
6.8 $ln(x_{eff})$ spectrum for DIS and reconstructed Q^0 decay events. 115
6.9 W^2_{eff} spectrum for quasi-elastic ν and reconstructed Q^0 decay events. 116
6.10 Energy spectrum for DIS, photon, and Q^0 decay events. 118

7.1 Kinematic distributions for data and Monte Carlo events in the multi-track sample. 123
7.2 Normalization distributions for data and Monte Carlo. 124

8.1 Transverse vertex distribution for Q^0 passing reconstruction cuts. . . 127
8.2 Transverse vertex distribution for photons passing reconstruction cuts. 128

8.3 Log likelihood distribution for photon and Q^0 events. 130
8.4 Branching ratio versus lifetime plot for the KARMEN signal and the exclusion regions (90% C.L.) from the NuTeV and PSI experiments. 131
8.5 Branching ratio versus lifetime plot for the NuTeV limit for $\pi \to e + Q^0$. 132

9.1 NuTeV limit on U_μ^2 mixing from D and K production. 135
9.2 Branching ratio for $B^\pm \to D^0\mu^\pm N^0$ and $B^\pm \to \mu^\pm N^0$. 137
9.3 Branching ratios for N^0 decays. 138
9.4 Lego plot of total number of B-produced N^0's decaying to muons as a function of mass and mixing. 140
9.5 Feynman diagram of neutral current N^0 production in berm. 141
9.6 Lego plot of total number of berm-produced N^0 decaying to muons as a function of mass and mixing. 142
9.7 Feynman diagram of neutralino production at target. 143
9.8 Number of neutralinos expected as a function of decay length. 144

10.1 Monte Carlo N^0 decay to $\mu^+\mu^-\nu$. 146
10.2 Muon transverse momentum from a 5 GeV/c^2 decay to $\mu\mu\nu$. 147
10.3 Opening angle for $\mu^+\mu^-$ pair for a 5 GeV/c^2 decay to $\mu\mu\nu$. 148
10.4 Longitudinal resolution for an N^0 decay to $\mu\mu\nu$. 149
10.5 Depiction of a DIS charged current background event. 156

11.1 Longitudinal vertex position for all events in the decay channel fiducial volume. 161
11.2 Distance of longitudinal vertex position from the closest chamber for events in the longitudinal sample without the z vertex requirement. . 162
11.3 Data/Monte Carlo ratio for all high mass search sideband studies. . . 165

12.1 Event 1: $\mu\mu(\nu)$ data event passing final cuts. 169
12.2 Event 2: $\mu\mu(\nu)$ data event passing final cuts. 170

12.3 Event 3: $\mu\mu(\nu)$ data event passing final cuts. 171

13.1 Kinematic distributions for a 5.0 GeV/c^2 N^0 decay. 175
13.2 More kinematic distributions for the 5.0 GeV/c^2 N^0 Monte Carlo. . 176
13.3 The muon energy asymmetry in N^0 decays. 177
13.4 Kinematic distributions for $\mu\mu$ events from background Monte Carlo. 178
13.5 More kinematic distributions for $\mu\mu$ background events. 179
13.6 The muon energy asymmetry for background $\mu\mu$ events. 180
13.7 NuTeV limit on neutralino production. 190

14.1 Timing distribution of neutrino events in the KARMEN neutrino detector from their Run II data. 193
14.2 Projected MiniBooNE single event sensitivity on the Q^0 branching ratio for one year of running. 195
14.3 Design for a proposed Q^0 TPC detector at the ISIS spallation facility. 196
14.4 Schematic of the NOMAD neutrino detector. 198
14.5 $|U_\mu|^2$ for one year of running from a muon storage ring. 201

A Note of Thanks...

With a bang, this is how our life begins.

- Jaymi Formaggio

This section was the hardest to write. This work would have been impossible without the help of so many others.

I should begin properly; I should begin with Mike Shaevitz, my advisor and mentor. I remember timidly entering his office my first year, fumbling as to whether I should address him as "Professor Shaevitz" or "Mike". He welcomed me, insisting that I address him in the familiar. From that moment, Mike has made all efforts to include me into this great family. I could write pages and pages about his expertise in physics; his ability to explain intricate concepts with remarkable clarity; his skill at finding problems invisible to others. But all this is well known. What I have found even more significant is the way he has made me part of his family. He has welcomed me into his home and comforted me during times of hardship. Mike, you forever have my loyalty. Our home will always be open to you and your family.

I have a second mentor. She is Janet Conrad. Janet's enthusiasm and love for physics is matched only by her devotion to her students. I have always told the story that I joined Janet and Mike's group because of Janet's persistence. This is not true. I joined the group because I knew that I had found someone that really cared about her students. Her protection and guidance allowed me to develop my own abilities and

talents. Janet, you lead by your example. I hope that during my stay at Columbia I have captured some of the fire that makes you who you are.

I would also like to thank Eric Zimmerman, our post-doc. Since joining our group at Columbia, Eric has provided me with guidance in daily life. His remarkable attention to detail helped me focus my own thinking. Like myself, Eric will be leaving Columbia for what is sure to be a bright future. I hope he will always take time to hike across uncharted territory. I hope he will always stop and take a picture, capture the beauty around him.

My thanks extend to another important scientist in my life, Jae Yu. Jae, I hope you are proud of the work we have done together. Always an advocate, always diligent, I have learned a lot from our Monday calls. You have taught me that even 850 miles shrink to nothingness; that a team is not bounded by geography. You have taught me that a handshake expresses more than words can. Thank you.

I would like to express warm gratitude to Paul Nienaber. Paul has always lent an ear to what I have had to say, always treating me as an individual with a voice. You have taken time to console my family during our darker moments. This is no surprise. You extend this compassion to all those you care about. May I always be worthy of your friendship.

I wish to thank Todd Adams for his care and guidance during my studies at NuTeV and Columbia. I have had the pleasure of witnessing Todd as he matured into a dedicated scientist. It was under his leadership that the UFP paper became a work of art that the entire collaboration, regardless of their private feelings, was able to stand behind. The credit for much of what you see here in these pages goes to him. I am honored to have worked with you and I hope the opportunity presents itself to do so again.

My gratitude also extends to an important member of the Columbia faculty, Allan

Blaer. It was because of his kindness that I ultimately made my decision to come to Columbia. He is devoted to all his students, and has always encouraged me to prove myself both as a scientist and a teacher. I also wish to extend my thanks to Jerry Packer. Jerry, like Allan, has always taken special care and pride in each graduate student class. Jerry's enthusiasm extends to the students, even now that he is technically "retired". To Allan and Jerry, I wish you both well.

There are so many more names that need to be inserted here. There is Tim Bolton, who from the beginning has always supported my work at NuTeV. There is Debbie Harris, who has always encouraged me and has always helped me when I didn't understand. There is Panagiotis Spentzouris who, via example, has always advocated that I speak my mind and demand to be heard. There is Randy Johnson, who manages to combine good teaching with good humor. There is Bill Seligman, who has never hesitated to share his expertise on physics and computers, nor to cast a benevolent spell. There is Bill Louis, who always has a smile and kind word for everyone. There is Kevin McFarland, whose critical eye and attention to detail is balanced with his willingness to compliment me for a job well done. There is Arie Bodek, who always imparts his wisdom with a hearty, contagious laugh. There is Bob Bernstein, with whom I have had both constructive arguments, good laughs, and the occasional Italian exchange.

Then, there are my fellow students. From them I have learned so much: that five people in a van will NOT necessarily kill each other, that 1020 is the greatest bar ever, and that one can indeed survive the Quals. Bonnie Fleming (a.k.a. Binnie) and Sam Zeller have demonstrated by their example how much potential all of us young scientists have to succeed. I have immense pride in their work and immense gratitude for all their help in getting to this point in my life. The same pride extends to other students whom have come and gone through NuTeV and MiniBooNE... Jenn Raaf, Sarah Case, Jesse Goldman, Drew Alton, Jeff McDonald, Sergei Avvakumov,

Max Goncharov, and Artur Vaitaitis. And now I look at the new Columbia students, Michel Sorel and Jocelyn Monroe. You guys have such incredible potential and talent. *In boca a lupo* to both of you. Hayn, we miss you. Come back soon.

I want to reserve a small space here for Matthew Sharp. I will always refer to Matthew as "my first student", and I hope all my students will be as talented and as kind as he is. He has always graced the office with a desire to learn, as well as a good joke to lighten the mood. You will go far, Matthew. Just wait and see.

There are so many others I wish to thank –people I have come to know well enough to know I would like to know them better. There is Len Bugel, Peter Meyers, Andrew Bazarko, Rex Tayloe, Eric Hawker, Jerry Garvey, Bob Drucker, Donna Naples, Sally Koutsoliotas, and Un-Ki Yang – all of whom have helped me to get to this point. There is also the wonderful staff here at Columbia; the unsung heroes of the Ivy halls. How far would I have really gotten without the help of Lalla, Ann, and Britt? How much duller would my days have been if not for Ray asking me each morning how my family was doing? How can I thank them properly?

I wish to make special mention here of the Gang and thank them for all the help and support they have given to me and my family throughout the years. Jose, Pax, Cos, and Mike, you guys are truly "Men for Others." Every day, you convince me of this.

Jaymi, there are no words which can properly describe how I feel knowing that you are and always will be part of my life. More important than a simple thank you, I hope that my actions –whether they be my smile as you wake me in the morning, or my devotion to the future we are building, or my simple kiss as you drift into sleep –will always reflect the love and gratitude I have for you. I hope when you look at me, you always see the man that you have helped me become. I hope you always see us.

There is one more person I should mention here. You do not have a name yet or know what the world is like. But let me assure you that there is a beautiful world out here, filled with magic and wonder. We cannot wait to hold your hand and show you.

I finally wish to extend my immense gratitude to my parents. Their love is unconditional, unpredicated on any accomplishments but rather on the simple fact that I am their son. There are no words or gestures to repay what they have done for me. I especially wish to thank my father. You have taught me the value of hard work, through your own sweat. I remember you returning home with the smell of keys and other metals on your hands. Only now do I realize that it was all for us. This is thanks for all that you have done. This work is dedicated to you.

OK, it is time to begin. And this thesis will begin as all theses really should (Janet, this is for you).

`''It was a dark and stormy night...''`

A Physics

by Heather McHugh

When you get down to it, Earth
has our own great ranges
of feeling – Rocky, Smoky, Blue–
and a heart that can melt stones.

The still pools fill with sky
as if aloof, and we have eyes
for all this and more, for Earth's
reminding moon. We too are ruled

by such attractions– spun and swaddled,
rocked and lent a light. We run
our clocks on wheels, our trains
on time. But all the while we want

to love each other endlessly – not only for
a hundred years, not only six feet up and down.
We want the suns and moons of silver
in ourselves, not only counted coins in a cup. The whole idea
of love was not to fall. And neither was
the whole idea of God. We put him well
above ourselves, because we meant,
in time, to measure up.

Introduction

The discipline of neutrino physics is currently one of the most active areas of research in particle physics. Part of this enthusiasm is due to the fact that neutrinos have a vast impact on our understanding of natural laws. Knowledge of the basic properties of neutrinos has important implications for both particle physics, by providing the first window into physics beyond the Standard Model, and cosmology, by providing insight into how the universe evolves over time. It is the scope of this work to probe the properties of neutrinos in order to test various theories which extend beyond the accepted framework of the Standard Model.

This thesis documents two distinct searches for exotic particles performed at the NuTeV neutrino experiment at Fermilab. The first search focuses on exotic particles with masses below 0.3 GeV/c^2 which decay to electrons. The low mass study specifically addresses the KARMEN timing anomaly, which has been interpreted as a signal for an exotic particle with a mass of 33.9 MeV/c^2. The second search – the high mass search– focuses on particles with masses above 2.2 GeV/c^2. The latter is a more general search for exotic particles in a region previously unexplored.

This thesis is divided into four parts. Part I addresses topics that are common to both searches: theoretical foundations, detector descriptions, and general event reconstruction. Part II documents the NuTeV search for the KARMEN timing anomaly. Part III catalogs the details of the high mass search, along with possible interpre-

tations of the gathered results. Finally, Part IV summarizes the results from both searches and gives an outlook for future experiments.

Another search undertaken during this project – a search for lepton family number violation – is not discussed in the main text of this thesis. However, some highlights and details of the search are given in the Appendix.

Part I

The NuTeV Decay Channel

Chapter 1

Theoretical Background

I have done a terrible thing.
I have postulated a particle that cannot be detected.
- W. Pauli

1.1 History of the Neutrino

Since its original postulation by Wolfgang Pauli in 1930 [1] and Enrico Fermi in 1933 [2], the neutrino has provided the scientific community, as well as the general public, with a wealth of information about the fundamental workings of the natural world. The study of the neutrino led to the discovery of a new "weak" force, which led to a sound understanding of nuclear decay and a direct window into the basic symmetries of nature. Further study of the neutrino may provide a path into uncharted territory of new physics.

Although more than 70 years have passed since it was originally postulated, the neutrino is still the least understood particle in the Standard Model. Though its properties fit well within the context of the Standard Model, many questions regarding

its basic properties still remain unanswered. Do neutrinos have mass? If so, current experimental evidence demonstrates that it must be small [3]. Can an extremely small neutrino mass be explained by a larger, more encompassing theory? Do neutrinos have yet undetected partners that may explain their small mass? Does the neutrino possess a magnetic moment? Seventy years later these questions still remain, fueling the continued study of neutrino physics.

The neutrino was born out of Pauli's theory to explain the process of beta decay while maintaining energy conservation. As it was understood at the time, beta decay allowed an element to change its proton and neutron content via the emission of an electron:

$$(N, Z) \rightarrow (N-1, Z+1) + e^{-}. \tag{1.1}$$

Since this process is formulated as a two-body decay, the electron should be mono-energetic. However, a series of experiments demonstrated that the electron energy spectrum from β decay was broad, apparently indicating that energy was not conserved.

It was Pauli who first postulated that perhaps an additional particle was created in the decay. The particle would have to be of half-integer spin (to conserve angular momentum), have a small interaction probability, and have a small (though not necessarily vanishing) mass. A few years later, Enrico Fermi placed Pauli's particle into his theoretical framework of the weak force [4], thus providing a basis to explain beta decay within quantum field theory:

$$n \rightarrow p + e^{-} + \bar{\nu}_e. \tag{1.2}$$

Later, Hans Bethe calculated the cross-section for the reverse process, *inverse beta decay* [5]:

$$\overline{\nu}_e + p \rightarrow n + e^+. \tag{1.3}$$

Inverse beta decay introduced the physics community to a process by which the neutrino could interact, opening a window by which the neutrino could be directly detected in the laboratory. Reines and Cowan proceeded via a series of pioneering experiments in 1953-1956 to find evidence of neutrino interactions using nuclear reactors as their neutrino source [6]. Reines was awarded the Nobel Prize in 1995 for this discovery.

It was not until 1962 that experiments at Brookhaven were able to demonstrate the existence of a second neutrino, separate in character from the neutrino observed in beta decay [7]. The neutrino emitted in beta decay is always associated with the production of an electron. Experiments at Brookhaven, in combination with earlier work done by Pontecorvo and Schwartz [8, 9], were able to demonstrate the existence of a second type of neutrino, associated only with a muon, and never with an electron. This observation gave rise to the distinction between a muon neutrino (ν_μ) and an electron neutrino (ν_e), each associated with their respective lepton partners. Letterman, Schwartz, and Steinberger were awarded the 1988 Nobel prize in physics for their discovery.

When Perl discovered of a third family of leptons – the τ lepton – theory pointed to the existence of a third neutrino as well, the tau neutrino[10]. Direct observation of the tau neutrino occurred in 2000 by the DONUT experiment[11]. The existence of three, and only three, neutrino species was further confirmed by the LEP experiment at CERN [12]. By measuring the decay width of the Z^0 boson (a particle which couples directly to neutrinos), one can measure the number of species directly:

$$N_\nu(\Gamma_{Z^0}) = 2.994 \pm 0.012. \tag{1.4}$$

This result, along with many more not mentioned here, helped give a fuller understanding not just of neutrino physics, but of all particle physics.

1.2 Neutrino Physics and the Standard Model

The Standard Model is a coherent framework by which one can describe all particles and the forces exchanged between them [13]. The Standard Model categorizes particles according to their spin. Particles of spin $\frac{1}{2}$ are known as *fermions* and constitute all matter in the visible universe. The various fermions can participate in four known types of gauge interactions – electromagnetic, weak, strong, and gravitational – by exchanging particles of integer spin, known as *bosons*. Bosons serve as the carriers of forces between particles: photons carry the electromagnetic force, the $W^{\pm}$ and Z^0 bosons carry the weak force, and gluons carry the strong force. Gravity currently is the only known force which does not fit within the framework of the Standard Model. A complete list of all Standard Model fermions and bosons can be found in Table 1.1 and 1.2.

Fermions are further subdivided into leptons and quarks. The distinction between leptons and quarks is based on the particles which they are are able to exchange. Only quarks, for example, are able to couple to the strong force via the exchange of gluons. Charged leptons, on the other hand, couple only to the electromagnetic and weak forces. Finally, the neutral leptons (neutrinos) only couple to the weak force via the exchange of the $W^{\pm}$ and Z^0 bosons. Both the quarks and the leptons share the same structure, in that they are both divided into three separate generations.

The Standard Model also incorporates the existence of a massive spin 0 particle called the Higgs, which is responsible for attributing mass to both the vector bosons and all fermions. The Higgs is the sole particle yet to be directly observed at the time of this writing.

Table 1.1: Fermions and their properties.

Quarks

1st Gen.	2nd Gen.	3rd Gen.	Charge	Forces
u	c	t	$+\frac{2}{3}$	Electromagnetic, Strong, Weak
d	s	b	$-\frac{1}{3}$	Electromagnetic, Strong, Weak

Leptons

1st Gen.	2nd Gen.	3rd Gen.	Charge	Forces
e	μ	τ	-1	Electromagnetic, Weak
ν_e	ν_μ	ν_τ	0	Weak

Table 1.2: Bosons and their properties.

Bosons

Boson	Charge	Mass (GeV/c^2)	Force Carried
Photon (γ)	0	0	Electromagnetic
Gluon (g)	0	0	Strong
$W^{\pm}$, Z^0	± 1, 0	80.4, 91.2	Weak
Higgs (H^0)	0	> 114.1	Responsible for Masses

1.2.1 The Free Neutrino Field

The neutrino, as understood within the framework of the Standard Model, has some unique properties which distinguish it from other fermions. The neutrino, being a neutral lepton, possesses no color or electromagnetic charge. Therefore, the neutrino can only interact via $W^{\pm}$ and Z^0 exchange. The Standard Model neutrino is also the only fermion which has no mass. This property has important consequences regarding the spin nature of the neutrino, as will be explained below.

Let us first consider the neutrino field in terms of a free field, devoid of interactions or exchange of forces. In this context, the neutrino field is described by the following Lagrangian:

$$\mathcal{L} = i\overline{\psi}(\gamma^{\mu}\partial_{\mu} - m)\psi, \tag{1.5}$$

where ψ represents the neutrino field. This simplifies to the Dirac equation when solving for the field:

$$(\gamma^{\mu}\partial_{\mu} - m)\psi = 0. \tag{1.6}$$

Within the Standard Model, neutrinos are massless. This assumption is consistent with most direct experimental observations. It is also the simplest way to explain the feature of "handedness" associated with neutrinos. To understand handedness, it is simplest to begin by discussing "helicity," since for massless particles helicity and handedness are identical.

For a spin $\frac{1}{2}$ particle, helicity is the projection of a particle's spin ($\vec{\sigma}$) along its direction of motion $\hat{\mathbf{p}}$, with operator $\sigma \cdot \hat{\mathbf{p}}$. Helicity has two possible states: spin aligned opposite the direction of motion (negative, or "left helicity") and spin aligned along the direction of motion (positive or "right helicity"). If a particle is massive,

then the sign of the helicity of the particle will be frame dependent. When one boosts to a frame where one is moving faster than the particle, the sign of the momentum will change but the spin will not, and therefore the helicity will flip. For massless particles, hence traveling at the speed of light, one cannot boost to a frame where helicity changes sign.

Handedness (or chirality) is the Lorentz invariant (i.e. frame-independent) analog of helicity for both massless and massive particles. There are two states: "left-handed" and "right-handed". For the case of massless particles, including Standard Model neutrinos, helicity and handedness are identical. A massless fermion is either purely left-handed or right-handed, and, in principle, can appear in either state.

If one is to rewrite the Dirac equation for a massless particle, Equation 1.6 simplifies to the expression:

$$(\gamma^{\mu}\partial_{\mu})\psi = 0. \tag{1.7}$$

In this scenario, it is easier to represent the neutrino field in terms of left- and right-handed components (also known as *Weyl spinors*), since these components are eigenstates of the helicity operator.

Unlike the electromagnetic and strong interactions, the weak interaction involving neutrinos has a definite handedness. In the late 1950's, it was shown that neutrinos are left-handed and anti-neutrinos are right-handed [14]. To see how to include this in calculations, consider the following argument using the Weyl, or chiral, spinor representation. A spinor can be written in terms of left-handed and right-handed components, $\psi = \psi_L + \psi_R$, and operating with the matrix γ^5 gives: $\gamma^5\psi_{L,R} = \mp\psi_{L,R}$. We can project out the left-handed and right-handed portions of the general spinor, ψ through the operation:

$$\psi_{L,R} = \frac{1}{2}(1 \mp \gamma^5)\psi. \tag{1.8}$$

The above substitution allows us to rewrite the Dirac equation *solely in terms of chirality components* (with the appropriate mass term):

$$\mathcal{L} = i(\overline{\psi}_L + \overline{\psi}_R)(\gamma^\mu \partial_\mu - m)(\psi_L + \psi_R). \tag{1.9}$$

As will be shown later in this chapter, the concept of chirality is intricately connected with the concept of neutrino mass.

1.2.2 Electroweak Interactions

So far we have only discussed the case of the free field, where neutrinos are non-interacting particles. We wish to extend the discussion to include neutrino interactions with other particles via the exchange of bosons. Successful representation of interacting particles has come from constructing Lagrangians which are both Lorentz invariant and preserve gauge invariance. Under gauge invariance, a transformation of the type $\psi \rightarrow e^{i\alpha(x)}\psi$ leaves the equations of motion unchanged. One successful example of gauge invariance is found in describing the electromagnetic force. Consider once again the non-interacting Lagrangian:

$$\mathcal{L} = i\overline{\psi}(\gamma^\mu \partial_\mu - m)\psi. \tag{1.10}$$

If we apply the gauge transformation to ψ, one finds:

$$\mathcal{L} \rightarrow \mathcal{L} - \overline{\psi}\gamma^\mu \psi \partial_\mu \alpha(x). \tag{1.11}$$

Invariance can be restored if one replaces the partial derivative with a covariant derivative:

$$\partial_\mu \rightarrow \mathcal{D}_\mu \equiv \partial_\mu + ieA_\mu, \tag{1.12}$$

where, A_μ is a vector field and e is the coupling constant. The vector field A_μ has exactly the same properties as predicted by Maxwell's equations. Gauge invariance leads directly to a representation of the electromagnetic force. Such a local gauge invariance is known as a $U(1)$ symmetry.

One can consider more complex symmetries in trying to describe forces beyond electromagnetic interactions. It turns out that both the electromagnetic and the weak force can be described in a single gauge symmetry $SU(2) \times U(1)$. Under this symmetry, we consider the following transformation:

$$\psi \rightarrow e^{i\vec{\sigma}\cdot\vec{\alpha}(x)}\psi. \tag{1.13}$$

Here $\vec{\sigma}$ represents the ordinary Pauli matrices. The covariant derivative needed to keep the Lagrangian invariant is of the form:

$$\partial_\mu \rightarrow \partial_\mu + igB_\mu + ig'\vec{\sigma}\cdot\vec{W}_\mu. \tag{1.14}$$

Here, g and g' are coupling constants related to each interaction, and B_μ and $\vec{W}_\mu$ are independent gauge field potentials.

Glashow, Weinberg, and Salam proposed the $SU(2)\times U(1)$ symmetry as a possible method to explain the weak and electromagnetic interactions. As written, there are four vector fields available. By re-writing the vector fields as linear combinations of one another, one can extract the vector bosons responsible for both the weak and electromagnetic force:

$$W^{\pm} = (W^1 \mp iW^2)/\sqrt{2}; \tag{1.15}$$

$$Z_\mu = \frac{gW^3_\mu - g'B_\mu}{\sqrt{g^2+g'^2}}; \text{ and} \tag{1.16}$$

$$B_\mu = \frac{gW^3_\mu + g'B_\mu}{\sqrt{g^2+g'^2}}. \tag{1.17}$$

The "Higgs mechanism" in the theory predicts that the weak force carriers are massive, while the electromagnetic force carrier is massless (as expected for the photon). Having a complete theory of electroweak interactions, one can now write the full Lagrangian for neutrino interactions:

$$\mathcal{L}_{ew} = -\frac{e}{\sqrt{2}\sin\theta_W} j^\mu_\pm W^\pm_\mu - \frac{e}{\sin\theta_W \cos\theta_W} j^\mu_Z Z_\mu - e j^\mu_{em} A_\mu \tag{1.18}$$

where $\sin\theta_W \equiv g'/\sqrt{g^2+g'^2}$.

The j terms describe the appropriate current associated with each interaction. The currents are given as:

$$j^\mu_\pm = \frac{1}{2}\overline{\psi}_{L,R}\gamma^\mu\sigma_\pm\psi_{L,R}; \tag{1.19}$$

$$j^\mu_{em} = \overline{\psi}\gamma^\mu Q\psi; \text{ and} \tag{1.20}$$

$$j^\mu_Z = \frac{1}{2}\overline{\psi}\gamma^\mu(c_V - c_A\gamma^5)\psi; \text{ where} \tag{1.21}$$

$$\sigma_\pm = \sigma_1 \pm i\sigma_2 \text{ (Pauli matricies)} \tag{1.22}$$

The first term describes what is known as the charged current (CC) weak interaction. The charged current interaction exchanges charge between two fermions via

Table 1.3: Vector (c_V) and axial vector (c_A) couplings for fermions.

Fermion	c_V	c_A
ν_e, ν_μ, ν_τ	$\frac{1}{2}$	$+\frac{1}{2}$
e^-, μ^-, τ^-	$-\frac{1}{2} + 2\sin\theta_W{}^2$	$-\frac{1}{2}$
u, c, t	$\frac{1}{2} - \frac{4}{3}\sin\theta_W{}^2$	$+\frac{1}{2}$
d, s, b	$-\frac{1}{2} + \frac{2}{3}\sin\theta_W{}^2$	$-\frac{1}{2}$

the exchange of the $W^\pm$ boson. When a $W^\pm$ is emitted, charge conservation at the vertex requires that if a neutral (charged) lepton enters, then a charged (neutral) lepton exit the interaction. This is also called the flavor changing interaction, since it converts a neutrino to its charged partner. Note that the exchange occurs only between left-handed fermions because there is no evidence as of yet for right-handed neutrinos. The above term accounts for beta decay, inverse beta decay, and other neutrino processes.

The second term in the Lagrangian describes the neutral current (NC) interaction. In this case, particles exchange a massive vector boson known as the Z^0 boson. The c_V and c_A terms are directly related to the electromagnetic and weak charges of the particles and the Weinberg angle $\sin^2\theta_W$ (see Table 1.3)[17].

The third term is the ordinary electromagnetic interaction. It is proportional to the charge of the particles (Q) and thus is zero for neutrino interactions.

The Glashow-Weinberg-Salam model was a crowning achievement in particle physics, uniting the electromagnetic and weak force into a single theory. Together with electroweak symmetry breaking, the theory accounts for the fact that the weak bosons are massive, it accounts for the properties of the weak interaction (CP violation, V−A structure, etc.), and accurately predicts the mass ratio between the W and Z

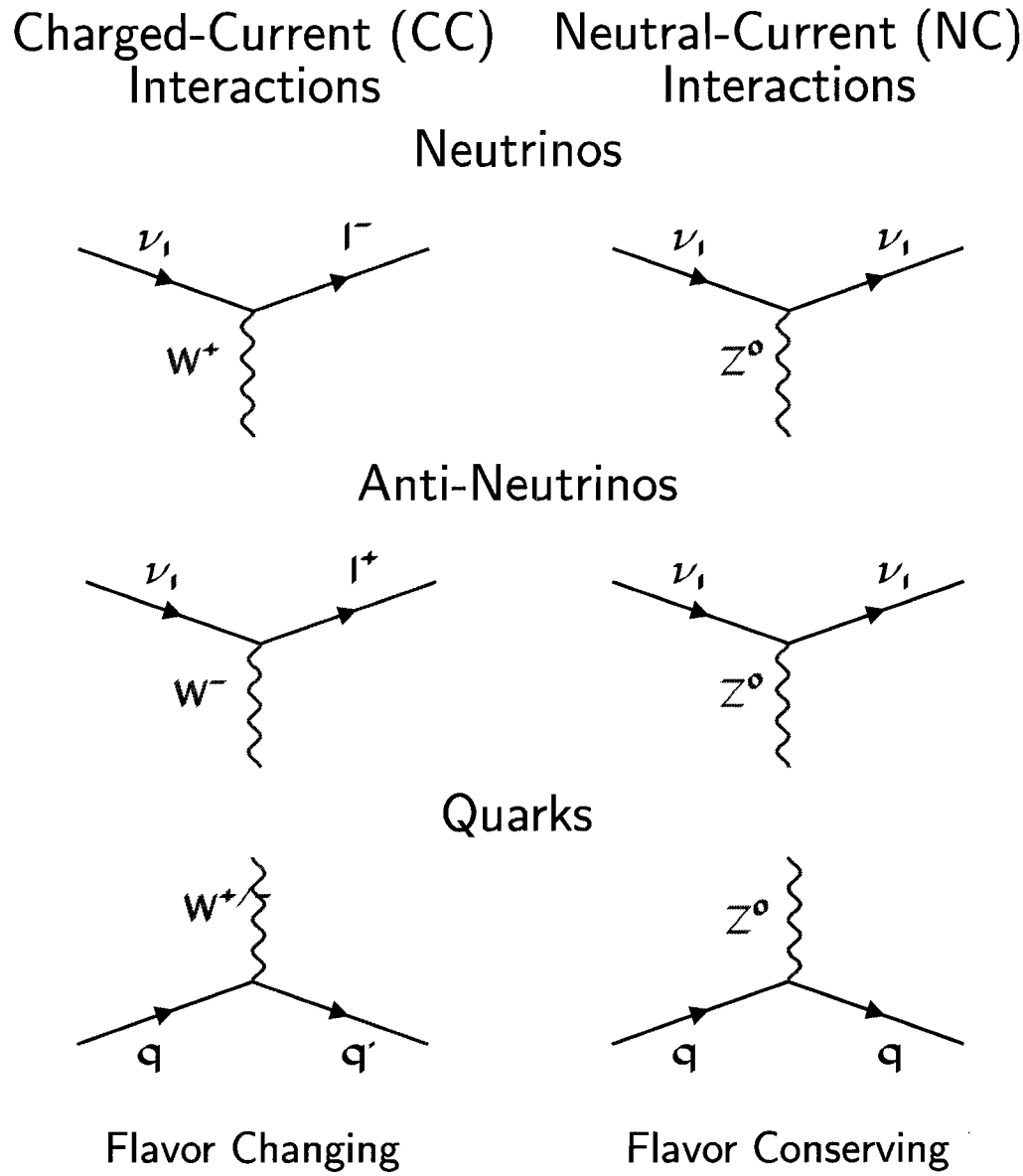

Figure 1.1: Feynman diagrams for charged current and neutral current interactions of neutrinos, anti-neutrinos, and quarks.

bosons. Along with the theory of the strong force ($SU(3)_C$), it provides the basis of the Standard Model.

1.3 Implications of Massive Neutrinos

Let us go back to the original free neutrino field and now consider the case where neutrinos do possess mass (Equation 1.9). There exist two distinct methods to attribute mass to a neutrino. The first method is to assign what is known as a Dirac mass. Mass terms in the Lagrangian arise from terms of the form $m\overline{\psi}\psi$. If we consider the left- and right- handed components separately, we find that the following terms survive:

$$m\overline{\psi}\psi = m(\overline{\psi}_R\psi_L + \overline{\psi}_L\psi_R). \tag{1.23}$$

(Note here that both terms $\overline{\psi}_L\psi_L$ and $\overline{\psi}_R\psi_R$ cancel).

The above expression works well for the charged fermions in the Standard Model, since such particles have both left- and right- handed components. This is not the case for the neutrino, however. So far, only left-handed neutrinos (or right-handed anti-neutrinos) have been observed. The existence of a Dirac mass term, therefore, implies the existence of right-handed neutrinos. The Standard Model would need to be extended to incorporate right-handed neutrinos to account for a Dirac mass term.

There exists a second mechanism to allow for neutrino mass. The neutrino is the only fundamental particle which is a neutral fermion. It is possible that the neutrino be its own anti-particle; such a particle is known as a *Majorana* particle. Under this premise, one can rewrite the neutrino field in terms of Majorana spinors rather than Dirac spinors:

$$\psi = \psi_L + \psi_R^c, \tag{1.24}$$

where ψ_R^c is the charge conjugate of the left-handed spinor. It is important to note that ψ_R^c is constructed solely from the left-handed neutrino, though it behaves exactly like a right-handed antineutrino. If neutrinos are really Majorana particles, then it is possible to have a mass term without having a right-handed neutrino:

$$m\overline{\psi}\psi = m(\overline{\psi}_R^c\psi_L + \overline{\psi}_L\psi_R^c). \tag{1.25}$$

Thus, the mass term is constructed entirely from the left-handed neutrino and right-handed antineutrino without needing to introduce a right-handed neutrino or a new vector boson. However, since the Majorana neutrino is its own anti-particle, lepton number is not conserved; which again violates the prediction of the Standard Model.

It is important to stress the point that the Standard Model, as currently formulated, *cannot account for neutrino mass.* If neutrino mass is confirmed, extensions to the Standard Model must be applied, either in the form of right-handed neutrinos (which may be difficult to observe) or via lepton-number violation. Introducing these terms into the Standard Model is possible, but it does suggest that there exists some deeper theory that allows one to explain such arbitrary insertions.

1.4 See-Saw Mechanism

As seen from the previous sections, the neutrino mass term can be introduced via a Dirac mass term or a Majorana mass term. In principle, the two terms are not mutually exclusive. In fact, the Lagrangian can possess both a left-handed *and* a

right-handed Majorana mass term. Thus, one can write the most general Lagrangian mass term as the following:

$$\mathcal{L} = m_D(\overline{\psi}_R\psi_L + \overline{\psi}_L\psi_R) + \frac{1}{2}m_L(\overline{\psi}^c_R\psi_L + \overline{\psi}_L\psi^c_R) + \frac{1}{2}m_R(\overline{\psi}^c_L\psi_R + \overline{\psi}_R\psi^c_L). \quad (1.26)$$

Notice that we have introduced a new right-handed field ψ_R to accommodate both the Dirac and right-handed Majorana term. The whole expression of Equation 1.26 can be rewritten simply as:

$$\mathcal{L} = m_D(\overline{\phi}_R\phi_L + \overline{\phi}_L\phi_R) + m_L(\overline{\phi}_L\phi_L) + m_R(\overline{\phi}_R\phi_R). \quad (1.27)$$

For simplicity, we define $\phi_{L,R} = \psi_{L,R} + \psi^c_{L,R}$. The equation can also be rewritten as:

$$\mathcal{L} = (\bar{\phi}_L\ \bar{\phi}_R)\mathcal{M}\begin{pmatrix} \phi_L \\ \phi_R \end{pmatrix}. \quad (1.28)$$

Equation 1.28 is a matrix equation where $\mathcal{M}$ contains both the Dirac and Majorana mass terms:

$$\mathcal{M} = \begin{pmatrix} m_L & m_D \\ m_D & m_R \end{pmatrix}. \quad (1.29)$$

The mass matrix implies that the weak eigenstates are not identical to the mass eigenstates, and that in fact there exists mixing between the two states. Solving for the weak eigenstates from the above equation leads to the following relation:

$$|\nu_i\rangle = \cos\theta|\phi_L\rangle + \sin\theta|\phi_R\rangle, \text{ and} \quad (1.30)$$

$$|L^0\rangle = -\sin\theta|\phi_L\rangle + \cos\theta|\phi_R\rangle. \tag{1.31}$$

where $\tan(2\theta) = \frac{2m_D}{m_R - m_L}$, $|L^0\rangle$ is the eigenstate of the right-handed Majorana state, and $|\nu_{i=e,\mu,\tau}\rangle$ is the weak eigenstate of the ordinary neutrinos. The matrix equation also leads to the mass eigenvalues for states ν_i and L^0:

$$m_{\nu_i} = \frac{1}{2}\sqrt{4m_D^2 + (m_R - m_L)^2} - \frac{m_L + m_R}{2}, \tag{1.32}$$

$$m_{L^0} = \frac{1}{2}\sqrt{4m_D^2 + (m_R - m_L)^2} + \frac{m_L + m_R}{2}. \tag{1.33}$$

By making the assumption $m_L \ll m_D \ll m_R$, the above expressions become much simpler:

$$m_{\nu_i} \approx \frac{m_D^2}{m_R}, \tag{1.34}$$

$$m_{L^0} \approx m_R, \text{ and} \tag{1.35}$$

$$\theta^2 \approx \frac{m_{\nu_i}}{m_{L^0}} \equiv U_i^2. \tag{1.36}$$

The above simplification is known as the *see-saw mechanism*, since the mass eigenstate of the light neutrinos is inversely proportional to the heavy mass state. We have thus introduced a new massive particle into the theory. Such a particle, known as a *neutral heavy lepton* or *sterile neutrino* cannot couple directly to the $W^\pm$ or Z^0 boson, since these bosons only couple to left-handed particles. Instead, it can only interact via *mixing* with its lighter neutrino partner (see Figures 1.2 and 1.3). The rate at which this mixing takes place is governed by the mixing parameter U_i^2, which in the see-saw mechanism is directly related to the mass of the particles. In the see-saw mechanism, both the light and heavy states behave as Majorana particles,

masses and neutrino oscillations. In so doing, the model has introduced a right-handed isosinglet partner to the neutrino which can be observed in the laboratory. Part of the attraction of a generic model such as the see-saw mechanism comes from the fact that many extensions to the Standard Model lead to this exact framework[15]. One class of such theories, known as *Grand Unified Theories* (GUTs), is constructed to unify the strong and electroweak interactions much the same way the electromagnetic and the weak interactions are united into the electroweak theory. Grand Unified Theories resort to higher gauge symmetries (such as $SU(5)$ and $SO(10)$); under such frameworks, the quarks and leptons are united into a single representation. This has the following consequences: (1) strong, electromagnetic, and weak forces are all manifestations of a single force; (2) neither lepton nor baryon number is conserved (leading to proton decay); (3) heavy right-handed neutrinos are naturally introduced into the theory; and (4) a mechanism for neutrino mass – as well as theoretical justification as to why left-handed neutrino masses are so small – is provided.

A crucial test of the validity of GUT will be in the signature of proton decay, which is predicted by the theory [19]. However, studies of neutrino mass and the existence of other massive neutrinos may also provide evidence (at least, indirectly) to the theory of Grand Unification.

1.6 Phenomenology

From an experimental standpoint, one places emphasis not on the theoretical framework which gives rise to heavy neutrinos, but rather the generic properties by which such particles are produced and detected. Thus, one wishes to produce an expression that will enable one to search for a given particle without necessarily being sensitive to the particular details of the given model.

From the previous section, it is clear that any experiment which has the capability

to produce neutrinos also has the capability to produce L^0's. Since neutrinos are produced from meson decays, one can normalize the probability of producing an L^0 particle versus producing a neutrino:

$$N_{L^0} = N_{meson} \cdot BR(meson \to L^0). \tag{1.37}$$

where $BR(meson \to L^0)$ is the branching ratio of a meson decaying to an L^0 particle.

This time, however, we must treat the neutrino weak eigenstates as mixtures of the neutrino mass eigenstates:

$$|\nu_\alpha\rangle = \Sigma_i U_{\alpha i} |\nu_i\rangle, \tag{1.38}$$

where i and α take on the values of the three ordinary neutrinos (e, μ, τ), plus a fourth L^0 state. This is simply an extension of the notation introduced in the previous sections. To get the proper branching ratio, one needs to sum over all allowed states:

$$\frac{BR(\text{meson} \to L^0)}{BR(\text{meson} \to \nu)} = \frac{\Gamma(\text{meson} \to L^0)}{\Sigma_i\, \Gamma(\text{meson} \to \nu_i)} \approx U^2 \Phi. \tag{1.39}$$

Here, N_{meson} is the number of mesons present in the beam, BR is the branching ratio for a particular meson decay to L^0's or neutrinos, and Φ is the phase space suppression due to the L^0 mass. In the case where the meson undergoes a two-body decay (i.e. $\pi \to \mu L^0$), Φ can be solved explicitly:

$$\Phi = \sqrt{\lambda} \cdot \frac{(\delta_l + \delta_{L^0} - (\delta_l - \delta_{L^0})^2)}{\delta_l (1 - \delta_l)^2}, \text{ where} \tag{1.40}$$

$$\lambda = 1 + \delta_l^2 + \delta_{L^0}^2 - 2\delta_l - 2\delta_{L^0} - 2\delta_l \delta_{L^0}, \tag{1.41}$$

$$\delta_l = \frac{m_l^2}{m_{\text{meson}}^2}, \text{ and} \tag{1.42}$$

$$\delta_{L^0} = \frac{m_{L^0}^2}{m_{\text{meson}}^2}. \tag{1.43}$$

Here m_i refer to the masses of the meson, lepton, or L^0. We have assumed a V−A type of interaction for the above expression. Note that Φ is a pure kinematic factor and thus depends only on the masses of the particles involved. For the case of three-body decays (i.e. $B^+ \to D^0\mu^+L^0$), non-closed expressions do exist which calculate the branching ratios properly [20].

Since the L^0 is massive, it remains unstable and thus decays into lighter particles. Both partial and total decay widths have been computed assuming the L^0 mixes with ordinary neutrinos [20, 21]. In addition, one can consider the effects of polarization on the kinematics of the decay (see Appendix B) [23]. If one computes the lifetime (τ), then one can calculate explicitly the number of L^0's which will decay.

$$N_{L^0}^{seen} = N_{L^0}\mathcal{L}(\tau) \cdot \epsilon \cdot \frac{\Gamma_{vis}}{\Gamma_{tot}}, \text{ where} \tag{1.44}$$

$$\mathcal{L}(\tau) = e^{-\frac{z_b}{\gamma\beta c\tau}} \cdot (1 - e^{-\frac{z_d}{\gamma\beta c\tau}}). \tag{1.45}$$

Here, γ and β are the ordinary relativistic variables for the L^0, z_b is the longitudinal distance from the detector to the production source, z_d is the length of the detector, ϵ is the efficiency of the given detector, and Γ_{vis} and Γ_{tot} refer to the partial and total decay widths of the L^0 particle. If one assumes that the decay products are massless, then the lifetime of the L^0 particle is approximately:

$$\tau \approx \frac{192\pi^3}{G_F^2 m_{L^0}^5 U^2}. \tag{1.46}$$

We can now put all the above expressions together to calculate explicitly the number of L^0 events one would expect to see in a given detector.

$$N_{L^0}^{seen} = U^2 \cdot N_{\text{meson}} \cdot \epsilon \cdot \frac{\Gamma_{vis}}{\Gamma_{tot}} \cdot \Phi \cdot \mathcal{L}(\tau). \tag{1.47}$$

Note that in the limit of long lifetimes, this expression becomes sensitive only to the partial width. As an example, take the case of a 100 GeV L^0 particle with a mass 30 MeV/c^2 and mixing parameter of $U^2 = 10^{-3}$. If the beam produces 1.5×10^{15} pions at about 1 km away from the detector, and if the detector is approximately 30 meters in length, then would would expect to see about 25 events in the fiducial region of the detector (assuming perfect efficiency).

Apart from the U^2 term, which is specific to sterile neutrino mixing, the above expression holds true for *any* particle produced from meson decay and which later decays in a far detector. It is thus generic for both low mass particles and high mass particles. With minor alterations, one can similarly describe exotic particle production from pair production, rather than meson decay:

$$N_{L^0}^{seen} = N_{pot} \cdot d \cdot N_A \cdot \rho \cdot (\frac{d\sigma}{d\Omega} \cdot d\Omega) \cdot \epsilon \cdot \frac{\Gamma_i}{\Gamma_{tot}} \cdot L(\tau), \tag{1.48}$$

where N_{pot} is the total number of protons on target, d is the length of the target, N_A is Avogadro's number, ρ is the target density, $d\sigma/d\Omega$ is the differential cross-section, and $d\Omega$ is the solid angle subtended by the detector. Such parameters depend only on the specifics of the detector, rather than a particular theoretical model.

The above expressions thus hold true for non-sterile neutrino events as well other long-lived, weakly-interacting neutral particles, such as neutralinos and other supersymmetric particles [24]. This allows a given experiment to remain fairly flexible to search for a given phenomenon regardless of the specific mechanism involved. The above expressions will be used for both the high mass and low mass searches.

Chapter 2

The NuTeV Neutrino Detector

In searching for the existence of non-Standard Model particles, an ideal experiment must have at its disposal both the means to produce such particles and the means to detect them. In the case of particles such as neutral heavy leptons and massive sterile neutrinos, high intensity neutrino facilities provide the necessary conditions for such searches to take place.

High energy neutrino beamlines are ideal places to produce L^0 particles, since large numbers of protons interact in these beamlines. L^0's may be produced by a number of available mechanisms. Some of these mechanisms include:

- Primary interactions of the protons with the target.
- Decays of mesons produced in the target, including non-prompt pions and kaons, and prompt charmed and bottom mesons.
- Neutrino interactions in the shielding material preceding the main neutrino detector.

The NuTeV neutrino experiment at Fermilab (E815) [25] has constructed a dedicated helium decay channel to search for non-Standard Model particles [26]. The

instrumented decay channel makes use of the high energy neutrino beam as a potential source of L^0 particles. The decay channel employs a helium decay region in order to minimize the background from neutrino-nucleon interactions, and a series of drift chambers to track the decay products of the L^0. With this decay channel, NuTeV achieves increased sensitivity in detecting exotic particles. In this chapter, I describe the general elements of the detector. Details in performance relevant to the analyses in this thesis are provided in later chapters.

2.1 The Neutrino Beamline

The Fermilab TeVatron accelerator provides NuTeV with the high-energy protons necessary for the production of NuTeV's intense neutrino beam. The Fermilab TeVatron ring is currently the most energetic accelerator in the world. Protons are accelerated to energies as high as 980 GeV for the collider operation, and up to 800 GeV for the fixed target beamlines. The production and acceleration of protons to these high energies occurs via several stages, as shown schematically in Figure 2.1.

The protons used by the TeVatron and fixed target lines are originally transported in the form of H^- ions collected by a cesium cathode immersed in hydrogen gas. The H^- ions are accelerated to 750 KeV using multiple electrostatically-induced potential drops; they are then passed to the Linac, where their energy is increased to 200 MeV. At this point, the ions are stripped of their electrons by passing them through a carbon foil as they exit the Linac. The protons then enter the 70 m radius Booster ring, where they are accelerated to 8 GeV. The protons are next injected into the Main Ring – a 1 km radius synchrotron ring which can accelerate the protons to 150 GeV in energy. Finally, the protons are channeled into the TeVatron where they are either accelerated to 1 TeV collider energies, or they are accelerated to 800 GeV and passed to the fixed target beamlines.

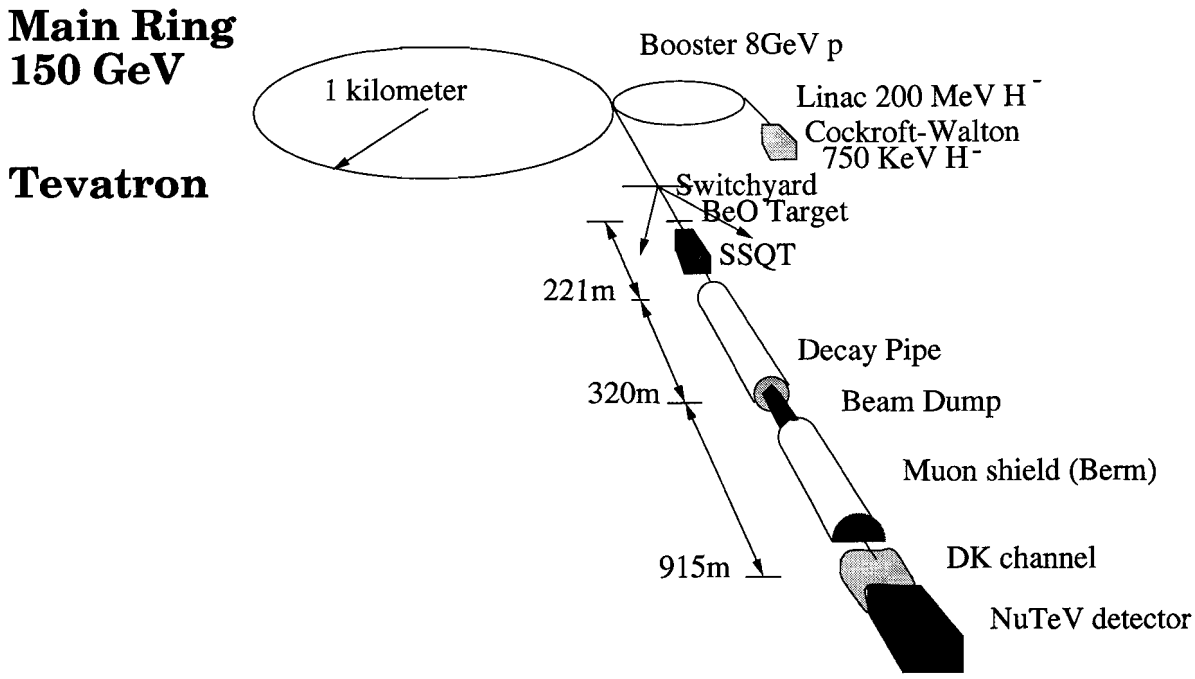

Figure 2.1: Fermilab Tevatron and Fixed Target Area

One important feature of the incoming proton beam is its timing structure. Short, intense proton pulses give the neutrino beam a distinct timing signature which allows neutrino events to be separated from the continuous cosmic ray background. A schematic of the timing structure of the proton beam is shown in Fig. 2.2. NuTeV receives the 800 GeV protons over a 60-second cycle. Each cycle contains both a fast spill (total duration: 2 s) and a slow spill (total duration: 18 s). The fast spill is delivered in a series of 5 short pulses ("pings"), 5 ms long and 0.5 s apart. NuTeV receives on average about 2×10^{12} protons on target per ping.

The slow spill, following 1.4 seconds after the fast spill, is used as the NuTeV calibration beam. The calibration beam delivers muons, electrons, and hadrons with specified energies ranging from 4 to 190 GeV. The beam thus provides a simultaneous calibration of the calorimeter response throughout the fixed target run.

NuTeV produces its high energy neutrino beam from proton interactions with

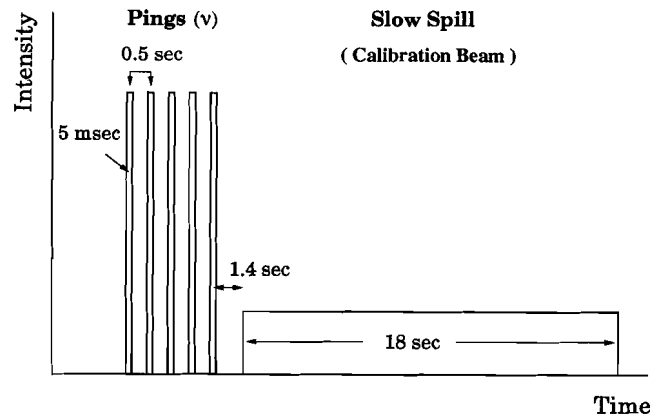

Figure 2.2: Timing structure for NuTeV primary proton beam.

a one-interaction length (30.5 cm) beryllium oxide (BeO) target. Pions and kaons produced in the interaction are focused using the Sign-Selected Quadrupole Train (SSQT)[28]. The SSQT is a series of dipole and quadrapole magnets designed to bend and focus only pions and kaons of a particular charge. The charge-selected mesons are focused down into a 541 m long evacuated decay region, which is angled at 7.8 mr with respect to the primary proton beam, and pointed toward the detector. All other particles – including protons, pions and kaons with the opposite charge, and neutral particles – are pointed away from the detector and stopped at series of beam dumps. The correct-sign mesons later decay in the pipe, to produce neutrinos. A steel dump located at the end of the pipe absorbs any remaining protons or mesons. A total of $(1.4 \pm 0.1) \times 10^{15}$ pion decays and $(3.6 \pm 0.4) \times 10^{14}$ kaon decays occurred in the pipe during the running of the experiment.

The SSQT configuration brings about two important consequences for the experiment. First, since only pions and kaons of a given charge are focused toward the detector, NuTeV can select between neutrino and anti-neutrino running, with positively charged mesons giving neutrinos and negatively charged mesons giving anti-neutrinos. Second, by focusing only charged particles, NuTeV systematically reduces the number of unwanted ν_e's in the beam produced from neutral kaon decays.

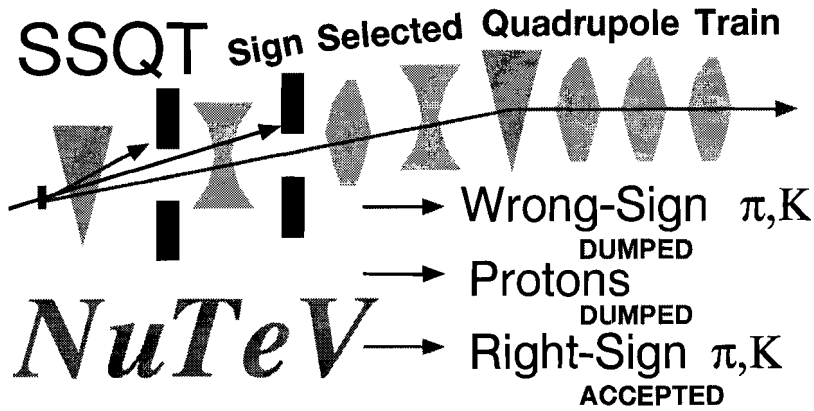

Figure 2.3: NuTeV's Sign-Selected Quadrupole Train (SSQT)

Table 2.1: Breakdown of neutrino beam composition.

Decay Process	Fraction in ν mode	Fraction in $\overline{\nu}$ mode
$\pi \rightarrow \mu\ \nu_\mu$	78.6%	85.6%
$K \rightarrow \mu\ \nu_\mu$	20.1%	13.3%
$K \rightarrow \pi\ e\ \nu_e$	1.24%	0.81%
Wrong Sign Neutrino	0.16%	0.29%

The end result is an extremely pure ν_μ (or $\overline{\nu}_\mu$) beam pointed toward the NuTeV detector. During each running mode, the beam contamination was small: less than 2% of the beam contained ν_e's and less than 0.3% of the beam contained neutrinos of the wrong sign. Integrating over the entire 1996-97 fixed target run, NuTeV received a total of 3.15×10^{18} protons on target. The fractional running times for neutrino and anti-neutrino modes were 45.5% and 54.5% respectively. The NuTeV decay channel was not active during the early part of the run; thus the total number of protons received while the decay channel was fully operational was 2.55×10^{18} protons on target. For this subset of the data, the $\nu : \bar{\nu}$ ratio is 1:1.24.

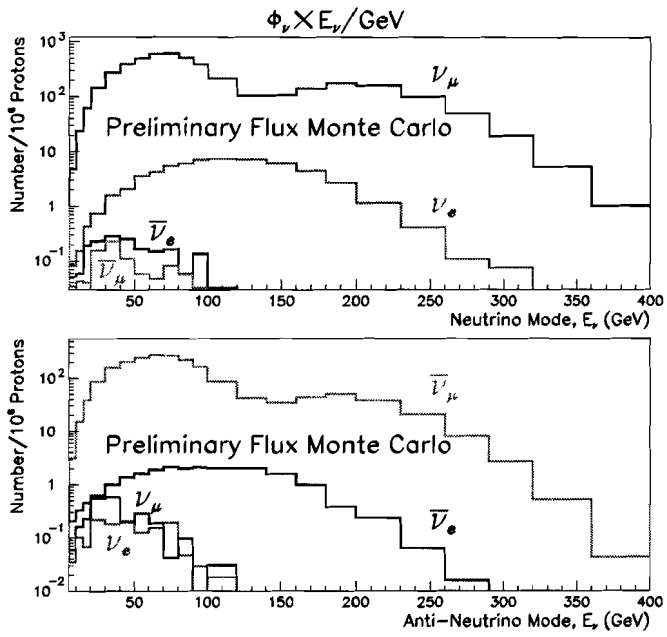

Figure 2.4: Flux distributions for ν_μ, $\bar{\nu}_\mu$, ν_e, and $\bar{\nu}_e$ in neutrino (top) and anti-neutrino (bottom) running.

The corresponding neutrinos and L^0's produced by the NuTeV sign-selected beamline finally traverse an additional 915 m before reaching the detector (241 m of steel shielding; 582 m of earth-berm shielding). This ensures that the only remaining particles which reach the detector from the primary target are sterile or weakly-interacting. However, it should be noted that the NuTeV beamline was designed primarily to measure $\sin^2\theta_W$, and thus is not optimized for an L^0 decay search.

2.2 The Decay Channel

The NuTeV decay channel (see Figure 2.5; also described in [27]) is located 1.4 km downstream of the neutrino production target. The decay channel consists of three main components:

- Veto wall,
- Helium bags, and
- Drift chambers.

The veto wall ensures that NuTeV trigger only on neutral particles entering the decay channel. Once the L^0 enters the decay channel, the helium bags provide a low-mass background region where the particle can decay. Finally, the drift chambers track all charged decay products and thus allow for full reconstruction of the kinematics of the event. The search is further aided by the presence of the main NuTeV high mass neutrino detector, located downstream of the decay channel. The first part of this detector, the NuTeV sampling calorimeter, provides both particle identification and hadronic energy measurement for any tracks entering from the decay channel region. The second part of the detector, the magnetic spectrometer, provides energy measurements for muon tracks. The use of both the instrumented decay channel and the sampling calorimeter enables NuTeV to have increased sensitivity to L^0 decays.

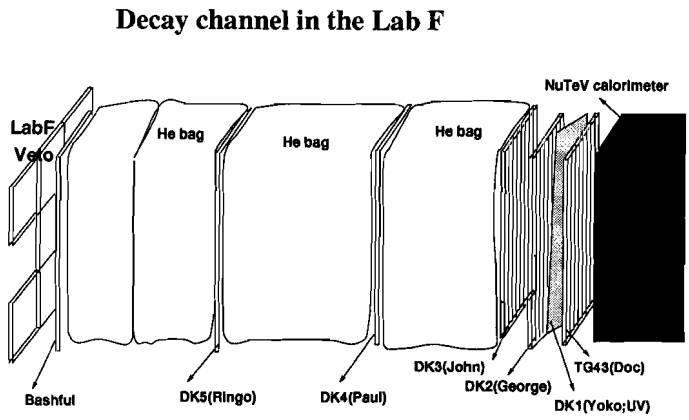

Figure 2.5: NuTeV decay channel, showing the veto wall, helium bags, six drift chambers, and calorimeter.

2.2.1 Veto Wall

The Lab F veto wall provides the detector with the means necessary to determine that the particles entering the decay channel volume have zero charge. The veto wall operates by looking for scintillation light emitted by charged particles passing through each panel. The veto wall consists of 19 scintillation panels arranged into two adjoining walls. Each scintillator panel is composed of Bicron BC-408 and enveloped in black covering to prevent optical leaks. Sixteen of the 19 panels measure 152.4 cm $\times$ 152.4 cm $\times$ 2.54 cm; the remaining three are smaller, measuring 50.8 cm $\times$ 228.6 cm $\times$ 1.27 cm. Each panel overlaps with its neighbors to ensure that there are no gaps between the two walls. At each panel, photomultiplier tubes (PMTs) are attached to green shifter bar light guides that cover the edges of the counter. As a charged particle passes through the scintillator, visible and near ultra-violet light is created and then sent via wave guides to the PMTs. The PMTs convert the collected light into an electrical signal which is then sent to the veto wall electronics. A schematic of the veto wall array is shown in Fig. 2.6.

The signal from the PMTs is used to determine whether a charged particle has

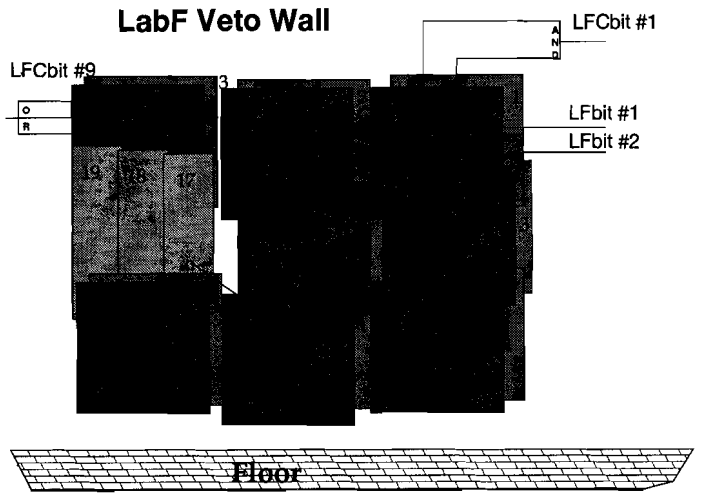

Figure 2.6: Schematic of veto wall array.

entered the decay channel volume. A schematic of the logic used to arrive at a veto wall trigger is shown in Fig. 2.7. The signals from the two PMTs are combined via a logical fan-in module, and are discriminated at a level which separates particle activity from noise. In the case of the smaller scintillator panels, the logical OR of all three tubes is used instead. The resulting output pulse is known as an "LFbit". The LFbit is stored along with the time at which a given panel was activated.

As a charged particle enters from upstream of the detector, it activates panels in both the upstream and downstream veto wall arrays. To take advantage of this scenario, the veto wall triggering searches for coincidences between scintillator panels which occupy the same transverse position. The LFbits from two facing panels are combined into a coincidence LFCbit. There are a total of 19 LFbits and 10 LFCbits in the veto wall array. The ninth LFCbit is the logical OR of all smaller panels, while the tenth LFCbit is the logical OR of the remaining 9 LFCbits.

Hits in the upstream veto wall are recorded with a multi-hit time-to-digital converter. On average, 1.7 counters will fire per trigger. The timing resolution of the veto wall panels is 3.8 ns. The average efficiency per panel for vetoing charged particles

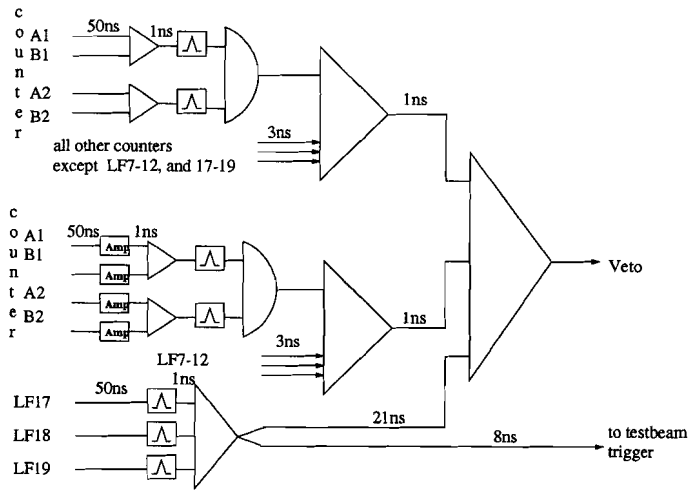

Figure 2.7: Logic for veto wall trigger.

entering the decay channel is $99.88 \pm 0.01\%$. This efficiency is measured both from cosmic ray studies (performed off-line) and from muons entering from upstream of the decay channel. The overall rejection efficiency of the veto wall is $99.94 \pm 0.01\%$.

2.2.2 Drift Chambers

In performing an L^0 decay search, it is essential that backgrounds that can mimic signal events be minimized or completely removed. This background reduction can be achieved both from clever selection criteria *and* optimal detector construction. In the case of the NuTeV decay channel, the instrumented decay volume is optimized for searches by providing a low-mass environment for L^0 particles to decay with little material for interactions. This feature ensures that the background from neutrino-nucleon scattering is substantially reduced.

To construct the low-mass environment, the fiducial volume of the decay channel consists of a series of helium bags interspersed with drift chambers. The drift chambers are able to track the particles from the decay and reconstruct the point of origin. A total of six drift chambers are present in the decay channel. From upstream

to downstream, the chambers are labeled DK5 through DK1, followed by TG43 at the front face of the neutrino detector. A NuTeV calibration beam drift chamber (Bashful) is positioned immediately downstream of the veto wall and offset from the center of the decay channel. This chamber is not used in this analysis, but is included as a source of material for background calculations.

Each drift chamber is divided into two views; each designed to record the x (y) position of incoming tracks. All panels contain 24 vertical (horizontal) aluminum cells; each cell measuring 12.7 cm across and 1.9 cm thick. The cells are filled with a 50-50% ethane-argon gas mixture. A single, high-voltage gold-plated tungsten wire runs along the center of each cell (see Fig. 2.8). As a charged particle passes through the gas mixture, ionized electrons are created and collect along the wire. The ethane gas quenches the electrons that cascade near the wire to achieve faster response times. The electric field used to focus the electrons is shaped using copper-clad G-10 plates mounted along the side of the aluminum cell. A full catalog of the various materials in the drift chamber can be found in Table 2.2. The average mass of each drift chamber is 2.87 g/cm^2.

As mentioned above, chambers DK5 through DK1 contain a single sense wire per cell ("single-wire" chambers), resulting in a left-right ambiguity in the hit position. This ambiguity is reduced by staggering the positions of the single-wire chambers in x and y. Chamber TG43 is of a "three-wire" (two sense wires and one field-shaping wire per cell) design, which helps resolve any remaining left-right ambiguities.

Positions of charged particles passing through each drift plane are measured using the drift times of the electrons to travel across the aluminum cell. Drift speeds in the ethane-argon mixture average 52 μm/ns. In order to ensure proper tracking resolution, care is taken to align each drift chamber. Alignment accounts for any offsets in the position, timing, or drift velocity of each drift chamber panel. To align each chamber, we have used a sample of straight-through muons. The muons are required to

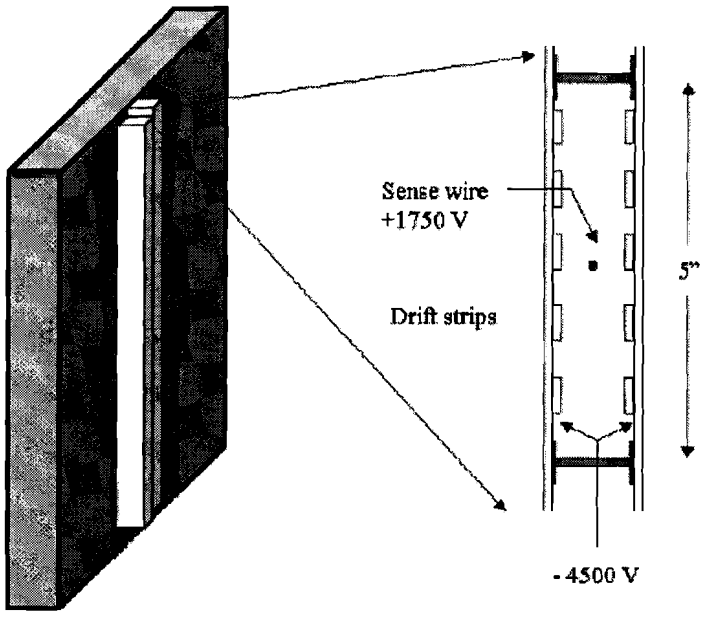

Figure 2.8: Sketch of the decay channel single-wire drift chambers.

Table 2.2: Material composition of decay channel drift chambers.

Component	Material	Length (cm)	Density (g/cm^3)	Mass (g/cm^2)
Al hexcel	Al	0.32	2.70	0.86
Al I-beam	Al	0.06	2.70	0.15
G10	SiO_2-CH_2O	0.64	1.70	1.12
Copper wire	Cu	0.08	8.96	0.74
Gas	Ar-C_2H_6	1.91	0.0016	0.00
Total for drift chamber		3.65		2.87
Helium gas	He	3400	0.00018	0.61

traverse the entire decay channel and calorimeter and to have a total energy above 50 GeV. The high energy requirement allows greater sensitivity to misalignments rather than to multiple scattering. The muons are also required to have a small angle with respect to the beam axis ($\leq$ 20 mr). In order to remove bias from cosmic ray activity, the muon also has to be within $\pm$76.2 cm of the center of the detector.

Individual hits from a given chamber are compared with muon track projections in order to determine the resolution of each drift plane (see Fig 2.9). Track projections take into account multiple scattering effects on the muon trajectory (which is why the downstream chambers have broader residuals than the upstream chambers). The average intrinsic resolution of all decay channel chambers, after subtracting multiple scattering effects (including correlations), is 380μm.

In addition, it is possible to compare the overall alignment of the decay channel drift chambers with the main calorimeter. This coordinate alignment is done by comparing the muon track projections and slopes of the decay channel to those of the calorimeter. Figure 2.10 shows that the calorimeter and decay channel coordinate systems match within tolerance levels.

Decay channel drift chambers were reasonably efficient throughout the fixed target run. However, on certain occasions drift chambers did fail to function. One common cause for this inefficiency was the surrounding helium bags placing any stress or strain on a chamber. The inefficiency of individual cells was measured by looking at the cell's hit occupancy from straight-through muons. The overall decay channel single track inefficiency due to malfunctioning or inefficient cells was $3.3 \pm 0.1\%$. The above measurement takes into account only the inefficiency of individual cells; it does not include correlation efficiencies between multiple cells, or the overall inefficiency of an entire plane. An attempt has been made to try to measure correlated inefficiencies between the x and y drift planes. For one chamber (DK4), we measured a correlated inefficiency of $0.1 \pm 0.07\%$. Finally, there was an additional overall inefficiency due to

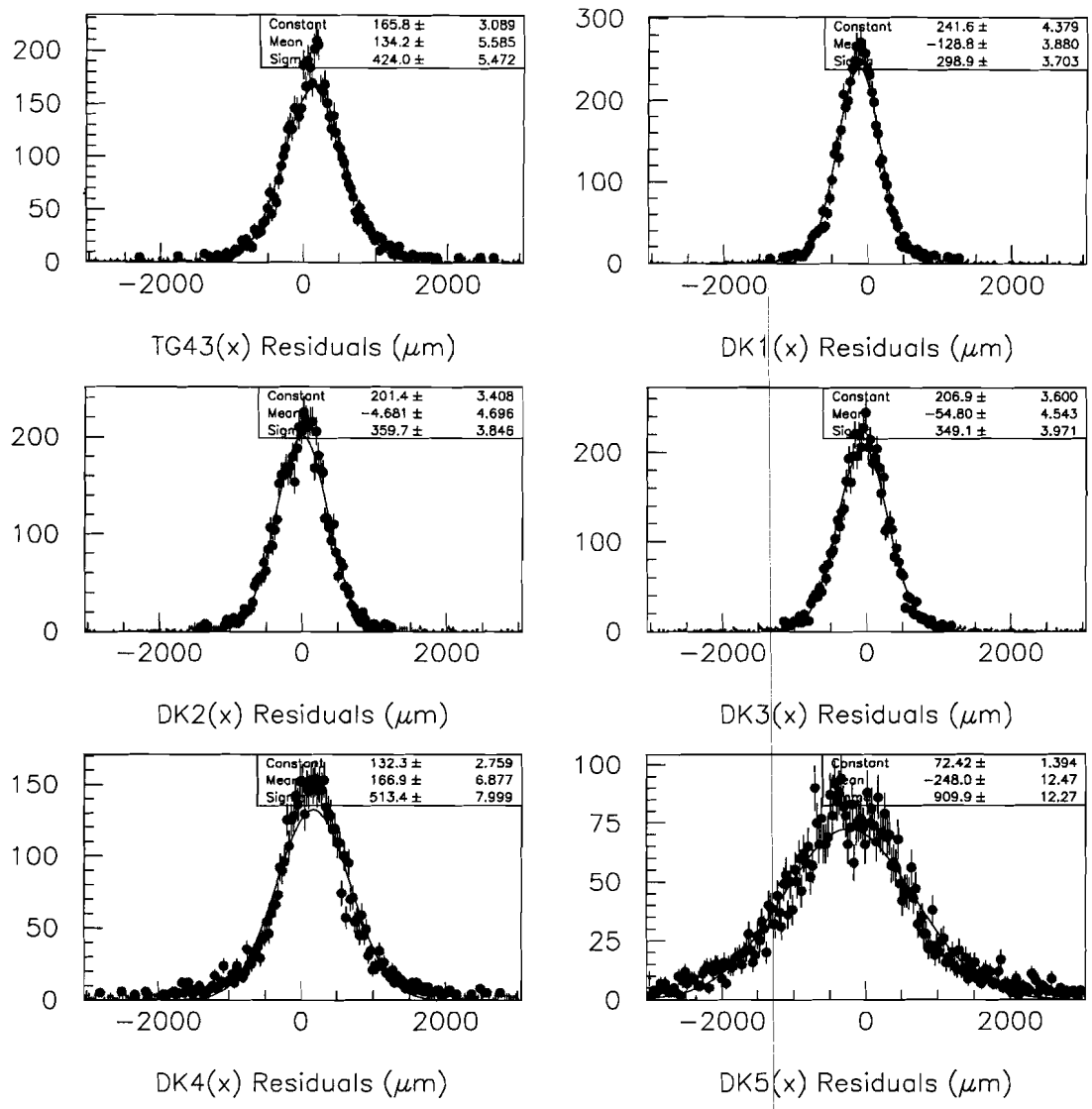

Figure 2.9: Residuals of the decay channel drift chambers (x planes only). Residual distributions are fit to Gaussian functions to determine the average resolution of each chamber for a given data run period.

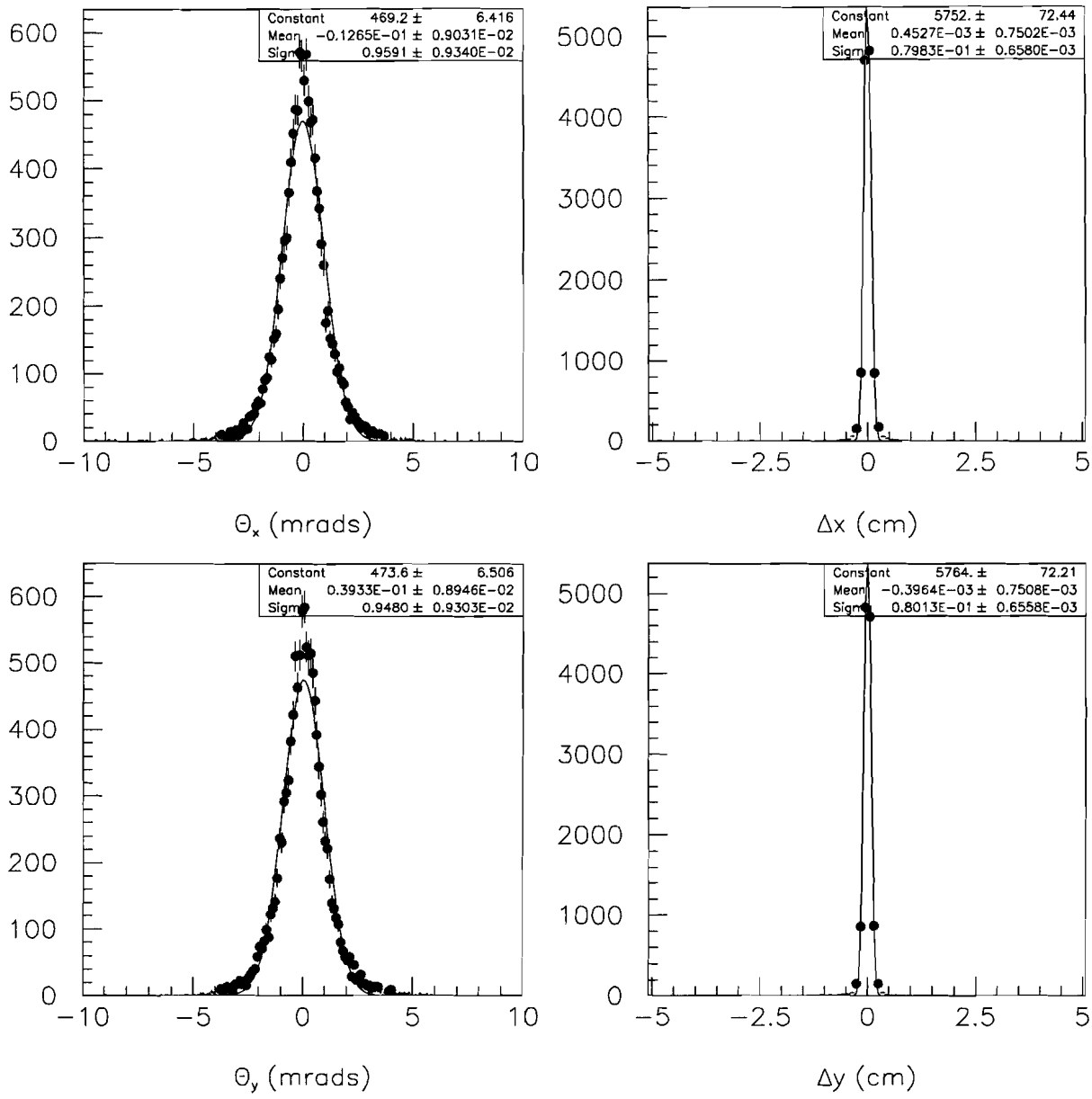

Figure 2.10: Residuals between decay channel and calorimeter tracks for muons traversing the NuTeV experiment for the x (top) and y (bottom) planes. Any position or angle misalignment between the calorimeter and decay channel would appear as an overall offset in the above distributions.

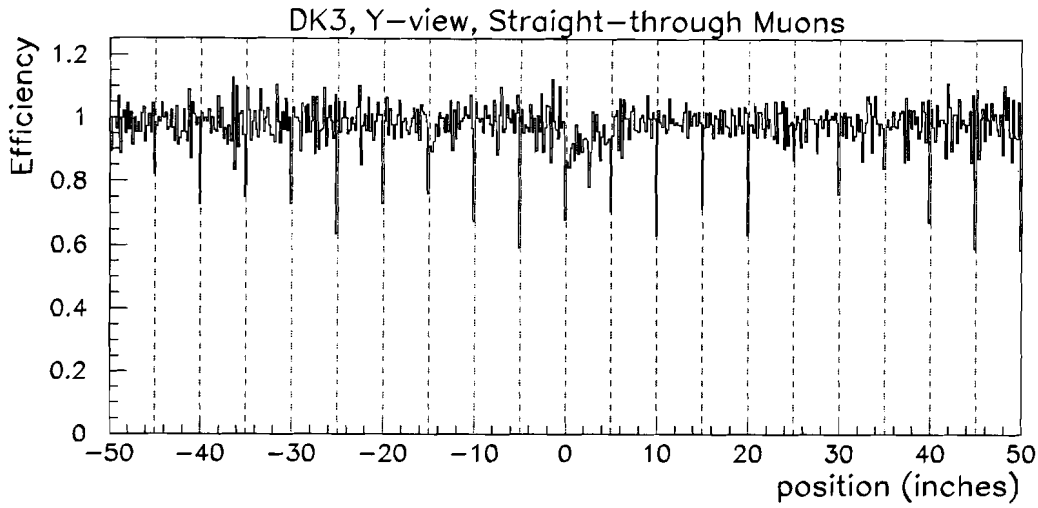

Figure 2.11: Efficiency of drift chamber across the plane. Dashed lines correspond to the I-beams locations.

the non-active region of the aluminum I-beams surrounding each cell. The effect of the I-beams can be clearly seen in Figure 2.11. The aluminum I-beams constituted about 2% of the given drift chamber.

Drift chambers DK2-5 and TG43 have each of their drift planes oriented along the x and y coordinate axes. If only x-y information is accessible and multiple tracks are present within a given event, then there exists an ambiguity as to which x hits correspond to which y hits. To resolve this ambiguity, one of the downstream drift chambers (DK 1) is rotated by 47 mr clockwise about the beam direction. The information from this tilted (also known as "UV") chamber is enough to resolve any x-y ambiguities for events with multiple charged tracks.

2.2.3 Helium Bags

Between adjacent drift chambers are cylindrical plastic bags filled with helium. Helium provides an effective way to reduce the number of neutrino-nucleon interactions occurring in the fiducial volume; desirable since νN interactions constitute the main

source of background for the L^0 decay search. The three helium bags extend 4.9 meters in diameter and a total of 39 meters in length. The helium gas is fed directly from the Fermilab helium supply system. Both the pressure and helium flow rate are monitored to minimize the pressure from helium bags on the drift chambers. The purity levels for the helium entering the decay channel bags is above 99.9%. Using helium instead of air reduces the level of background by a factor of seven within the fiducial region.

2.3 Target Calorimeter

The NuTeV target calorimeter [29, 30] sits downstream of the decay channel and constitutes the main portion of the NuTeV experiment. It is a massive sampling calorimeter designed to study neutral and charged current neutrino interactions in iron. Some of the physics topics addressed by the NuTeV calorimeter include precise determination of the weak mixing angle [31], neutrino-nucleon structure function measurements [32], dimuon cross-section measurements [33], lepton number violation searches [34], and nucleon charm sea measurements [35]. The target calorimeter also serves an important role in the decay channel search by providing triggering, energy measurements, and particle identification for all tracks from the channel.

The NuTeV detector consists of a segmented iron-scintillator sampling calorimeter followed by a toroid spectrometer. It has a mass of 690 metric tons, is 17.7 m long, and measures 3.05 m $\times$ 3.05 m in the transverse direction. The calorimeter is composed of 42 segments, each segment consisting of four 5.15 cm thick steel plates, two liquid scintillator counters, and one drift chamber (see Fig. 2.12). Since the NuTeV calorimeter was originally built to measure charged current and neutral current neutrino interactions, its design optimizes the measurement of the following quantities:

Table 2.3: Composition in interaction and radiation length of one unit of the NuTeV calorimeter.

Material	z (cm)	X_0	λ_I
4 Steel Plates	20.7	11.75	1.24
2 Scint. Counters	13.0	0.51	0.16
1 Drift Chamber	3.7	0.17	0.03
Total	37.4	12.43	1.43

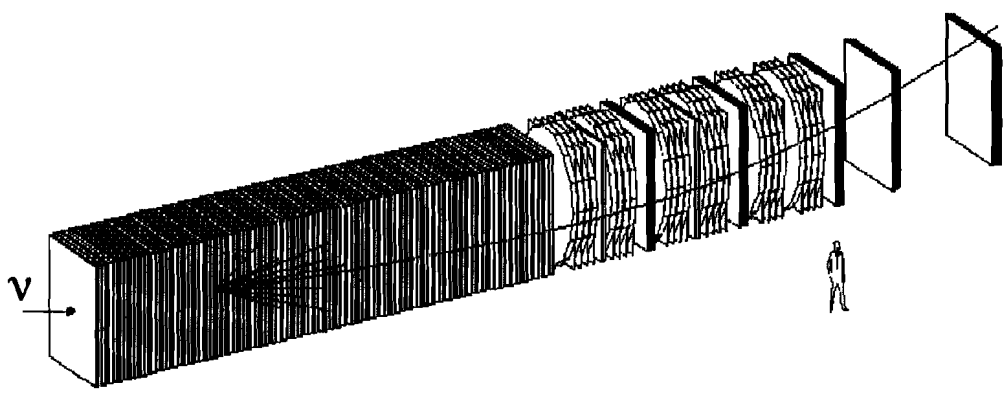

Figure 2.12: The NuTeV target calorimeter.

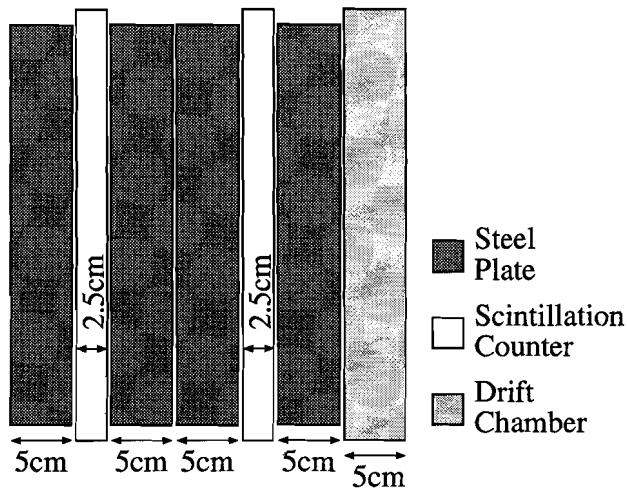

Figure 2.13: Schematic of a single calorimeter unit.

- The hadronic energy of the neutrino interaction (E_{had}),
- The muon energy of the neutrino interaction (E_μ),
- The muon angle (θ_μ), and
- The interaction vertex position (v_x, v_y, and v_z).

The hadronic energy of the event is measured using the scintillation counters interspersed within the iron target. There are 84 counters, each filled with Bicron 517L scintillator oil. As charged particles pass through the counter depositing energy, visible and near-UV light is released from the scintillator and eventually collected by one of four photomultiplier tubes located at each corner of the scintillator counter. The pulse heights from the photoelectrons gathered in the PMT is then recorded and converted to an energy measurement.

The energy resolution and response of the detector is measured directly using the hadrons, muons, and electrons from the calibration beam at various energies. The hadronic energy resolution of the calorimeter is $\sigma/E = (0.024 \pm 0.001) \oplus (0.874 \pm$

$0.003)/\sqrt{E(\mathrm{GeV})}$, and the electromagnetic energy resolution is $\sigma/E = (0.04 \pm 0.001) \oplus (0.52 \pm 0.01)/\sqrt{E(\mathrm{GeV})}$[36].

One also wishes to measure the muon's trajectory. To accomplish this, the NuTeV calorimeter is interspersed with 42 drift chambers designed to measure the transverse position of the muon track as it travels through the detector. The drift chambers are quite similar to those used in the helium decay channel. The only significant difference to note is that each x and y cell is equipped with three wires (two "sense wires" immediately adjacent to a central field-shaping wire) rather than a single wire. This feature removes the left-right ambiguity which exists in the helium decay channel chambers. The intrinsic resolution of the calorimeter drift chambers is 255μm, but the muon trajectory resolution is dominated primarily by multiple scattering in the iron.

NuTeV uses a toroid spectrometer to accurately measure the momentum and charge of the muon [29]. The muon spectrometer sits downstream of the iron calorimeter and is composed of three toroidal iron magnets instrumented with acrylic counters and drift chambers. The iron toroids have a 1.78 m outer radius and a 12.7 cm inner radius. A total current of 1250 A running through the axial coils magnetizes the iron to a field ranging from 1.9 T near the center to 1.55 T at the outer edge. With this configuration, a 100 GeV muon would bend about 24 mr before reaching the end of the spectrometer. Using a set of five drift chambers interspersed in the toroid, it is possible to track the trajectory of the muon as it passes through the spectrometer.

The charge of the muon is measured from the direction of the bend. The toroid field is set to focus muons produced by interactions of the neutrino sign selected by the SSQT. The energy of the muon is measured directly from the magnitude of the bend through the magnetic field. Using again a calibration beam of muons with predefined energies, it is possible to get an excellent calibration of the muon momentum. The resolution of the muon momentum as determined by the toroid

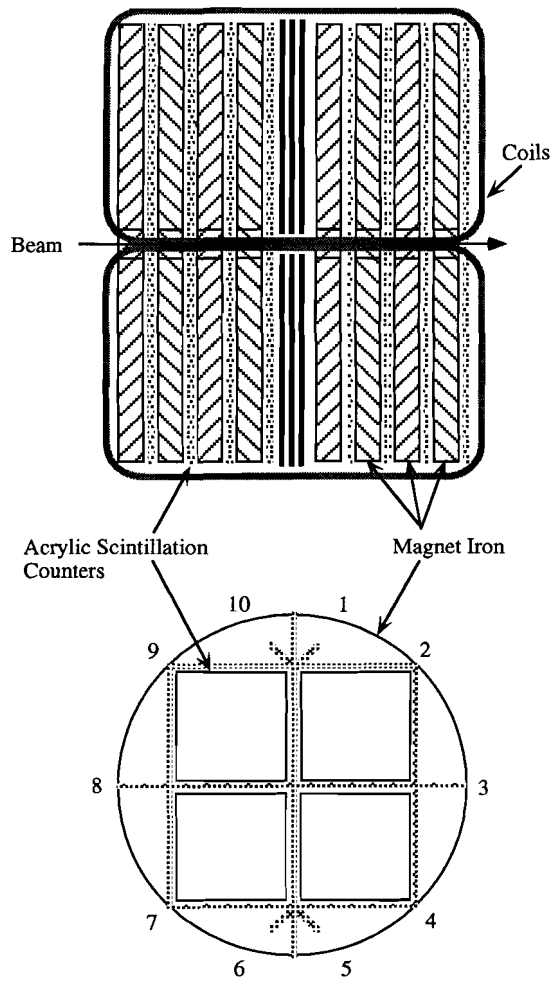

Figure 2.14: Schematic of the toroid spectrometer. Top overhead view; bottom, transverse view, with photomultiplier tube locations numerically marked.

spectrometer is $\Delta p/p = 11\%$, limited predominantly by multiple scattering.

The NuTeV sampling calorimeter is thus able to measure the muon and hadronic energies and muon angles necessary to reconstruct a neutrino-nucleon interaction. The same information accessible to the NuTeV calorimeter can be used to obtain information about tracks exiting the decay channel. The combination of both the decay channel and the NuTeV calorimeter provides all the necessary tools to perform exotic particle searches.

2.4 Triggering

The trigger represents the first step in selecting events of interest to the analysis. Each trigger instructs the data acquisition system to accept the event and thus record the full response of the detector. Typically, a trigger will only use a subset of the detector to make an accept/reject decision for the event. Data triggers enable one to preselect events and minimize the amount of background/noise events that are written to tape.

The combination of NuTeV triggers are constructed as minimum-bias triggers, so that most activity that occurs in the detector is recorded to tape. Each NuTeV trigger is listed in Table 2.4 and explained below.

- **Trigger 1 (Toroid Muon Trigger):** This data trigger selects candidate neutrino-nucleon charged current interactions. Since the outgoing particles from this interaction include a high energy muon, the trigger selects events with a muon traversing at least a third of the toroid system.

- **Trigger 2 (Neutral Current Trigger):** This trigger selects neutral current events, whose interaction leaves a hadronic shower with no exiting muon. The trigger demands that the event deposit a total of 8 GeV of energy over eight adjacent counters.

Table 2.4: NuTeV data triggers.

Trigger	**Function**
1	Toroid Muon Trigger
2	Neutral Current Trigger
3	Target Muon Trigger
4	Redundant Toroid Muon Trigger
5	Test Beam Trigger
6	Straight-Through Muon Trigger
7	$\ll$ Not in Use $\gg$
8	Cosmic Ray Trigger
9	Decay Channel Trigger
10 - 12	Pedestal Triggers

- **Trigger 3 (Target Muon Trigger):** This trigger selects events where a muon is produced in the target calorimeter. The trigger requires that 16 counters fire, with 4 out of a subset of 8 counters showing 4 GeV or more.

- **Trigger 4 (Redundant Toroid Muon Trigger):** This trigger serves as a systematic check to Trigger 1. The trigger requires shower energy to be deposited in the calorimeter and a muon track to pass through the toroid.

- **Trigger 5 (Test Beam Trigger):** This trigger registers events from the slow spill calibration beam.

- **Trigger 6 (Straight-Through Muon Trigger):** This trigger selects muons which were produced upstream of the helium decay channel. These muons come from neutrino charged current interactions in the earth-berm shielding preceding the detector. The trigger requires a muon to penetrate the toroid, and the veto wall to fire. Trigger 6 events are ideal for alignment, calibration, and efficiency studies of both the decay channel and the main calorimeter.

- **Trigger 8 (Cosmic Ray Trigger) :** This trigger allows one to extract information about cosmic rays hitting the calorimeter. The trigger requires the beam to be off and at least 40 counters to have energy deposited in them.

- **Trigger 9 (Decay Channel Trigger) :** This trigger selects candidates for L^0 decaying in the decay channel. It requires that three out of four of the upstream counters fire, as well as four out of seven of the next counters fire as well. The trigger then requires either that a total of 13 counters to fire (muon requirement), or that at least 5 GeV of energy be deposited in the first few counters (pion/electron requirement). All Trigger 9 events are a subset of Triggers 1, 2, and 3.

- **Trigger 10-12 (Pedestal Triggers) :** Pedestal triggers allow one to extract

information when activity in the detector is minimal. Pedestals are taken systematically during each run when no other triggers have fired.

The triggers enable one to preselect data events which could be potential candidates for L^0 decays. L^0 candidates are selected if they satisfy Triggers 1, 2, 3, or 9, and have minimal activity in the decay channel drift chambers. The trigger requirements are purposely minimal to avoid eliminating potential candidates before analysis.

2.5 Data Acquisition

The raw signals from the decay channel, calorimeter, and muon spectrometer come in one of two forms: (1) pulse heights from the scintillation panels and counters, and (2) timing pulses from the drift chambers. Once one particular hardware trigger has been satisfied, the raw information from the veto wall, drift chambers, and calorimeter is prepared for storage via the NuTeV data acquisition system (DAQ).

In the case of the decay channel, the most relevant information comes from the drift chambers and the veto wall counters. Signals from drift chambers are amplified and sent to time-to-digital converters (TDC). A TDC board takes inputs from 16 channels on two 8-pair ribbon cable headers at the front of the board. Single wire chambers have two planes with 24 sense wires per plane, providing 48 channels for 3 TDC boards. To read out signals from the decay channel chambers, 15 TDC boards are used for the decay channel drift chambers and 3 TDCs are used for the veto wall readout. The data are received as ECL differential signals, each signal transported over a twisted pair. The TDC digitizes the time of the pulse in 4 ns bins, over a total live time window of 2 μs. Since the maximum drift time is 1.3 μs, the time window buffers the full drift range of the cell. The timing of the event is set not by the drift

chambers but rather by the event trigger. It is the arrival time of the drift chamber pulse on one wire relative to the event time that determines the particle position, with greater precision than the size of the drift chamber cell. The write clock is provided by an external synchronous clock generator module. The TDCs transfer the data from 16 circular buffers into the global first-in-first-out (FIFO) buffer memory and then pass the information to the DAQ system at the end of the cycle.

Readout information pertaining to the energy deposited in the calorimeter is gathered using 11-bit analog-to-digital converters (ADC). There exists a wide range of energies that can be deposited in a counter during an event. For example, a muon would deposit only the minimum ionizing particle (MIP) (about 0.15 GeV), while a hadronic shower can deposit up to 100 GeV in a single counter. As a result, three separate gains are used to measure the energy: HIGHS, LOWS, and SUPERLOWS (see Figure 2.15). The HIGHS are the signals formed by the sum of each of the four photomultiplier tubes, amplified by 10. The LOWS is the digitized signal from each of the four PMTs. Finally, the SUPERLOWS are the digitized sums of 8 PMT signals which come from 8 different counters, each separated by 10 counters. Each signal feeding into the SUPERLOWS is attenuated by 1/10th. A typical MIP signal produces 80 ADC counts in the HIGH channel, 2 ADC counts in each LOW channel, and 0 counts in the SUPERLOW channel. Further details regarding the calorimeter readout can be found elsewhere [36].

The data acquisition system is based on a VME-bus system build around a Motorola MVME167 68040 processor board. Information from the VME board is later stored to tape for off-line analysis. The off-line analysis uses the raw information gathered from the DAQ to reconstruct event observable, such as muon energies, track angles, etc.

Having described the major components of the NuTeV detector, we now begin to detail various aspects of the event reconstruction techniques.

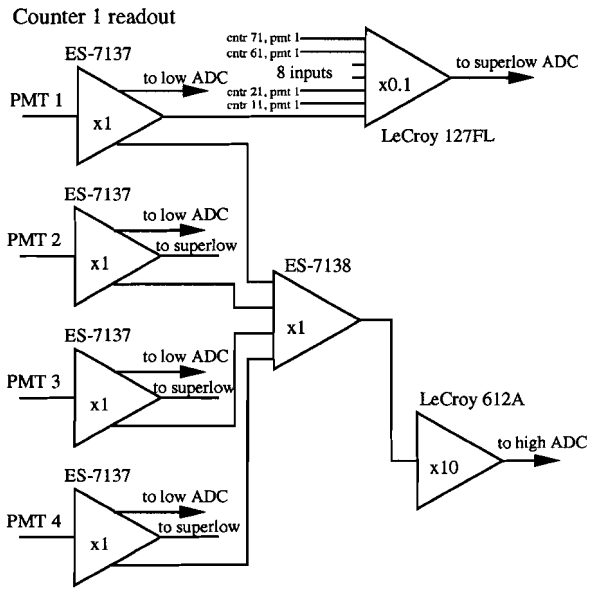

Figure 2.15: Schematic diagram of the NuTeV calorimeter readout electronics.

Chapter 3

Event Reconstruction

The NuTeV decay channel and calorimeter provide the tools necessary to detect L^0 decays. The challenge now lies in transforming the raw hit positions and energy depositions into kinematic information about the event. The full method of how events are reconstructed and analyzed is presented in this section.

3.1 Track Reconstruction

Event reconstruction of the decay channel activity begins with charged particle track reconstruction. Track reconstruction is based on an iterative algorithm by which tracks are fit and re-fit as more information is gathered and processed. In general, tracks are assumed to travel along straight lines, since no magnetic field is present in the decay channel, and multiple scattering effects are small.

Primitive tracks are first constructed from hits in "seed" chambers (DK2-DK4 and TG43), separately for the x and y planes. Upstream and downstream seed chamber hits are joined together by straight lines. If a hit is found to lie between two seed chambers at a minimum distance ≤ 3 cm from the projected track, that hit is added

to the track. A search is then performed along each track for hits in the downstream chambers (DK1-DK4 and TG43). For single-wire chambers, both the left and right positions of hits are used. For the tilted UV chamber, hits in one view are combined with all partner hits in the other view. If a track with three or more hits is found, a linear fit is performed to find the slope, intercept, and the initial timing (T_0) of each track. Tracks which have $T_0 \geq 48$ ns are not considered to fall within the time frame of the trigger and are subsequently removed.

At this point, a large library of possible track combinations has been accumulated from the original seed tracks, with hits often shared by two or more tracks. Tracks are now sorted according to the quality of each linear fit. The quality of each track (Q) determines the order in which tracks are sorted. The track quality is defined as:

$$Q \equiv N - 5 \times (\sigma^2 - \max[\theta, 150\text{mr}]). \tag{3.1}$$

Q depends on the number of hits (N) in each track, the error on the fit (σ), and the track slope (θ). If a track has a very large slope (≥ 150 mr), the quality of the track is decreased. Hits which are shared between two or more tracks are now only assigned to the tracks with the highest quality factor. After all tracks have been scanned, only tracks with the highest quality are kept and re-fit. Hits from the UV chamber are now used to match x and y tracks together to form three-dimensional tracks. At this point, enough information is available to start reconstructing event vertices in the decay channel.

3.2 Vertex Formation

Vertex formation serves as a key component in all L^0 searches. Once three-dimensional tracks have been reconstructed, the track information is used to reconstruct a single

event vertex. At first, the 3-dimensional tracks are matched to find groups of tracks with a common origin within a defined distance of closest approach. Information from clustering and energy measurements (see next section) is now added to the tracks. In addition, hits from the upstream chambers (DK4 and DK5) and additional hits from downstream chambers (DK1-DK3) are added to the reconstructed tracks as well.

Now that each track has all its hits associated with it, the track is fit again taking into account multiple Coulomb scattering effects. The multiple scattering fit depends on both the intrinsic resolution of the chamber and the momentum of the track. Since hits in a multiple scattering fit are correlated, we make use of the full error matrix when computing the fit. The fit minimizes the χ^2 function formed by the expected multiple scattering width over each track segment:

$$\chi^2 = \sum_i \sum_j (x_i - x_i^p(\alpha, \beta)) \cdot M_{ij}^{-1} \cdot (x_j - x_j^p(\alpha, \beta)), \tag{3.2}$$

where x_i are the measured hit positions at chamber i and $x_i^p(\alpha, \beta)$ are the projected positions for a track of intercept α and slope β. The full error matrix M_{ij} is defined by:

$$M_{ij} = \sum_{k=1}^{i} \sigma_0^2 \delta_{ij} + \sigma_k^2 [(z_k - z_i) \cdot (z_k - z_j)] \begin{cases} k > i, k > j \text{ for } z_k < z_{fit} \\ k < i, k < j \text{ for } z_k > z_{fit} \end{cases} \tag{3.3}$$

where z_i is the position of the i-th chamber and z_{fit} is the arbitrary position from where the fit takes place. The fit is constructed such that only chambers upstream of z_{fit} affect chambers upstream and only chambers downstream of z_{fit} affect chambers downstream. Note that the fit depends on both the intrinsic resolution σ_0 and the multiple Coulomb scattering width σ_k, which is defined as:

$$\sigma_k = \frac{13.6 \text{ MeV}}{p_\mu} \sqrt{L/X_0} \, [1 + 0.038 \ln (L/X_0)]. \tag{3.4}$$

For the decay channel drift chambers, L/X_0 is 12.4%. The χ^2/dof from this fit is stored and used later as an indication of track quality.

Finally, a full constrained fit is performed to a single vertex for all tracks associated with the vertex. This final fit yields the longitudinal and transverse position of the event vertex used in the subsequent analysis. Since one and only one vertex is used, only the most upstream vertex is selected. This selection allows for the formation of δ-rays downstream of the reconstructed vertex.

The longitudinal position resolution of the vertex depends strongly on the opening angle of the charged tracks. Table 3.1 shows the longitudinal and transverse resolution of muon tracks from a high mass L^0 decay as a function of opening angle. Resolution deteriorates substantially for events with very small opening angles. This is an issue of concern for decays from particles with low mass, because the opening angle of the decay particles is very small. For example, the average opening angle from a 33.9 MeV/c^2 particle decaying into $e^+e^-\nu$ is 2.5 mr. For such near-parallel events, it is impossible to separate events which occur in the chambers from those which occur in the helium. As one moves higher in mass, the longitudinal resolution of the vertex improves. For example, the average longitudinal resolution for a 5 GeV/c^2 L^0 decay is 8.8 cm. The transverse resolution, on the other hand, is far less dependent on the opening angle of the two charged tracks. The typical transverse resolution for low mass decays is 0.67 cm (see Figure 3.1), while the transverse resolution for high mass decays is 0.13 cm.

3.3 Clustering

As each particle enters the calorimeter, it deposits energy in the counters and leaves a shower of particles in the tracking drift chambers. The distribution of hits left by a particle traversing the calorimeter is called a *cluster*. Clusters are used in conjunction

Table 3.1: Longitudinal and transverse resolution as a function of opening angle. Resolution is quoted for 5 GeV/c^2 L^0 Monte Carlo events which decay to $\mu\mu\nu$.

Opening Angle (mr)	Longitudinal (cm)	Transverse (cm)
0 - 10	106 ± 56	1.18 ± 0.39
10 - 20	12.6 ± 1.2	0.15 ± 0.01
20 - 100	4.6 ± 0.2	0.11 ± 0.01
100 - 200	2.6 ± 0.2	0.12 ± 0.01

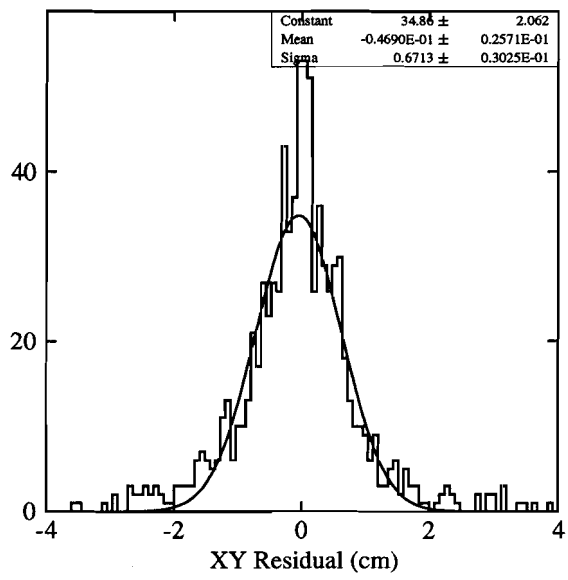

Figure 3.1: X and Y residuals for a 33.9 MeV/c^2 decay to $e^+e^-\nu$.

with decay channel tracks in order to determine each particle's energy and identity.

Clusters are determined by the distribution of hits in both the x and y views. Hits which are less than 15.2 cm apart are grouped together into a single cluster. Clusters in the x and y planes are mapped to a single cluster by linking projected three-dimensional decay channel tracks to each cluster.

The hit and energy distributions of each cluster are unique to the particle type. This information can be harvested to distinguish muons, pions, and electrons. Details on particle identification are given in the next section.

3.4 Particle Identification

A given track is identified based on the information pertaining to the cluster's hit and energy distribution. Particles are identified as either muons, electrons, or pions. All charged hadrons (π, K, p) are labeled as pions. Each type of particle has a unique shower profile which distinguishes it from other particles. Muons, for example, tend to have long, penetrating tracks with only minimum ionizing energy deposited in each scintillator plate. Muons with energy as low as 15 GeV traverse the entire steel calorimeter, leaving only single hits along their trajectories (see Figure 3.2). Muons with energies above 15 GeV are identified correctly more than 99% of the time.

Pions and electrons, on the other hand, tend to have far shorter tracks in the calorimeter steel. Each set of four steel plates extends 11.75 radiation lengths, forcing the electron to have very short electromagnetic showers, typically spanning no more than two counters. All of the shower energy is deposited in the first two counters (see Figure 3.3). The probability of identifying electromagnetic showers is also high – above 90% – for electrons with energies above 15 GeV. Pions tend to have intermediate shower lengths since the four steel places only extend 1.25 interaction lengths. Pions

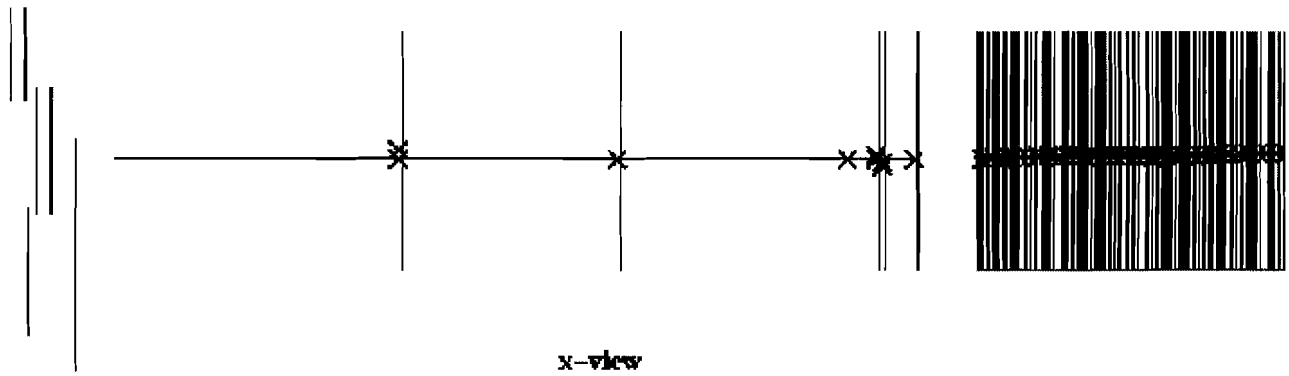

Figure 3.2: Sample event with deep penetrating muon traversing the NuTeV decay channel and calorimeter.

shower into multiple particles as they interact with the surrounding steel, resulting in a wide shower extending several counters.

One can take advantage of the different shower and energy profiles to identify different particles. For historical reasons, two separate particle identification schemes are used in this analysis: one targeted to identify electrons and reduce pion mis-identification (used for the low mass analysis), the other targeted to identify muons (for the high mass analysis). Both algorithms make use of the hit and width density distributions of a given cluster, as well as the cluster's total length and energy (see Figure 3.4). The algorithm uses a log-likelihood function to decide whether a given cluster is a muon, pion, or electron. The structure of the likelihood function is given below:

$$L_i \equiv \frac{e^{-\chi_i^2/2}}{\Sigma_j e^{-\chi_j^2/2}}, \tag{3.5}$$

where $L_{i=e,\mu,\pi}$ is the probability of the particle being of type i. The χ^2 is formed by comparing the given event to Monte Carlo distributions:

$$\chi_i^2 = (w - w_i'(E))^2 + (n - n_i'(E))^2, \tag{3.6}$$

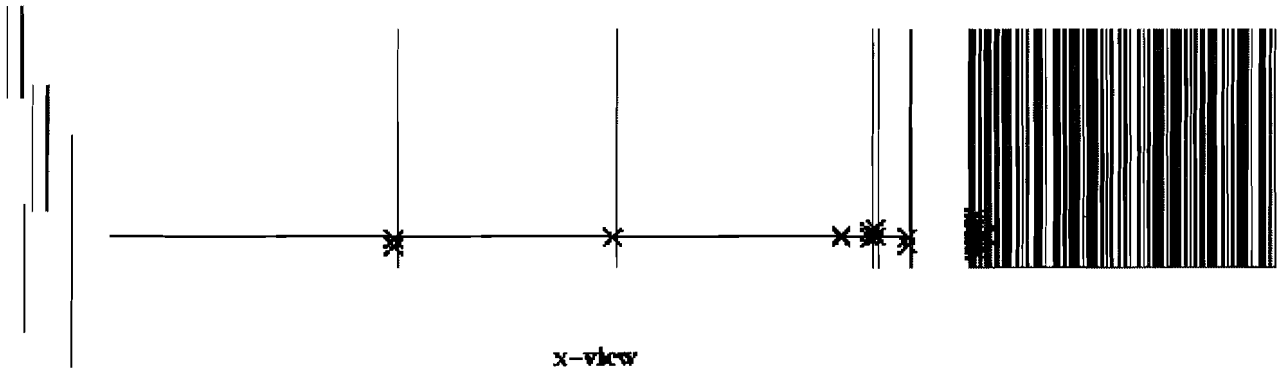

Figure 3.3: Sample electron event with short electromagnetic shower in the NuTeV decay channel and calorimeter.

where $w(n)$ and $w_i'(n_i')$ correspond to the width (hit) data and Monte Carlo density distributions, respectively. The Monte Carlo width and hit distributions vary as a function of cluster energy (E). Clusters which extend beyond twenty counters are automatically identified as muons. Clusters with no more than one hit are identified as noise hits.

Particle identification efficiencies can be measured with Monte Carlo simulations and calibration testbeams. The performance of the algorithm as a function of particle energy is illustrated in Figure 3.5. The performances of the two algorithms are similar over most of the energy ranges in question.

Both the low mass and high mass particle searches need to identify two particles in an event rather than one. The efficiency of two-particle algorithms cannot be tested with the calibration beam, but still can be tested with the Monte Carlo. Results for two-particle identification efficiencies are reported in the appropriate signal sections of the thesis.

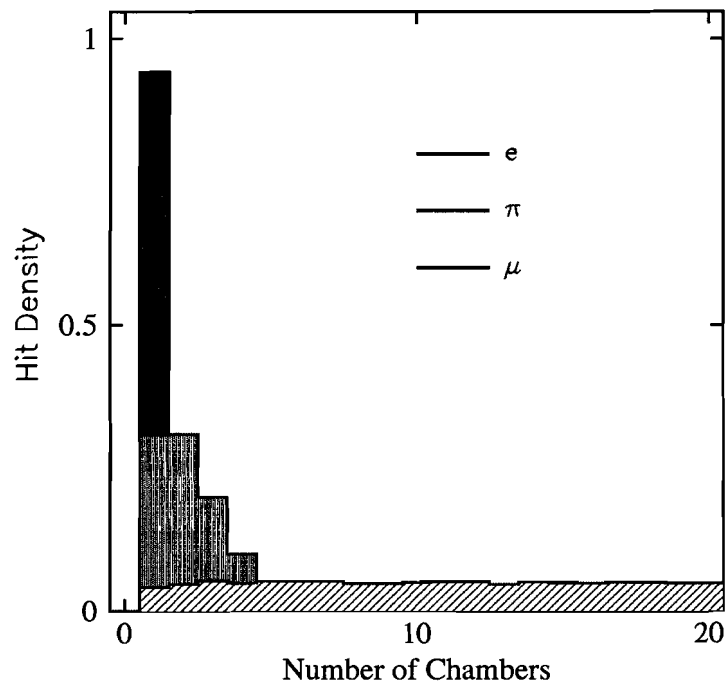

Figure 3.4: Hit density distribution for first 20 counters penetrated by a 50 GeV electron (black), pion (red), and muon (blue).

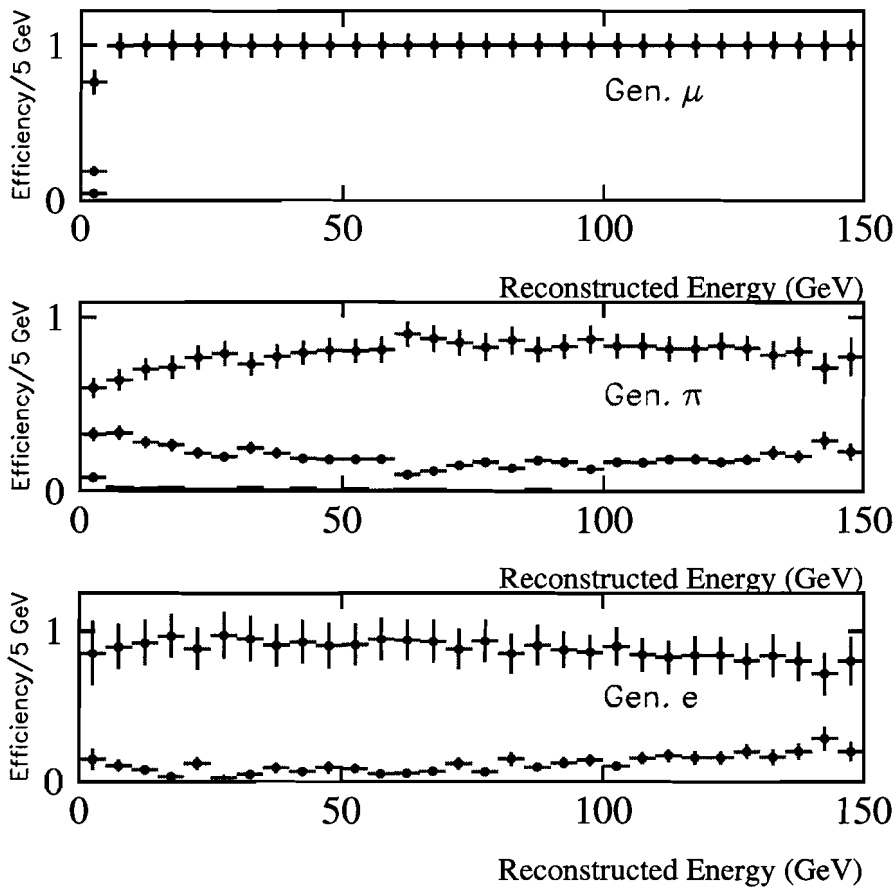

Figure 3.5: Probability to identify a particle as a muon (black), pion (red), or electron (blue) with the original particle being a muon (top), pion (middle), or electron (bottom). These plots illustrate the efficiency of the high mass algorithm.

Table 3.2: Particle identification efficiency as a function of energy. Table shows efficiency for both low mass and high mass algorithms.

		Low Mass Algorithm			High Mass Algorithm		
Rec. Energy (GeV)	Gen. Particle	Rec. μ	Rec. π	Rec. e	Rec. μ	Rec. π	Rec. e
0 - 10	μ	63.4%	36.4%	0.0%	88.1%	9.4%	2.5%
	π	1.1%	66.0%	32.9%	5.1%	61.7%	33.2%
	e	0.0%	12.7%	87.3%	0.0%	12.6%	87.4%
10 - 50	μ	100.0%	0.0%	0.0%	100.0%	0.0%	0.0%
	π	0.0%	81.2%	18.8%	1.4%	76.0%	22.6%
	e	0.0%	10.0%	90.0%	0.0%	7.0%	93.0%
50 - 100	μ	100.0%	0.0%	0.0%	100.0%	0.0%	0.0%
	π	0.0%	89.3%	10.7%	0.4%	84.6%	15.0%
	e	0.0%	10.6%	89.3%	0.0%	9.6%	90.4%

3.5 Energy Measurements

3.5.1 Muon Energy

Most high energy muon tracks are able to penetrate the entire length of the calorimeter and reach the toroid. If a muon reaches the toroid, then the particle's bend in the magnetic field is used to determine its momentum. In a constant magnetic field B, the bend of the muon track is given by the following equation:

$$P = \frac{0.3BR}{\sin\theta}, \tag{3.7}$$

where R is the length of the track (in meters), P is the measured momentum (in GeV/c), and θ is the angular bend of the track. The energy resolution from the toroid measurements is quite good, with $\Delta E/E = 11\%/\sqrt{E}$, limited mostly by multiple scattering.

If the muon does not reach the toroid and loses all its energy in the calorimeter itself, then one can measure the muon energy directly from the range of the muon track. Using this method, the muon energy resolution is ± 310 MeV.

Finally, a muon track could simply exit from the fiducial volume before it either reaches the toroid or looses all of its energy. In such cases, we resort to a momentum fit based on the multiple scattering of the track (higher energy tracks will tend to have less multiple scattering than a low energy track). By using the root mean square deviation from a simple straight line fit, one can estimate the momentum of the track. For a 50 GeV/c muon, the energy resolution from this method is about 42%.

3.5.2 Pion and Electron Energy

In the case of electrons and pions, pulse height information from the counters is used to determine particle energy deposition. The hadronic energy resolution of the calorimeter, as measured from the testbeam, is $\sigma/E = (0.024 \pm 0.001) \oplus (0.874 \pm 0.003)/\sqrt{E(\mathrm{GeV})}$. The electromagnetic energy resolution is $\sigma/E = (0.04 \pm 0.001) \oplus (0.52 \pm 0.01)/\sqrt{E(\mathrm{GeV})}$ [36]. If a μ and π cluster are merged, the muon's minimum-ionizing energy is subtracted and the remaining energy assigned to the pion. If two or more pion or electron clusters are present, the energy determined from the pulse heights is divided according to the number of drift chamber hits in each cluster. If two known tracks are so close together that only one cluster is found between the two tracks, the energy cannot be distributed according to the hit distribution. Instead, we use the multiple scattering of the tracks within the decay channel to determine the energy of each track. Unfortunately, the latter method has poor energy resolution due to the limited number of chambers available to measure the multiple scattering. Since what is important is the fractional energy distribution that is given to each track rather than the actual track energy, we quote the error on the energy asymmetry $((E_1 - E_2)/(E_1 + E_2)$. The resolution on the fractional energy distribution is $\approx 32\%$.

3.6 Event Formation

Combining the information from decay channel tracks, calorimeter clusters, energy depositions, and particle identification algorithms allows one to reconstruct the kinematics of all particles emanating from a single interaction or decay point. This event-forming algorithm is common to both the high mass and low mass searches.

3.7 A Note about Variables

There are two possible ways to interpret a given event in the decay channel once it has been analyzed. One way is to interpret the event as a *decay* event; the other is to interpret it as a neutrino *interaction.* In describing the kinematics of the event, some of the defined variables are more appropriate for describing it as a decay, while others for describing it as an interaction (for example, transverse mass is more descriptive for decay events). Both, of course, can be used interchangeably to describe the same event.

The two tables below list and describe some of the variables used in this analysis, appropriate for decay and interaction events, respectively. We use effective scaling variables to represent the kinematics of the reconstructed events when interpreted as a neutrino interaction . The effective scaling variables are calculated for each event assuming that the event is a charged current neutrino interaction ($\nu_\ell N \rightarrow \ell N' X$) and that the missing transverse momentum in the event is carried off by an undetected final state nucleon. In the decay interpretation of the event, we assume that the decaying particle travels parallel to the beam axis ($P_T^x = P_T^y = 0$). These variables will be used throughout the present discussion.

Having laid the groundwork for the theory and the experimental apparatus, we are now ready to proceed with the first exotic particle search.

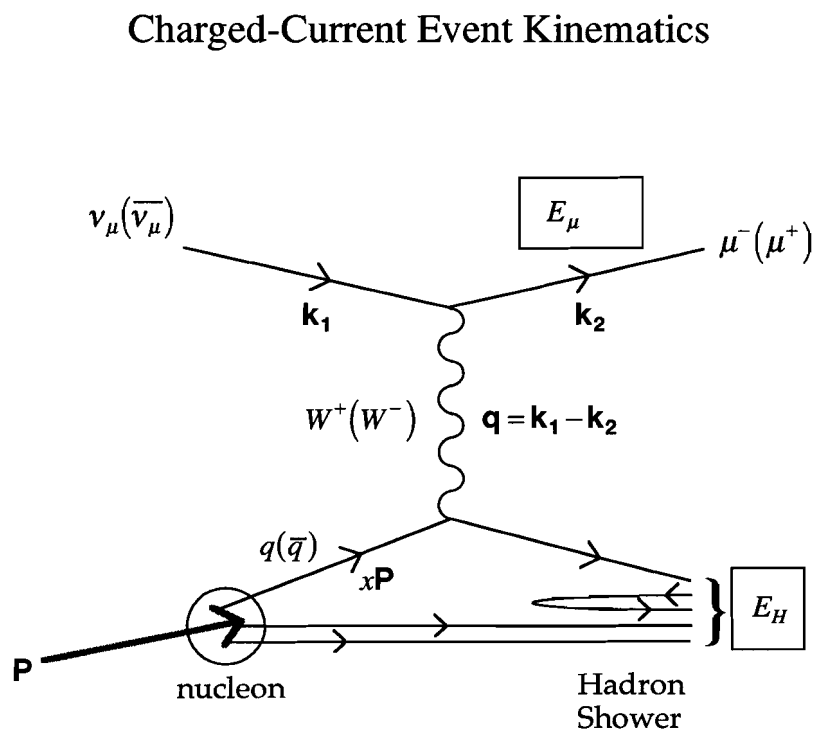

Figure 3.6: Kinematic variables used when event is interpreted as a neutrino-nucleon interaction.

Table 3.3: Kinematic variables used when event is interpreted as a νN interaction. E_μ and E_H represent the muon and hadronic energy of the event, $\mathbf{k_1}$ and $\mathbf{k_2}$ represent the incoming and outgoing lepton 4-vectors, and M_p represents the mass of the struck nucleon.

Variable	Definition	Description
E_ν	$E_\mu + E_H$	Neutrino Energy
Q^2_{eff}	$-(\mathbf{k_1} - \mathbf{k_2})^2$	4-Momentum Transfer
y_{eff}	E_H/E_ν	Inelasticity
x_{eff}	$\frac{Q^2_{eff}}{2M_pE_H}$	Fractional Momentum of Struck Nucleon
W_{eff}	$M_p^2 + 2M_pE_H - Q^2_{eff}$	Invariant Mass of Hadronic System

Table 3.4: Kinematic variables when event is interpreted as a decay. E_i represents the energy of each visible track, $\vec{p}_1{}^T$ and $\vec{p}_1{}^T$ represent the transverse monemtum of each track, and $\mathbf{p_1}$ and $\mathbf{p_2}$ represent the 4-momentum of each track.

Variable	Definition	Description
E_{vis}	ΣE_i	Total Visible Energy
p_T^2	$(\vec{p}_1{}^T + \vec{p}_2{}^T)^2$	Missing Transverse Momentum
m_V^2	$(\mathbf{p_1} + \mathbf{p_2})^2$	Invariant Mass of Visible Particles
m_T	$\lvert p_T\rvert + \sqrt{p_T^2 + m_V^2}$	Transverse Mass

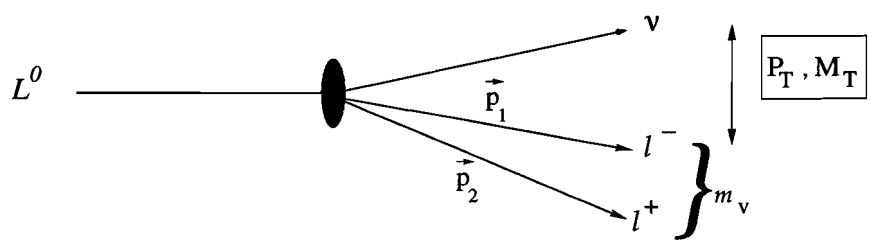

Figure 3.7: Kinematic variables used when event is interpreted as a decay.

Chapter 4

Monte Carlo Simulations

The confidence one may place on an exotic particle search rests primarily on the experiment's overall understanding of the background level within the signal region. As a result, a careful survey of all relevant backgrounds and detector effects is necessary. This analysis uses a full Monte Carlo simulation to estimate the level of background events in our signal-sensitive region. Whenever possible, background estimates are checked against data in the decay channel and in the main calorimeter. More information regarding data/Monte Carlo comparisons is presented in later chapters.

Monte Carlo simulations are used to model various aspects of the NuTeV decay channel; including (1) neutrino flux, (2) neutrino interactions in the NuTeV decay channel, (3) neutrino interactions in the surrounding material, (4) detector efficiency and response, (5) cosmic rays, (6) noise and accidental activity, (7) calibration beam contamination, and (8) normalization. Each topic is addressed in this chapter.

4.1 Neutrino Flux

The NuTeV neutrino beam flux model is simulated using the DECAY TURTLE simulation package [38]. TURTLE uses geometric magnetic optics to trace the trajectories of particles through the SSQT and decay pipe to their decay point. Adjustments to the magnetic field optics have been made in order to optimize agreement between data and Monte Carlo. The sample used to adjust the TURTLE flux comes from looking at charged current neutrino interactions in the main calorimeter. Figure 4.1 shows neutrino energy distributions between data and Monte Carlo for charged current events taking place in the calorimeter. The agreement between data and Monte Carlo is better than 5%. The neutrino flux spectrum also includes contamination from wrong-sign beam impurities and ν_e production [28, 39].

4.2 Neutrino Interactions in the Decay Channel

A significant portion of all activity in the NuTeV decay channel consists of neutrino-nucleon scattering in the helium and drift chambers. The drift chambers constitute 90.4% of the total mass within the fiducial region. Since neutrino interactions scale with the mass of the detector, the drift chambers represent the bulk source of background in the decay channel. Both neutral current and charged current neutrino interactions are a background concern for the high mass and low mass exotic particle searches.

4.2.1 Deep Inelastic Scattering

NuTeV uses the LEPTO/JETSET Monte Carlo program to simulate neutrino charged current and neutral current deep-inelastic scattering (DIS) events [40]. LEPTO uses leading order electroweak cross-sections and QCD leading order and next-to-leading

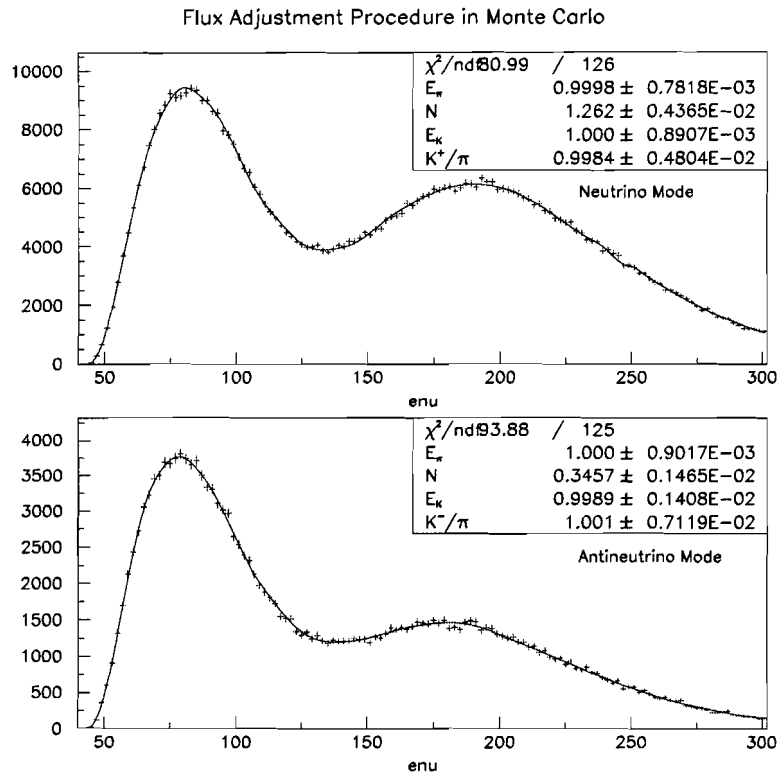

Figure 4.1: Data (crosses) and Monte Carlo (solid) neutrino and anti-neutrino energy distributions for charged current interactions in the main NuTeV calorimeter.

order corrections to properly represent lepton-nucleon interactions. The charged current deep-inelastic scattering (DIS) cross-section, on which the LEPTO generator is based, is written in the context of the quark-patron model:

$$\frac{d\sigma^{\nu,\bar{\nu}}}{dxdy} = \frac{G_F^2 M E_\nu}{\pi}[(1-y-\frac{Mxy}{2E_\nu})F_2(x,Q^2)+y^2xF_1(x,Q^2)\pm(y-\frac{y^2}{2})xF_3(x,Q^2)], \quad (4.1)$$

where G_F is the weak Fermi coupling constant, M is the mass of the struck nucleon, E_ν is the incident neutrino energy, Q^2 is the square of the four-momentum transfer to the nucleon, y is the inelasticity of the interaction, x is the Bjorken scaling variable, and $F_i(x,Q^2)$ are the structure functions of the nucleon. This simulation uses CCFR parton distributions [41], including the correct A-dependence [42]. LEPTO/JETSET uses a string hadronization model in order to simulate the fragmentation of the produced partons. LEPTO/JETSET has been tested extensively against EMC and WA21/WA22 neutrino experiments at CERN, with good agreement [43, 44, 45]. LEPTO/JETSET properly simulates DIS events in the range of $Q^2 > 0.1$ GeV^2 and $W > 2$ GeV.

4.2.2 Quasi-elastic and Resonance Neutrino Scattering

Quasi-elastic and resonance events are not covered in the LEPTO/JETSET event generator because such events lie outside the allowed kinematic range ($W \leq 2$ GeV; see Figure 4.2). Such low-Q^2, low-W events are modeled using separate production generators.

The quasi-elastic processes are:

$$\nu_l + n \rightarrow l^- + p, \text{ and} \quad (4.2)$$

$$\bar{\nu}_l + p \rightarrow l^+ + n. \quad (4.3)$$

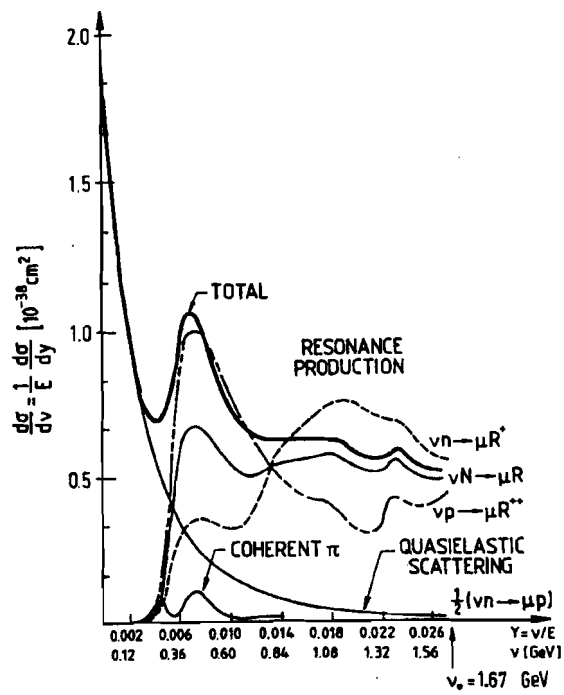

Figure 4.2: The differential cross-section $d\sigma/d\nu$ in the low hadronic energy region for $E_\nu = 60$ GeV. This plot is Fig.5 in Ref.[49]. LEPTO/JETSET does not model this portion of the neutrino cross-section.

We use the model of Llewellyn Smith [46] to calculate the quasi-elastic cross-section:

$$\frac{d\sigma}{dQ^2} = \frac{G_F^2 M_p^2 \cos\theta_c{}^2}{8\pi E_\nu^2}(A(Q^2) \pm B(Q^2)\frac{(s-u)}{M_p^2} + C(Q^2)\frac{(s-u)^2}{M_p^4}), \tag{4.4}$$

where $A(Q^2)$, $B(Q^2)$, and $C(Q^2)$ are the form factors of the struck nucleon. The total cross-section integrated over all Q^2 for a neutrino of 10 GeV is 0.98×10^{-38} cm^2. The theoretical cross-section agrees well with previous neutrino experiments [47].

The "generic" resonance process is :

$$\nu_l + N \rightarrow l^- + N + \pi. \tag{4.5}$$

To simulate neutrino resonance production, we used a low-Q^2, higher-twist approximation [48]. We found this method more accurate in averaging over all low-multiplicity states than the single-pion production model from Rein and Sehgal[49, 50]. The Rein and Sehgal model uses the Feynman, Kislinger, and Ravndal model of baryon resonances [51]. Though the processes are dominated mainly by Δ resonances, all resonances with masses below 2 GeV are included in the model. The model is only accurate in describing the data at the 15% level (see Figure 4.3).

The SLAC low-Q^2, low x approximation, by contrast, models the transition between resonance and DIS events smoothly:

$$\frac{d\sigma}{dxdy} = \frac{d\sigma_0}{dxdy}(1 + 0.672(\frac{x^{1.893}}{1-1.138x} - 0.236)/Q^2). \tag{4.6}$$

Comparing resonance activity in the main calorimeter shows the higher-twist approximation model describes the total hadronic activity to better than 2% (see Figure 4.4). Fragmentation of low hadronic energy activity uses a modeled based on the LEPTO/JETSET string fragmentation.

FERMILAB
LIBRARY

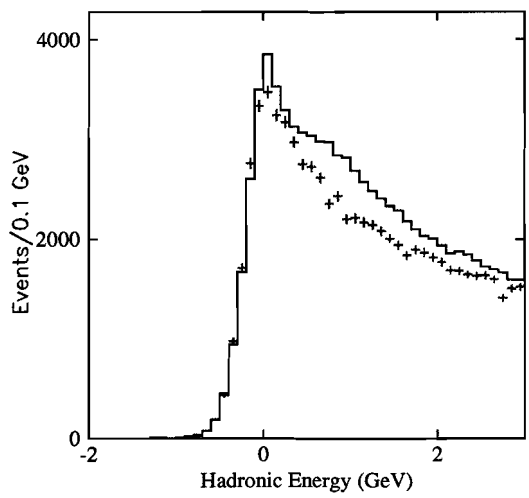

Figure 4.3: Data (crosses) and MC (solid line) resonance and quasi-elastic distributions of hadronic energy. Peak at 0 GeV region indicates presence of quasi-elastic events. Monte Carlo model shown here uses Rein and Sehgal resonance production scheme.

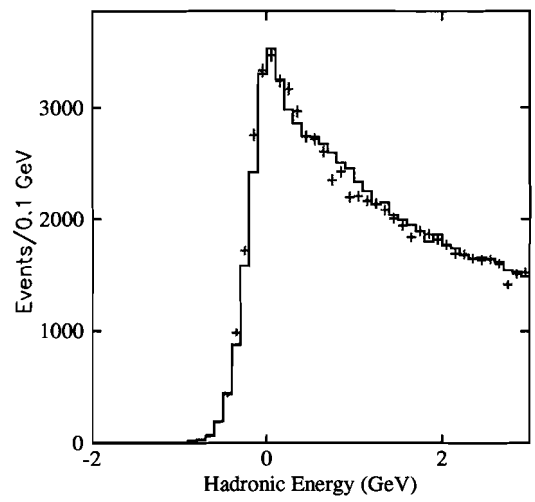

Figure 4.4: Data (crosses) and MC (solid line) resonance and quasi-elastic distributions of hadronic energy. Peak at 0 GeV region indicates presence of quasi-elastic events. Monte Carlo model shown here uses higher twist approximation scheme.

Nuclear effects such as Fermi motion[52] and Pauli suppression[46, 53] were also applied to the Monte Carlo simulations. For Pauli suppression, we use a simple gas model to account for suppression at very small energy transfers:

$$F = 1 - \frac{D}{N}, \text{ and} \tag{4.7}$$

$$D = \begin{cases} Z & r < (u-v)/2 \\ \frac{A}{2}(1 - \frac{3r}{4}(u^2+v^2) + \frac{r^3}{3} - \frac{3}{32r}(u^2-v^2)^2 & (u-v)/2 < r < (u+v)/2 \\ 0 & r > (u+v)/2 \end{cases} \tag{4.8}$$

where $u = (2N/A)^{1/3}, v = (2Z/A)^{1/3}, r = \frac{q}{2K_F}$, and q is the momentum transfer of the system. Momentum distributions of resonance events in the main NuTeV calorimeter show excellent agreement between data and Monte Carlo (see Figure 4.5). Proper modeling of low-hadronic events has been developed, not only for exotic searches, but

also for lepton-number violation searches (see Appendix F).

4.3 Neutrino Interactions in Surrounding Material

In addition to the neutrino activity in the fiducial volume of the detector, potential backgrounds may arise from neutrino interactions that take place in the material surrounding the decay channel. Regions such as the decay channel floor, the earth-berm shielding, and other material surrounding the decay channel are all potential sources for neutrino interactions. Although neutrino reactions in these regions do not pose a significant background issue, neutral particles created in these interactions (such as photons, neutrons, and K_L's) have the potential of entering the fiducial region and mimicking signal events.

Both the earth-berm shielding and decay channel floor are assumed to be composed entirely of concrete ($\rho \approx 2.5$ g/cm^3). For the earth-berm shielding upstream of the detector, we only consider a 5 m $\times$ 5 m $\times$ 4 m region. Neutrino-nucleon interactions in the surrounding material are simulated the same way as in the fiducial volume, using LEPTO/JETSET to develop the hadronization shower. Pion showers are parameterized according to GEANT shower profiles. If a neutral particle from the earth-berm shielding manages to enter the decay channel fiducial region without any charged particle activating the veto wall, the event is known as a *punch-through.* Punch-through events are then passed to GEANT for full detector simulation. Only photons and K_L events constitute potential backgrounds to the exotic searches.

Neutrino interactions in the floor are simulated using the full simulation package. Floor events extend from 1.67 m to 2.5 meters below the center of the beam axis. Other material surrounding the decay region is also included in the simulation.

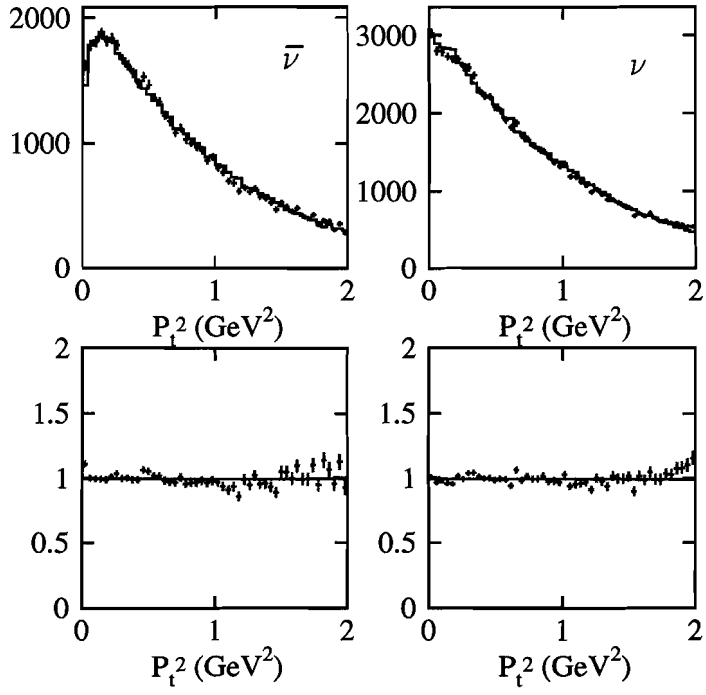

Figure 4.5: Data (crosses) and MC (solid line) resonance and quasi-elastic distributions of transverse momentum (P_t^2). Left: $\bar{\nu}$ distributions; right: ν distributions. The anti-neutrino dip at low P_t^2 illustrates the Pauli suppression effect. The peak at low P_t^2 in neutrino mode illustrates the presence of inverse muon decay events. Plots on the bottom show the ratio between data and Monte Carlo.

Table 4.1: Punch-through rates from earth-berm shielding.

Background Type	Punch-through rate
Photons	3400
Neutrons	5600
K_L	400
K_S	25

4.4 Detector Simulation and Response

Detailed Monte Carlo simulations of physics processes with detector effects are used to quantify the background from neutrino interactions after cuts. Input to the simulation is provided from the event generators mentioned previously. The event generators feed a GEANT-based [54] detector simulation that produces hit-level simulations of raw data. In addition to the material within the decay volume itself, the simulation package also accounts for activity in the regions surrounding the decay channel (floor, earth-berm shielding, etc). Cell-by-cell inefficiencies, dead regions due to internal chamber supports, and noise activity are all included in the simulation. Monte Carlo events are processed using the same analysis routines used for the real data. The detector response simulation is checked extensively using data from the calibration beam [36].

4.5 Cosmic Rays

Cosmic ray events are recorded during periods of beam inactivity between fast spills. Using this data set (also known as the *cosmic ray gate*), one can directly measure the cosmic ray contribution to the background. Since cosmic ray muons enter the decay

channel volume at large angles with respect to the beam axis ($\gg$ 100 mr), they are easily removed from the potential signal region. Of the 3973 cosmic ray events in the cosmic ray gate, none passes either search selection criteria. Since the cosmic ray gate covered 2.5 times the live time of the beam gate, this corresponds to a background level of 0.0 ± 0.4 events.

In order to improve further our estimate of cosmic ray background, we increased the cosmic ray sample by assuming a cosmic ray could become a background candidate if it came into the decay channel at an angle of < 0.01 radians, and one of the following occurred in the decay channel material:

- A hard bremsstrahlung photon was produced (energy $>$ 15 GeV for ee mode, $>$ 2 GeV for $e\mu$) ;
- A hard δ-ray was produced (energy $>$ 15 GeV for ee mode, $>$ 2 GeV for $e\mu$) ;
- The muon scattered inelastically.

The number of events of this type is estimated using straight-through muons which interact in the main calorimeter. These events are required to reconstruct as muons with small θ_{beam} and occur within the cosmic ray gate. Scaling by the ratio of the volumes of the decay channel and calorimeter (~ 2) and by the ratio of mass (1.1×10^{-3}), allows one to achieve far stricter limits on the cosmic ray contribution to background estimates (below 10^{-3} events).

4.6 Noise Simulation

Noise in the NuTeV decay channel is simulated on an event-by-event basis within the detector Monte Carlo using fast spill data. Noise can result from beam activity during fast spill, such as soft photon interactions, random and correlated activity in the drift

chambers, and random activity in the upstream veto panels. Noise and decay channel activity is simulated by combining Monte Carlo events with noise events present in the data. Events that have hits in the decay channel or veto wall *and* have a clear neutrino interaction in the downstream portion of the calorimeter are considered noise events. Introducing noise from the veto wall allows us to simulate the rejection of signal events in our detector by accidental veto wall activity.

4.7 Calibration Beam Contamination

During the 1996-1997 NuTeV data run, a small fraction of the fast spill overlapped with slow spill calibration runs, "leaking" events into the the detector. This leakage was isolated to specific runs where magnets malfunctioned. The leakage can be identified using the testbeam instrumentation and the energy and positions of particles (testbeam runs aimed only at specific locations within the front face of the calorimeter). The leakage manifested itself as an event build-up in specific locations of the detector. The contaminated runs corresponded to about 4% of the total data. These runs were removed from the analysis.

4.8 Normalization

For historical reasons, two separate normalization methods were adopted in order to scale the Monte Carlo sample to the data. The first scheme, used by the low mass search, scales the Monte Carlo sample to data events taking place in the iron calorimeter. The second scheme, used by the high mass search, utilizes data in the decay channel drift chambers to scale the Monte Carlo event sample. The two normalization methods agree within the 1σ level. Both methods are described below.

Table 4.2: Mass ratio for various components of the NuTeV decay channel relative to the NuTeV calorimeter.

Component	Mass Ratio
Calorimeter	1.0
Helium Fiducial Volume	1.13×10^{-4}
Single Drift Chamber	5.37×10^{-4}

Table 4.3: Deep inelastic scattering events occurring in NuTeV decay channel.

	Charged Current	Neutral Current	Total
ν	3100	1000	4100
$\bar{\nu}$	850	300	1150
Total	3950	1300	5250

The low mass normalization method uses charged current neutrino interactions in the main NuTeV calorimeter to determine the total number of neutrino interactions which occur in the decay channel. To scale the number of events from the calorimeter to the decay channel, a factor calculated from the ratio of masses is used (see Table 4.2). The normalization data sample contains 0.83(0.25) million neutrino (anti-neutrino) interactions with a mean energy of 140(120) GeV. After correcting for geometric and detector efficiencies, this corresponds to 2.41×10^6 charged current events in the fiducial volume of the calorimeter. Scaling by the mass of the helium decay channel and total protons on target available in the data, one expects about 4,000 charged current ν and $\bar{\nu}$ events in the decay channel fiducial volume (see Table 4.3). The error on this normalization sample is $\pm 12\%$.

The high mass normalization method uses data from the decay channel to scale the Monte Carlo event sample. Background calculations are normalized to the data using charged current DIS interactions in the decay channel drift chambers. Events in this sample are required to pass the following "normalization cuts": (1) a vertex within the transverse fiducial volume ($|x| < 127$ cm, $|y| < 127$ cm); (2) a z vertex within 76.2 cm of a drift chamber; (3) no coincidences within 50 ns of the trigger in the upstream veto system; (4) $\geq$1 GeV energy deposit in the front of the calorimeter; and (5) one toroid-analyzed muon matched to a decay channel track. The Monte Carlo was normalized to match the observed 154 data events with two or more tracks. Figures 4.6 and 4.7 show the level of agreement between the data and MC distributions from the normalization sample. The error (dominated by data statistics) on this normalization is 8%.

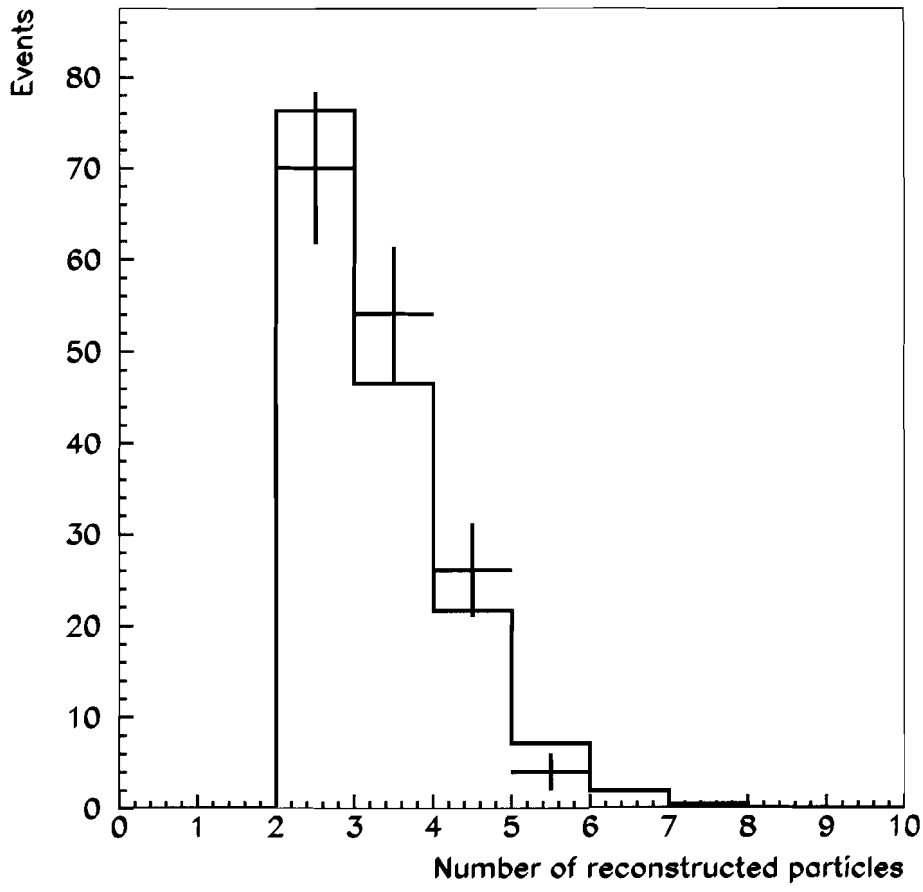

Figure 4.6: Distribution of number of tracks for data (crosses) and Monte Carlo (solid) normalization sample.

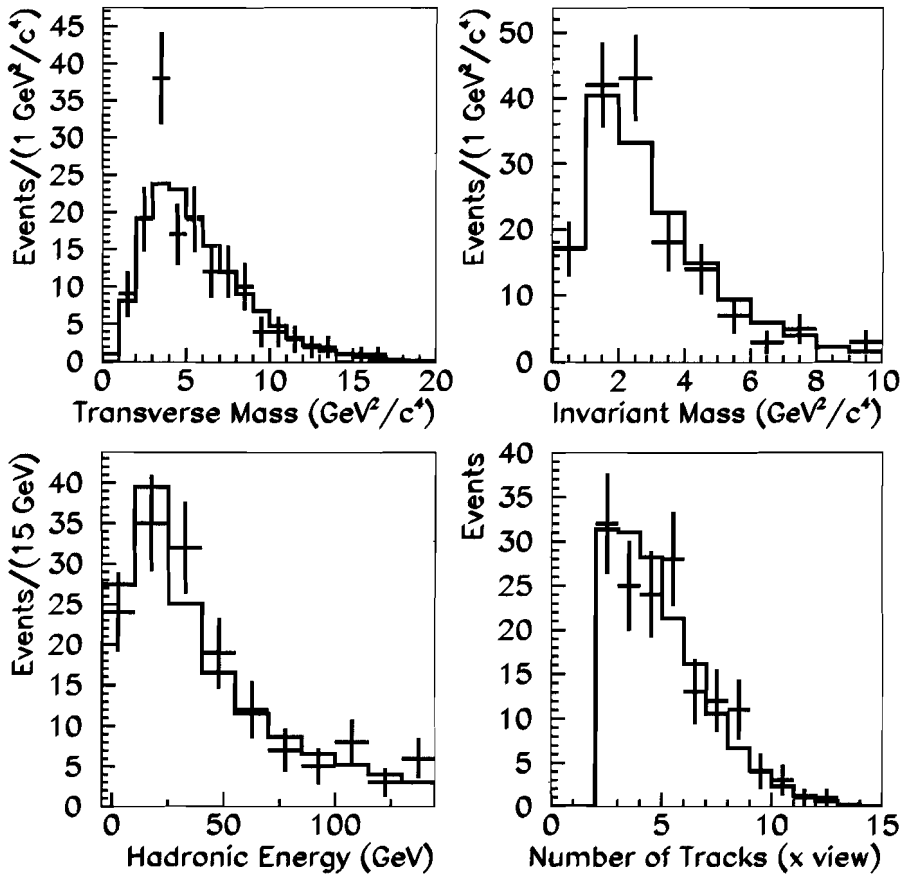

Figure 4.7: Distributions comparing data (points) and Monte Carlo (histogram) for charged current DIS interactions in the decay channel chambers. The distributions are: (a) transverse mass; (b) two-body invariant mass; (c) hadronic energy in the front of the calorimeter; (d) number of reconstructed tracks in the x view.

Part II

The Search for the Q^0

Books you were going to write with letters for titles.

Have you read his F?

Oh yes, but I prefer Q.

– *James Joyce*, Ulysses.

Chapter 5

The KARMEN Timing Anomaly

Searches for particular processes are often motivated either by a given theoretical framework that seeks to find verification, or by an experimental result which begins to suggest physics beyond an already accepted framework. In the case of our low mass search, the motivation came from the latter. The KARMEN neutrino experiment at the Rutherford Appleton Laboratory hinted at evidence for a new exotic particle with properties similar to a neutral heavy lepton with a mass of 33.9 MeV/c^2. Seizing the opportunity, NuTeV performed a direct search for this particle by making use of the instrumented decay channel. The method and results of this search are described in this section of the thesis.

5.1 The KARMEN Experiment

The main motivation for the NuTeV low-mass search stems from an anomalous result coming from the KARMEN neutrino experiment at the Rutherford Appleton Laboratory (RAL) [57]. RAL uses a pulsed neutrino beam resulting from stopped pions and muons to study in spectroscopic detail neutrino neutral current and charged cur-

rent interactions with carbon. The ISIS spallation facility (see Figure 5.1), uses a rapid-cycling synchrotron to create a 800 MeV pulsed proton beam. The synchrotron provides two 100 ns long pulses 325 ns apart, at an average beam current of 200 μA. The high-intensity, narrow pulsed beam collides with a massive Ta-D_2O target, providing low energy pions which are then stopped in the target. The first decay, $\pi \rightarrow \mu + \nu_\mu$, occurs rapidly ($\tau_\pi = 26$ ns), creating a short 30 MeV muon neutrino pulse which eventually reaches the KARMEN detector. The muons produced from the decay are also stopped in the massive target and eventually decay to neutrinos ($\mu^+ \rightarrow e^+\nu_e\overline{\nu}_\mu$), with energies ranging up to 53 MeV. However, their lifetime is much longer than the beam pulse ($\tau_\mu = 2.2\mu s$). The $\bar{\nu}_\mu$ and ν_e produced from muon decay thus have a rate which reflects the exponential decay of the parent muon, while the ν_μ produced in pion decay appears essentially prompt. KARMEN receives neutrinos with a very well-understood timing distribution: two sharp ν_μ pulses from pion decays and an exponential spectrum of ν_e and $\overline{\nu}_\mu$ from μ^+ decay (see Figure 5.2).

The KARMEN neutrino detector is located 17.7 m away from the primary target. The detector, designed to look for neutrino oscillations at the level of $\delta m^2 \approx 1$ eV^2 [58], consists of 512 optically independent vessels filled with liquid scintillator. Each vessel measures 17.8 cm $\times$17.4 cm $\times$353 cm, and provide a total coverage of 1.5 m $\times$1.5 m $\times$3 m fiducial volume. Though track reconstruction with the KARMEN detector is not possible, KARMEN can measure the energy, position, and timing of neutrino interactions in the carbon. KARMEN is thus sensitive to both $\nu_\mu, \bar{\nu}_\mu$, and ν_e neutral current and ν_e charged current interactions (the ν_μ and $\bar{\nu}_\mu$ charged current interactions cannot take place due to the threshold for μ production).

The KARMEN neutrino detector is also sensitive to cosmic rays and neutron induced background from their intense proton source. The well-defined timing spectrum allows KARMEN to study its cosmic ray background after each beam pulse (20 ms duration) in great detail. The KARMEN detector also shields itself from both

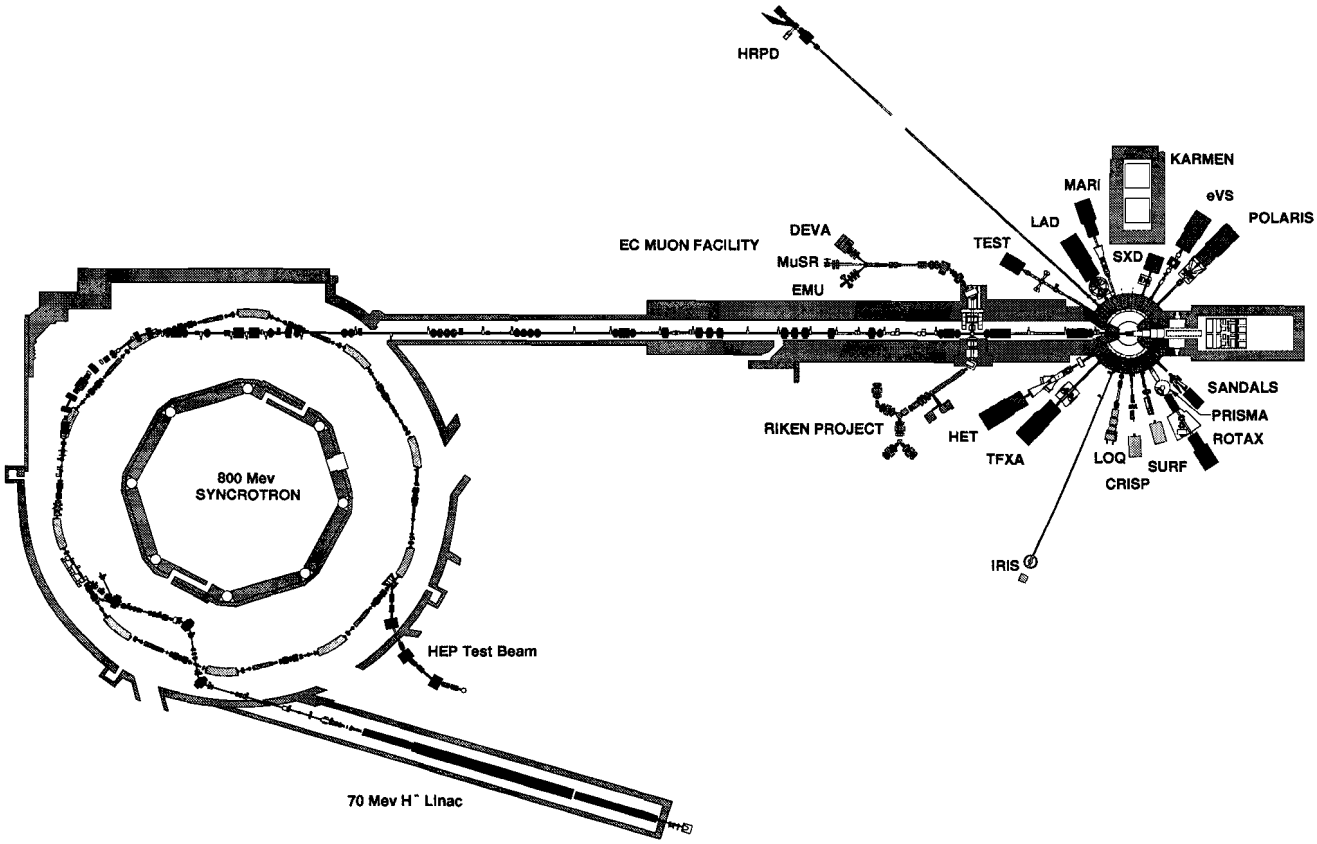

Figure 5.1: Schematic of the ISIS spallation source and KARMEN neutrino detector *(courtesy of K. Eitel).*

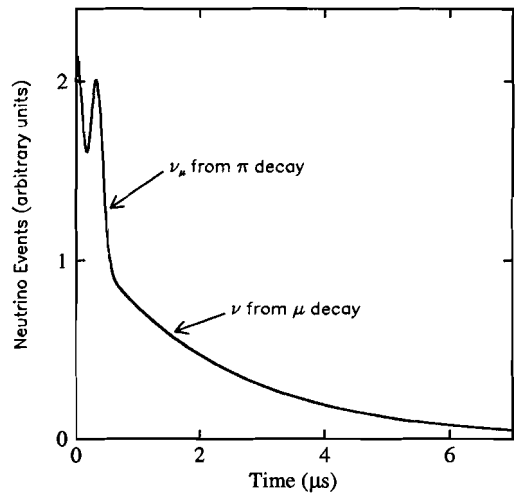

Figure 5.2: Timing structure of KARMEN neutrino beam. The ν_μ peaks are not to scale.

cosmic rays and neutron background by using 10 meters of iron plate shielding – a total mass of 7000 t. Both the timing structure of the neutrino beam and overburden of the detector allow KARMEN to study in detail the nature of the experiment's primary backgrounds.

Staring with their 1990 Run 1 data, the KARMEN neutrino timing distribution began showing serious deviations from expectation. Figure 5.3 shows the distribution of neutrino events in the detector as a function of time. One can see the exponential decay characteristic of the 2.2 μs muon decay. However, at 3.6 μs one can see an excess of 83$\pm$23 events above expectation. Based on rates alone, this excess represents a 3.5σ deviation ($P < 0.1\%$). More detailed analysis of the anomaly have taken into account correlations between the position and timing of the events. These two quantities would be correlated for a traveling particle, but would be uncorrelated for a statistical background fluctuation. By looking at position and timing distributions, the excess events seem consistent with a slow moving particle rather than a neutrino interaction.

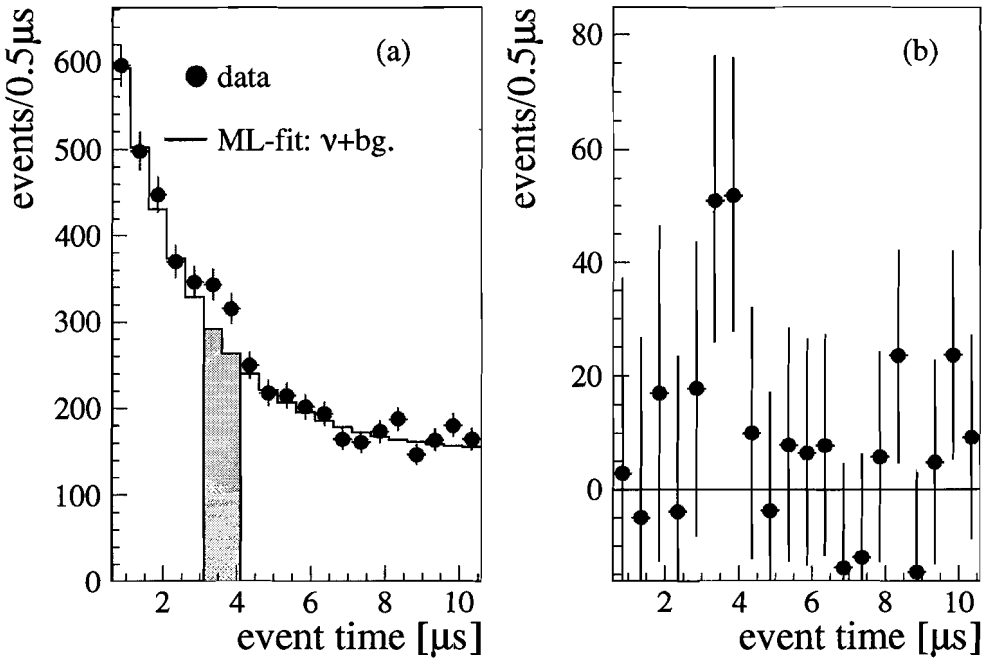

Figure 5.3: Timing distribution of neutrino events in the KARMEN neutrino detector from muon decay. There is a significant deviation from the expected curve at 3.6 μ s. The excess is further emphasized on the plot to the right, where Monte Carlo has been subtracted from data *(courtesy of K. Eitel).*

A likelihood analysis shows that the events have a 4.5σ deviation ($P < 0.03\%$) from expectation [59].

No beam or detector related effects can account for the anomalous, time-dependent excess of events in the KARMEN detector. Aside from an unlikely statistical fluctuation, the only explanation for the excess seems to reside in physics beyond the Standard Model. KARMEN thus postulates that a new particle is being produced from pion decay at rest:

$$\pi^+ \rightarrow \mu^+ + Q^0. \tag{5.1}$$

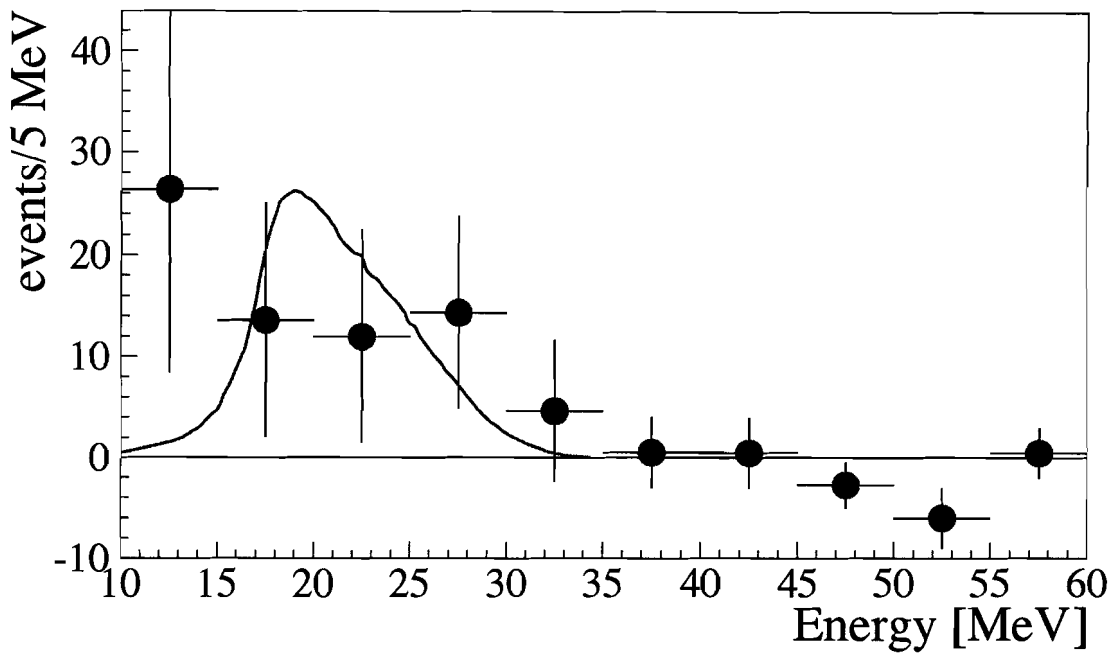

Figure 5.4: Energy distribution of Q^0 excess events in the KARMEN detector. The curve shows the expected distribution from a three-body decay *(courtesy of K. Eitel).*

Using the timing information of the excess events, KARMEN measures the velocity of the Q^0 particle at 4.87 ± 0.04 m/μs. Assuming the particle is produced directly from pion decay, one can determine the mass:

$$m_{Q^0} = \sqrt{m_\pi^2 + m_\mu^2 - 2m_\pi m_\mu \gamma} = 33.905 \pm 0.005 \text{ MeV}. \tag{5.2}$$

where γ is the ordinary relativistic variable. Because of the heavy shielding surrounding their detector, the particle lacks both electromagnetic and strong interactions. Based on the energy deposition of the excess events, the particle must eventually decay electromagnetically; either to $\gamma\nu$ or $e^+e^-\nu$. Energy distributions (see Figure 5.4) are more consistent with a three-body decay rather than a monochromatic 15.1 MeV photon expected from $\gamma\nu$ decay.

Based on the number of excess events in their detector, the KARMEN experiment reports the signal as a function of pion branching ratio $B(\pi \to Q^0 + \mu) \cdot B(Q^0 \to$ visible) and the Q^0 lifetime. The branching ratio reaches as low as 10^{-16} for short lifetimes (see Figure 5.8).

Due to the implications of the result, the Q^0 timing anomaly has stimulated both the experimental and theoretical community to provide a physical explanation or interpretation of their signal.

5.2 Experimental Searches: PSI

The Paul-Scherrer-Institut (PSI) [60] has performed a number of experimental searches to address the KARMEN timing anomaly. Rather than look directly for the decay product Q^0, PSI experiments study in detail the kinematics of the two-body decay $\pi^+ \to \mu^+ Q^0$ using a muon magnetic spectrometer. By studying the production mechanism rather than the Q^0 directly, PSI is insensitive to the lifetime of the particle.

The PSI experiment uses a high intensity pion beam at well-defined momenta; $p_\pi = 150$ MeV/c with a momentum spread of 1.2% at 95% C.L. The pions travel through a decay region, where they decay to muons. Using their beamline as a muon spectrometer, the experiment scans through muon momenta ranging from 103 MeV/c to 124 MeV/c. In this momentum range, the muons from $\pi^+ \to \mu^+ \nu_\mu$ decays have an angle of 255 mr from the beam axis, thus never entering the μ beamline. However, muons from $\pi^+ \to \mu^+ Q^0$ only have a ≤ 5 mr opening angle and thus can be detected. Using both the time of flight and muon momentum allows the experiment to be sensitive to the non-Standard Model decay. The signature would be an excess of muons with momenta of 113.5 MeV/c. Seeing no excess in their data, PSI has set a limit on the pion branching ratio to the Q^0:

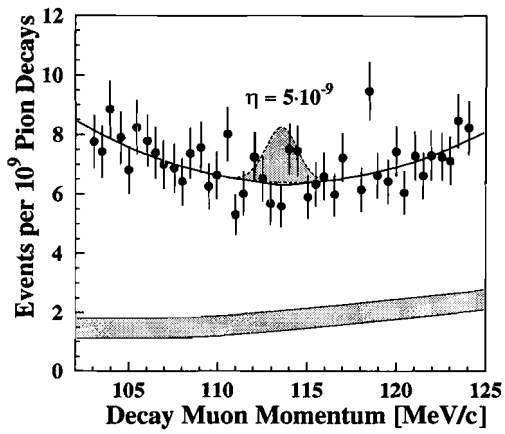

Figure 5.5: Data from the PSI experiment showing sample signal (Gaussian) with branching fraction at 5×10^{-9} level against expected background. Shaded band shows contribution from irreducible radiative corrections.

$$\frac{\Gamma(\pi^+ \to \mu^+ + Q^0)}{\Gamma(\pi^+ \to \mu^+ + \nu_\mu)} \leq 6 \times 10^{-10} \text{ (90\% C.L.)} \tag{5.3}$$

This limit is an order of magnitude improvement on their earlier result [61]. A similar search has been done for the decay chain $\pi^+ \to e^+ Q^0$, placing a limit on the branching ratio below 9×10^{-7} [62].

5.3 Theoretical Explanations

One of the difficulties of the KARMEN timing anomaly is providing a theoretical basis for the signal. Though the experimental signature seems robust, the theoretical basis of the signal fails to have a strong foundation.

5.3.1 A Conspiracy of Masses

The first theoretical bias against interpreting the excess of the signal comes from the mass of the particle itself. As measured from timing, the Q^0 mass is determined to be:

$$m_{Q^0} = 33.905 \pm 0.005 \text{ MeV}. \tag{5.4}$$

This is remarkably similar to the mass difference between the pion and the muon:

$$m_\pi - m_\mu = 33.91156 \pm 0.00035 \text{ MeV}. \tag{5.5}$$

How could two particles, in essence so different from one another (one a composite particle made of quarks, the second a fundamental lepton) conspire to be the mass of the Q^0? This evidence alone seems to shed doubt into the validity of the result, since only a particle with a mass in this range could be detected as a timing anomaly. However, the experimental result cannot and should not be dismissed on these grounds alone.

5.3.2 Q^0 Interpretation : ν_τ

One of the first explanations that presented itself for the Q^0 relied on only modest modifications on the Standard Model. The signal could be explained solely with Standard Model particles if one assumed that Q^0 was nothing more than the ν_τ with a mass of 33.9 MeV:

$$\pi \rightarrow \mu + \nu_\mu \rightarrow \nu_\tau \tag{5.6}$$

The ν_τ would appear either via neutrino oscillations or by lepton family number violation. This interpretation, however, was quickly ruled out by the LEP experiments [63]. Limits from looking at the kinematic spectrum of $\tau \rightarrow \nu_\tau + 5\pi$ placed a strict upper limit on the ν_τ mass at 18 MeV at 90% C.L. Thus, the Q^0 interpretation as the ν_τ lost favor, forcing the postulation of an entirely new particle not found in the Standard Model.

5.3.3 Q^0 Interpretation: Neutral Heavy Lepton

Neutral heavy leptons provides a natural framework to explain the Q^0. Many of the properties of the Q^0 are shared by neutral heavy leptons: neutrino mixing, weak interaction, no direct coupling to Z^0, and decay to lighter particles. However, if the Q^0 is indeed a neutral heavy lepton, then there exists a direct correspondence between the lifetime of the particle and its branching ratio. A great deal of work has been done to explain the Q^0 within the framework of neutral heavy leptons [64, 65]. In the most general case, the Q^0 would have couplings to all Standard Model neutrinos. As shown in Equation 1.47, the fraction of Q^0's produced from pion decay is:

$$N_{Q^0} = N_\pi \cdot \epsilon \cdot BR(\pi \rightarrow \mu + Q^0) \cdot \frac{\Gamma_{visible}}{\Gamma_{tot}} \cdot \mathcal{L}(\tau), \tag{5.7}$$

where $N_{Q^0}^{seen}$ is the number of Q^0 events detected, ϵ is the detector and geometric efficiency, and N_π is the number of pions produced at the target. The term $BR(\pi \rightarrow \mu + Q^0)$ can be determined explicitly for π decay:

$$BR(\pi \rightarrow \mu + Q^0) = \frac{\Gamma(\pi^+ \rightarrow \mu^+ Q^0)}{\Sigma_i\, \Gamma(\pi^+ \rightarrow \mu^+ \nu_i)} = \frac{0.0293 U_\mu^2}{(1 - U_\mu^2 + 0.0293 U_\mu^2)}. \tag{5.8}$$

The visible decay width ($\Gamma_{visible}$) is determined by either weak decay ($Q^0 \rightarrow \nu e^+ e^-$) or radiative decay ($Q^0 \rightarrow \gamma\nu$) (see Figures 5.6 and 5.7):

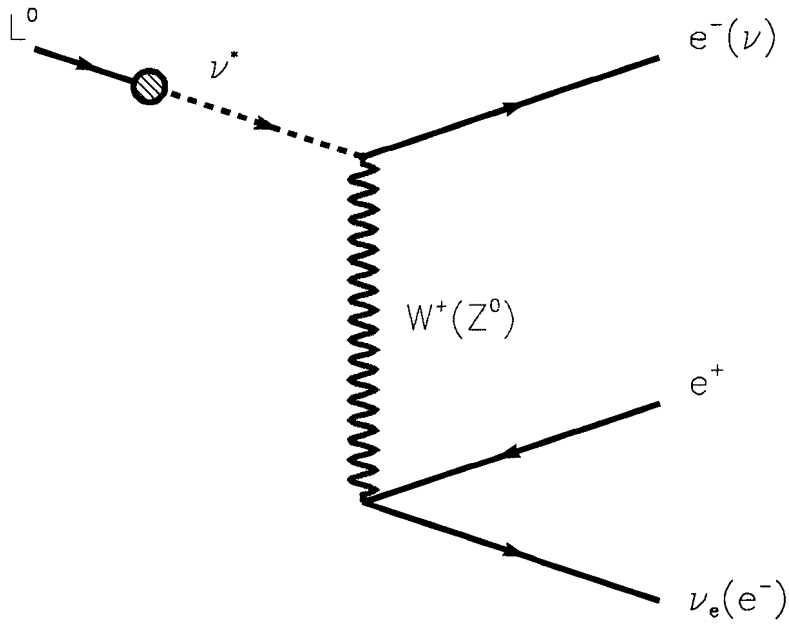

Figure 5.6: Feynman diagram for Q^0 isosinglet decay to $e^+e^-\nu$.

$$\Gamma_{visible} = \Gamma_{Q^0 \to \nu e^+ e^-} + \Gamma_{Q^0 \to \gamma\nu}. \tag{5.9}$$

One can solve for both decay widths directly:

$$\Gamma_{Q^0 \to \nu_i e^+ e^-} = \{\frac{1}{8}\sum_\alpha |U^\dagger_{i\alpha} U_{\alpha Q^0}|^2 (1+\rho^2) + |U^\dagger_{ie} U_{eQ^0}|^2 - \frac{1}{2} Re(\sum_\alpha |U^\dagger_{i\alpha} U_{\alpha Q^0} \cdot U^\dagger_{ie} U_{eQ^0}|)(1+\rho)\}\Gamma_{Q^0}, \text{ where} \tag{5.10}$$

$$\Gamma_{Q^0} = \frac{G_F^2 m_{Q^0}^5}{192\pi^3} \text{ ; and} \tag{5.11}$$

$$\rho = 1 - 4\sin\theta_W{}^2. \tag{5.12}$$

For the radiative contribution, we have:

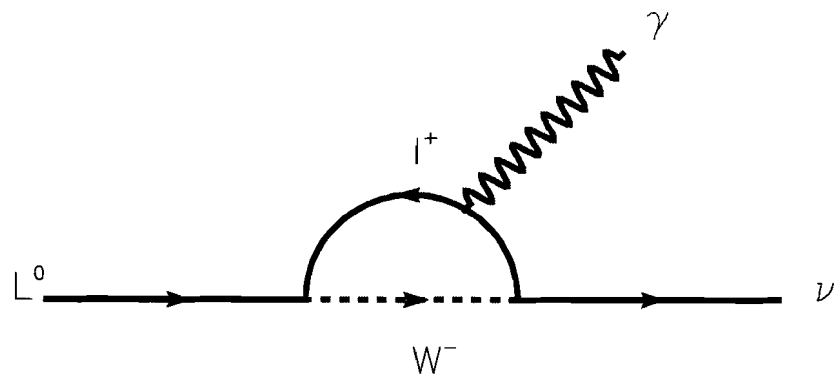

Figure 5.7: Feynman diagram for Q^0 isosinglet radiative decay to $\gamma\nu$.

$$\Gamma(Q^0 \to \nu_i\gamma) = \frac{27\alpha}{8\pi}|\sum_\alpha |U^\dagger_{i\alpha}U_{\alpha Q^0}|^2 \cdot \Gamma_{Q^0}. \tag{5.13}$$

The constraint from KARMEN is that the combination between the branching ratio and the visible decay width must be constant:

$$BR(\pi \to \mu + Q^0) \cdot \Gamma_{visible} \approx 3 \times 10^{-11} s^{-1}. \tag{5.14}$$

Since the Q^0 is only coming from pion decay, under the isosinglet model, one can rewrite the constraint as follows:

$$\frac{0.0293U_\mu^2}{1 - U_\mu^2 + 0.0293U_\mu^2}[929U_e^2(1-U_e^2) + 208U_\mu^2(1-U_\mu^2) + 208U_\tau^2(1-U_\tau^2)] = 3 \times 10^{-11}s^{-1}. \tag{5.15}$$

Direct experimental constraints on U_μ^2 and U_e^2 from PSI severely limit the neutral heavy lepton interpretation. Mixing purely to muons ($U_e^2 = U_\tau^2 = 0$) or to muons and electrons ($U_\tau^2 = 0$) is completely ruled out by the current data. The only remaining possibility is mixing to muon and tau neutrinos, constraining U_τ above 5×10^{-2}. It is

possible that a detailed analysis of τ decay to $5\pi + \nu$ could be done to completely rule out the neutral heavy lepton interpretation. Results from ALEPH are still pending.

5.3.4 Q^0 Interpretation : Supersymmetric Models

Calculations have been done trying to interpret the Q^0 as a light supersymmetric particle [66].

$$\pi \rightarrow \mu + \tilde{\gamma}(\tilde{Z}). \tag{5.16}$$

Possible candidates such as the zino or photino seem to fit the basic descriptions imposed by the observation. In order to accommodate the observation, one must include R-parity violating terms in the supersymmetric model, which though not ideal, are not forbidden by the theory. Theoretical calculations place the branching ratio above 10^{-8}. This scenario has been ruled out by the latest PSI limits.

5.4 Remarks on the KARMEN Result

The KARMEN timing anomaly seems to be a solid experimental signature without a strong significant theory to provide adequate interpretation. In a case such as this, the natural inclination is to make use of other experiments to either confirm or refute the result. Chapters 6-8 will explain in detail the NuTeV search for this elusive particle. Chapter 14 will provide an outlook as to the future of the Q^0, as well as more recent interpretations and searches made to the experiment.

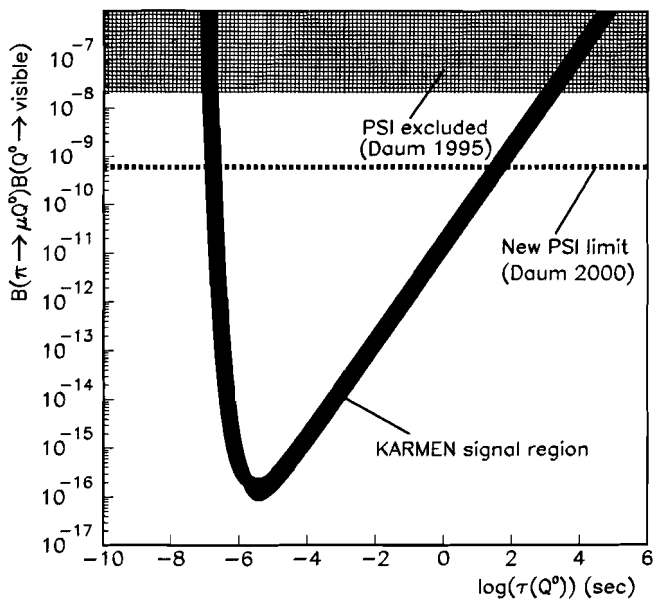

Figure 5.8: Branching ratio versus lifetime plot for the KARMEN signal and the exclusion regions (90% C.L.) from the PSI experiments. Note that the second PSI limit was published after this search was completed.

Chapter 6

Q^0 Event Selection

The KARMEN timing anomaly search at NuTeV involves quite different methodologies and systematics than those of the KARMEN experiment. KARMEN relies on the timing signature of the event to distinguish the Q^0 from the surrounding background, taking advantage of the non-relativistic time-of-flight of the Q^0 particle. NuTeV, however, uses a far more energetic production source (800 GeV protons, as opposed to 800 MeV). As a result, the particles travel at higher relativistic speeds. This makes using of the time of flight impossible, given the NuTeV decay channel design (see Fig. 6.1). NuTeV's advantage instead comes from the experiment's ability to see the tracks from the Q^0 decay to $e^+e^-\nu$.

6.1 Q^0 Signal

Since the Q^0 production stems from pion decay, it is essential to model the energy and momentum distributions of pions in our beam. Pion production is simulated using the DECAY TURTLE beam Monte Carlo program [38]. Figure 6.2 shows the pion energy spectrum for the 800 GeV proton beam. Production mechanisms have

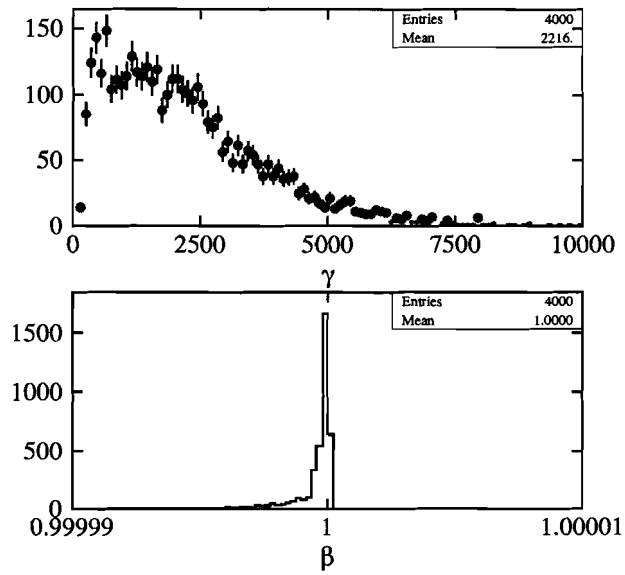

Figure 6.1: Relativistic gamma (top) and beta (bottom) distributions for Q^0 produced in the NuTeV neutrino beamline.

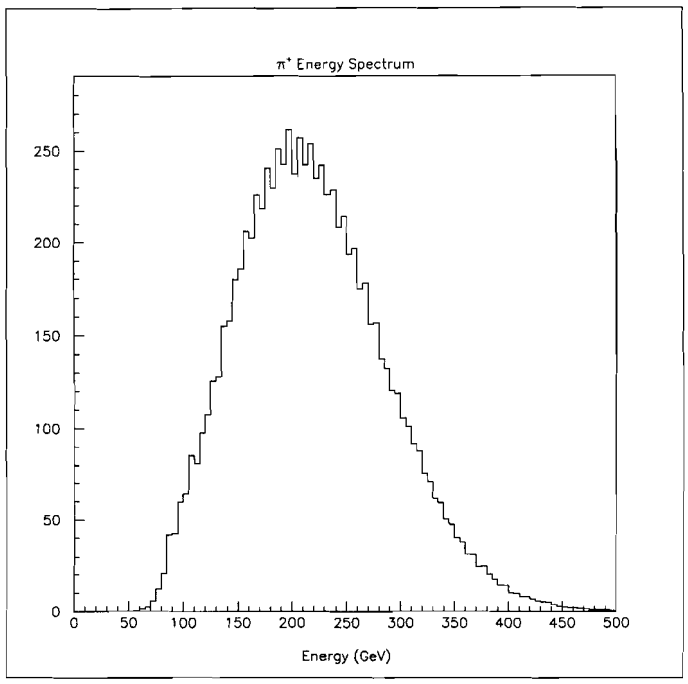

Figure 6.2: Energy spectrum of pions created from the 800 GeV protons in the NuTeV neutrino beamline.

been extensively checked with data from charged current neutrino interactions that take place downstream in the main NuTeV calorimeter [55].

As the pion decays to the Q^0, the energy release from the decay is very small, sending the Q^0 nearly parallel to the original pion trajectory. The result is a very well-collimated beam of Q^0's aimed at the NuTeV decay channel. This is a far more focused beam than what one would expect from the photons produced in the NuTeV neutrino beam. This unique feature of the expected Q^0 signal will be exploited in the analysis and is discussed in greater detail in Chapter 8.

The Q^0 decay kinematics provide a unique topology which enables one to distinguish it easily from common backgrounds. A sample Monte Carlo event is shown in Fig. 6.3. Although the tracks are nearly parallel, two tracks are clearly visible in the decay channel (see zoomed frame in Fig. 6.4). The average opening angle between

Table 6.1: Particle identification efficiency for Q^0 decay events.

	Reconstructed Event					
Generated Event	ee	$e\pi$	$e\mu$	$\mu\pi$	$\pi\pi$	$\mu\mu$
ee	90.1 %	0.0 %	0.0 %	0.0 %	9.9 %	0.0 %

the e^+e^- pair is 2 mr. The small opening angle has for adverse consequences to the analysis. First, the error on the longitudinal vertex is too large to determine whether the event came from the helium or the drift chamber. Although we can still require the vertex to be within the decay channel, the poor vertex resolution introduces an additional source of background in our sample, since most νN interactions come from the drift chambers. The second complication that comes from this topology is that the cluster in the calorimeter from the electron-positron pair is merged. Thus, only the energy of the entire cluster can be determined, and not the energy of each electron. Nevertheless, the Q^0 decay topology significantly separates it from the background. Furthermore, the efficiency for identifying the electromagnetic cluster as an ee pair is high (see Table 6.1).

6.2 Q^0 Background

The kinematic features of the Q^0 decay enable us to easily separate signal events from background. However, some background still persists at the sub-event level from (1) neutrino-nucleon interactions, (2) photon production in the earth-berm shielding, (3) K_L production, (4) π diffraction, (5) cosmic rays, and (6) other negligible sources.

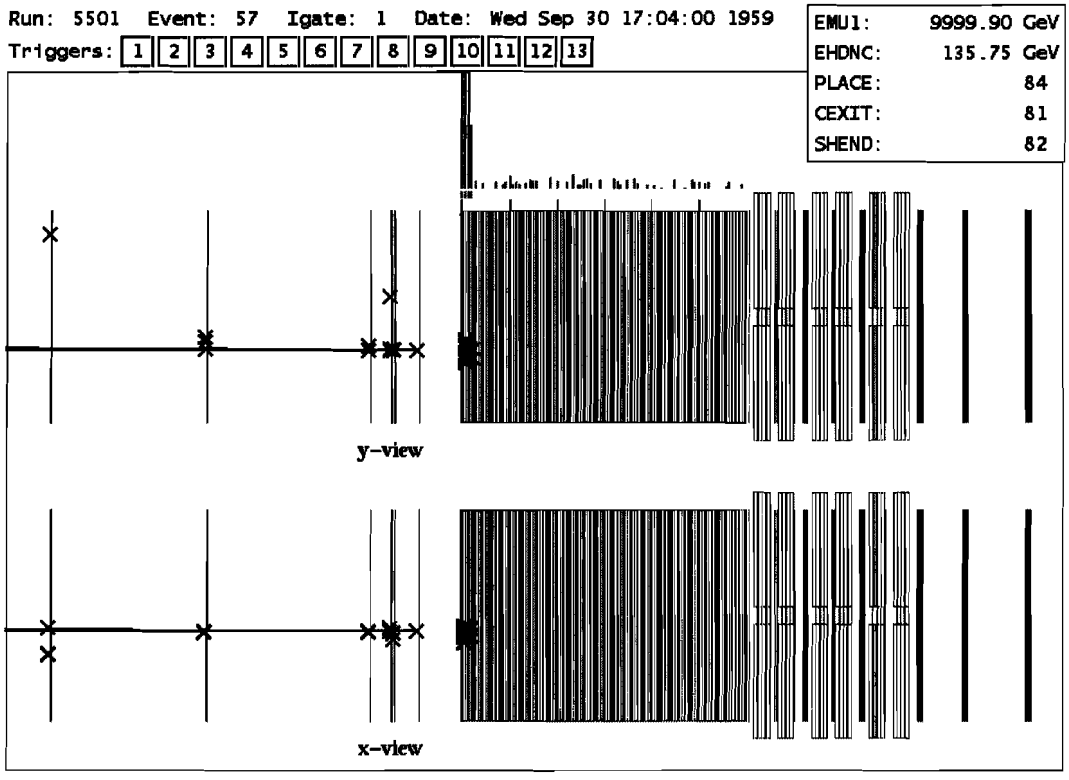

Figure 6.3: Monte Carlo Q^0 decay to $e^+e^-\nu$ within the fiducial volume of the NuTeV decay channel. Note the nearly parallel tracks leading to a single electromagnetic cluster in the NuTeV calorimeter.

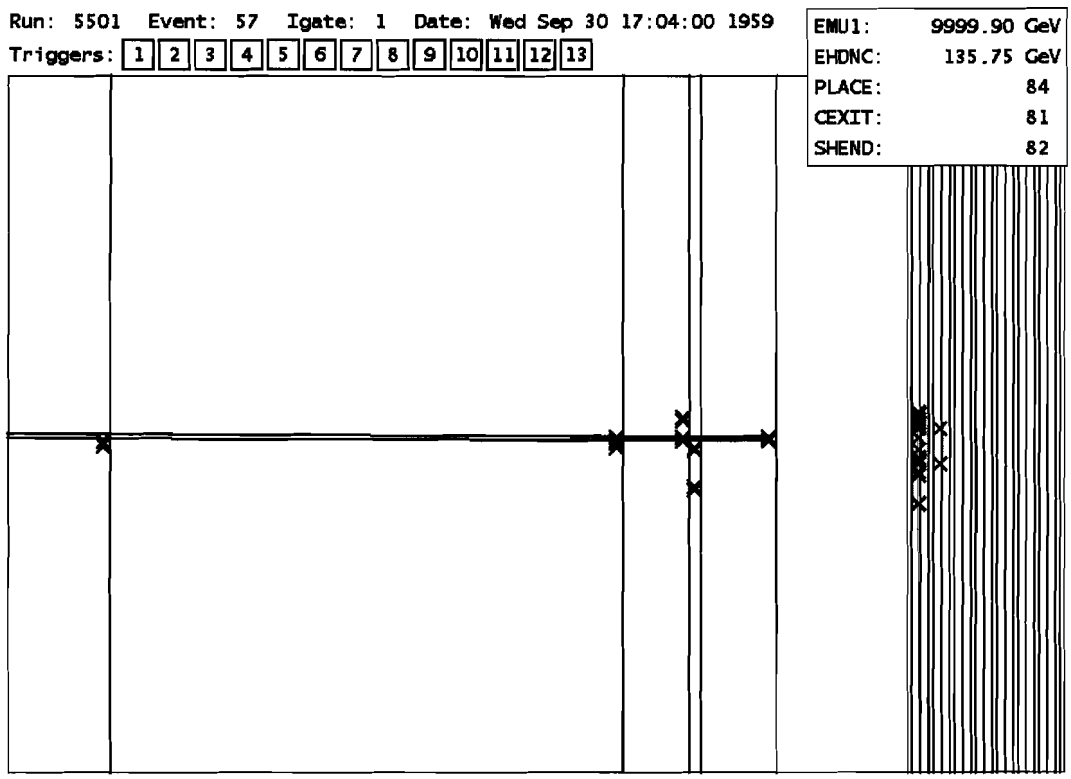

Figure 6.4: Same Monte Carlo Q^0 decay as in Figure 6.3, zoomed in to see the separation of the e^+e^- tracks.

6.2.1 Neutrino-Nucleon Interactions

Most of the activity in the decay channel consists of DIS charged current and neutral current interactions. Such backgrounds typically do not pose a significant background issue for the Q^0 search since most of the events have kinematic features that are quite distinct from typical signal events. DIS events events tend to have high multiplicities and wide angle tracks. Typical reconstructed m_T distributions lie well above 250 MeV/c^2. In addition, charged current DIS events (which constitute about 75% of all DIS events) have a muon associated with the event, allowing one to easily remove it from the sample. Nevertheless, a misreconstructed neutral current DIS or resonance event with a π^0 present in the hadronic shower can mimic a potential signal. Reconstruction and kinematic cuts have been developed to minimize such backgrounds to the sub-event level.

6.2.2 Photon Production

In addition to activity in the fiducial volume, backgrounds can be introduced by activity in the material surrounding the decay channel, such as neutrino-nucleon scattering in the earth-berm shielding. Most berm activity is removed by the veto wall panels. However, the veto wall is only effective for charged particles. Neutral particles such as photons and K_L's would not be vetoed by the scintillator.

Photons constitute the largest background to the Q^0 search. Photons are particularly dangerous to the analysis since they can pair produce e^+e^- particles with a small enough opening angle as to mimic the Q^0 signal. Photons are produced mainly from the electromagnetic decay of $\pi^0 \rightarrow \gamma\gamma$ present in the hadronic showers in neutrino-nucleon scattering. If a photon manages to reach the fiducial volume of the decay channel, it has $\approx$ 11% probability of converting in a given chamber. Fortunately, most photons have low energies and wide opening angles to distinguish them from

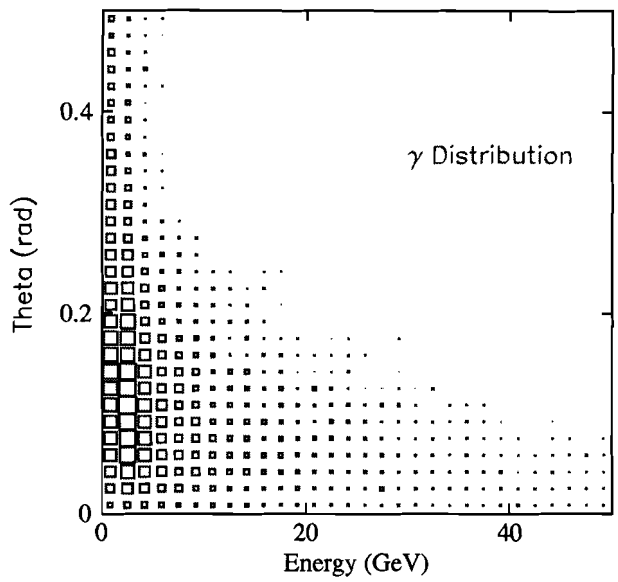

Figure 6.5: Energy and angle distributions for photons entering the decay channel from the earth-berm shielding.

the signal (see Figure 6.5). Photon production from neutrino-nucleon interactions has been estimated using the LEPTO/JETSET Monte Carlo. In addition, photon production from secondary pion interactions has been achieved using a parameterization of the GEANT pion distributions. Photons from secondary pion interactions has been found negligible compared to primary photon production (see Table 6.2).

6.2.3 K_L Production

Neutral kaons (K_L and K_S) are also produced in the earth-berm shielding and do not activate the veto wall. K_L's can be a potential source of background because they can decay to $\pi^{\pm}e^{\pm}\nu_e$ which could be mistaken for signal. K_L's occur at lower rates than photon production and have a soft energy spectrum. The K_L and K_S simulation is the same that is used for photon production. K_L production from secondary pion

Table 6.2: Photon production probability in GEANT pion showers.

Energy bin (GeV)	15-25	25-50	50-100	100-200
Pions in bin per ν interaction	0.2392	0.1553	0.0398	0.0043
Simulated π energy	25	50	100	200
Photons > 2 GeV per pion	0.118	0.216	0.392	0.621
Photons > 2 GeV per ν int.	0.028	0.034	0.016	0.003
Photons > 15 GeV per pion	0.003	0.015	0.047	0.100
Photons > 15 GeV per ν int.	0.0007	0.0023	0.0019	0.0004

interactions, however, are not considered in the simulation. The background expected from K_L production is below the 10^{-3} event level.

6.2.4 Diffractive π Production

The Q^0 search has the possibility of being sensitive to the diffractive processes $\nu N \rightarrow \nu\pi^0 N$ and $\nu_\mu N \rightarrow \mu\pi^\pm N$. Diffractive production is calculated using Vector Meson Dominance (VMD) and Partially-Conserved Axial Current (PCAC) models normalized to a previous measurement with the NuTeV calorimeter data [56]. Background levels from diffractive contributions are below 0.01 events in the signal region.

6.2.5 Negligible Sources

A number of other possible background sources have been found to be negligible because they very rarely produce reconstructed vertices in the decay channel. These include cosmic ray showers, conversions of photons produced in surrounding material, interactions from muons scattered from surrounding material, "leakage" of charged particles from the testbeam beamline (which occurred only during a few isolated

data collection periods, see Chapter 4), and multiple neutrino interactions in the decay channel. These background sources were constrained by data measurement and Monte Carlo study.

6.3 Event Selection

The signal Monte Carlo has been used to devise a series of cuts to select the Q^0 topology. Our selection criteria can be sub-divided into two broad categories: reconstruction cuts and kinematic cuts. Both sets of criteria are described below.

6.3.1 Reconstruction Cuts

The reconstruction requirements isolate events with two tracks within the fiducial volume of the decay channel. A list of the cuts used is given below:

- **Two Tracks:** This cut selects events with only two charged particles associated with a common vertex.
- **Fiducial Cut:** This cut ensures that the transverse position of the vertex is within 127 cm of the beam axis. It also ensures that the track projection to the front face of the calorimeter is within 127 cm of the beam axis. Finally, we also require that the longitudinal position of the vertex be within the upstream and downstream edges of the helium decay channel. Though the vertex longitudinal resolution is poor, the vertex can be constrained within the fiducial volume using the drift chamber hits as constraints. The total defined fiducial volume is 206.5 m^3.
- **Track and Vertex Quality Cuts:** Track and vertex χ^2 quality cuts are imposed in order to remove false vertices and poorly reconstructed tracks. The

cut requires that the track $\chi^2/\text{dof} \leq 15$ and that the vertex $\chi^2/\text{dof} \leq 10$.

- **Particle Identification:** The two tracks must both be identified as electrons. Because of the small opening angle of the two tracks, the two electron showers manifest themselves as a single electromagnetic cluster within the calorimeter.

- **Track Slope Cut:** To remove cosmic rays from our sample, we require that each track have $\theta_{(x,y)} \leq 10$ mr.

- **Track Projection Cut:** We require that each track when projected upstream to the veto wall fall within 127 cm of the beam center. This requirement ensures that any potential Q^0 candidates come from the neutrino beam rather than from interactions from material surrounding the decay channel.

- **Match XY Views:** Each track is required to have matching information in both the x and y views. The matching information comes from hits in the UV chamber (DK1). If no proper matching is found, the event is removed.

- **Match Tracks to Clusters:** Each vertex track is required to have a corresponding cluster in the calorimeter.

- **Remove Tracking Problems:** This cut removes events where either track has associated hits *upstream* of the reconstructed vertex.

- **Veto Wall Cut:** To ensure that the selected event does not come from a charged particle, strict requirements are imposed on activity in the veto wall. Events with coincident activity in the front and back veto wall panels within a ± 33 ns timing window from the trigger are removed. To further ensure that the event comes from a Q^0 decay rather than a photon interaction, we require that any track, when projected back to the veto wall, had no activity in that given panel. This cut removes events where a photon was produced in the upstream veto wall panel itself, where a veto wall coincidence cannot occur.

Table 6.3: Reconstruction cut efficiency for Q^0 search. Efficiency is taken relative to the number of generated events within the decay channel fiducial volume.

Cut	Cumulative Efficiency
Two Tracks Found	50.1%
Fiducial Volume	25.5%
Track and Vertex Quality	21.2%
Particle Identification	19.8%
Track Slope	18.6%
Track Projection	18.5%
Match XY Views	18.2%
Track-Cluster Match	18.2%
Remove Bad Tracks	18.1%
Veto Wall Cut	18.1%

The cumulative efficiencies of each of these cuts is shown in Table 6.3. All the above cuts ensure that the topology of the event matched that of a Q^0.

6.3.2 Kinematic Cuts

Further background reduction is achieved by applying a series of *kinematic* criteria upon the selected event. Some of the variables used in this analysis have already been defined in Chapter 3. A full list of the kinematic cuts used for this analysis is shown in Table 6.4 and explained in detail below.

- **Transverse Mass Cut:** We require that the reconstructed transverse mass m_T be less than 250 MeV/c^2. This cut helps remove DIS events which tend to

Table 6.4: Q^0 kinematic cuts. Individual efficiencies are quoted relative to events passing reconstruction cuts.

Cut	Purpose	Individual Efficiency
Transverse Mass Cut	Select Q^0 : Remove DIS	91.0%
x_{eff} Cut	Remove DIS	95.9%
W_{eff} Cut	Remove Quasi-Elastic Events	94.7%
Total Energy Cut	Remove Photons	90.0%

have much larger reconstructed transverse mass values due to their wide angle tracks (see Figure 6.6). The cut, however, is limited by the multiple scattering within our detector, as shown in Fig. 6.7.

- x_{eff} **Cut:** For this cut, we require $x_{eff} < 0.001$. The x_{eff} cut singles out the high energy and small opening angle topology of a Q^0 decay, since $x_{eff} \equiv \frac{Q^2_{eff}}{2M_p E_H}$. Figure 6.8 shows that x_{eff} has remarkable separation power between ν deep-inelastic scattering and Q^0 decays.

- W_{eff} **Cut:** This cut removes all events with $W^2_{eff} < 6.25$ GeV^2. The W_{eff} cut helps remove events with small center-of-mass energy, such as quasi-elastic scatters and resonance events. These events are particularly dangerous since they tend to have low multiplicity and small angle tracks [49]. However, since most of these events have $W_{eff} < 2$ GeV^2, a W_{eff} cut efficiently removes these events from our sample (see Figure 6.9).

- **Energy Cut:** We require that the total energy deposited by the e^+e^- pair be greater than 15 GeV. This cut is especially important to remove photons which may convert in our detector and mimic our signal. Since most photons come from secondary particles created in the earth-berm shielding, they tend to have

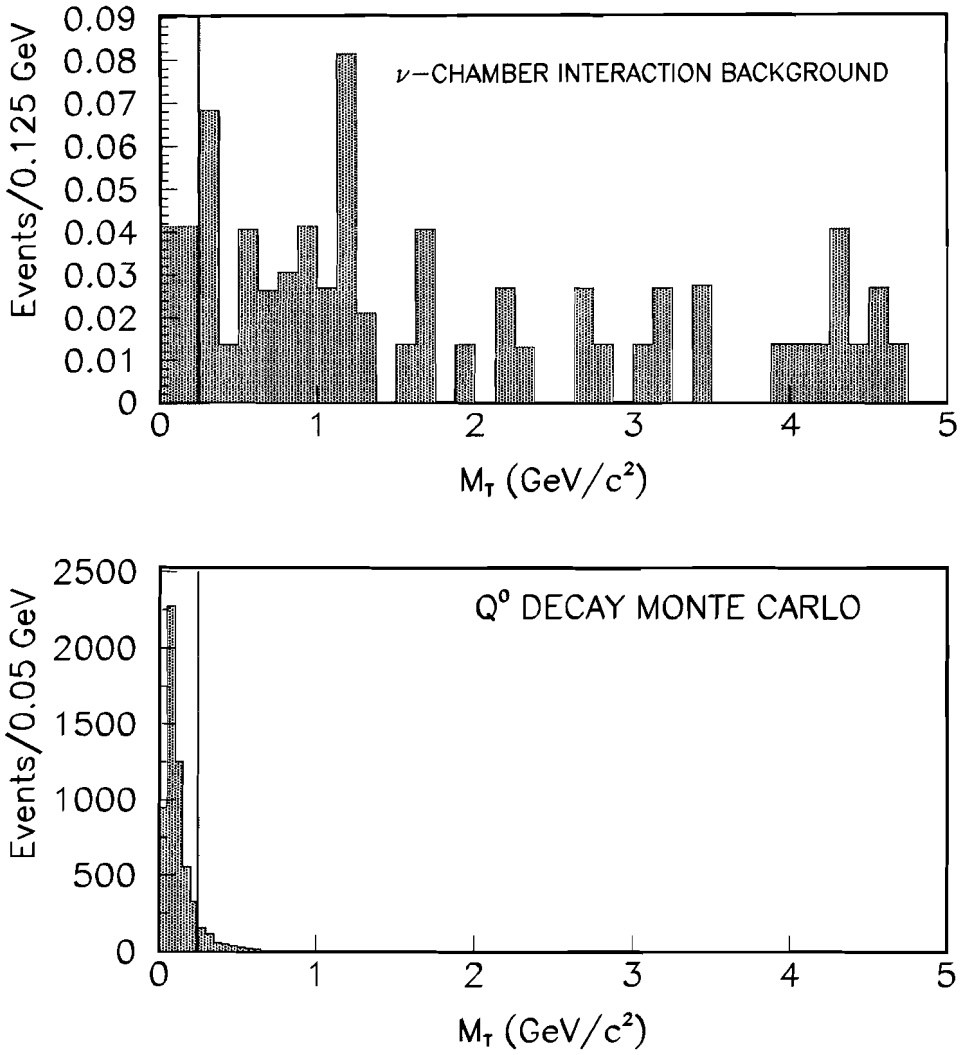

Figure 6.6: Transverse mass spectrum for DIS (top) and reconstructed Q^0 decay events (bottom). The line shows the cut used for this analysis.

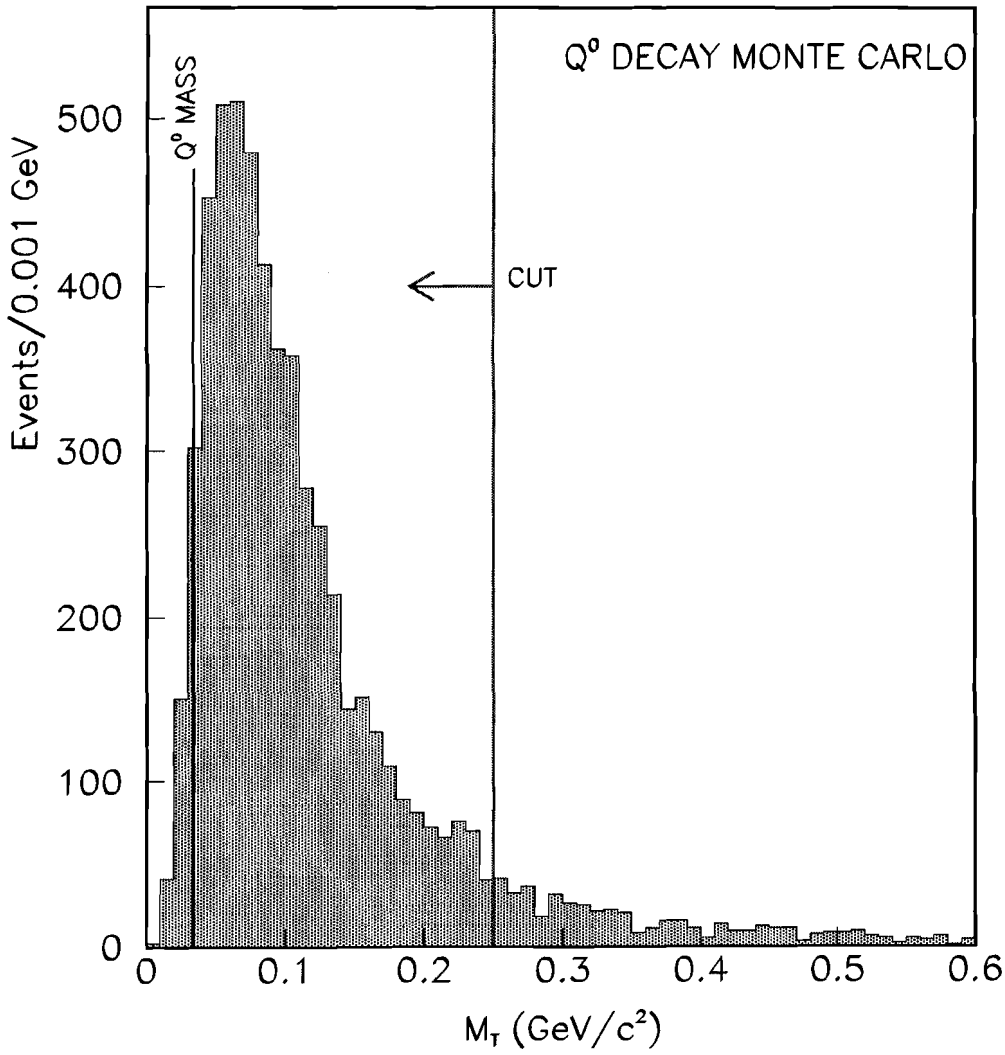

Figure 6.7: Blowup of the transverse mass spectrum of the reconstructed Q^0 decay. Although the theoretical limit for m_T is below 33.9 MeV, multiple scattering drives the reconstructed mass far above this. To retain most events, the cut is moved to 250 MeV.

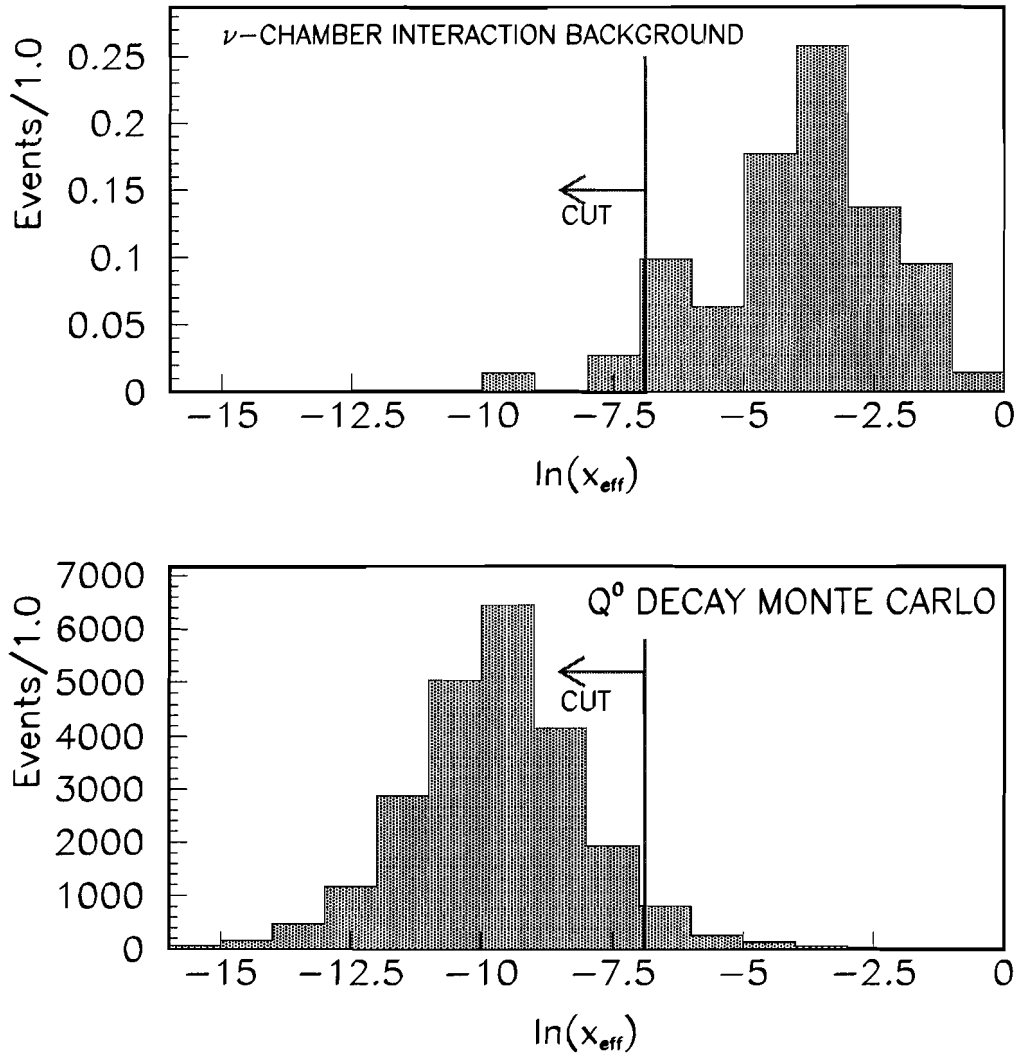

Figure 6.8: $ln(x_{eff})$ spectrum for DIS (top) and reconstructed Q^0 decay events (bottom). The line shows the cut used for this analysis.

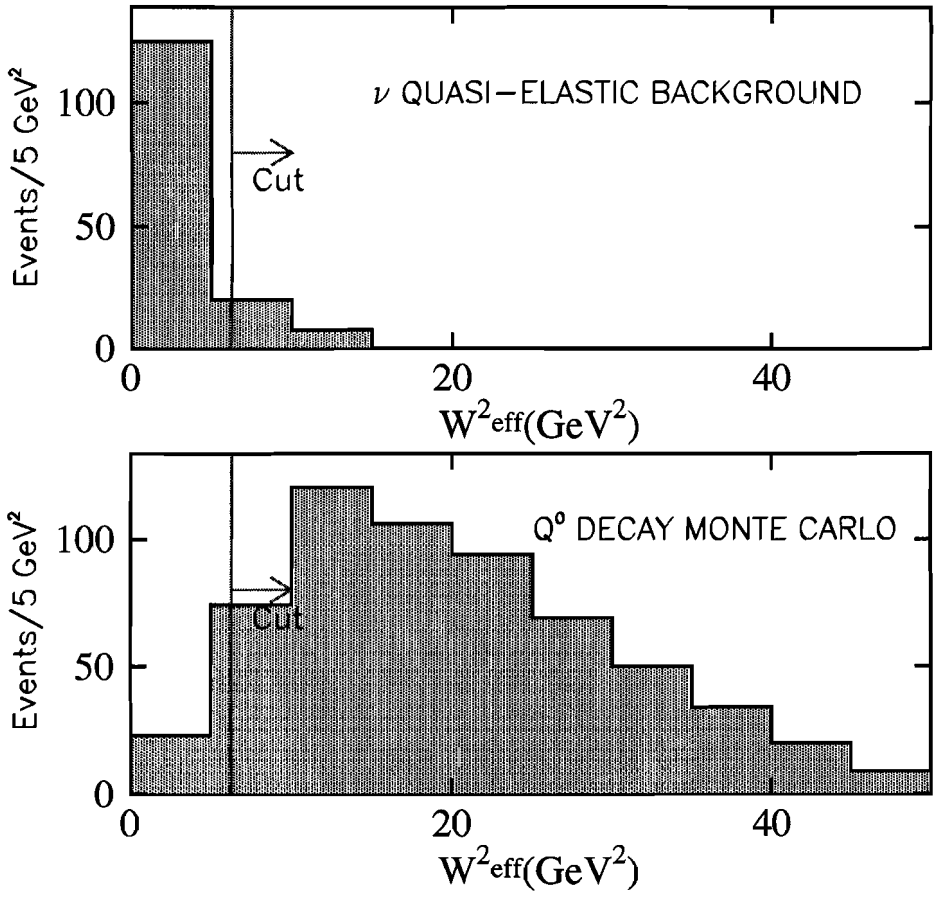

Figure 6.9: W^2_{eff} spectrum for quasi-elastic (top) and reconstructed Q^0 decay events (bottom). The line shows the cut used for this analysis.

Table 6.5: List of Q^0 backgrounds in signal region.

Background	Number of $ee\nu$ Expected
Neutral Current DIS	0.02 ± 0.02
Charged Current DIS	0.00 ± 0.04
Photons	0.04 ± 0.03
K_L	$\ll 0.001$
Diffractive π	$\ll 0.001$
Resonance Events	$\ll 0.005$
Cosmic Rays	$\ll 0.001$
Surrounding Material	$\ll 0.001$
Total	0.06 ± 0.05

softer energies spectra than their Q^0 counterparts (see Figure 6.10). Photons can be easily eliminated to sub-event levels using a simple energy cut.

The total acceptance for Q^0 events in the fiducial region after all cuts are applied is 15.6%.

6.4 Summary of Backgrounds

The total expected background level in the signal region after all cuts have been applied is 0.06 ± 0.05 events. The error on the background estimation is dominated by Monte Carlo statistics. A list of all backgrounds to the Q^0 signal region is given in Table 6.5.

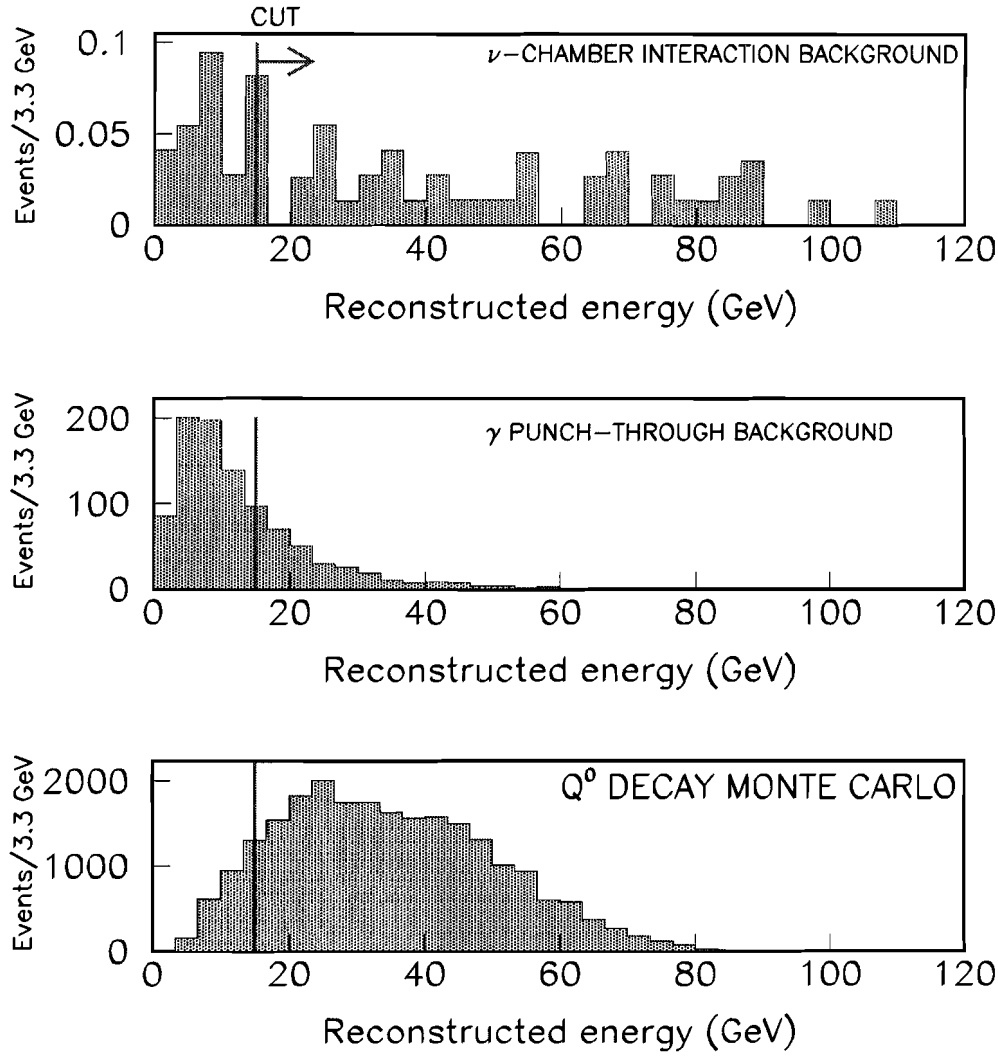

Figure 6.10: Energy spectrum for DIS (top), photon (middle), and Q^0 decay events (bottom). The line shows the cut used for this analysis.

Chapter 7

Q^0 Sideband Studies

Before examining the data in the signal region, we performed a series of studies to verify our background estimates. An effective method of doing this is to perform sideband studies: comparisons of Monte Carlo and selected data events which have similar characteristics to the expected signal but are outside the signal region itself. Sideband studies are effective in verifying normalizations, cut efficiencies, and detector simulations. Using the Monte Carlo event sample, we have made predictions for the following quantities: 1) the number of low energy (below 15 GeV) and high transverse mass (above 500 MeV/c^2) background events; 2) the number of $\mu\pi$ events; and 3) the number of multi-track events occurring within the decay channel. The results of these studies demonstrate good agreement between data and the Monte Carlo predictions. In the case of the multi-track sideband, where a larger sample of events was available, there is also good agreement for various kinematic distributions (Fig. 7.1).

7.1 The Low Energy/High Transverse Mass Sideband Study

Both photon production in the earth-berm shielding and neutrino-nucleon interactions in the helium and drift chambers constitute the main background sources to this search. It is imperative to verify the magnitude and distributions of these backgrounds using data. The first sideband study makes direct data/Monte Carlo predictions in the low energy/higher transverse mass region, where photon and neutrino backgrounds dominate.

The cuts used to isolate the low energy/high transverse mass sideband are quite similar to those used in the signal region. Except where noted, the reconstruction cuts listed in Table 6.3 are the same for the sideband region and the signal region. The kinematic cuts, however, have been altered to make the sideband sensitive to background rather than signal. Because photons tend to emerge at wide angles, we relax the track slope requirement from $\theta_(x, y) \leq 10$ mr to ≤ 100 mr. We also require that the event must have an electromagnetic shower and be identified as a μe, $e\pi$, or ee event. To increase the number of DIS events in our sample, we loosen the x_{eff} requirement to $x_{eff} \leq 0.05$ and change the center of mass energy requirement such that $W_{eff} \leq 8$ GeV. Finally, we require a specific range of energy and transverse mass. The event must have either 0.5 GeV $< m_T <$ 2.0 GeV and 2.2 GeV $> E_{vis}$ *or* have 0.25 GeV $< m_T <$ 2.0 GeV and 2.2 GeV$< E_{vis} <$ 15 GeV.

Results (shown in Table 7.1) agree reasonably well with the predicted Monte Carlo background rates. Note, however, that the total expected rate is systematically higher than what is seen in data. The probability of seeing 2 events where 4.2 ± 0.4 were expected is 13.4%. The low yield indicates a slight overestimation of the Monte Carlo, which yields a conservative background estimate. Furthermore, the mode which is most sensitive to Q^0 background (the ee mode) shows no apparent excess of

Table 7.1: Event rates for low energy/high transverse mass sideband.

Background	ee	$e\pi$	$e\mu$	Total
Monte Carlo	2.0 ± 0.2	1.2 ± 0.2	1.0 ± 0.2	4.2 ± 0.4
Events Seen	1	1	0	2

background and agrees very well with Monte Carlo expectations.

7.2 The $\mu\pi$ Sideband Study

Neutrino-nucleon deep inelastic scattering dominates the activity in the decay channel region. One of the low multiplicity signatures of DIS activity is $\nu N \rightarrow \mu\pi X$. We can test how well the Monte Carlo models DIS events by looking for events with a $\mu\pi$ in the final state. Because this study selects $\mu\pi$ final states rather than electromagnetic ones, the study is sensitive only to general activity in the decay channel region rather than specific Q^0 backgrounds.

Again, the cuts used in this study are similar to those used in the signal region. Most of the fiducial and reconstruction cuts the same, except that the veto wall projection cut has been removed and the angle projection cut has been raised from ≤ 10 mr to ≤ 100 mr. We require the energy of the muon to be above 2.2 GeV, while the energy of the pion to be above 5 GeV. Because $\mu\pi$ events from DIS tend to have large angles, we loosen the x_{eff} and m_T cuts to < 0.1 and < 2 GeV respectively. We also require $W_{eff} > 2$ GeV; and, of course, we require the event to be identified as a $\mu\pi$.

With the above requirements, the Monte Carlo predicted a total of 4.1 ± 0.3 events in this sideband region. A total of 3 events were seen in the data, showing consistency

between data and Monte Carlo.

7.3 The Multi-Track Sideband Study

One way to check the overall normalization of events is to examine samples with high statistics. Events with higher multiplicities yield much higher rates than previous sidebands. For this study, we require the presence of at least three tracks from a common vertex. All other reconstruction cuts are applied, except for the track projection to the veto wall and the tight angle requirement. The energy of each particle is required to be above 2.2 GeV, with a total visible energy above 15 GeV. The total transverse mass of the system must be below 10 GeV.

The total number of events expected from this sample is 13.7 ± 0.6; 10 were seen in the data. Since the study yielded a marginally higher number of events, it was possible to perform a much more detailed study of the different kinematic distributions. The distribution in Figure 7.1 demonstrate very good agreement between data and Monte Carlo.

7.4 Normalization Sideband

Finally, one last check is performed in order to accurately assess the overall normalization used for the Q^0 search. In order to check the normalization, a high statistics sample is selected from the NuTeV decay channel data. Minimal requirements are imposed in order to increase the statistical power of the sample. We require that a vertex with three or more tracks be found in the upstream fiducial region (downstream of DK5) of the decay channel. Track angle, track χ^2/dof, and veto wall cuts used for the signal region are still imposed, but all other requirements are removed. A

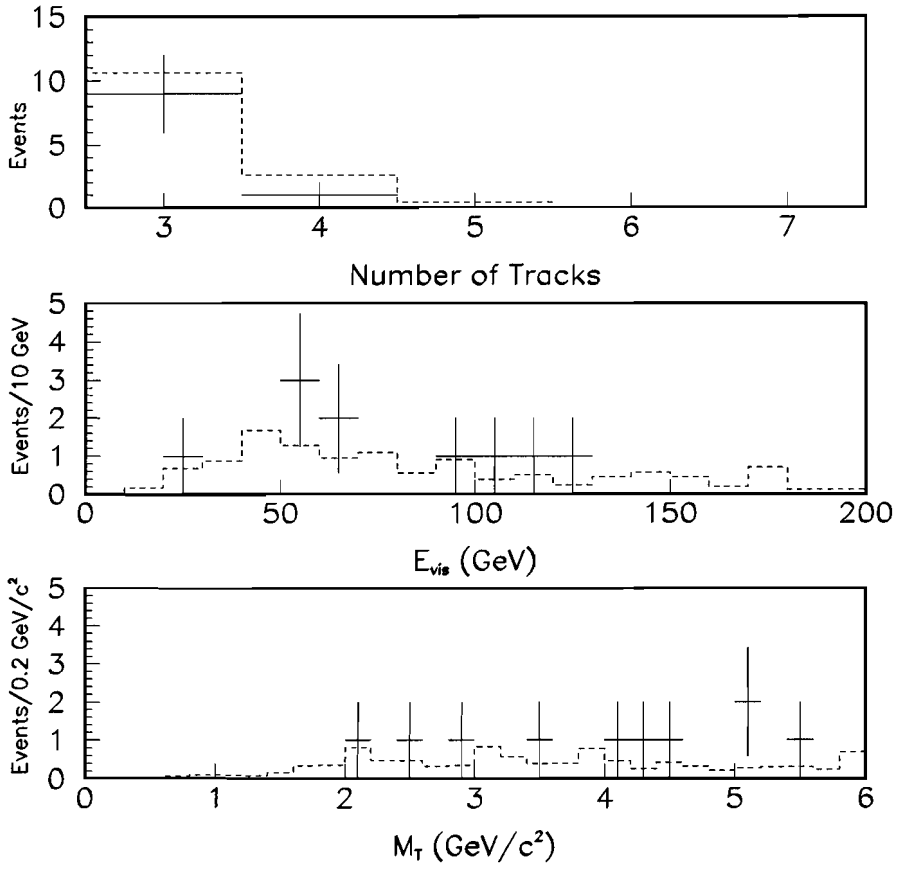

Figure 7.1: Kinematic distributions of multiplicity, energy, and transverse mass for data (crosses) and Monte Carlo (dashed) events in the multi-track sample. Monte Carlo is absolutely normalized.

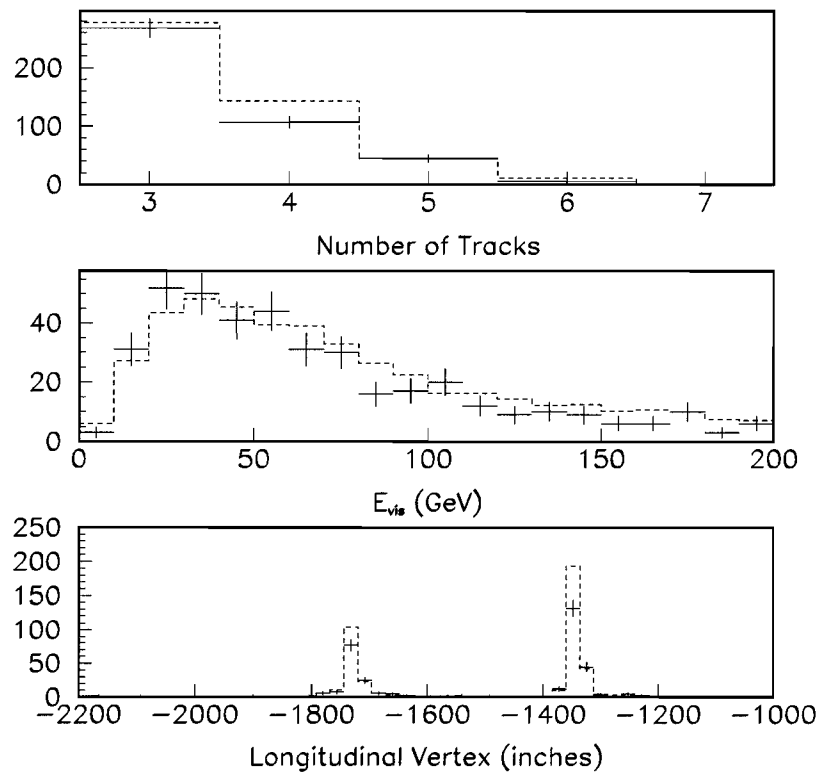

Figure 7.2: Normalization distributions for data (crosses) and Monte Carlo (dashed line) for number of tracks, energy, and vertex position

total of 479 MC events were predicted; 428 events were seen in the data. Kinematic distributions from the sample, however, agree with MC predictions (see Figure 7.2).

7.5 Summary of Sideband Studies

In conclusion, the sideband study proves to be an excellent tool to study the simulation of background events. It provides an opportunity to look for events which had not been simulated, check the over background level to within 2σ, and verify that our LEPTO/GEANT approach yields reasonable kinematic and event level predictions.

Table 7.2: Summary of Q^0 sideband studies.

Type of Event	Events Predicted	Events Seen
High Transverse Mass	4.2 ± 0.4	2
$\mu\pi$ Events	4.1 ± 0.6	3
Multiple Track Events	13.7 ± 1.8	10
Normalization	479 ± 22	428

This study provides a solid basis for accessing the signal region.

Chapter 8

Q^0 Search Results

8.1 Transverse Position Dependence

When we do open the signal region and look at the potential events which lie within, the first question that will come to mind is obvious: is this real evidence for new physics, or is this still an unforeseen background coming from neutrino interactions? Though the sideband study provides evidence that background events are modeled well, there are additional handles which will allow us to distinguish between background and signal events. One such handle is to use a position-dependent likelihood function.

Because the Q^0 has a mass that is almost at the limit of the kinematically allowed region for $\pi \rightarrow \mu + Q^0$, the Q^0 particles tend to travel in directions that are nearly parallel to the original pion. This results in a more focused transverse distribution of Q^0's as they pass through the front face of the calorimeter. By contrast, neutrino-induced background (i.e., photons coming from neutrino-berm interactions), exhibit a much more uniform spread across the front face of the calorimeter (see Figures 8.1 and 8.2). We utilize this feature to provide a likelihood function to distinguish Q^0

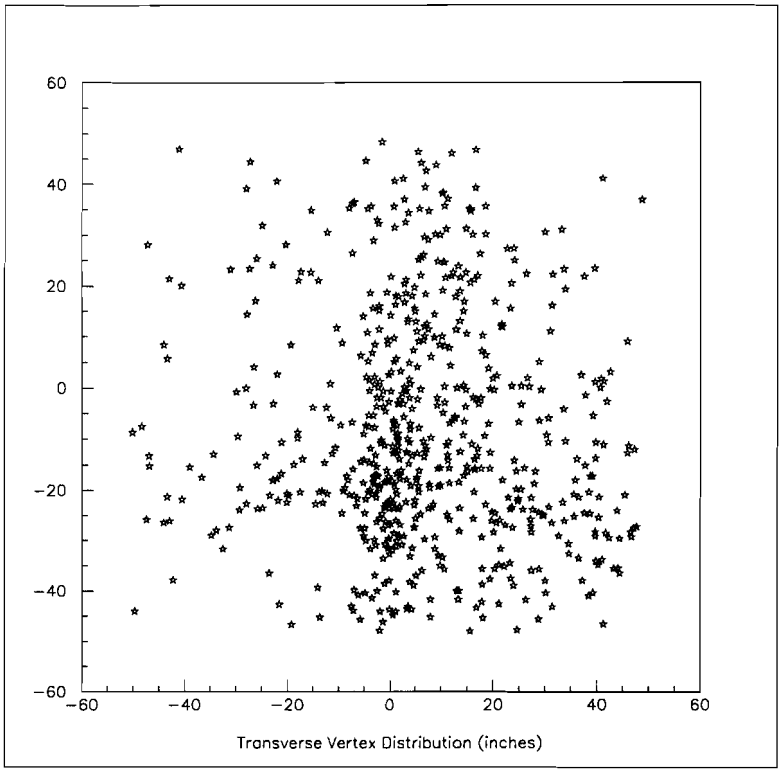

Figure 8.1: Transverse vertex distribution for Q^0 passing reconstruction cuts.

events from background events.

The log-likelihood function can be defined as:

$$L = \log \frac{\rho_{Q^0}(x, y)}{\rho_\gamma(x, y)}, \tag{8.1}$$

where ρ is the density of events in a given vertex position bin.

To calculate the density function ρ, we divide the number of events in a given bin by its area. The bins are not uniform in size, and have been chosen to ensure that

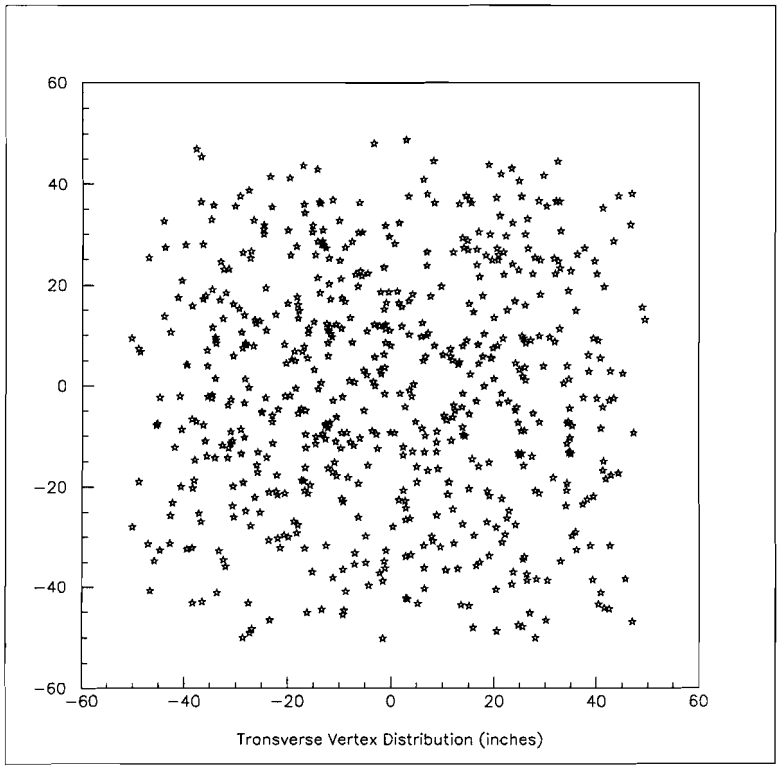

Figure 8.2: Transverse vertex distribution for photons passing reconstruction cuts.

enough events populated each bin. This method yields a modest separation of 1σ between signal and Monte Carlo, making it a more effective tool if multiple events appear in the signal region.

8.2 The Signal Region

Based on our Monte Carlo study, we expected 0.06 ± 0.05 total background events within our signal region. One can calculate the probability of seeing N events with background $\mu \pm \sigma$ using the following algorithm:

$$P(N) = \frac{F(N)}{\sum_{j=1}^{\infty} F(j)}, \text{ where} \tag{8.2}$$

$$F(N) = \int_0^\infty G(\mu, \sigma, x) P_n(N, x) dx, \tag{8.3}$$

$$P_n(N, x) = \frac{e^{-x} x^N}{N!}, \text{ and} \tag{8.4}$$

$$G(\mu, \sigma, x) = A e^{-(x-\mu)^2/2\sigma^2}. \tag{8.5}$$

The probability of seeing zero events from an expected background of 0.06 ± 0.05 is 94%.

When we analyzed the signal region, no events passed the selection criteria. There were also no events seen which were identified as either $e\pi$ or $e\mu$. Using Eq. 5.7, a 90% C.L. limit can be set on the branching ratio $B(\pi \to \mu + Q^0) \cdot B(Q^0 \to \text{visible})$. The limit uses the unified approach from Feldman and Cousins [67]. This limit places a severe restriction on the small lifetime solution of the KARMEN timing anomaly. NuTeV is sensitive to this region of phase space due to the energy and baseline of the neutrino beamline.

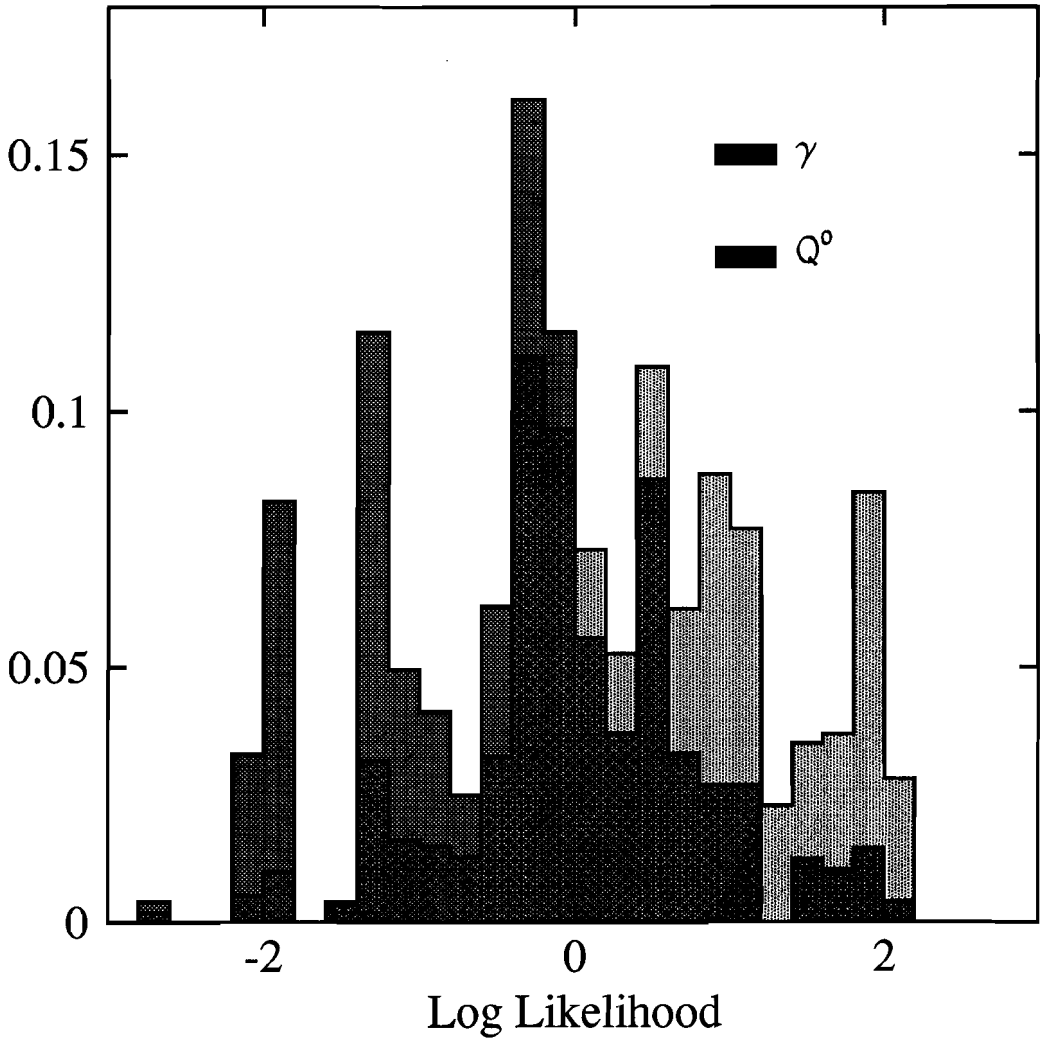

Figure 8.3: Log likelihood distribution for photon events (black) and Q^0 events (red).

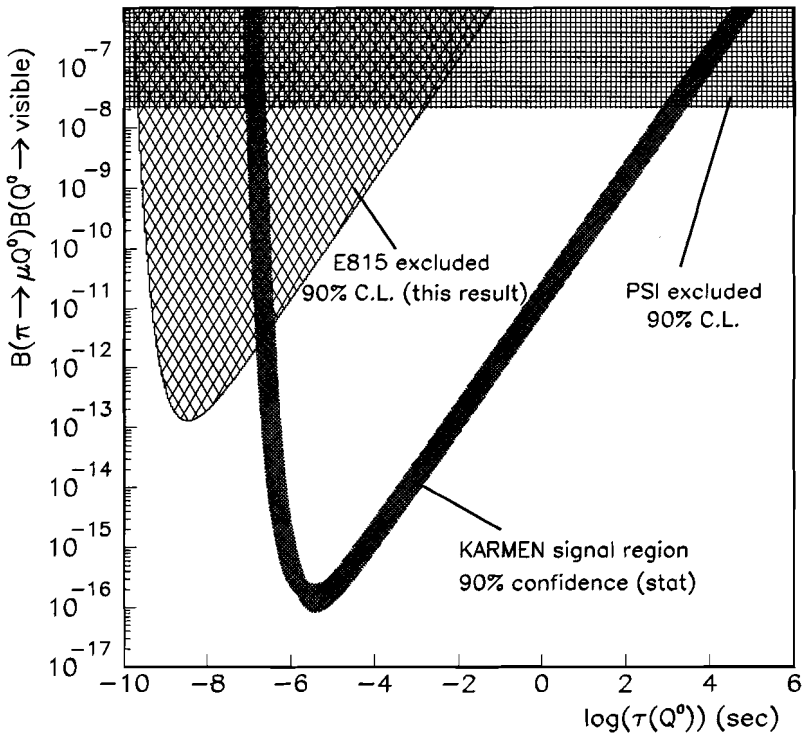

Figure 8.4: Branching ratio versus lifetime plot for the KARMEN signal and the exclusion regions (90% C.L.) from the NuTeV and PSI experiments.

In addition, NuTeV is also sensitive to the reaction $\pi \to e + Q^0$. The limit for this reaction is shown in Fig. 8.5. Note that the KARMEN timing anomaly region is not present in this curve because their signal comes only from pion decay to muons.

This result excludes a region of parameter space which extends as low as four orders of magnitude below previous limits on the short lifetime solution to the KARMEN anomaly. An experiment with significantly more pion decays will be necessary to completely confirm or rule out the longer lifetime and lower branching ratio regions.

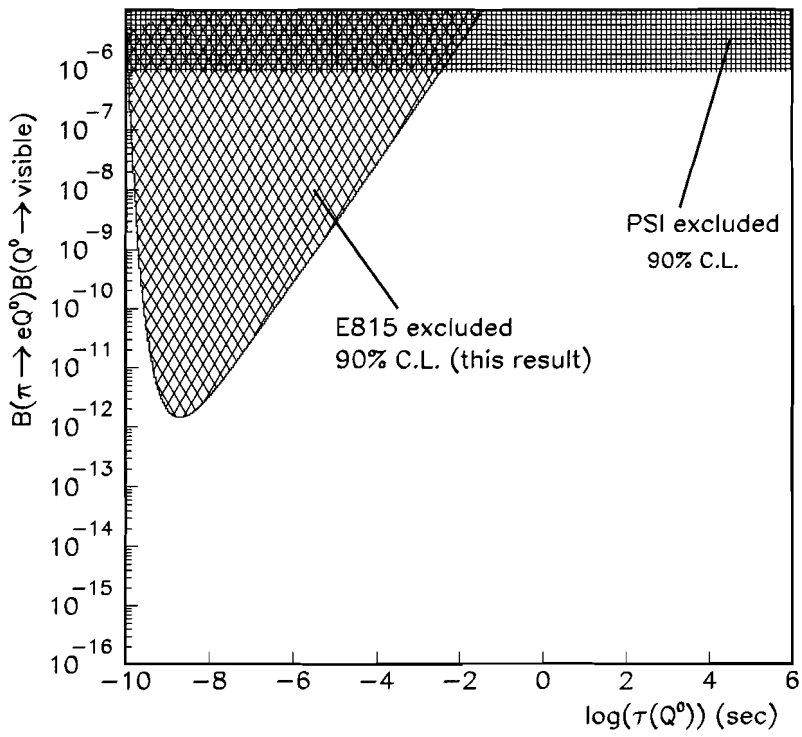

Figure 8.5: Branching ratio versus lifetime plot for the NuTeV limit for $\pi \to e + Q^0$.

Part III

The High Mass Search

"If you open the box and see no events,
you'll set a nice limit and everything will be fine.
... If you see any events, your life will be hell."
–T. Bolton

And I will show you something different from either
Your shadow in the morning striding behind you
Or your shadow at evening rising to meet you;
I will show you fear in a handful of dust.

–*T.S. Eliot,* The Waste Land

Chapter 9

Motivation for the High Mass Search

NuTeV previously searched for massive sterile neutrinos in the mass region between 0.3 to 3.0 GeV/c^2 with at least one final state muon [27]. The study addressed neutral heavy leptons that could be produced in the decay of K and D mesons, whose hadronic production rate is relatively well-measured [68]. This mass region has low background from deep inelastic neutrino events in the decay channel. We wish to extend the reach of that analysis in order to address exotic particle production for masses above 2.2 GeV/c^2. The search will focus on particles that may have zero electric charge, long lifetimes, and small interaction rates with ordinary matter. We shall refer to these particles as N^0's.

The search for events with masses above 2.2 GeV differs from the previous searches in two respects. First, the backgrounds from neutrino interaction events in the decay channel are more severe, because such events tend to be reconstructed with high m_T. Reducing this potential background source requires tighter selection criteria than previous analyses. Second, production mechanisms are quite different. N^0 particles

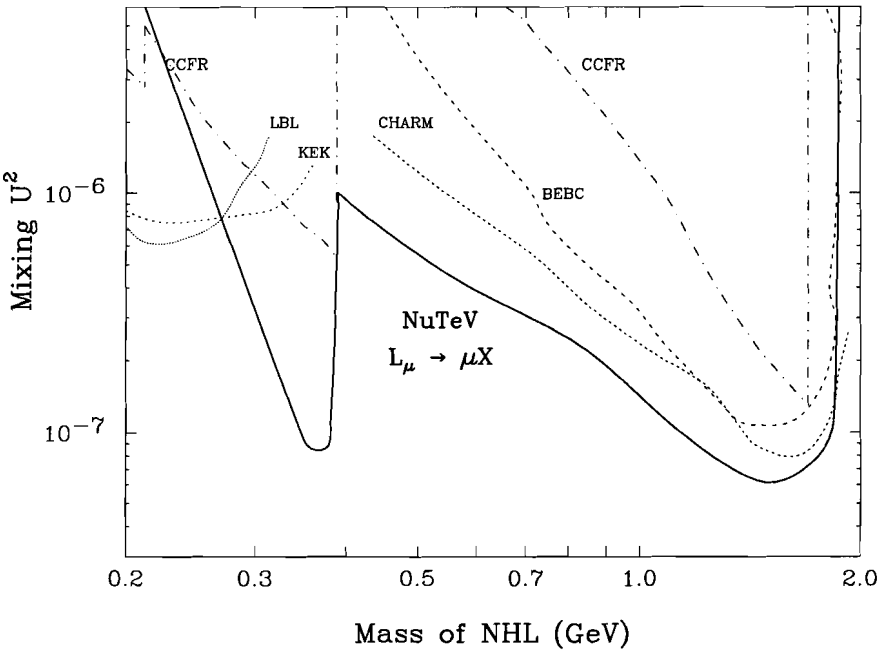

Figure 9.1: NuTeV 90% confidence level limit on U_μ^2 mixing from D and K production. Limit shows over an order of magnitude improvement over previous results [71, 72, 73, 74]

with masses above 1.8 GeV can only be produced at NuTeV in decays of B mesons, by neutrino interactions in earth-steel shielding upstream of the detector [70], or by primary production by protons in the target.

This search for N^0 particles in the 2.2-10 GeV/c^2 range has significant implications for current and future extensions of the Standard Model. Neutral heavy leptons and light supersymmetric particles are two theoretical models which this search can potentially address.

9.1 Neutral Heavy Lepton Production

Many Grand Unified Theories (GUTs) predict neutral heavy leptons and observing them would give important guidance to theoretical work. Neutral heavy leptons are produced and decay through mixing with Standard Model neutrinos. NuTeV has already performed a search for these particles with masses below 2.2 GeV/c^2. Above this mass, production is limited to B decay and neutrino scattering.

9.1.1 B Production

Fermilab E771 has measured the cross-section for B production in 800 GeV proton-nucleon collisions [69]. The measured value of 43^{+27}_{-17} (stat)$^{+7}_{-7}$ (syst) nb is much lower than charm production cross-sections. N^0 production from B decay is slightly enhanced due to the higher N^0 mass, which reduces the helicity suppression. However, the branching ratio is also suppressed by the mixing parameter $|U^2|$. The branching ratios of the dominant decay modes ($B^\pm \to D^0\mu^\pm N^0$ and $B^\pm \to \mu^\pm N^0$) are shown in Figure 9.2 for $|U^2| = 1$.

The neutral heavy lepton mixing parameter $|U^2|$ describes the mixing of the N^0 with a Standard Model neutrino and determines the number of N^0's produced from

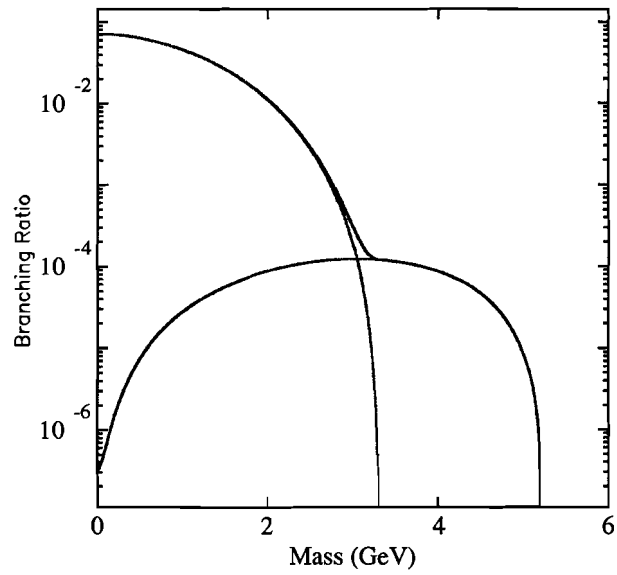

Figure 9.2: Branching ratio for $B^{\pm} \to D^0\mu^{\pm}N^0$ (red curve) and $B^{\pm} \to \mu^{\pm}N^0$ (blue curve) for $|U^2| = 1$.

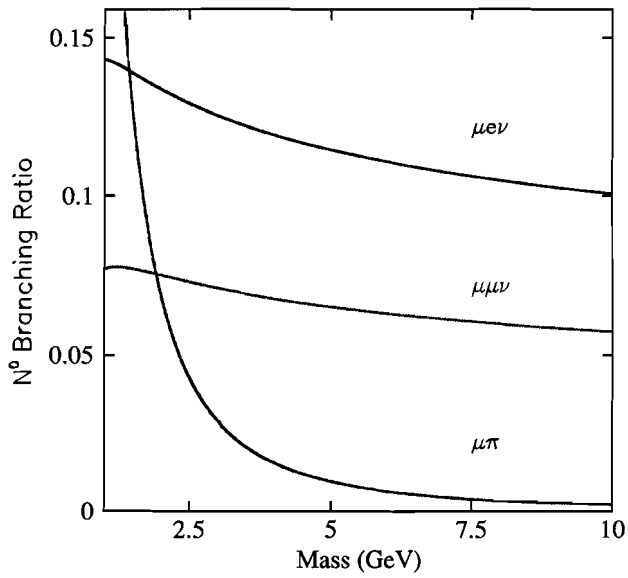

Figure 9.3: Branching ratio for N^0 decay to $\mu e\nu$, $\mu\mu\nu$, and $\mu\pi$.

B decays and the lifetime of such particles. At such high masses, the N^0 lifetime is well-defined:

$$\tau_{N^0} \approx (4.49 \times 10^{-12} s) \cdot (m_{N^0}/1 \text{ GeV})^{-5.12}/U_\mu^2. \tag{9.1}$$

For masses above 0.5 GeV, N^0's predominately decay to hadrons ($\geq 60\%$). Using the above lifetime calculation, one can infer the branching ratio for N^0's to decay to muons, a process to which our analysis is sensitive (see Fig. 9.3). On average, a 5 GeV/c^2 N^0 will decay to $\mu\mu\nu$ 6.5% of the time, to $\mu e\nu$ 11.5% of the time, and to $\mu\pi$ 0.9% of the time.

Unfortunately, because the B cross-section is small and the distance to the decay region is large, NuTeV is not sensitive to neutral heavy leptons from B decays. To make the lifetime of the N^0 long enough to reach the decay channel, a small $|U^2|$ is needed, but then the branching ratio to N^0 would be suppressed by $|U^2|$. Figure 9.4

shows the number of N^0 events which decay to a final state muon within the NuTeV decay channel (without having taken efficiency into account). Most of the region above 2.2 GeV/c^2 is below the single event sensitivity.

9.1.2 Neutral Current Production

Neutral current neutrino scattering in the shielding between the beamline and detector can produce neutral heavy leptons via mixing (see Figure 9.5)[70, 75]. Again, the production rate depends on the mixing, while the decay rate depends upon both the mixing and the mass. In the high mass region (above 2 GeV/c^2), these exotic particles decay so quickly such that any produced in the shielding would decay before reaching the detector (see Figure 9.6).

9.2 Neutralino Production

Supersymmetry is a popular extension of the Standard Model which predicts the existence of a large number of undiscovered particles. Each Standard Model particle has a corresponding supersymmetric particle (e.g., electron:selectron; neutrino:sneutrino; bottom:sbottom). In addition, there exist other possible supersymmetric particles which do not have direct Standard Model partners, such as neutralinos and charginos.

Recent searches for supersymmetric particles at LEP and the Tevatron have concentrated on the high mass (5-100 GeV/c^2) and short lifetime regions [37]. However, the unconstrained Minimal Supersymmetric Standard Model (uMSSM) allows for supersymmetric particles with lifetimes sufficiently long such that they might escape a collider experiment before decaying.

Fixed target experiments with large numbers of proton-nucleon interactions may be sensitive to previously undiscovered, long-lived, low-mass supersymmetric parti-

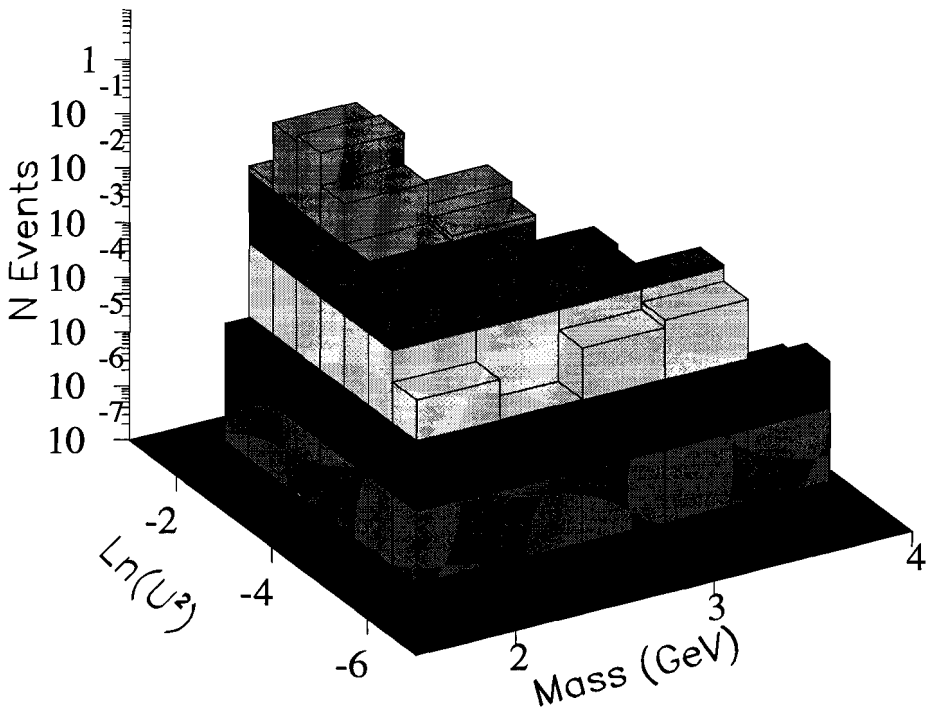

Figure 9.4: Lego plot of total number of B-produced N^0's decaying to muons visible in the NuTeV decay channel as a function of mass and mixing (U_μ^2).

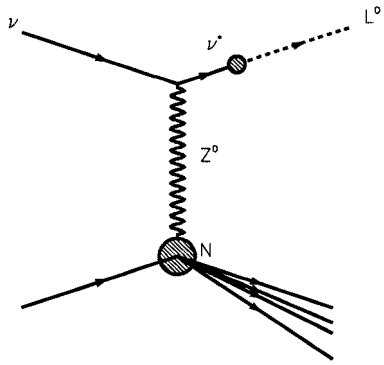

Figure 9.5: Feynman diagram of neutral current N^0 production in the earth-berm shielding (bottom).

cles. Production can occur through $q\bar{q}$ annihilation creating a pair of neutral supersymmetric particles such as neutralinos(see Figure 9.7). If the decay length is sufficient to reach the NuTeV decay channel ($\gamma c\tau > 1.4$ km), these particles could be detected via decays. Only the lightest supersymmetric particle (LSP) will have a long enough lifetimes to travel such long distances. If the neutralino is the lightest supersymmetric particle, then R-parity violation is required.

The number of N^0 particles observable by the NuTeV experiment is given by the product of the number of proton-nucleon interactions, the N^0 differential production cross-section ($d\sigma/d\Omega$), and the detection efficiency/acceptance (ϵ). Given the number of proton interactions NuTeV recorded, this can be written as:

$$N_{N^0} \approx (2.4 \times 10^{14}\text{mb}^{-1}\frac{d\sigma}{d\Omega}) \times (1 - e^{-\frac{3.5\times10^3\ \text{cm}}{\ell}})(e^{-\frac{1.5\times10^5\text{cm}}{\ell}}) \times \epsilon, \qquad (9.2)$$

where $\ell = \gamma c\tau$ is the N^0 decay length in the lab, and ϵ is the total geometric and reconstruction efficiency [24] (see also Figure 9.8). Note that this formulation is nearly identical to the equations used in Chapter 1. The proton-nucleon center-of-mass energy $\sqrt{s} = 38$ GeV allows for the pair production of particles up to approximately 15

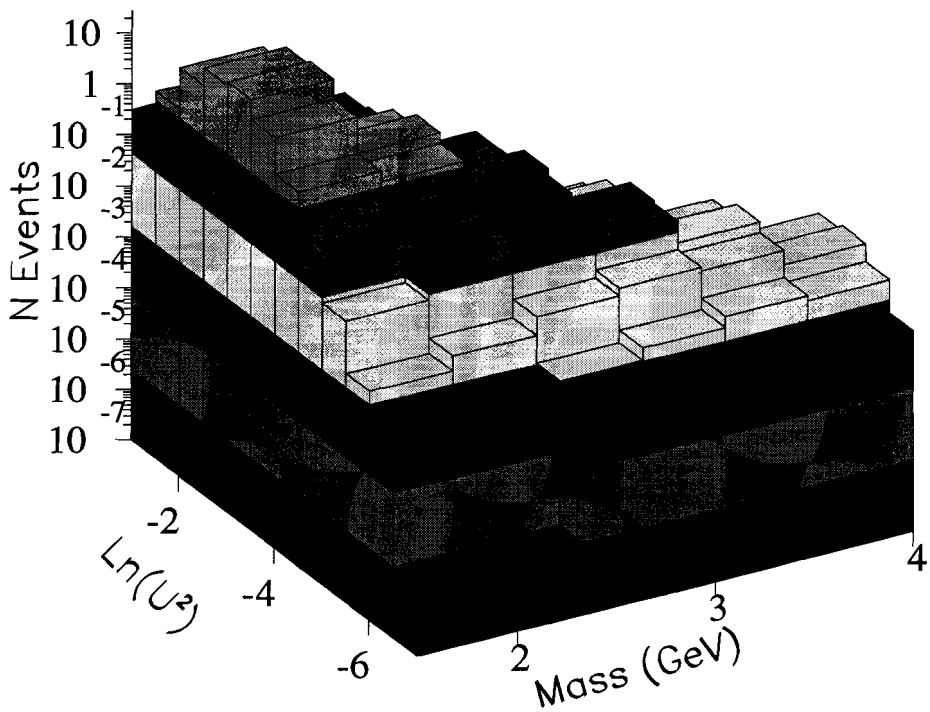

Figure 9.6: Lego plot of total number of berm-produced N^0's decaying to muons visible in the NuTeV decay channel as a function of mass and mixing (U_μ^2).

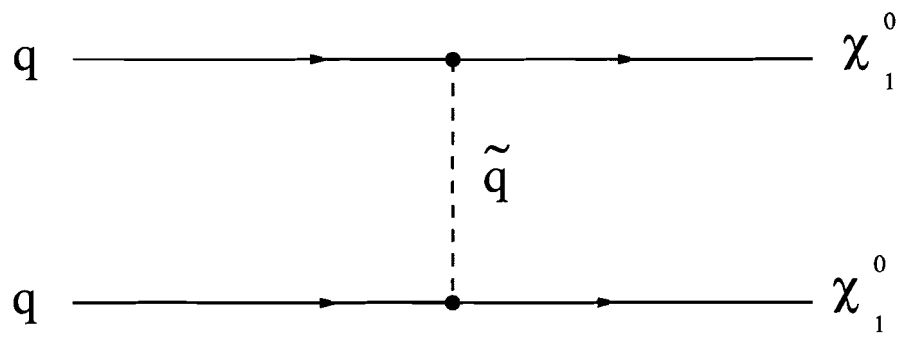

Figure 9.7: Feynman diagram of neutralino production at the BeO target.

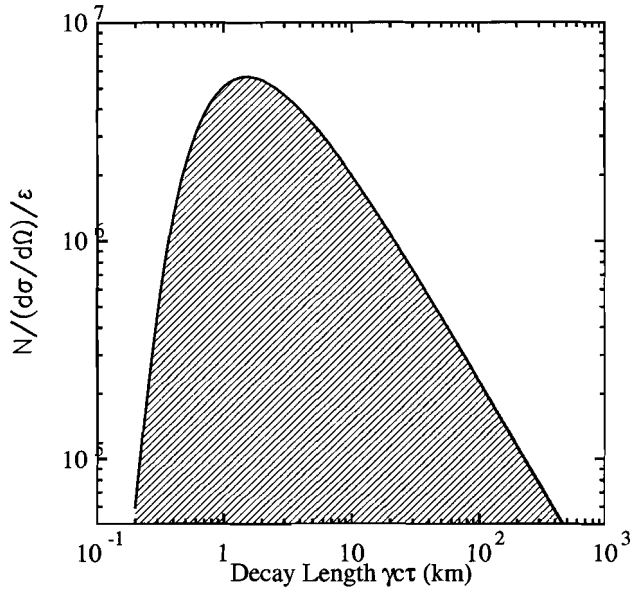

Figure 9.8: Number of neutralinos expected ($N/\epsilon\frac{d\sigma}{d\Omega}$) as a function of decay length $\gamma c\tau$. Minima occurs at $l \approx 1.5$ km.

GeV/c^2; the cross-section, however, drops quickly for masses above 10 GeV/c^2. The mass range between 2.2 GeV/c^2 and 10.0 GeV/c^2 is open to this analysis. Chapter 10 will discuss the data selection and backgrounds for this analysis; Chapters 12 and 13 will discuss and analyze the results of this search.

Chapter 10

High Mass Event Selection

Much of the foundation for the high mass search has been set in our earlier 0.3-3.0 GeV/c^2 neutral heavy lepton search [27]. By extending the available mass range, the search becomes particularly sensitive to long-lived neutralino production. Since the cleanest and most sensitive channels contain muons, we have restricted our search to N^0 decaying to only muonic final states: $\mu\pi, \mu e$, and $\mu\mu$. The dimuon channel, as will be shown, is the most sensitive due to the lowest background.

10.1 N^0 Signature

Figure 10.1 shows a Monte Carlo N^0 decay to $\mu\mu\nu$. The high mass decay events share many characteristics with the Q^0 events. Both are clean low-multiplicity two-track events evenly distributed in the decay channel. Unlike the Q^0, however, the N^0 particles reconstruct much more cleanly in the decay channel. The large transverse momentum (see Figure 10.2) and wide opening angle between the two visible tracks (see Figure 10.3) enables one to locate the decay vertex with greater precision. This feature is extremely helpful if one wishes to use vertex position to help differentiate

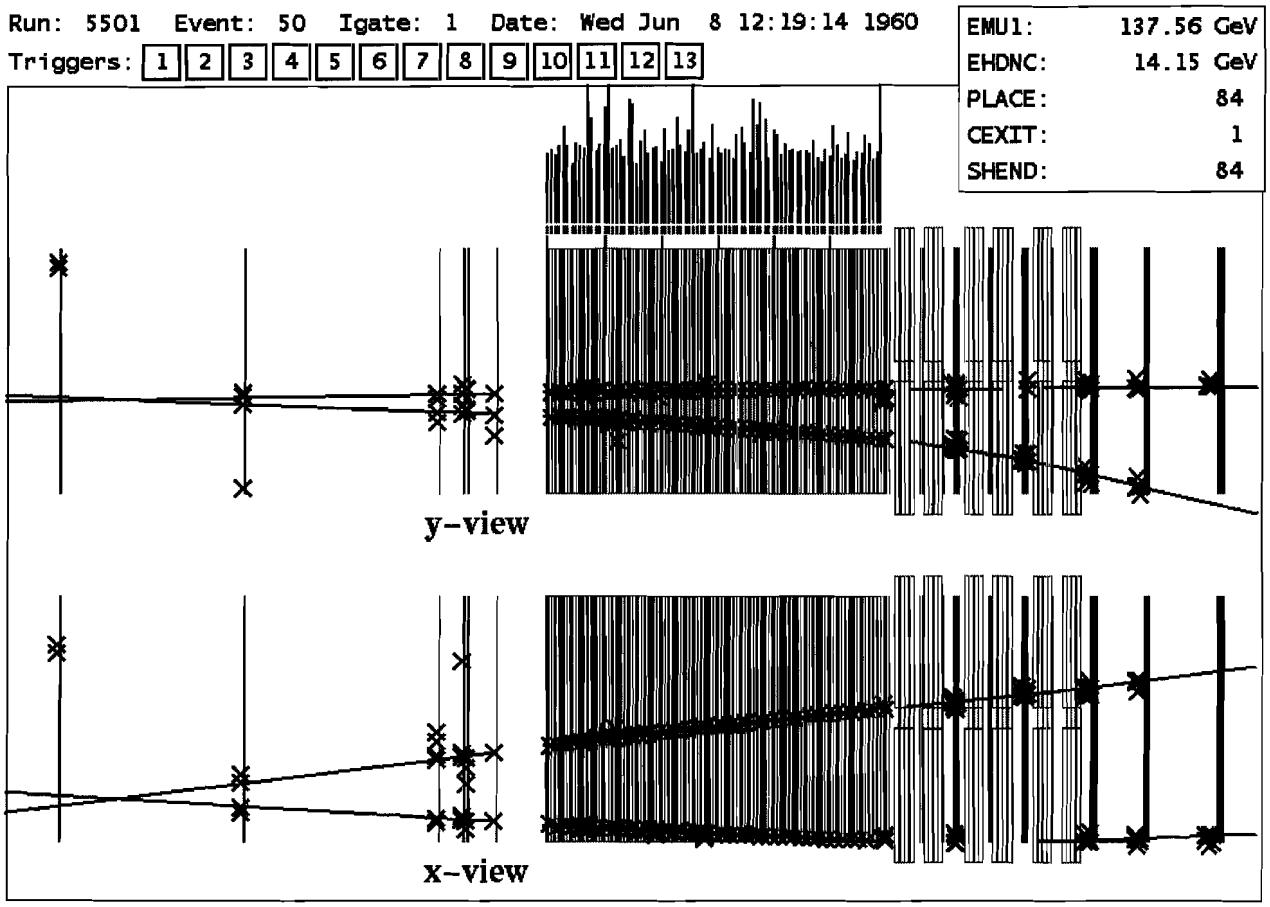

1

Figure 10.1: Monte Carlo N^0 decay to $\mu^+\mu^-\nu$ within the fiducial volume of the NuTeV decay channel. Note the features of two clean muon tracks traversing the NuTeV calorimeter.

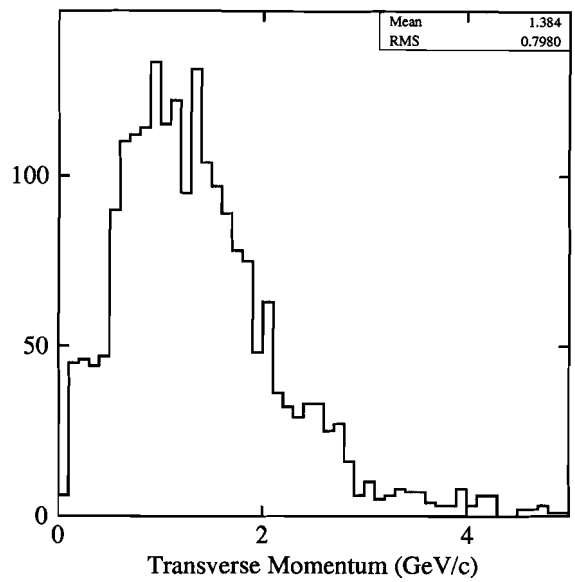

Figure 10.2: Muon transverse momentum from a 5 GeV/c^2 decay to $\mu\mu\nu$.

between signal and background.

Unfortunately, N^0 backgrounds tend to be much higher than for the Q^0 search, in part because neutrino deep-inelastic scattering tends to produce events at high momentum transfers, which mimic high mass N^0 decay. Thus, the same features which make the high mass search an clear signature also make it more sensitive to potential backgrounds.

One significant cut is the longitudinal vertex requirement. Since the largest background is from νN interactions in the chambers, good longitudinal resolution is necessary to remove false candidates. Figure 10.4 shows the N^0 vertex resolution from a 5 GeV/c^2 $\mu\mu\nu$ decay. The typical resolution on the longitudinal vertex is 8.8 cm. The chamber cut ensures that the N^0 vertex does not come from the chambers. Of course, this cut does not remove hadron decays or neutrino interacting in the helium itself.

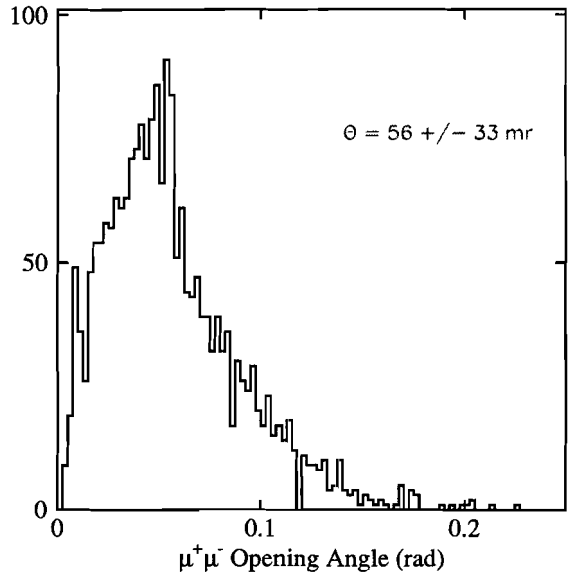

Figure 10.3: Opening angle for $\mu^+\mu^-$ pair for a 5 GeV/c^2 decay to $\mu\mu\nu$. The wide opening angle between the dimuon pair allows for easy separation between the two tracks, both in the decay channel and the calorimeter.

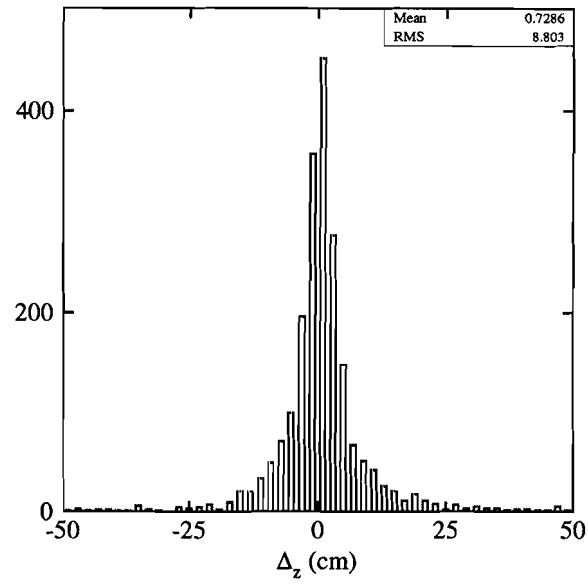

Figure 10.4: Longitudinal resolution (Δ_z) for an N^0 decay to $\mu\mu\nu$.

Particle identification of all tracks involved in an N^0 decay is quite good. The identification rate is high because N^0 decays typically involve well separated high-energy tracks. Reconstruction efficiencies for 5 GeV/c^2 particles are shown in Table 10.1.

10.2 Sources of Background

10.2.1 ν Deep Inelastic Background Events

Backgrounds to the high mass search originate from neutrino scattering, with the largest source arising from deep inelastic scattering (DIS) of neutrinos or anti-neutrinos in the drift chambers, helium gas, and materials surrounding the decay channel. The DIS event rate is largest at high m_T ($>$ 2 GeV/c^2) and represents the dominant background for the high mass analysis.

Table 10.1: Particle mis-identification probability for a 5 GeV/c^2 N^0 decay.

Parent Pair	$\mu\mu$	μe	$\mu\pi$
$\mu\mu$	$100^{+0.0}_{-0.3}\%$	$0.0^{+0.3}_{-0.0}\%$	$0.0^{+0.3}_{-0.0}\%$
μe	$0^{+0.3}_{-0.0}\%$	$89 \pm 2\%$	$11 \pm 2\%$
$\mu\pi$	$1 \pm 1\%$	$25 \pm 3\%$	$74 \pm 3\%$

Table 10.2: Origin of DIS background events that pass analysis cuts. The percentage corresponds to the DIS events category in Table 10.5.

Mode	Origin in Helium	Origin in Chambers/Surrounding	Ratio
$\mu\mu$	21%	79%	0.27
μe	62%	38%	1.63
$\mu\pi$	70%	30%	2.33
Total	57%	43%	1.33

Most of the neutrino DIS events that pass the analysis cuts originate from the chambers or the helium. Table 10.2 shows the distribution of DIS events that originate in the helium versus chambers and surrounding material for each channel. The high chamber/helium ratio seen in the $\mu\mu$ mode arises because most $\mu\mu$ background events are due to π decay (60% of the time) and K decay (33% of the time). In a K decay, the vertex position is often misreconstructed due to the high decay transverse momenta.

10.2.2 Low-multiplicity Backgrounds

Low-multiplicity interactions present a particular challenge, due to their higher acceptance for "clean cut" and other selection conditions. Examples of such interactions

include: (1) diffractive π, K, ρ, and charm production from neutrino interactions in the chambers or the helium; (2) neutrino-induced nucleon resonance production, characterized by a high-energy muon accompanied by a low-energy pion track; and (3) neutral kaons produced in surrounding material that may enter the fiducial volume and decay with a relatively high apparent transverse mass if the kaon enters with a large angle. Fortunately, the small cross-sections for these processes result in small contributions to the background.

10.2.3 Negligible Sources

A number of other possible background sources have been found to be negligible because they very rarely produce reconstructed vertices in the decay channel. These include cosmic ray showers, conversions of photons produced in surrounding material, interactions from muons scattered from surrounding material, "leakage" of charged particles from the testbeam beamline (which occurred only during a few isolated data collection periods and were excluded from the sample; see Chapter 4), and multiple neutrino interactions in the decay channel. These background sources were constrained by data measurement and Monte Carlo study.

10.3 Event Selection

The selection criteria for the high mass search were based primarily on the earlier 0.3-3.0 GeV neutral heavy lepton search. Our selection criteria can be subdivided into two broad categories: *reconstruction* cuts and *clean* cuts. Reconstruction cuts help select N^0 candidates. Clean cuts use specific event topologies to remove candidate neutrino-nucleon scattering backgrounds.

10.3.1 Reconstruction Cuts

The reconstruction requirements isolate events with two track vertices within the fiducial volume. A list of cuts is given below; cut efficiencies for N^0 events are shown in Table 10.3:

- **Two Track Requirement:** This cut requires a vertex with only two charged particle tracks associated with it.
- **Fiducial Cut:** This cut ensures that the transverse position of the vertex is within 127 cm of the beam axis. It also ensures that the track projection to the front face of the calorimeter is within 127 cm. The high inefficiency apparent in this cut is due to the fact that most tracks from high mass particle decays tend to have wide angle tracks that are likely to miss the front face of the calorimeter.
- **Chamber Exclusion:** This cut requires that the reconstructed vertex be *either* 101.6 cm *or* $3\sigma_{vertex}$ away from the chambers, whichever is greater. The cut eliminates background activity originating in the chambers. This cut removes 12.7% of the volume available from the helium. The total fiducial volume, with the two drift chambers removed, corresponds to 180 m^3.
- **Track and Vertex Quality Cuts:** Track and vertex χ^2 quality cuts are imposed in order to remove false vertices and poorly reconstructed tracks. The cut require both the vertex and track $\chi^2/d.o.f \leq 10$. These cuts retain 99% of the N^0 signal when all other cuts are applied.
- **Track Slope Cut:** To remove cosmic rays from our sample, we require that each track have $\theta_{(x,y)} \leq 100$ mr. This requirement differed from the Q^0 analysis since the opening angle tends to be much wider than expected from Q^0 decay.
- **Track Quality Cut:** This cut removes events where either track has associated hits *upstream* of the reconstructed vertex.

- **Particle Identification:** The two tracks must be identified as either $\mu\pi$, μe, or $\mu\mu$.

- **Particle Energies:** There are energy thresholds which ensure that the particle is properly identified. This cut requires that muon tracks have at least 2.2 GeV energy, and that pion and electron tracks have at least 10 GeV energy.

- **XY Matching:** Each x-view track is required to match a y-view track. This matching information comes from hits from the UV chamber (DK1). If no proper matching is found, the event is removed.

- **Match Tracks to Clusters:** Each vertex track is required to have a corresponding cluster in the calorimeter.

- **Veto Wall Cut:** This cut ensures that there is no in-time activity in the veto wall for the event. The cut looks for coincidences between upstream and downstream veto wall panels. Events with coincident activity in the front and back veto wall panels within a ± 33 ns timing window from the trigger are removed from the sample.

- **Transverse Mass Cut:** This cut selects events which have a reconstructed transverse mass $m_T \geq 2.2$ GeV/c^2.

10.3.2 Clean Cuts

The reconstruction criteria help remove a significant fraction of the background while still retaining signal events. However, in order to achieve single event sensitivities, it is necessary to reduce background levels further still. The introduction of the clean cuts helps remove neutrino deep inelastic scattering events.

Table 10.3: Reconstruction cuts for N^0 search. Efficiencies shown are for a 5 GeV/c^2 N^0 decay. Efficiencies are quoted relative to the number of MC generated events in the fiducial volume.

	Cumulative Efficiency		
Cut	$\mu\mu(\nu)$	$\mu e(\mu)$	$\mu\pi$
Two Tracks Found	98.5%	70.8%	74.2%
Fiducial Volume	54.7%	41.8%	38.6%
Remove Chambers	52.3%	40.1%	38.6%
Track and Vertex Quality	50.4%	33.4%	34.8%
Track Slope	46.8%	32.2%	33.5%
Remove Bad Tracks	46.3%	32.0%	33.3%
Particle Identification	37.2%	31.5%	31.2%
Particle Energies	34.4%	30.2%	31.2%
Match XY Views	34.4%	30.2%	30.2%
Track-Cluster Match	34.1%	30.0%	28.5%
Veto Wall Cut	34.0%	30.0%	28.5%
Transverse Mass	31.1%	28.7%	28.4%
Clean Cuts	17.0%	16.4%	10.6%

Deep inelastic events tend to have high transverse mass. These events are also characterized by a large number of tracks in the decay channel. The high multiplicity manifests itself in the form of extra tracks in either the x or y views, neutral clusters, photons, and extra hits from exiting tracks (see Fig. 10.5). The clean cuts uses these characteristics to enhance signal with respect to background.

The description of the clean cuts is given below:

- **Track Segment Cut:** This cut requires that there be no more than three track segments in each view. DIS events tend to produce particles at large angles or at the edge of the fiducial volume, thus depositing only sufficient hits to form a track in a single view. The cut still allows the possibility of an extra δ-ray track to be associated with one of the tracks downstream of the reconstructed vertex.

- **Extra Hits Cut:** This cut removes events with hits which are not associated with a reconstructed track. If the first chamber downstream of the vertex exceeds four hits in either view or the first two chambers downstream of the vertex exceed seven hits in both views, the event is removed from the sample.

- **Cluster Cut:** This cut removes events with clusters in the calorimeter which have no associated decay channel track. Excess clusters are often associated with neutral particles, such as γ's, K_L's, or neutrons produced in neutrino deep inelastic scattering.

- **γ Conversion Cut:** This cut removes events where a photon is produced and then converts downstream of the reconstructed vertex. If a track which has been identified in the calorimeter as an electron has a missing hit in both the x and y view immediately downstream of the reconstructed vertex, the event is removed.

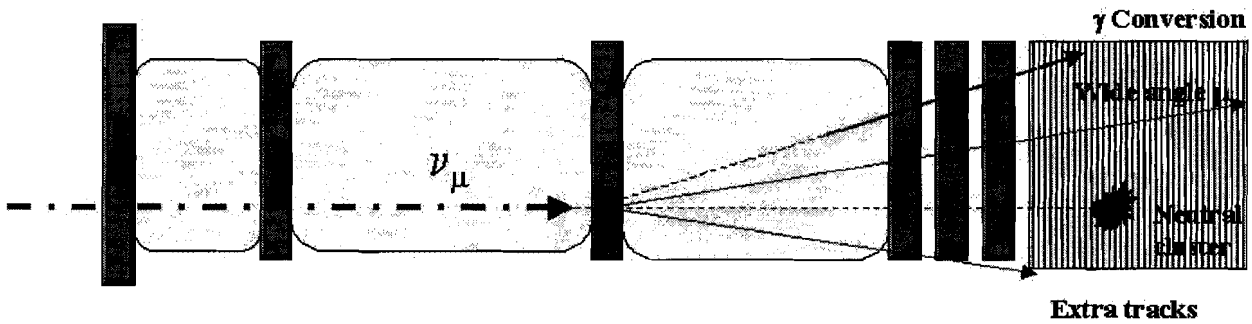

Figure 10.5: Depiction of a DIS charged current background event. Such events are typically associated with wide angle tracks, neutral clusters, and photon conversions.

Table 10.4: Geometric acceptance (A) and reconstruction efficiency (ϵ) for the allowed channels. Efficiencies are quote for a 5 GeV/c^2 mass particle.

Mass (GeV/c^2)	Decay Mode	A	ϵ	Total
3	$\mu\mu\nu$	45.2%	28.7%	13.0%
	$\mu e\nu$	40.9%	36.8%	15.0%
	$\mu\pi$	38.7%	30.1%	11.7%
5	$\mu\mu\nu$	52.3%	32.5%	17.0%
	$\mu e\nu$	40.1%	41.0%	16.4%
	$\mu\pi$	38.6%	27.5%	10.6%
10	$\mu\mu\nu$	42.2%	36.0%	15.2%
	$\mu e\nu$	39.2%	40.4%	15.8%
	$\mu\pi$	34.6%	21.9%	7.6%

- **Energy Cut:** This cut requires the total energy of all reconstructed particles to be $\geq$ 12 GeV. This cut is designed to remove $K_L \rightarrow \mu^+\mu^-\nu_\mu$ decays, which tend to have a soft energy spectrum.

The cumulative efficiencies of each of the selection criteria are shown in Table 10.3. Both the geometric and reconstruction efficiencies are fairly stable over the range of masses we are interested in. We define geometric efficiency as the fraction of events which pass the two tracks, fiducial volume, and chamber removal cuts, and we define the reconstruction efficiency as the fraction of events passing all other cuts, including clean cuts. The final geometric and reconstruction efficiencies are given in Table 10.4. The average total efficiency is $\approx$ 14% over all masses.

Table 10.5: Estimated background rates to the $N^0 \to \mu\mu(\nu), \mu e(\nu)$, and $\mu\pi$.

Source	$\mu\mu(\nu)$ events	$\mu e(\nu)$ events	$\mu\pi$ events
DIS events	$(6.8 \pm 1.0) \times 10^{-2}$	$(1.3 \pm 0.2) \times 10^{-1}$	$(1.4 \pm 0.2) \times 10^{-1}$
Diffractive charm	$(1.3 \pm 0.1) \times 10^{-3}$	$(2.0 \pm 0.3) \times 10^{-3}$	$(1.3 \pm 0.2) \times 10^{-3}$
Diffractive π	$(1.9 \pm 0.2) \times 10^{-4}$	$(1.0 \pm 0.1) \times 10^{-4}$	$(4.1 \pm 0.3) \times 10^{-4}$
Diffractive K	$(4.0 \pm 0.3) \times 10^{-7}$	$(2.9 \pm 0.2) \times 10^{-7}$	$(9.7 \pm 0.8) \times 10^{-7}$
K_L^0 decays (shielding)	$(3.9 \pm 3.9) \times 10^{-4}$	$(3.9 \pm 3.9) \times 10^{-4}$	$(3.9 \pm 3.9) \times 10^{-4}$
Other sources	$\ll 2.5 \times 10^{-4}$	$\ll 1.6 \times 10^{-4}$	$\ll 1.6 \times 10^{-4}$
Total Background	$(6.9 \pm 1.0) \times 10^{-2}$	$(1.3 \pm 0.2) \times 10^{-1}$	$(1.4 \pm 0.2) \times 10^{-1}$

10.3.3 Final Background Estimates

After all cuts, the expected background is 0.069 ± 0.010 events in $\mu\mu$ mode, 0.13 ± 0.02 events in μe mode and 0.14 ± 0.02 events in $\mu\pi$ mode. The background contributions to each mode are listed in Table 10.5.

Chapter 11

High Mass Sideband Studies

As was discussed earlier in the Q^0 search, much of the strength and validity of a search relies on how well the Monte Carlo can describe in detail the experimental data. Sideband studies are excellent tools in testing the validity of the Monte Carlo because they directly compare to existing data and may highlight systematic uncertainties in the simulation. This section will highlight some of the sideband studies used in the high mass N^0 search.

11.1 Longitudinal Vertex Study

The longitudinal vertex study provides a high-statistics comparison between data and Monte Carlo for events occurring in the decay channel. The purpose of the study is to determine how well we understand the longitudinal distribution of events across the decay channel. Since the background increases by an order of magnitude for events near the chambers, understanding the event distribution as a function of distance from the drift chambers is essential.

For this particular study, emphasis was placed upon gathering high statistics, to

populate events in both the helium and the chambers. For this sideband study, the vertex was required to be within the decay channel fiducial volume, with $|x| < 127$ cm, $|y| < 127$ cm, allowing the z position to be either in the chambers or the helium. Tight track angle cuts ($\theta \leq 68$ mr for each track) were imposed to remove cosmic rays. In addition, events which had veto wall coincidences, or which had a track pointing to an active veto wall panel, were removed. Other cuts on reconstruction, particle identification, and vertex fit quality were not imposed in this study.

The majority of the events in this sample are high multiplicity νN interactions coming from the chamber material or the laboratory floor. In the data, 495 events were found; 116 events had vertices reconstructed in the helium, where the helium is defined as >101.6 cm from the nearest drift chamber. The Monte Carlo predicted (514±82) events with (96±15) events reconstructed in the helium. It is interesting to note that only 33% of events reconstructed in the helium actually were created there. Most helium events come from either misreconstructed chamber events or events where a $\pi^{\pm}$ or $K^{\pm}$ has decayed. Comparisons between data and Monte Carlo show that the Monte Carlo agrees well with the longitudinal distribution of events in the decay channel (see Figures 11.1-11.2). Kinematic and multiplicity data distributions are also well described by the Monte Carlo.

11.2 Chamber And Intermediate Region Sideband

The chamber sideband is a test of how well both the cuts and backgrounds are modeled in our Monte Carlo. The sideband uses exactly the same cuts as used for the N^0 search, except for the longitudinal position cut. Instead of requiring the events to be inside the helium, candidate events are required to have a vertex within ±15.24 cm of the two upstream drift chambers. This sideband has a two-fold purpose. First, it tests how well each cut is modeled in the Monte Carlo, since all other cuts used for

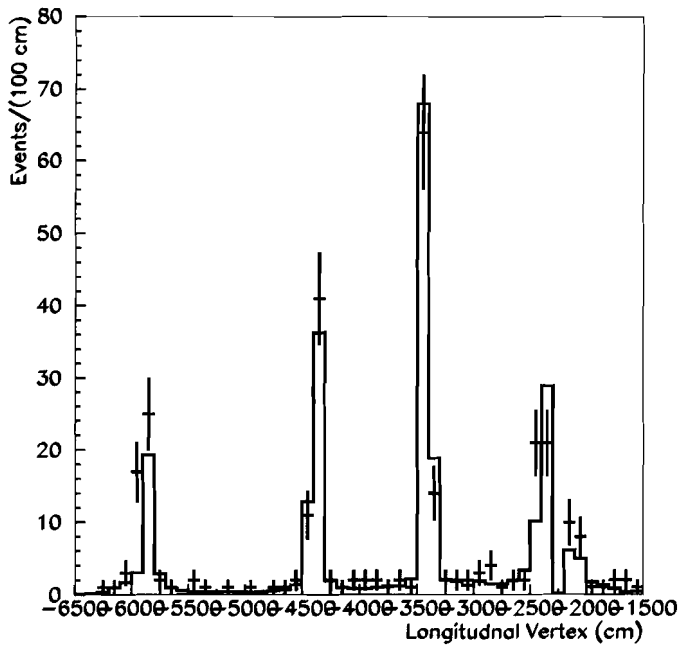

Figure 11.1: Longitudinal vertex position for all events in the decay channel fiducial volume. (Crosses: data; histogram: Monte Carlo). Peaks correspond to interactions in veto wall and testbeam chamber (left) and drift chambers DK5 and DK4 (center and right).

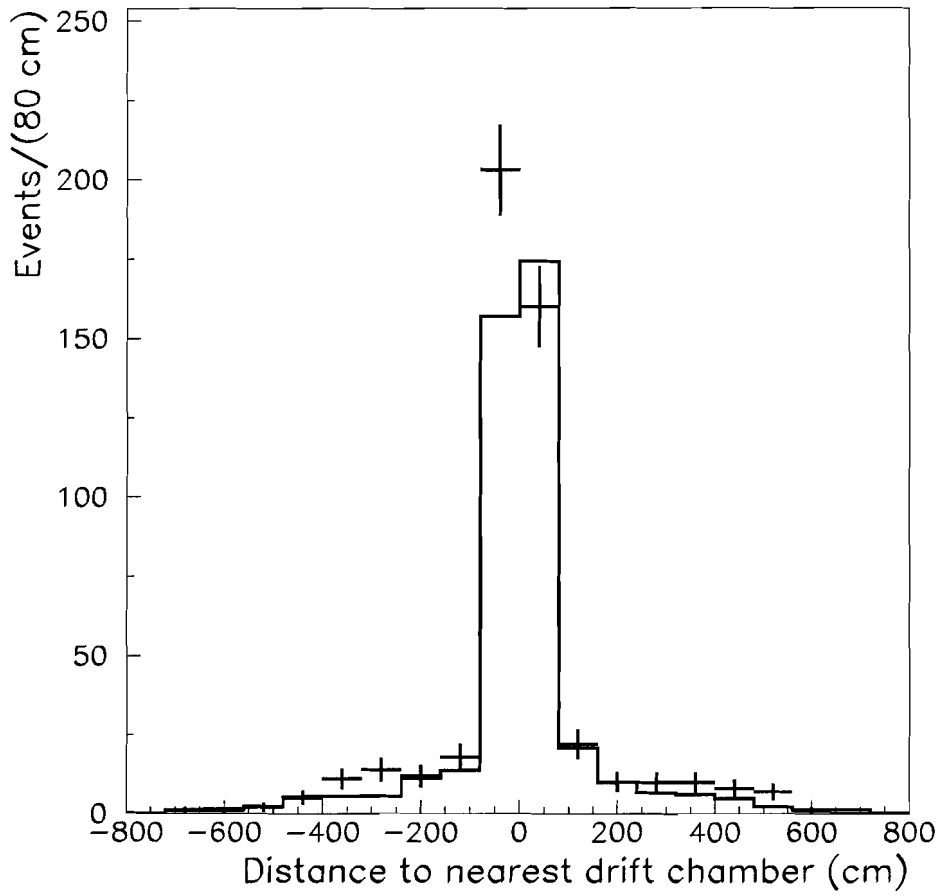

Figure 11.2: Distance of longitudinal vertex position from the closest chamber for events in the longitudinal sample without the z vertex requirement. (Crosses: data; histogram: MC.)

this sample are identical to the cuts used in the signal region. Second, because one expects about nine times as many events to occur in the chambers as in the helium, it is an excellent tool in determining if the background level is simulated properly. This also tests whether important backgrounds (such as, for example, $\nu + N \rightarrow D_s^* + X$) have been omitted, since for most ν interactions backgrounds we would expect to see many more events in the chambers than in the helium. This sideband, however, only indirectly checks the rates for background expected from non-prompt sources (for example, $\nu + N \rightarrow \mu + X + K \rightarrow \mu + \nu$). In order to remedy this drawback, we have also developed the intermediate region sideband, which looks at events 15.3 to 101.6 cm from the chambers. The intermediate region is also efficient at checking the resolution tails for chamber interactions.

Monte Carlo predictions and data statistics are shown in Table 11.1. There is very low statistics but the agreement between data and Monte Carlo in both the chamber and intermediate regions is good. No unmodeled background is apparent in either of these sideband regions.

11.3 $\mu\pi$ Sideband

The $\mu\pi$ sideband selected $\mu\pi$ events with looser cuts. The sample was similar to the chamber region sideband, but the events were required to have a muon and a pion. The transverse mass cut was lowered to 0.5 GeV/c^2, and the pion energy cut was lowered to 5 GeV. The total energy cut of 12 GeV was removed. In addition, no clean cuts were applied to this sample.

By loosening the requirements on the $\mu\pi$ sample, one can effectively extract the most common background event in the decay channel, in which a neutrino charged current interaction produces a muon and a pion, and other unmeasured particles. A total of 9.8 ± 1.0 events were expected in this sideband region; 9 events were seen in

Table 11.1: Data and Monte Carlo prediction for high mass chamber ($|\Delta z| < 15.24$ cm) and intermediate (15.24 cm$< |\Delta z| < 101.6$ cm) regions.

Sideband	Decay Mode	Data	Monte Carlo
Chamber	$\mu\mu$	0	0.20 ± 0.02
	μe	1	1.7 ± 0.2
	$\mu\pi$	1	1.1 ± 0.1
Intermediate	$\mu\mu$	0	0.16 ± 0.02
	μe	0	0.37 ± 0.04
	$\mu\pi$	1	0.4 ± 0.04

the data. Again, there is good agreement between data and Monte Carlo predictions in this sideband study.

11.4 Summary of High Mass Sideband Studies

There is overall agreement between data and Monte Carlo for each sideband studies listed here. Figure 11.3 shows the summary of data and Monte Carlo predictions for all sidebands listed in this section. The average data/Monte Carlo ratio is 1.04 ± 0.06. Having confidence in the Monte Carlo background estimation, we are now ready to venture into the signal region.

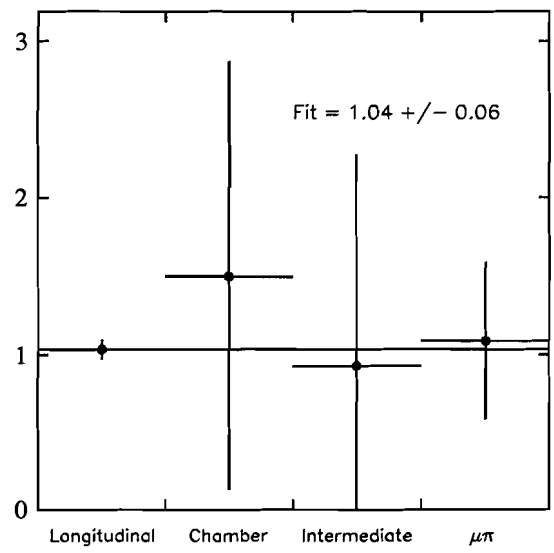

Figure 11.3: Data/Monte Carlo ratio for all high mass search sideband studies.

Chapter 12

High Mass Search Results

Three events were found in the signal region. All three events were identified as $\mu\mu$ events; no events were identified as either $\mu\pi$ or μe. The probability of seeing 3 $\mu\mu$ events where 0.069 ± 0.010 were expected is 5.4×10^{-5}. If one combines all available channels, 0.34 ± 0.03 events are expected and the probability of seeing three events in the signal region is 4.7×10^{-3}. With this large excess of $\mu\mu$ events, we have investigated in detail the nature and characteristics of the observed events. This chapter will describe in detail the characteristics of each events. Chapter 13 will describe in detail various hypotheses that may account for the anomalous excess.

Table 12.1: Predicted and observed events passing all N^0 signal cuts.

Decay Mode	Predicted Events	Observed Events
$\mu\mu(\nu)$	0.069 ± 0.010	3
$\mu e\,(\nu)$	0.13 ± 0.02	0
$\mu\pi$	0.14 ± 0.02	0

12.1 Description of the Three Events

All three events are clearly identified as $\mu\mu$ events with one high-energy muon accompanied by a low-energy muon. Each of the events occurred during good runs distributed throughout the NuTeV decay channel running period, where no significant malfunctions or problems were recorded. The first event (designated as Event 1) has a well-reconstructed vertex in the helium with no additional activity aside from those other than that associated with the two charged tracks. The second event (Event 2) also occurred in the helium region, but with a much poorer reconstructed vertex. Finally, the third event (Event 3) contains two muons, where both muons failed to reach the toroid for charge analysis. The event also has an additional track downstream of the vertex which seems to be consistent with a δ-ray (see below). All three events are shown in Figures 12.1, 12.2 and 12.3. All characteristics for each event are listed in detail in Table 12.2. For technical details, one can also consult Appendix C.

All three events had minimal activity recorded in the veto wall during the event, and all activity occurred well outside the time-scale consistent with the event. The veto wall panels have an average of 1.7 counters firing per trigger, and a timing resolution of 3.8 ns. Event 1 had two hits at +404, +536 ns, where a positive(negative) sign indicates hits after(before) the trigger. Event 2 had only one hit at +24 ns, while Event 3 had four hits at −256, +320, +320, and +1192 ns. Each of these hits are at least 6σ out-of-time with the trigger. In addition, Event 1 had activity recorded in the upstream calibration beam drift chamber (Bashful). However, this chamber had persistent noise and high voltage problems. The activity recorded is consistent with instrumental noise.

All three events occurred during neutrino running mode. In the two events where the muon charge was measured, the negative charge was consistent with a primary

μ^- from a neutrino charged current interaction. All three events have a large muon energy asymmetry $A \equiv |E_1 - E_2|/(E_1 + E_2)$.

While Event 1 has no significant reconstruction issues, the other two events have a few reconstruction characteristics to note. Event 2 has relatively poor track quality for both muons. Both Event 2 and Event 3 have poor vertex quality compared to the signal Monte Carlo (see next chapter). Event 3 is missing three of four hits in the chamber immediately downstream of the vertex (DK4). The probability of this occurring by random coincidence is less than 3×10^{-5}. DK4 had persistent high voltage problems throughout the run. There is some evidence for a "coherent" (linked) inefficiency between the x and y views in DK4 at a level of $(1.0 \pm 0.7) \times 10^{-3}$ probability. However, the drift chamber readout string shows no indication the chamber was misbehaving for this event and good tracks through this chamber are observed for events proximate in time. This event also has a third track attached to a downstream vertex which deposited no significant energy in the calorimeter. This is consistent with an interpretation of a δ-ray.

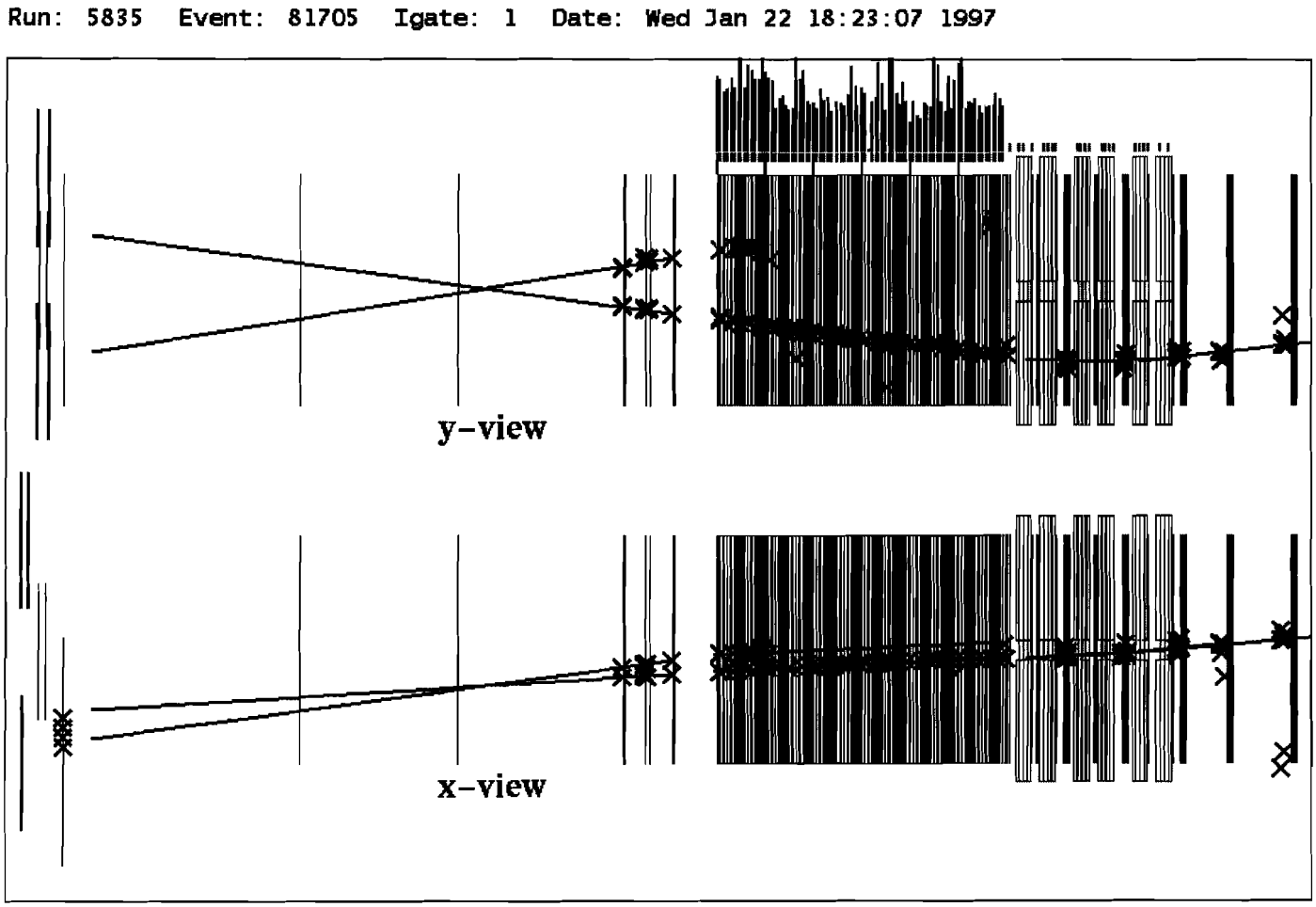

Figure 12.1: Event 1: $\mu\mu(\nu)$ data event passing final cuts.

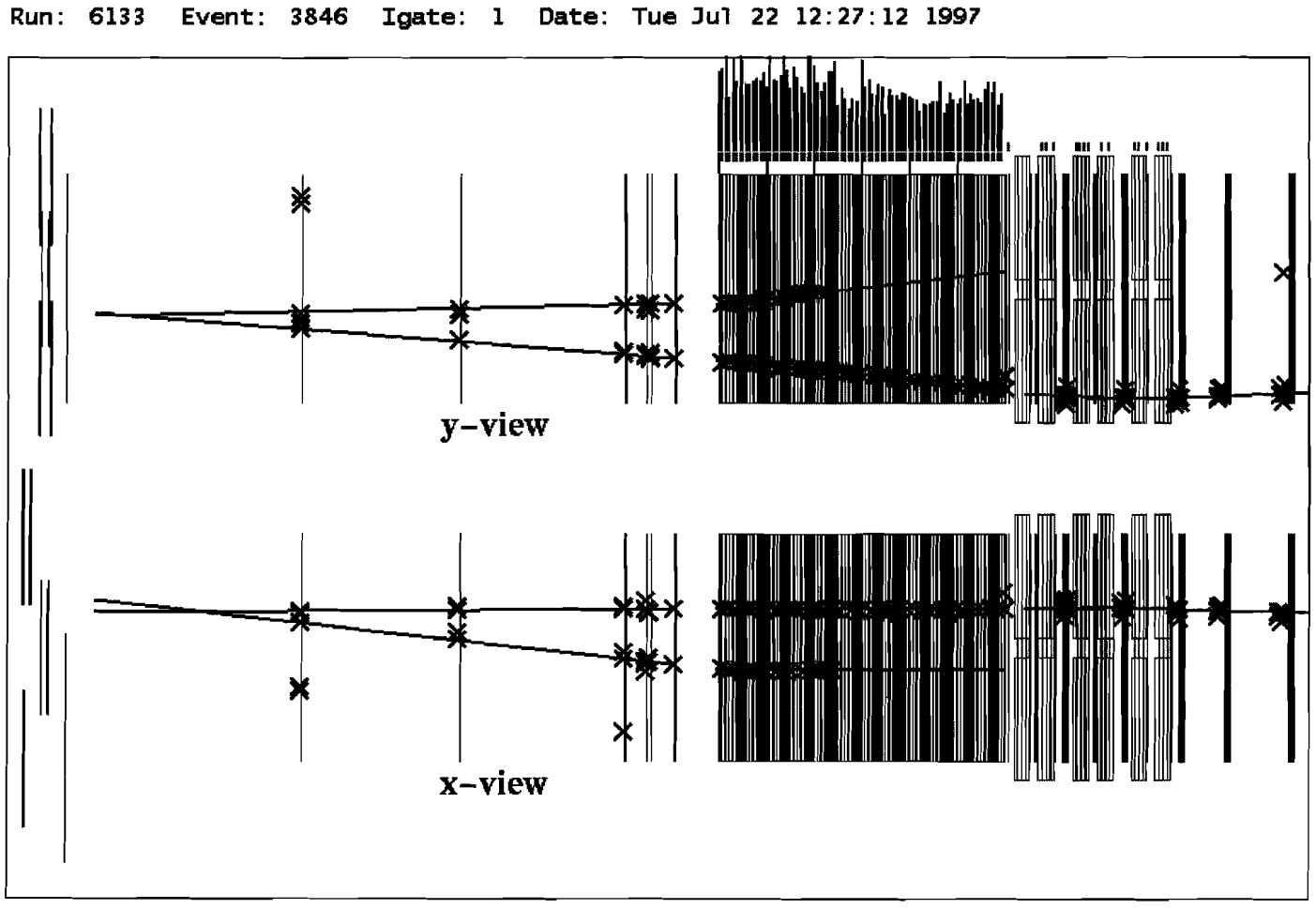

Figure 12.2: Event 2: $\mu\mu(\nu)$ data event passing final cuts.

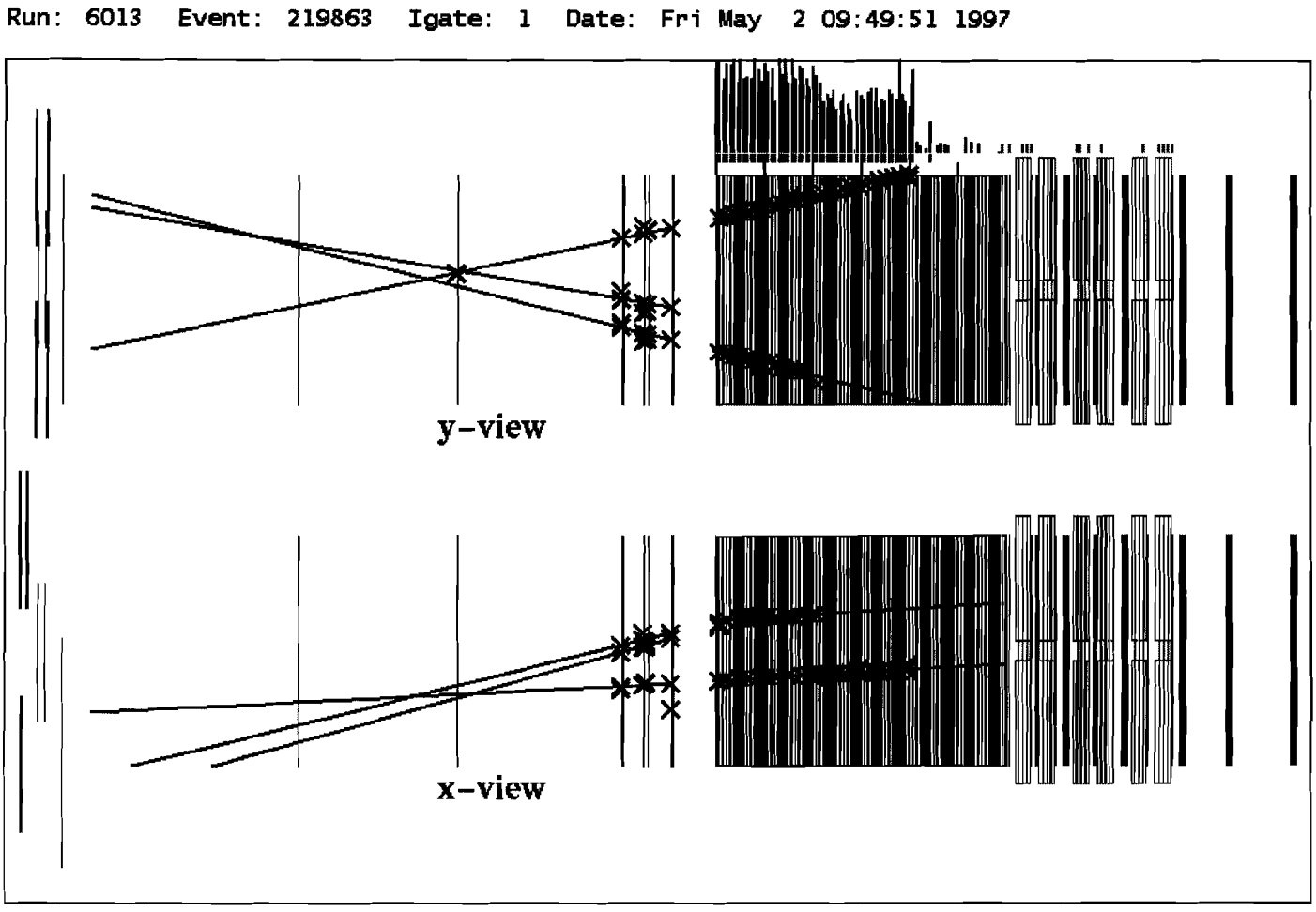

Figure 12.3: Event 3: $\mu\mu(\nu)$ data event passing final cuts.

Table 12.2: Kinematic and reconstruction quantities for the three candidate $N^0 \rightarrow \mu\mu(\nu)$ events. Some of the variables listed refer to the muons energies ($E_{\mu 1}$, $E_{\mu 2}$), missing transverse momentum (P_T), two muon invariant mass ($m_{\rm inv}$), transverse mass (m_T), transverse vertex position (v_x, v_y), longitudinal distance to nearest drift chamber ($|\Delta z|$), the vertex and muon track χ^2/dof, and the muon asymmetry (A).

Event	1	2	3
Run Number	5835	6133	6013
Date	01/22/97	07/22/97	05/02/97
Running Mode	ν	ν	ν
$E_{\mu 1}$ (GeV)	77.4	92.0	48.0
$E_{\mu 2}$ (GeV)	2.56	5.85	4.34
$\theta_{\mu 1}$ (rad)	0.031	0.016	0.045
$\theta_{\mu 2}$ (rad)	0.045	0.020	0.074
$\phi_{\mu 1}$ (rad)	-1.146	-1.513	1.353
$\phi_{\mu 2}$ (rad)	0.895	-0.552	-0.771
Charge($\mu 1/\mu 2$)	-1/NA	-1/NA	NA/NA
P_T (GeV/c)	2.38	1.42	2.04
$m_{\rm inv}$ (GeV/c^2)	1.10	0.88	1.57
m_T (GeV/c^2)	5.00	3.10	4.62
v_x (cm)	-46.5	48.0	-57.5
v_y (cm)	3.4	-38.3	15.0
v_z (cm)	-3220.	-5187.6	-3600.07
χ^2_{vert}/dof	0.32	9.53	3.04
$\chi^2_{\mu 1}/dof$	0.11	0.40	3.33
$\chi^2_{\mu 2}/dof$	0.43	1.09	3.34
$\|\Delta z\|$ (cm)	193	657	-188
Asymmetry (A)	0.936	0.881	0.834
δ-ray ?	No	No	Yes

Chapter 13

High Mass Event Analysis

I want to believe.

- The X-files

The high mass search has yielded a significant excess of observed events above background. One can question whether the excess is due to a potential signal or an unmodeled background. This section will provide a detailed analysis for the events under several background and signal hypotheses.

13.1 Considerations under an N^0 Hypothesis

The first hypothesis considered is whether the events are from N^0 decay. The $\mu\mu$ events are consistent with this hypothesis in several ways. First, the excess events appear in the $\mu\mu$ channel, the most sensitive channel for exotic phenomena and the one for which background levels are lowest. The observation occurs at a rate that is 40 times above background, and has a Poisson probability of 5.4×10^{-5} to be a statistical fluctuation. The μe and $\mu\pi$ channels, which are more sensitive to most

backgrounds, show no excess. Second, certain characteristics of the events are consistent with the hypothesis of an 5 GeV/c^2 N^0 decaying to $\mu\mu\nu$ (the N^0 Monte Carlo is a neutral heavy lepton decay model). All three reconstruct well within the fiducial volume and away from the drift chambers. The observed events are evenly distributed throughout the decay channel and have low track multiplicities. Third, several kinematic characteristics of the events are also consistent with a 5 GeV/c^2 N^0 decay. The transverse mass, invariant mass, and missing P_T are all consistent with a 5 GeV/c^2 N^0 decay (Fig. 13.1). Other variables, such as Q^2_{eff} and total visible energy (Fig. 13.2), are also consistent with a possible signal. Finally, the non-observation of a $\mu\pi$ excess over background is consistent with its suppressed rate in N^0 decay relative to leptonic decays.

One common feature of the three events, however, is *not* consistent with the N^0 hypothesis. It is improbable that N^0's would decay with such strong energy asymmetry. Figure 13.3 shows the distribution for the 5 GeV/c^2 N^0 simulation compared to the three data events. All three events have a muon energy asymmetry which is greater than 0.83. The probability that this occurs in our N^0 decay model is less than 0.5% (including acceptance and polarization effects [23]).

13.2 Considerations under a Background Hypothesis

For the background hypothesis, we look for consistency of the events with neutrino scattering processes. Some aspects of the candidate events are consistent with those from neutrino interactions. All three events occurred during the higher-flux ν-mode as opposed to $\overline{\nu}$-mode running periods; the ν to $\overline{\nu}$ event ratio is expected to be 4:1 for all events and 1.5:1 for low-multiplicity events. In the two events where the charge of

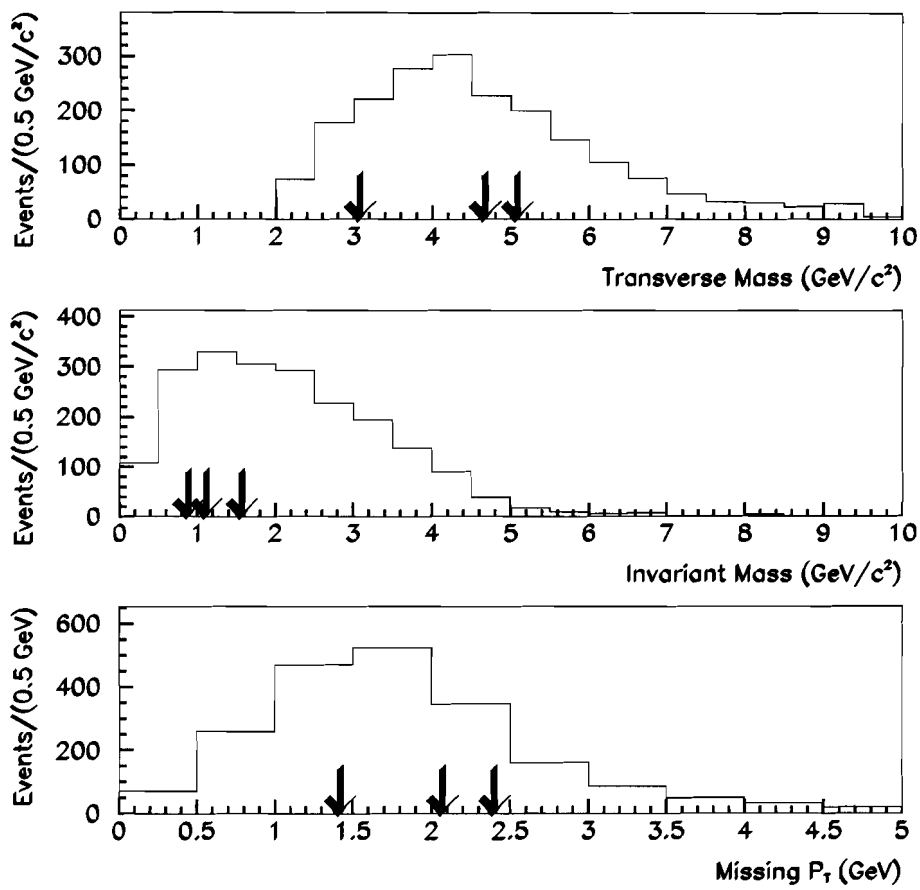

Figure 13.1: Kinematic distributions (transverse mass, invariant mass and missing transverse momentum) for a 5.0 GeV/c^2 N^0 Monte Carlo. The histograms show the MC; the arrows indicate the three observed events.

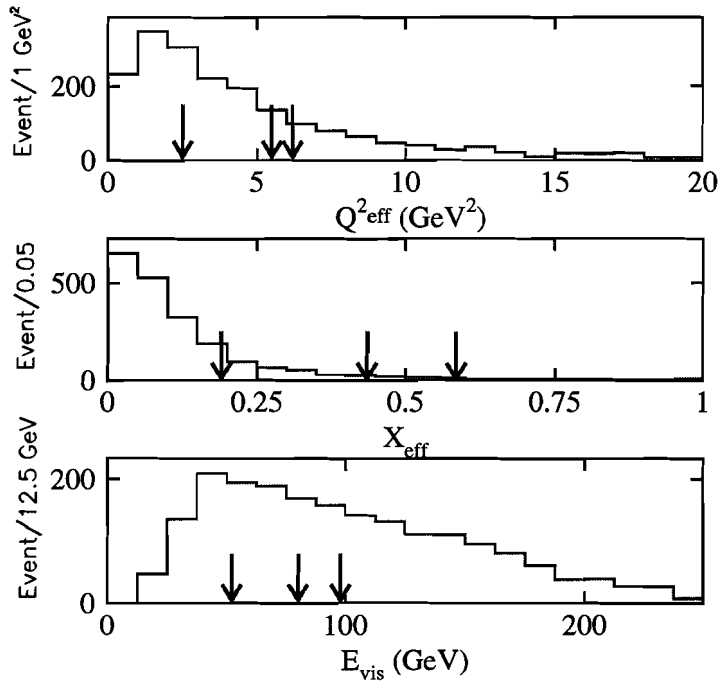

Figure 13.2: More kinematic distributions (x_{eff}, Q^2_{eff} and E_{vis}) for the 5.0 GeV/c^2 N^0 Monte Carlo. The histograms show the MC; the arrows indicate the three observed events.

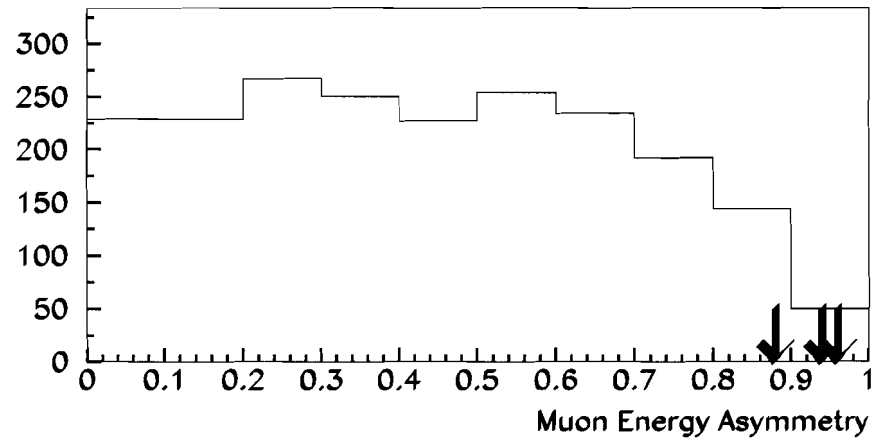

Figure 13.3: The muon energy asymmetry $(|E_1 - E_2|)/(E_1 + E_2)$. The histogram shows the 5 GeV/c^2 N^0 MC; arrows indicate the three observed events.

the higher-energy muon is measured, the charge is negative, consistent with a primary muon from a charged current neutrino interaction.

The event kinematics are also consistent with the background simulation. For both the decay variable distributions (Fig. 13.4) and the νN distributions (Fig. 13.5), the observed events are consistent with the predicted distributions of neutrino DIS backgrounds.

Another feature which seems to favor the background interpretation of the anomalous events is the quality of the track and vertex. Background events which reconstruct in the helium are often due to pion or kaon decay, which often results in a poorly reconstructed vertex. Though Event 1 has a well-reconstructed vertex, Events 2 and 3 have poor track and vertex χ^2/dof. One can assess this by computing the probability that a given event have a χ^2/dof at or above the measured value. Table 13.1 shows probabilities for both Monte Carlo signal (5 GeV/c^2 N^0 decay) and background events which pass all $\mu\mu(\nu)$ cuts. Such distributions are more consistent with a background interpretation.

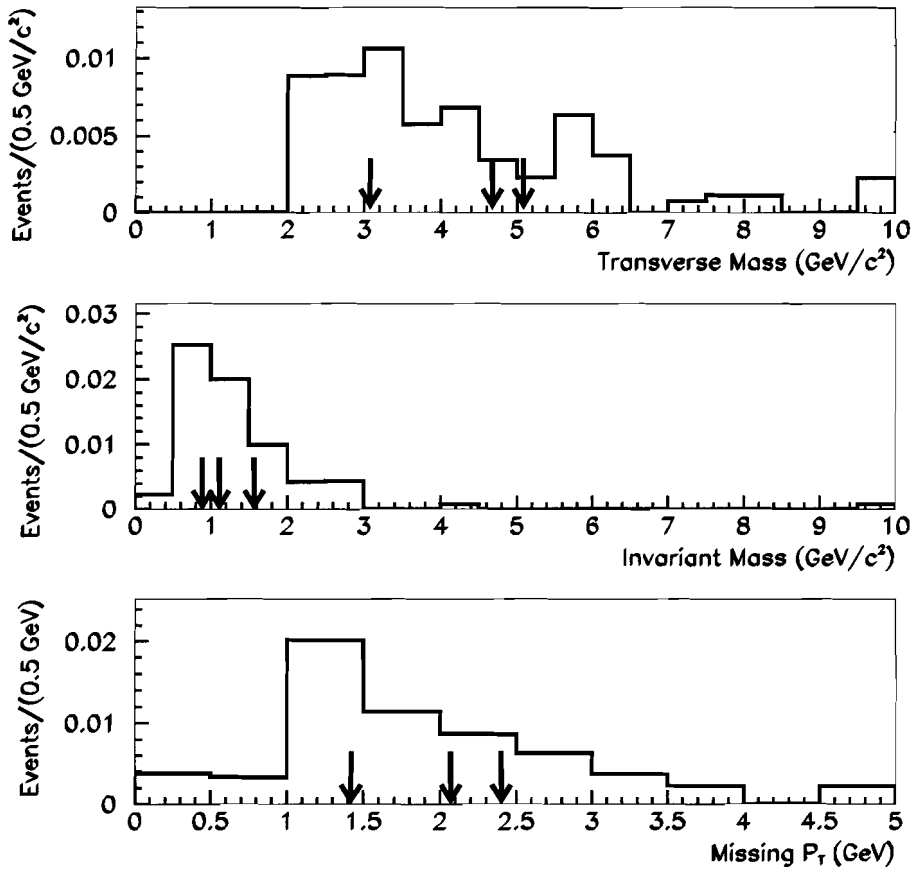

Figure 13.4: Kinematic distributions (transverse mass, invariant mass and missing transverse momentum) for $\mu\mu$ events from the background Monte Carlo. The histograms shows the MC; arrows indicate the three observed events.

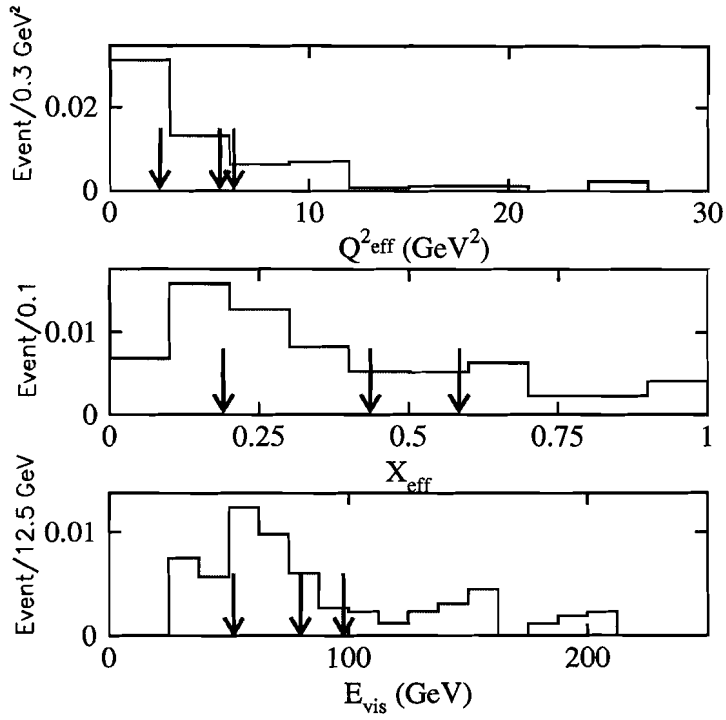

Figure 13.5: M ore kinematic distributions (x_{eff}, Q^2_{eff} and E_{vis}) for $\mu\mu$ background Monte Carlo. The histograms show the MC; the arrows indicate the three observed events.

Table 13.1: Vertex probability ($\mathcal{P}_{vert}$), first muon track probability ($\mathcal{P}_{\mu 1}$), and second muon track probability ($\mathcal{P}_{\mu 2}$). The probabilities are measured the with signal(background) Monte Carlos.

Event	1	2	3
($\mathcal{P}_{vert}$)	0.81(0.94)	0.011(0.30)	0.043(0.48)
($\mathcal{P}_{\mu 1}$)	0.95(0.96)	0.51(0.73)	0.034(0.18)
($\mathcal{P}_{\mu 2}$)	0.49(0.70)	0.15(0.39)	0.034(0.18)

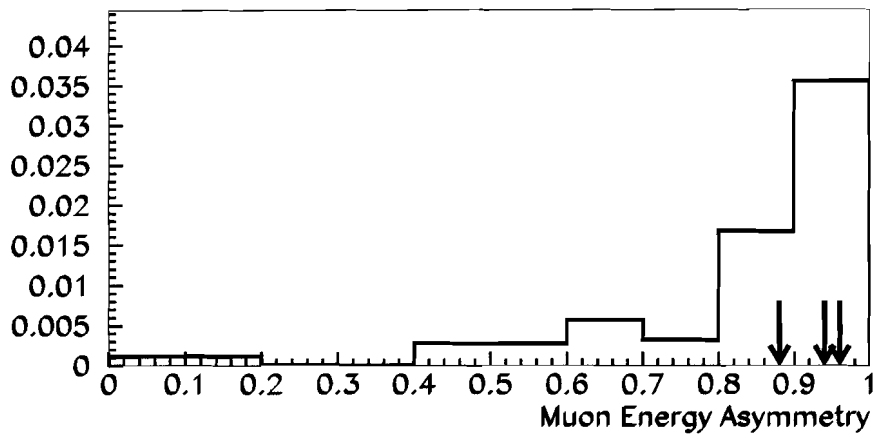

Figure 13.6: The muon energy asymmetry $(|E_1 - E_2|)/(E_1 + E_2)$. The histogram shows the $\mu\mu$ background Monte Carlo; arrows indicate the three observed events.

Perhaps the most striking feature in favor of the background hypothesis is the muon asymmetry of the three events. Neutrino scattering favors production of asymmetric muons (Fig. 13.6), because most dimuon N^0 backgrounds come from either π or K decay. Low energy π or K mesons have a higher probability to decay than high energy mesons. The decay process produces a low energy muon seen in conjunction with the high energy muon from the neutrino charged current process. The probability for three neutrino scattering events which pass the $\mu\mu(\nu)$ cuts to have the observed energy asymmetry is high (38%).

On the other hand, it is difficult to explain the rate of these events as background. If these events were due to charged current neutrino interactions, the rate is a factor of 40 greater than that predicted by the Monte Carlo. If such a source was not included in our simulations, we would expect between 1.2 and 30.4 additional events $\mu\mu$(at 99% confidence level [67]) in the chambers. We observe 0 $\mu\mu$ chamber events.

One can also limit the contribution of prompt $\mu\mu$ events in the helium by examining the number of $\mu\mu$ events present in the calorimeter. Based on the observation

of three helium events, one expects to see between 300 and 8,200 events at 99% confidence level in the calorimeter. We observe only 54 events with similar kinematics in the calorimeter [56].

13.3 Further Cross-Checks

Several additional samples were used to compare Monte Carlo to data. These samples were super-sets which included the signal region and test how the data behaves as the kinematic and reconstruction space is expanded. These regions were created by removing or loosening criteria singly and in combinations.

The first sample examined data and Monte Carlo rates as the criteria were gradually loosened. The first step relaxed the clean cuts. Restrictions on extra drift chamber hits downstream of the vertex, extra calorimeter clusters and electrons with missing hits were removed. One additional $\mu\mu$ event was observed in the data. The topology of this additional event was consistent with a DIS event (extra track segments, excess of neutral energy, and extra hits). No μe or $\mu\pi$ events were observed. The second step increased the fiducial volume to include the chamber and intermediate regions while maintaining the relaxed clean cuts. Finally, the third step removed all energy and particle identification (PID) cuts. Table 13.2 shows the number of observed events and the expected background for each step. In each step, the Monte Carlo is in agreement with the data except for the three candidate events.

This study was repeated to include an $N^0 \rightarrow \mu\mu\nu$ Monte Carlo in addition to the background expectation. The N^0 decay Monte Carlo was normalized to 3 events passing the final sample criteria. Table 13.3 shows the combined expectation compared to data for each step.

A third study removed criteria one at a time or in pairs. At each step all previously removed requirements were restored. Under most conditions, no extra data events

Table 13.2: Observed events and expected background as cuts are sequentially released.

Sequential Change to Cuts	Event Type	Data Events	MC Prediction
All cuts	$\mu\mu$	3	0.07
	μe	0	0.13
	$\mu\pi$	0	0.14
Remove the Clean Cuts	$\mu\mu$	$3+1$	0.26
	μe	0	0.60
	$\mu\pi$	0	0.77
Include the chamber region	$\mu\mu$	$3+2$	1.4
	μe	2	5.3
	$\mu\pi$	8	8.6
Release energy & PID requirements	$\mu\mu$	$3+3$	2.5
	μe	7	12.0
	$\mu\pi$	12	17.5

Table 13.3: Predicted and observed $\mu\mu$ events as cuts are sequentially released. Prediction shows the expected background and expected N^0 signal from N^0 decay Monte Carlo, where the signal has been normalized to 3 events with all cuts applied.

Event Type	Background	N^0-decay	Data
$\mu\mu$ with standard cuts	0.07	3.0	3
Releasing the clean cuts	0.26	5.4	4
Including chamber regions	1.4	6.4	5
Removing E & PID	2.5	6.5	6

entered the sample when a single criteria was removed, demonstrating that most data events were removed by more than one selection criteria. The longitudinal vertex requirement was investigated in the chamber and intermediate regions (see Chapter 11). Removing the "no extra track segments" requirement allowed one $\mu\pi$ event to enter the sample. Removing the "no extra clusters" requirement revealed one μe event. This is consistent with Monte Carlo expectation, where the extra cluster is due to photons from a π^0 decay which cause the event to look electromagnetic. When both of these cuts were removed, two more events enter the sample. Their topology was consistent with DIS events. In summary, this cross-check did not reveal events which were similar to the candidates.

A final study removed/loosened criteria to select a larger "clean" sample. Energy cuts were set to 2.2 GeV for all particles, the transverse mass cut was removed and the z vertex was allowed in the helium or chamber regions. Table 13.4 details the observed and predicted number of events in all three modes for both the chamber and helium regions. The three signal events lie within the helium $\mu\mu$ sample. Note that the ratio of predicted chamber to helium events is a factor of 7 for μe and $\mu\pi$ events,

Table 13.4: Observed events and expected background for sample with loosened energy and M_T criteria.

Sample	Event Type	Data Events	Monte Carlo Prediction
Chamber	$\mu\mu$	0	0.26
	μe	1	2.2
	$\mu\pi$	2	3.3
Helium	$\mu\mu$	3	0.096
	μe	1	0.31
	$\mu\pi$	1	0.41

but only a factor of 2.6 for $\mu\mu$ events. This feature is due to the fact that $\mu\mu$ tend to come from meson decays where the primary interaction occurs in the chamber. The μe and $\mu\pi$ sample tend to reconstruct closer to the point of origin, and thus reduce significantly in rate as one moves into the low mass helium region. Aside from the three events, that data show no significant excess in any of the available channels.

13.4 Null Hypotheses

Three possible sources of neutrino scattering appear most likely to produce two muon events which reconstruct in the helium. They are chamber interactions with the vertex mis-reconstructed, $\mu\pi$ events with a $\pi \rightarrow \mu\nu$ decay, and μK events with a $K \rightarrow \mu\nu$ decay. These sources are already included in the Monte Carlo background estimate, but are explored in greater detail below.

13.4.1 Hypothesis 1: Chamber Interaction

The first hypothesis assumes that the events were neutrino interactions in the chambers that produced $\mu\mu$ events that are mis-reconstructed in the helium. A study was performed with each of the three signal events. The vertex was forced to lie within the nearest drift chamber. For each event, the vertex $\chi^2_{\text{vertex}}/\text{dof}$ increased significantly. Forcing the vertex reconstruction for Event 1 into the nearest upstream drift chamber (DK4), the $\chi^2_{\text{vertex}}/\text{dof}$ goes from 0.32 for the standard fit to 4.6 for the forced fit. The original fit for Event 2 had a $\chi^2_{\text{vertex}}/\text{dof}$ of 9.53 while the forced fits were worse: the $\chi^2_{\text{vertex}}/\text{dof}$ is 27.9 for the chamber downstream of the vertex (DK5), and it is 5288 for the calibration drift chamber upstream of the original vertex. Finally, forcing the vertex reconstruction for Event 3 into the nearest downstream drift chamber (DK4), the $\chi^2_{\text{vertex}}/\text{dof}$ goes from 3.04 for the standard fit to 27.3 for the forced fit to DK4 and 101.8 for the forced fit to DK5. If the third track is also forced to be on the vertex, the $\chi^2_{\text{vertex}}/\text{dof}$ decreases to 20. If one does not require the vertex to be in the drift chamber, but requires all three tracks to come from the same vertex, then one obtains 14.4.

This hypothesis has other difficulties. No $\mu\mu$ events are observed in either the chamber or intermediate region which implies a $\mu\mu$ source which always mis-reconstructs badly enough to move into the helium. Also, no μe or $\mu\pi$ events are observed to mis-reconstruct. Finally, no mechanism has been identified for this type of mis-reconstruction.

13.4.2 Hypothesis 2: Pion Decay

A second background hypothesis attributes the $\mu\mu$ events to unsimulated $\nu + X \rightarrow \mu + \pi + Y$ interactions, where the pion decays to produce the second muon and the other particles in the reaction (signified by Y) are not seen. Pion decay is a primary

source for second muons in neutrino interactions. Particles produced in the decay channel travel a significant distance between the vertex and the calorimeter (3-30 meters), allowing a small fraction of pions to decay. Of all pions created in Bashful, DK5, DK4, and the helium, approximately 15% of them decay to $\mu\nu_\mu$ before reaching DK3. Only 4.1% of all pions, however, decay with energies greater than 2.2 GeV, and only 3.5% of all pions create a muon with an energy above 2.2 GeV.

This hypothesis has two major difficulties. Since only 3.5% of the pions decay to a visible muon, there should be a significant number of $\mu\pi$ events, whereas no $\mu\pi$ events are observed in the data. Furthermore, if these events are created in the chambers a mechanism is necessary to move them into the helium. The transverse momentum associated with pion decay is very small, so the muon track generally points back to the original chamber vertex (or into the intermediate region). No significant excess is observed in either region.

Quantitatively, the data in complementary samples can be compared to scalings of the observed three $\mu\mu$ events. The DIS Monte Carlo predicts a ratio of helium $\mu\pi$ to $\mu\mu$ events of 2.0 for the sample with all the standard cuts. With this ratio, the probability of seeing the observed 3 $\mu\mu$ events and 0 $\mu\pi$ is 1.2%. The ratio of the predicted $\mu\mu$ events in the helium to $\mu\pi$ events in or near the chambers is 21.7. Only 2 $\mu\pi$ events were seen near the chambers. Using these numbers as input, the probability of observing 2 $\mu\pi$ events near the chambers and 3 $\mu\mu$ events in the helium is 3.4×10^{-5}.

13.4.3 Hypothesis 3: Kaon Decay

A third background hypothesis is that the candidates are neutrino interactions in the chambers producing a $\mu K(Y)$ final state followed by a $K \rightarrow \mu\nu$ decay. Kaons in the decay channel decay to $\mu\nu_\mu$ 22% of the time before reaching DK3; 11% of all kaons

Table 13.5: Results for the fits to kaon decay hypothesis. Table shows new vertex χ^2/dof, the minimum and maximum decay distance from nearest chamber ($\Delta z_{min,max}$), the kaon energy at the minimum and maximum points (E_K), and the approximate probability of decay ($\mathcal{P}$). Two values are quoted for the energy at the maximum Δz value because of a quadratic ambiguity in the kaon energy.

Event	1	2	3
χ^2/dof	1.00	1.02	1.85
Δz_{min} (cm)	919	1875	953
$E_K^{z_{min}}$ (GeV)	5.0	11.2	8.3
Δz_{max} (cm)	157	732	381
$E_K^{z_{max}}$ (GeV)	2.6 / 51.0	6.3 / 53.9	4.5 / 51.4
$\mathcal{P}_{decay}$	17.6%	11.6%	8.2%

decay to a muon with an energy above 2.2 GeV. Not only are these decay probabilities higher than those for pions, but kaon decays produce large enough transverse momenta that chamber events might reconstruct in the helium. To study this possibility, each of the three candidate events have been re-fit requiring the vertex to be within a drift chamber but allowing for a decay kink in the second low energy track. The fit is constrained such the kink does not exceed the allowed P_T from kaon decay. These fits show the kaon decay hypothesis is kinematically possible, often yielding good χ^2/dof for finding the vertex in the chambers (see Table 13.5). Using the kaon momenta calculated from the fit, the probabilities are 18%, 12%, and 8% for the kaon to decay. Because of the simple two-track planar topology, most two-track vertices, including most simulated N^0 events, can also be reconstructed as chamber produced events with kaon decays with a displaced vertex.

The kaon decay hypothesis certainly proposes to be an attractive explanation for the three events. However, the hypothesis has several difficulties. It has the same problem as the pion decay hypothesis in that more $\mu\pi$ (really μ-hadron) events should have been observed than are seen in the data. Direct production of kaons is Cabibbo-suppressed and is most likely in $\bar{\nu}$ running, whereas the events are only seen in ν running periods. Approximately 20% of events produce kaons through fragmentation, but this happens mainly in high multiplicity events which would be removed by the "clean cuts."

Because kaon decays have large P_T, only 45% of the μK producing two muons in the calorimeter will have a vertex formed by the two muons. In the other cases, the decay plane is aligned such that the two muons fail to verticize in the decay channel. Such unaligned dimuon events consistent with all cuts but the vertex requirement are not observed in the data.

Once a kaon decay is properly reconstructed, however, there is a high probability that it will be mis-reconstructed in the helium. About 60% of kaon decays generated in the chambers are reconstructed in the helium; 29% are reconstructed in the intermediate region, and only 11% are reconstructed within 15 cm of the chamber.

As in the case for the pion decay hypothesis, we can use scaling arguments to compare observed data to the predictions of this hypothesis. In the data, there are one μe and two $\mu\pi$ chamber events with all the standard cuts but with the track energy requirements removed. Since about 20% of the events in the sample are from kaons, the scaling factor between μK events in the drift chambers and μK events which produce a $\mu\mu$ event in the helium is 48.3. Under this hypothesis, the probability to see, as observed, three or fewer μ-hadron events in the chambers given the three $\mu\mu$ events in the helium is 10^{-5}. Therefore, the paucity of μ-hadron events in the chambers excludes above the 99.99% confidence level the possibility of an unsimulated μK source large enough to explain the three observed $\mu\mu$ events in the helium.

13.5 Limits

Even with careful analysis of the observed events, and under several hypotheses, the source of the excess events is not clear. On the one hand, the observed events are inconsistent with expected background rates. Furthermore, any false modeling or unsimulated background should have appeared in one of our many sideband studies. On the other hand, the muon asymmetry and kinematic distributions are more consistent with a neutrino interaction than a massive particle decay. Given this ambiguity, we have decided to be conservative and place a limit based on the observation.

Using Eq. 1.48 (restated below), an interesting limit can be set on the pair production of N^0's at the primary proton target:

$$N_{L^0}^{seen} = N_{pot} \cdot d \cdot N_A \cdot \rho \cdot (\frac{d\sigma}{d\Omega} \cdot d\Omega) \cdot \epsilon \cdot (1 - e^{-\frac{3.5\times10^3 \text{ cm}}{\ell}})(e^{-\frac{1.5\times10^5 \text{cm}}{\ell}}). \tag{13.1}$$

For the NuTeV experiment, we see 2.55×10^{18} protons on target. Two-thirds of the 800 GeV protons interacting in a one-interaction length (30.5 cm) BeO target, while the remaining protons interact in the beam dump. The density of the target is 2.7 g/cm^3. The angle of the primary proton beam with respect to the detector is 7.8 mr at the target and 6.9 mr (9.8 mr) at the neutrino (antineutrino) beam dump. The average angle subtended by the detector in the center-of-mass frame of the pair-production is $\approx 6.7 \times 10^{-3}$ strad. The result is shown in Figure 13.7. This limit is determined by calculating one-sided limits using a frequentist approach [76] where 3 events were observed with $0.069. \pm 0.01$ background expected. Because the source of the events is unclear, the unified approach of Feldman and Cousins [67] has deliberately *not* been used.

One can set a generic limit on unstable, long-lived particles that are produced at the primary target using the parameters associated with the high mass search. The

lation signal [80], can also look for Q^0 decays by making use of the timing structure of the MiniBooNE neutrino beam. The experiment will receive 8 GeV protons from the Fermilab Booster ring, incident on a beryllium target. This will primarily produce pions, which will decay in flight in a 50 m air-filled decay pipe. The BooNE detector, located 500 m downstream, will be a spherical tank 6.1 m in radius filled with 800 tons of mineral oil, with an inner tank structure at 5.8 m radius supporting 1280 eight inch photomultiplier tubes facing into the tank. This inner region is optically isolated from the outer veto region of the tank. About 240 photomultiplier tubes will be mounted on the tank wall to examine the veto region. The BooNE experiment will receive approximately 5×10^{20} protons on target per year.

Due to the timing structure of the proton pulses out of the Booster, the MiniBooNE experiment is sensitive to Q^0 production in its neutrino beam. The beam arrives in tight 1.5 ns-wide pulses, with 18.94 ns spacing between each pulse. Since the Q^0 mass is very close to the kinematic limit for the decay $\pi \rightarrow \mu Q^0$, the Q^0 particles will be traveling non-relativistically compared to the neutrinos produced from the pion decays. The Q^0 from a 2 GeV pion will arrive between the 1.5 ns pulses, where neutrino backgrounds will be minimal. Thanks to this timing structure, the time of arrival appears to be very effective in isolating the Q^0 signal. The MiniBooNE sensitivity for Q^0's in the short-lifetime solution will reach branching ratios of approximately 10^{-15} at 10% detector efficiency in one year of running (see Figure 14.2).

14.1.3 Future Detector at ISIS

Another possibility under consideration is the building of a dedicated Q^0 search experiment at the ISIS spallation facility [81]. The dedicated detector, KX, would consist of a gas Time-Projection-Chamber (TPC) downstream of the KARMEN neutrino

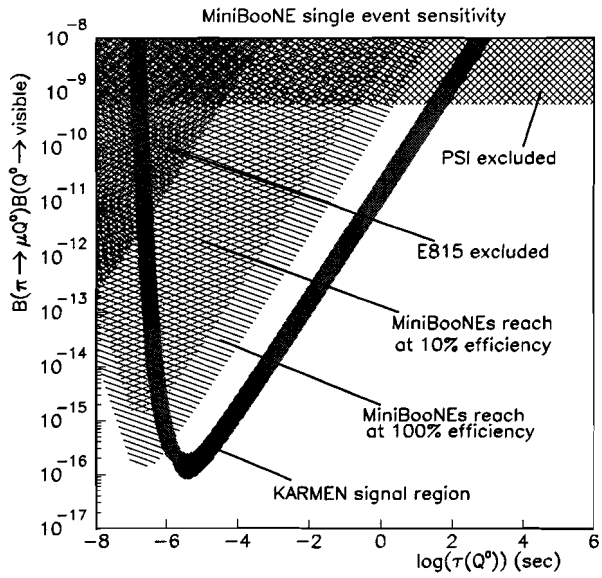

Figure 14.2: Projected MiniBooNE single event sensitivity on the Q^0 branching ratio for one year of running (*coutersy of M. Novak*).

beamline. The experiment offers several advantages over its previous detector for Q^0 searches: (1) it will utilize an already existing high intensity neutrino/Q^0 source; (2) it will reduce neutrino-induced backgrounds due to low-mass detector; and (3) it will offer track reconstruction of e^+e^- pairs from Q^0 decay. The detector is currently only in the pre-proposal stage. The KX design is a good platform for a detector dedicated to search for the KARMEN timing anomaly and can be transported to other low-energy fixed target facilities (e.g. the MiniBooNE beamline) with intense pion fluxes.

14.2 Future for the N^0

The anomalous observation of events from the high mass search at NuTeV may provide an interesting region for existing and future experiments to address. Unfortu-

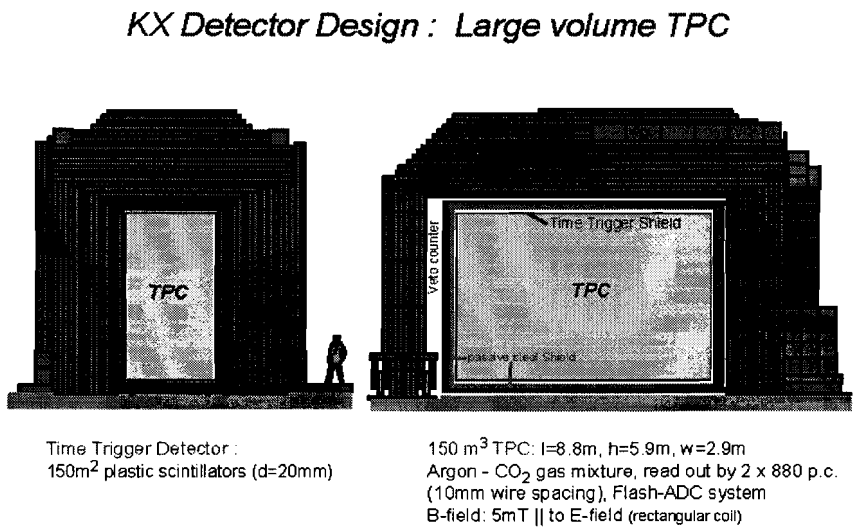

Figure 14.3: Design for a proposed Q^0 TPC detector at the ISIS spallation facility.

nately, there exists considerable difficulty in replicating the NuTeV experiment. Part of the difficulty stems from the high energy, high-intensity proton source necessary to produce high mass N^0 particles. If the production source for the anomalous high mass events comes from p-p collisions, then collider experiments such as D0, CDF, and the Large Hadron Collider (LHC) may be able to complete searches comparable to NuTeV. N^0's at a mass of 5 GeV/c^2 can be produced in collisions at these facilities. There are a number of issues, however, which make N^0 production and detection at colliders more difficult. Typical luminosities of the colliders are far smaller than fixed target experiments. Colliders may not be able to probe particles with very long lifetimes (though sensitivity exists).

Fixed target experiments, on the other hand, prove to be more ideal places to search for exotic N^0 decays. These experiments can produce high intensity, high energy beams that can be optimized for N^0 production. For example, the NOMAD neutrino experiment at CERN [82] (see Figure 14.4) may be able to address part or all

of the NuTeV observation of anomalous dimuons. NOMAD is also a high-energy, high-intensity fixed target experiment designed to search for $\nu_\mu - \nu_\tau$ oscillations. Neutrinos are produced using a 450 GeV proton beam source, located 835 m away from the detector. The NOMAD detector, with a fiducial volume of $2.6 \times 2.6 \times 4.0$ m^3, uses a heavy magnetized target to study neutrino interactions from their beam. NOMAD has at its disposal 6×10^{19} protons on target; 23 times more than NuTeV. It is possible that their high intensity may be able to probe part of the NuTeV region. However, the lower proton energy and reduced fiducial volume decreases NOMAD's sensitivity to N^0 production. Assuming the production cross-section scales as the B cross-section (reduction of 1/6) and the two detectors have similar efficiencies, NOMAD should see about 2.5-10 times the number of N^0's seen at NuTeV. The exact number depends partly on the lifetime of the N^0 particle (NOMAD will have greater sensitivities for small lifetimes due to the detector distance to the target). However, because their fiducial region is a massive neutrino target, backgrounds will be much greater in the fiducial region and need to be addressed carefully. Detector efficiencies and sensitivities to different models are yet to be calculated; analyses are currently underway [83].

14.3 Other Exotic Searches: Muon Storage Ring

The proposed muon storage ring may provide an optimal setting to extend the search for neutral heavy leptons in the lower mass ranges [84]. Neutrino physics at the muon storage ring offers ample opportunities, not only to continue testing current predictions of the Standard Model, but also to search for new phenomena in yet unexplored physical regions. The high intensity neutrino beam created by the muon storage ring provides an ideal setting to search for neutral heavy leptons with a mass below the muon mass, 105.6 MeV/c^2.

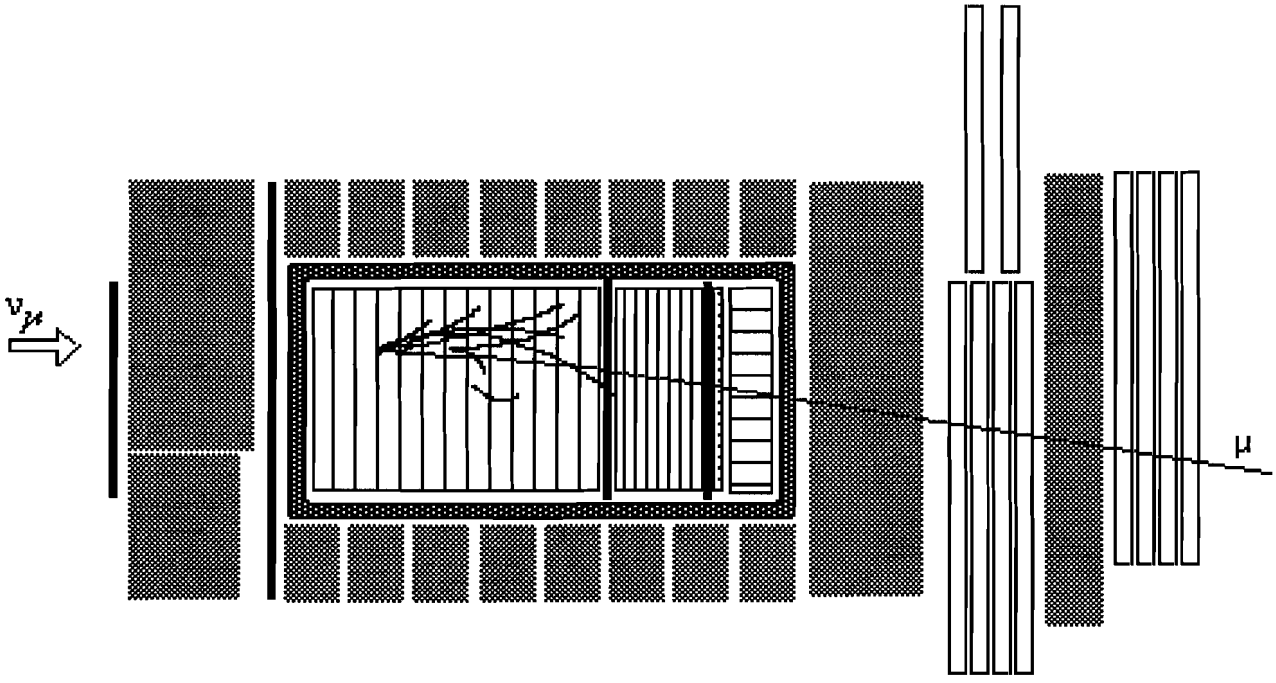

Figure 14.4: Schematic of the NOMAD neutrino detector.

It is postulated that neutral heavy leptons (L_0) could be produced from muon decay when one of the neutrinos mixes with its heavy isosinglet partner. Neutral heavy leptons can be produced via one of two channels:

$$\mu^- \rightarrow L_0 + \overline{\nu}_e + e^- \text{ , and} \tag{14.1}$$

$$\mu^- \rightarrow \nu_\mu + \overline{L}_0 + e^-. \tag{14.2}$$

Once produced, a neutral heavy lepton of such low mass will either decay via $L_0 \rightarrow \nu\nu\nu$, $L_0 \rightarrow \nu ee$, or $L_0 \rightarrow \gamma\nu$. The most viable mode for detection is via the double electron channel. For this particular decay mode, the L_0 can decay either via charged current or charged and neutral current interactions. The branching ratios for this decay process has been previously calculated [22].

The muon storage ring promises to be one of the most intense neutrino sources ever built, with projected intensities reaching 10^{20} neutrinos per year. Such an intense neutrino source would prove ideal in studying long and short baseline neutrino oscillations [85], but can also be extended to study other neutrino processes at high statistics. Neutral heavy leptons fall naturally in the latter category.

In testing the sensitivity of L_0 production at the muon storage ring, we make a few underlying assumptions. We assume that the storage ring utilizes a pure, unpolarized muon beam with straight sections such that 25 percent of the muons will decay to neutrinos pointing towards the detector. We assume that the detector is 3 meters in diameter and 30 meters in length, with enough resolution to detect the e^+e^- vertex from the L_0 decay. We assume for now that the background is negligible.

The sensitivity of the detector has been calculated for a number of different muon energies and beam intensities. The plots below show limits for the coupling constants as a function of L_0 mass. One achieves the best limits from using relatively low

energy/high intensity muon beams. This is a significant improvement over previous neutral heavy lepton searches, where limits do not reach below 6.0×10^{-6} in the low mass region [37, 21].

The single event sensitivity quoted here depends greatly on having minimal background levels in the signal region. Part of this can be achieved by requiring events to have only two electron tracks with very small transverse mass. However, it is estimated that even if the decay region is composed only of helium gas, that the number of neutrino interactions will approach a few thousand. The ideal detector, therefore, would consist of a long, compact, vacuum or quasi-vacuum pipe with appropriate segmentation for tracking. The decay pipe would be used in conjunction with larger neutrino detectors adapted for the muon storage ring.

The muon storage ring may prove to be an ideal location to continue the search for neutral heavy leptons. The high intensity neutrino beam allows for a neutral heavy lepton search to be sensitive to coupling constants in the low mass region. In addition, such a neutral heavy lepton program could easily interface with an already existing neutrino detector which utilizes the muon beam. It is also clear, however, that a neutral heavy lepton search would receive the most benefit at lower muon energies, and thus would yield best results at the earlier stages of the muon storage ring program.

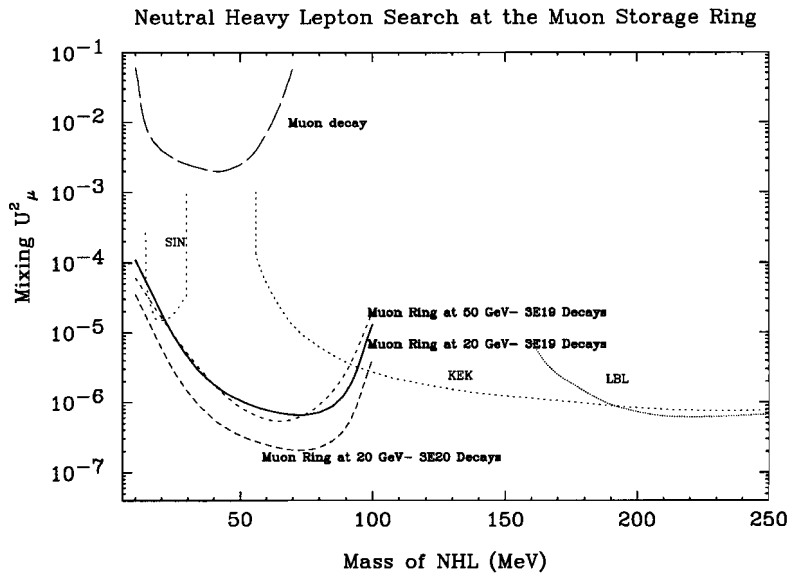

Figure 14.5: $|U_\mu|^2$ as a function of L_0 mass for one year of running. The curves show sensitivities for 20 GeV and 50 GeV muon energies. Sensitivities assume no background events in signal region [37, 86].

Chapter 15

Conclusion

This work has addressed two searches for exotic particles using a high energy neutrino beam. These searches for massive exotic particles could have important implications on our understanding of the Standard Model and its potential theoretical extensions. The results from these two searches place competitive limits on the available parameter space for theoretical models. In addition, this work made use of an innovative instrumented helium decay channel. The apparatus should provide the framework for future particle searches using a high energy neutrino beam.

In our first search, we specifically addressed the KARMEN timing anomaly, which predicts the existence of a particle with a mass of 33.9 MeV/c^2. Our results excluded a significant portion of the available parameter space of the particle, up to four orders of magnitude below current experimental limits. The result places restrictions on the existence of such a particle.

In our second search, we addressed the existence of exotic particles with masses above 2.2 GeV/c^2. We observed 3 $\mu\mu$, 0 μe and 0 $\mu\pi$ events with transverse mass above 2.2 GeV/c^2. The expected backgrounds were 0.069 ± 0.010, 0.13 ± 0.02, and 0.14 ± 0.02 events, respectively. The rate corresponding to the observed three events

is not consistent with Standard Model processes we have identified and the source of the events is not clear. On the other hand, the kinematics of the events are not consistent with a heavy particle decay and have led us to use the data to set limits. Based on this observation, we have set a limit on N^0 (including possible neutralino) production and decay. This is the first experiment to set limits on the production of long-lived neutralinos in this mass range which decay by R-parity violation.

Appendix A

Paper on the Q^0 Search at NuTeV

The following Appendix consists of the Q^0 search article submitted to *Physical Review Letters*. The article was published in Phys. Rev. Lett. **84**, 4043 (2000).

VOLUME 84, NUMBER 18 PHYSICAL REVIEW LETTERS 1 MAY 2000

Search for a 33.9 MeV/c^2 Neutral Particle in Pion Decay

J. A. Formaggio,[2] E. D. Zimmerman,[2] T. Adams,[4] A. Alton,[4] S. Avvakumov,[7] L. de Barbaro,[5] P. de Barbaro,[7] R. H. Bernstein,[3] A. Bodek,[7] T. Bolton,[4] J. Brau,[6] D. Buchholz,[5] H. Budd,[7] L. Bugel,[3] S. Case,[2] J. M. Conrad,[2] R. B. Drucker,[6] B. T. Fleming,[2] R. Frey,[6] J. Goldman,[4] M. Goncharov,[4] D. A. Harris,[7] R. A. Johnson,[1] J. H. Kim,[2] S. Koutsoliotas,[2] M. J. Lamm,[3] W. Marsh,[3] D. Mason,[6] K. S. McFarland,[7,3] C. McNulty,[2] D. Naples,[4] P. Nienaber,[3] A. Romosan,[2] W. K. Sakumoto,[7] H. M. Schellman,[5] M. H. Shaevitz,[2] P. Spentzouris,[2,3] E. G. Stern,[2] M. Vakili,[1] A. Vaitaitis,[2] V. Wu,[1] U. K. Yang,[7] J. Yu,[3] and G. P. Zeller[5]

[1]*University of Cincinnati, Cincinnati, Ohio 45221*
[2]*Columbia University, New York, New York 10027*
[3]*Fermilab, Batavia, Illinois 60510*
[4]*Kansas State University, Manhattan, Kansas 66506*
[5]*Northwestern University, Evanston, Illinois 97403*
[6]*University of Oregon, Eugene, Oregon 97403*
[7]*University of Rochester, Rochester, New York 14627*
(Received 27 December 1999)

The E815 (NuTeV) neutrino experiment has performed a search for a 33.9 MeV/c^2 weakly interacting neutral particle produced in pion decay. Such a particle may be responsible for an anomaly in the timing distribution of neutrino interactions in the KARMEN experiment. E815 has searched for this particle's decays in an instrumented decay region; no evidence for this particle was found. The search is sensitive to pion branching ratios as low as 10^{-13}.

PACS numbers: 14.80.-j, 12.60.-i, 13.20.Cz, 13.35.Hb

The KARMEN collaboration at the ISIS spallation neutron facility at the Rutherford Appleton Laboratory uses a pulsed neutrino beam resulting from stopped pion and muon decays to study neutrino-nucleon interactions. Their experiment has reported an anomaly in the timing distribution of neutrino interactions from stopped muon decays [1]. One possible explanation for the anomaly is an exotic pion decay, where a neutral weakly interacting or sterile particle is produced and travels 17.7 m to the KARMEN detector with a velocity of 4.9 m/μs. Upon reaching the KARMEN detector, the exotic particle decays to a partially electromagnetic state, such as $e^+e^-\nu$ or $\gamma\nu$. The $e^+e^-\nu$ decay is strongly favored by recent KARMEN data [2]. This slow moving exotic particle (hereafter denoted as Q^0) would have a mass of 33.9 MeV/c^2, which is near the kinematic threshold for $\pi \to \mu Q^0$ decay. Proposed explanations for the timing anomaly include heavy sterile neutrinos [3,4] and light neutralinos [5].

The KARMEN experiment reports a signal curve for pion branching ratio $B(\pi \to \mu + Q^0)B(Q^0 \to \text{visible})$ versus lifetime. Their signal region extends as low as 10^{-16} for a lifetime of 3.6 μs. For branching ratios above this minimum, there exist two solutions to the KARMEN anomaly (at small and large lifetimes). Certain portions of the KARMEN signal have already been excluded. Experiments at the Paul Scherrer Institute (PSI) [6,7] have performed searches for this exotic particle by studying the momentum spectrum of muons and electrons produced by π^+ decays in flight. PSI has excluded any exotic pion decays to muons with branching ratios above 2.1×10^{-8} at 90% C.L., and to electrons with branching ratios above 0.9×10^{-6} at 90% C.L. In addition, there exist astrophysical constraints on certain decay modes of the Q^0 which exclude lifetimes above 10^3 s. Despite the above limits, portions of the KARMEN allowed signal region remain to be addressed.

The E815 (NuTeV) neutrino experiment at Fermilab has performed a direct search for the Q^0 decay by combining the capabilities of a high intensity neutrino beam with an instrumented decay region (the "decay channel"). During the 1996–1997 fixed target run at Fermilab, NuTeV received 2.54×10^{18} 800 GeV protons striking a BeO target with the detector configured for this search. The secondary pions and kaons produced from the interaction were subsequently sign selected using a series of magnets and focused down a beam line at a 7.8 mrad angle from the primary proton beam direction. The pions and kaons could then decay in a 440 m pipe before hitting a beam dump. A total of $(1.4 \pm 0.1) \times 10^{15}$ pion decays and $(3.6 \pm 0.4) \times 10^{14}$ kaon decays occurred in the pipe. The neutral weakly interacting decay products (neutrinos and possibly Q^0's) traveled through approximately 900 m of earth berm shielding before arriving at the decay channel.

The instrumented decay channel (Fig. 1) consisted of a series of helium bags, extending a total of 34 m in length, interspersed with 3 m $\times$ 3 m multiwire argon-ethane drift chambers. The drift chambers were designed to track charged particles from decays occurring within the helium. Upstream of the decay channel stood a 4.6 m $\times$ 4.6 m array of scintillation plates, known as the veto wall, used to detect any charged particles entering from upstream of the detector. Downstream of the decay channel was the

 © 2000 The American Physical Society

VOLUME 84, NUMBER 18 PHYSICAL REVIEW LETTERS 1 MAY 2000

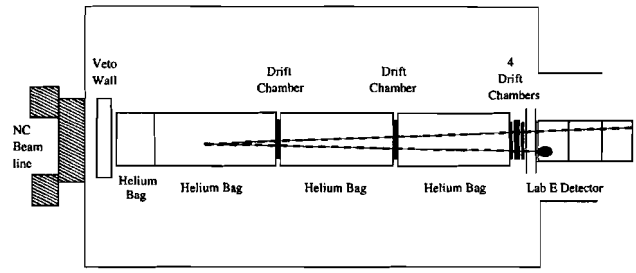

FIG. 1. Schematic of the NuTeV decay channel, including the veto wall, helium bags, drift chambers, and calorimeter.

Lab E neutrino detector, which consisted of a 690-ton iron-scintillator sampling calorimeter interspersed with drift chambers. The Lab E detector provided triggering, energy measurement, and final particle identification for tracks entering from the decay channel. Particles were identified by their penetration into the calorimeter: a muon produced a long track, a pion produced an elongated cluster of hits, and an electron or photon produced a compact cluster. More details of the decay channel and the calorimeter can be found elsewhere [8,9].

The decay channel was employed to search for the decay of the Q^0. The experimental signature of this decay is a low-mass, low-transverse momentum electron-positron pair having a vertex within the fiducial volume of the decay channel.

A series of analysis cuts isolated the Q^0 from the background. The cuts were divided into two categories: reconstruction and kinematic. Reconstruction cuts isolated two track events occurring within the fiducial volume of the decay channel. We required that two charged tracks originated from a common vertex, with no additional tracks associated with the vertex. By removing events with activity in the veto wall, we ensured that no charged tracks entered from upstream of the decay channel. We also required that each track had a small slope (<10 mrad) relative to the beam axis, and that, when projected upstream to the veto wall, it fell within 50 in. of the beam center. These cuts removed both cosmic rays and photons from neutrino interactions in the upstream berm. Finally, we required that each track be identified as an electron based on the shower shape in the calorimeter. Because of the small opening angle of the two tracks, the two electron showers manifested themselves as a single merged electronlike cluster within the calorimeter. The efficiency for identifying such an event as an ee pair was estimated from Monte Carlo studies to be $(90 \pm 3)\%$. The error on the identification efficiency was estimated from calibration beam studies. The cluster energy was divided between the tracks based on a fit to the amount of multiple scattering each track underwent in the decay channel.

Because of its mass, the Q^0 possesses unique kinematic features which can be used to distinguish it from potential background sources, such as photons and deep-inelastic neutrino interactions. We have used effective scaling variables to represent the kinematics of the reconstructed events. The effective scaling variables $x_{\rm eff}$ and $W_{\rm eff}$ were calculated for each event using the following assumptions: (1) the event was a charged current neutrino interaction ($\nu_\ell N \rightarrow \ell N' X$), and (2) the missing transverse momentum in the event was carried by an undetected final state nucleon. We have defined $x_{\rm eff} \equiv Q^2_{\rm vis}/2m_p\nu_{\rm vis}$ and $W_{\rm eff} \equiv \sqrt{m_p^2 + 2m_p\nu_{\rm vis}/c^2 - Q^2_{\rm vis}/c^2}$, where $Q_{\rm vis}$ is the visible reconstructed 4-momentum transfer, $\nu_{\rm vis}$ is the reconstructed hadron (or electron) energy, and m_p is the proton mass. Using the above definitions, we required that all reconstructed events have $x_{\rm eff} < 0.001$ and $W_{\rm eff} > 2.5\ {\rm GeV}/c^2$. In addition, we required that the reconstructed transverse mass m_T ($m_T \equiv |p_T| + \sqrt{p_T^2 + m_V^2}$, where m_V is the invariant mass of the two charged tracks and p_T is the momentum transverse to the beam axis) be less than $250\ {\rm MeV}/c^2$. Finally, we required that the total energy deposited by the e^+e^- pair be greater than 15 GeV. The effect of these cuts when applied to signal and typical background kinematic distributions can be seen in Fig. 2. The total acceptance for Q^0 events in the fiducial region was 15.6%. Systematic errors on the acceptance are accounted for in the overall normalization procedure described below.

The principal backgrounds originated from three main sources: neutrino interactions in the helium, neutrino interactions in the drift chambers, and neutral particles (mainly photons and kaons) from neutrino interactions in the berm and veto wall. Note that because the two electron tracks had a very small opening angle, the longitudinal vertex position resolution was quite poor ($\sigma \approx 7$ m). Thus, interactions in the chambers could not be removed using a vertex position cut. We used the Lund Monte Carlo program [10] to simulate the νp deep-inelastic interactions in both the berm and the decay channel. Separate Monte

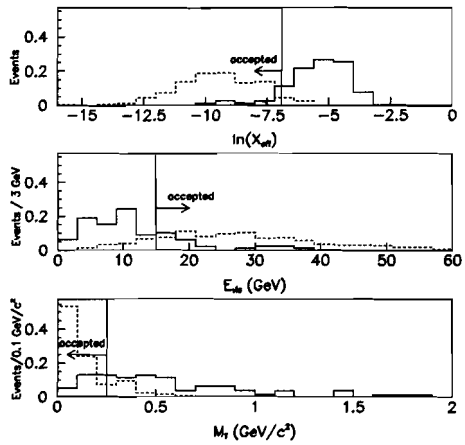

FIG. 2. Kinematic Monte Carlo distributions of $x_{\rm eff}$, visible energy, and transverse mass for neutrino interactions (solid line) and Q^0 (dashed line). All events shown have passed reconstruction cuts only and are relatively normalized.

Carlo programs were used to simulate hadronic resonance and diffractive single pion production [11,12]. The GEANT Monte Carlo program (version 3.21) [13] was used to simulate the decay channel and Lab E calorimeter. Based on our Monte Carlo study, we expected 0.06 ± 0.05 total background events within our signal region (see Table I). The uncertainty on this background estimate is dominated by Monte Carlo statistics.

A blind analysis was performed. The signal region was hidden while cuts were developed based on Monte Carlo studies of signal efficiencies and background rejection. Before examining the data near or in the signal region, we performed a series of studies to verify our background estimates. Using the Monte Carlo, we made predictions for the following three quantities: (1) the number of low energy (below 15 GeV) and high transverse mass (above 500 MeV/c^2) background events, (2) the number of $\mu\pi$ events, and (3) the number of multitrack events occurring within our decay channel. The results of these studies (shown in Table II) demonstrate good agreement between data and the Monte Carlo predictions. In the case of multitrack events, where a larger sample of events was available, there was also good agreement for various kinematic distributions (Fig. 3).

TABLE I. Total expected background events. Errors reflect Monte Carlo statistics.

Source	Rate
Photons	$0.04^{+0.02}_{-0.04}$
Kaons	$\ll 0.001$
Deep-inelastic charged current	0.00 ± 0.04
Deep-inelastic neutral current	0.02 ± 0.02
Cosmic rays	$\ll 0.001$
Quasielastic charged current	0.000 ± 0.008
Resonance neutral current	0.000 ± 0.003
Diffractive pions	0.00 ± 0.01
Total	0.06 ± 0.05

TABLE II. Background study results. Uncertainties are systematic.

Type of event	Events predicted	Events seen
High transverse mass	2.0 ± 0.3	1
$\mu\pi$ events	4.1 ± 0.6	3
Multiple track events	13.7 ± 1.8	10

The detection efficiency was estimated by simulating the Q^0 decay as having the kinematic characteristics of a heavy neutrino decay to $ee\nu$ [14,15]. We also considered additional decay models where the Q^0 decays to $\gamma\nu$ and $\gamma\gamma\nu$. The acceptances under these decay scenarios were (0.5 ± 0.1)% and (1.1 ± 0.1)%, respectively. The low efficiencies are due to the requirement that two tracks be reconstructed; this was only possible if a photon converted in the low-mass decay region before entering the calorimeter.

Systematic errors for this result were dominated by uncertainties on the number of pion decays in the pipe (6.8%) and the overall normalization. The sensitivity normalization was taken from a measurement of the number of neutrino interactions in the decay channel using very loose cuts. This number was (10.0 ± 4.3)% below a prediction normalized to the number of neutrino interactions in the

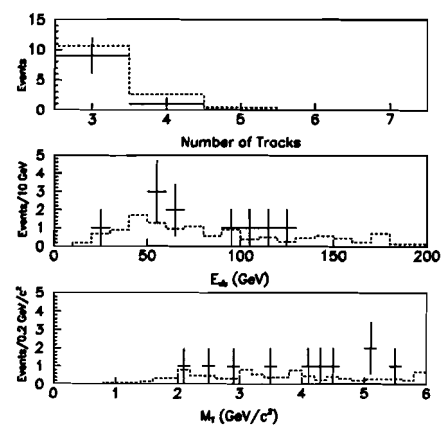

FIG. 3. Kinematic distributions of multiplicity, energy, and transverse mass for data (crosses) and background Monte Carlo (dashed line) multitrack events. Monte Carlo is absolutely normalized.

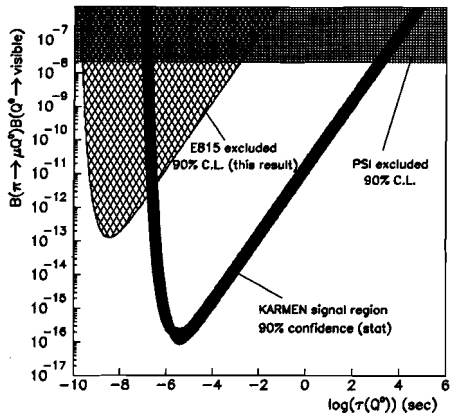

FIG. 4. Branching ratio versus lifetime plot for the KARMEN signal and the exclusion regions (90% C.L.) from the NuTeV and PSI experiments. Systematic errors (except for the decay model) have been included.

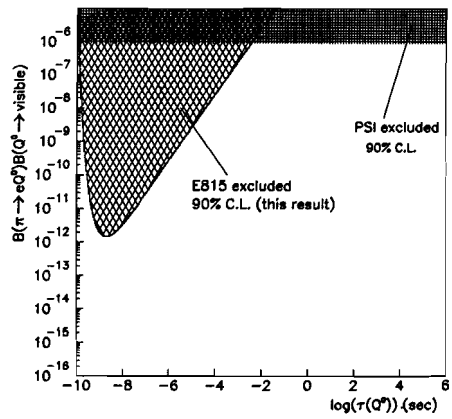

FIG. 5. Branching ratio versus lifetime plot for the NuTeV limit for $\pi \to e + Q^0$. Systematic errors (except for the decay model) have been included.

calorimeter. Considering this disagreement as a systematic error on the normalization, we have calculated a total systematic error of 12.1% on the sensitivity.

Upon analyzing the signal region, we found no events which passed the selection criteria. The probability of seeing zero events from an expected background of 0.06 ± 0.05 is 94%. We thus present an upper limit, shown in Fig. 4, on $B(\pi \to \mu + Q^0)B(Q^0 \to \text{visible})$. [A simple interpretation of the Q^0 is that the particle is a sterile heavy neutrino which mixes with the muon neutrino. This requires a branching ratio $B(\pi \to \mu + Q^0) \approx 6 \times 10^{-8}$, which has already been ruled out by the PSI limit. Still viable is a model where the heavy neutrino is produced by a smaller mixing with ν_μ and decays primarily via a larger mixing with ν_τ, such that $|\langle Q^0|\nu_\mu\rangle|\,|\langle Q^0|\nu_\tau\rangle| \approx 2 \times 10^{-6}$. Within this model, we set a limit on this product $|\langle Q^0|\nu_\mu\rangle|\,|\langle Q^0|\nu_\tau\rangle| < 1.4 \times 10^{-3}$ at 90% C.L.] NuTeV is also sensitive to $\pi \to e + Q^0$; the limit is shown in Fig. 5.

This result excludes a region of parameter space which extends as low as 4 orders of magnitude below current limits on the short lifetime solution to the KARMEN anomaly. An experiment with significantly more pion decays will be necessary to confirm or rule out the longer lifetime and lower branching ratio regions.

This research was supported by the U.S. Department of Energy and the National Science Foundation. We thank the staff of FNAL for their contributions to the construction and support of this experiment during the 1996–1997 fixed target run.

[1] B. Armbruster *et al.*, Phys. Lett. B **348**, 19 (1995).
[2] C. Oehler, Nucl. Phys. B, Proc. Suppl. **85**, 101 (2000).
[3] J. Govaerts, J. Deutsch, and P. M. Van Hove, Phys. Lett. B **389**, 700 (1996).
[4] V. Barger, R. J. N. Phillips, and S. Sarkar, Phys. Lett. B **352**, 365 (1995); Phys. Lett. B **356**, 617(E) (1995).
[5] D. Choudhury *et al.*, e-print hep-ph/9911365.
[6] M. Daum *et al.*, Phys. Lett. B **361**, 179 (1995).
[7] N. De Leener-Rosier *et al.*, Phys. Rev. D **43**, 3611 (1991).
[8] A. Vaitaitis *et al.*, Phys. Rev. Lett. **83**, 4943 (1999).
[9] D. A. Harris *et al.*, e-print hep-ex/9908056.
[10] G. Ingelman *et al.*, Comput. Phys. Commun. **101**, 108 (1997).
[11] D. Rein and L. M. Sehgal, Ann. Phys. (N.Y.) **133**, 71 (1981).
[12] T. Adams *et al.*, e-print hep-ex/9909041.
[13] CERN CN/ASD, GEANT detector description and simulation library, 1998.
[14] M. Gronau, C. N. Leung, and J. L. Rosner, Phys. Rev. D **29**, 2539 (1984).
[15] R. E. Shrock, Phys. Rev. D **24**, 1232 (1981).

Appendix B

Paper on Helicity Calculations

The following Appendix consists of the article submitted to *Physical Review, Brief Reports* on polarization effects in neutral heavy lepton decays. The article was published in Phys. Rev. **D57**, 7037 (1998).

PHYSICAL REVIEW D VOLUME 57, NUMBER 11 1 JUNE 1998

Helicity effects in neutral heavy lepton decays

Joseph A. Formaggio, Janet Conrad, Michael Shaevitz, and Artur Vaitaitis
Department of Physics, Columbia University, New York, New York 10027

Robert Drucker
University of Oregon, Eugene, Oregon 97403
(Received 25 September 1997; published 4 May 1998)

The search for the existence of neutral heavy leptons may provide valuable information regarding plausible extensions to the standard model. In order to accurately study the decay of neutral heavy leptons, it is essential to include the helicity effects which arise from their non-zero mass. In this paper, we specifically examine the effects of helicity on the leptonic and semi-leptonic decays of neutral heavy leptons. [S0556-2821(98)06211-0]

PACS number(s): 13.88.+e, 13.10.+q

INTRODUCTION

The search for the existence of neutral heavy leptons continues to be a prominent area of research in high energy physics. Neutral heavy leptons are plausible extensions to the standard model [1]. In several models, the neutral heavy leptons are heavy isosinglets that interact and decay by mixing with their lighter neutrino counterparts. Several studies have been devoted to neutral heavy leptons, and approximate lifetimes and cross sections have already been calculated [2–4]. However, the effects of polarization on the decay of the neutral heavy leptons so far have not been included in full detail [5]. This paper specifically addresses the helicity effects of neutral heavy leptons on the angular distribution of the decay products.

NEUTRAL HEAVY LEPTONS

Neutral heavy leptons (L^0) may exist as isosinglets that decay via W or Z boson exchange and mixing. Because of the non-zero mass, however, it is no longer possible to assume complete right or left handed helicities. If we take, for example, the decay $K^+ \rightarrow l^+ + L^0$, the helicity of the L^0 will vary as a function of its mass [1]. This example is illustrated in Figs. 1 and 2. A complete picture of the neutral heavy lepton decay must therefore include helicity effects.

In this paper, we address the effects of helicity on the decay of neutral heavy leptons. Specifically, we examine closely the effects of polarization on leptonic and semi-leptonic decays. The calculation provides a description of the distribution of the decay products of the neutral heavy lepton. This calculation is applicable to previous and ongoing L^0 searches in many experiments, including CCFR [6], NuTeV [7], CHARM [8], NOMAD, and CHORUS.

In particular, the NuTeV experiment is using an instrumented decay channel specifically designed to search for neutral heavy leptons. The neutral heavy leptons result via decays from pions, kaons, and charm mesons made by 800 GeV protons interacting with a beryllium target. A fraction of the neutral heavy leptons, in turn, would decay within the decay channel, which consists of 40 meters of instrumented helium bags located after 1.4 km of shielding. This decay channel allows NuTeV to be particularly sensitive to low-mass neutral heavy leptons decaying into $\mu\mu\nu$, $\mu e\nu$, $ee\nu$, $\pi\mu$, and πe. It is thus crucial that all effects due to non-zero mass, including helicity, be studied in order to correctly model and detect these exotic particles.

MATRIX ELEMENTS

The matrix element of the neutral heavy lepton decays can be derived from the appropriate set of diagrams. Let us take the simplest of the reactions, whereby the L^0 decays mixing via the W boson into two distinct charged leptons (l_i and $\bar{l}_j$) and a neutrino (ν_j). The matrix element is written as

$$M = \frac{G_F}{\sqrt{2}}[\bar{u}_{L^0}\gamma^\mu(1-\gamma^5)u_{l_i}][\bar{v}_{l_j}\gamma_\mu(1-\gamma^5)u_{\nu_j}]. \quad (1)$$

Squaring the matrix element, we find

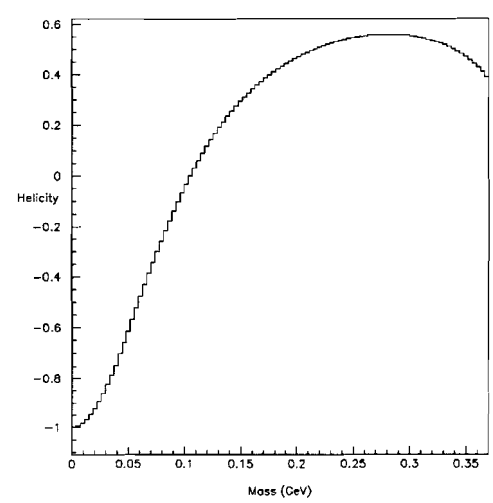

FIG. 1. Polarization of L^0 vs mass in decay $K^+ \rightarrow \mu^+ + L^0$.

 © 1998 The American Physical Society

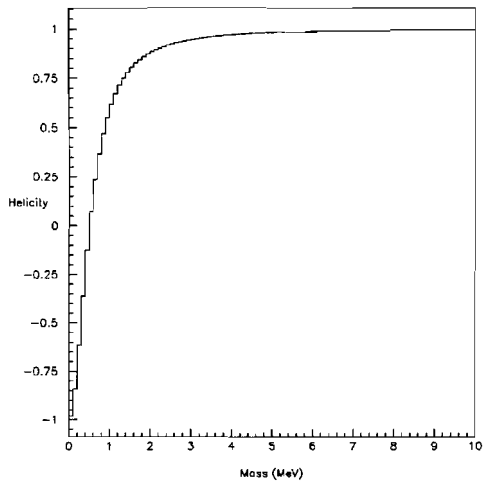

FIG. 2. Polarization of L^0 vs mass in decay $K^+ \to e^+ + L^0$.

$$|M|^2 = \frac{1}{2} G_F^2 Q_1 Q_2 \tag{2}$$

$$Q_1 = \mathrm{Tr}[u_{L^0}\bar{u}_{L^0}\gamma_\mu(1-\gamma^5)u_{l_i}\bar{u}_{l_i}\gamma_\sigma(1-\gamma^5)] \tag{3}$$

$$Q_2 = \mathrm{Tr}[v_{l_j}\bar{v}_{l_j}\gamma^\mu(1-\gamma^5)u_{\nu_j}\bar{u}_{\nu_j}\gamma^\sigma(1-\gamma^5)]. \tag{4}$$

Concentrating on the $u_{L^0}\bar{u}_{L^0}$ term in Q_1, we note that we can write this as

$$u_{L^0}\bar{u}_{L^0} = \frac{1}{2}(\not{p}_{L^0} + m_{L^0})(1+\gamma^5 \not{s}). \tag{5}$$

Here $\not{s}$ are the 4-polarizations of the neutral heavy lepton. It is possible to show that

$$u_{L^0}\bar{u}_{L^0}\gamma^\mu(1-\gamma^5) = \frac{1}{2}[(\not{p}_{L^0} - m_{L^0}\not{s})(\gamma^\mu(1-\gamma^5)) + (m_{L^0} - \not{p}_{L^0}\not{s})(\gamma^\mu(1-\gamma^5))]. \tag{6}$$

Thus we can make the simple substitution $p_{L^0} \to p_{L^0} - m_{L^0}s$ as we go from unpolarized solutions to polarized solutions, as long as the matrix element does not explicitly depend on the mass of the L^0, which for our cases it does not. In the case $L^0 \to l_i \bar{l}_j \nu_j$, our polarized matrix element is given by

$$|M_{unpol}|^2 = 2G_F^2(p_{L^0}\cdot p_{l_j})(p_{l_i}\cdot p_{\nu_j}) \tag{7}$$

$$\downarrow$$

$$|M_{pol}|^2 = 2G_F^2((p_{L^0} - m_{L^0}s)\cdot(p_{l_j}))(p_{l_i}\cdot p_{\nu_j}). \tag{8}$$

This substitution technique works in all the other cases considered in this paper.

Next we list the matrix element from $L^0 \to$ meson + lepton, with the polarization effects included:

$$|M_{unpol}|^2 = 2G_F^2 f_M^2[2(p_{L^0}\cdot p_M)(p_M\cdot p_l) - p_M^2(p_{L^0}\cdot p_l)] \tag{9}$$

$$\downarrow$$

$$|M_{pol}|^2 = 2G_F^2 f_M^2[2((p_{L^0} - m_{L^0}s)\cdot p_M)(p_M\cdot p_l) - p_M^2((p_{L^0} - m_{L^0}s)\cdot p_l)]. \tag{10}$$

Lastly, we calculate the matrix elements from $L^0 \to l^+ l^- \nu_l$. In this case, we must also consider the contribution due to Z^0 decay:

$$|M|^2 = 16G_F^2[\sigma(p_1\cdot p_{l^+})(p_{l^-}\cdot p_{\nu_l}) + \beta(p_1\cdot p_{l^-})(p_{l^+}\cdot p_{\nu_l}) - \gamma m_l^2(p_1\cdot p_{\nu_l})]. \tag{11}$$

where

$$\sigma = 8\sin\theta_w^4 \tag{12}$$

$$\beta = 2(2+\cos 2\theta_w)^2 \tag{13}$$

$$\gamma = 4(2+\cos 2\theta_w)\sin\theta_w^2 \tag{14}$$

and

$$p_1 = p_{L^0} - m_{L^0}s. \tag{15}$$

This last matrix element was calculated using HIP [9], a MATHEMATICA program designed to solve Feynman diagrams. HIP was also used as a consistency check for the other matrix elements. With polarization effects now part of our calculations, we proceed to calculate the decay rates as a function of helicity.

DECAY RATES AND DIFFERENTIAL DISTRIBUTIONS

We use the matrix elements listed above to calculate the decay rates and distribution of the decay products. We begin with the decay of $L^0 \to$ meson + lepton, working in the rest frame of the neutral heavy lepton. If we let θ be the angle between polarization vector and the lepton, then the differential decay rate becomes

$$\frac{d\Gamma}{d\cos\theta} = \frac{G_F^2 f_M^2 m_{L^0}^3 \sqrt{S}}{16\pi}\left[(1-\delta_l)^2 - \delta_M(1+\delta_l) - \frac{\sqrt{S}}{2}(1-\delta_l)\cos\theta\right]. \tag{16}$$

Here δ_M, δ_l, and S are defined as

$$\delta_M = \left(\frac{m_{Meson}}{m_{L^0}}\right)^2 \tag{17}$$

$$\delta_l = \left(\frac{m_{lepton}}{m_{L^0}}\right)^2 \tag{18}$$

$$S=1+\delta_M^2+\delta_l^2-2\delta_M-2\delta_l-2\delta_M\delta_l. \tag{19}$$

We can also calculate the differential decay width for $L^0\to l_i\bar{l}_j\nu_j$, where $i\neq j$. If we integrate over the appropriate variables, we find

$$\frac{d\Gamma}{dE_i dE_j d\cos\theta_i}=\frac{G_F^2}{128\pi^3}(m_{L^0}^2+m_j^2-m_i^2-2m_{L^0}E_j)\times(E_j+\sqrt{E_j^2-m_j^2}\cos\theta_j) \tag{20}$$

and for θ_j, we have

$$\frac{d\Gamma}{dE_i dE_j d\cos\theta_j}=\frac{G_F^2}{128\pi^3}(m_{L^0}^2+m_j^2-m_i^2-2m_{L^0}E_j)\times(E_j+\sqrt{E_j^2-m_j^2}\cos\theta_\nu\cos\theta_i) \tag{21}$$

where $\cos\theta_\nu$ is given as

$$\cos\theta_\nu=\frac{(m_{L^0}-E_i-E_j)^2-E_i^2+m_i^2-E_j^2+m_j^2}{2\sqrt{E_i^2-m_i^2}\sqrt{E_j^2-m_j^2}}. \tag{22}$$

(The i and j subscripts refer to the variables associated with the l_i and l_j leptons respectively.)

Lastly, we calculate the differential decay of $L^0\to l^+l^-\nu_l$. Letting θ_- and θ_+ be the angles of the lepton and anti-lepton respectively, we find

$$\frac{d\Gamma}{dE_+dE_-d\cos\theta_-}=\frac{G_F^2}{16\pi^3}[\sigma(E_-+p_-\cos\theta_-)+\beta(E_++p_+\cos\theta_-\cos\theta_\nu)-2\gamma m_l^2E_\nu(1+\cos\theta_\nu)] \tag{23}$$

and also

$$\frac{d\Gamma}{dE_+dE_-d\cos\theta_+}=\frac{G_F^2}{16\pi^3}[\sigma(E_-+p_-\cos\theta_+\cos\theta_\nu)+\beta(E_++p_+\cos\theta_+)-2\gamma m_l^2E_\nu(1+\cos\theta_\nu)] \tag{24}$$

where m_l is the mass of the lepton, and

$$p_\pm=\sqrt{E_\pm^2-m_l^2} \tag{25}$$

$$E_\nu=m_{L^0}-E_+-E_- \tag{26}$$

and σ, β, and γ are given by Eqs. (12)–(14).

Sample distributions for various decays and mass values are shown in Figs. 3 and 4. All distributions were created by randomly generating events with the appropriate matrix elements. Note that the $a+b\cos\theta$ behavior, as well as the mass dependence of the distributions, is clearly apparent.

As a result of the non-uniform angular distribution of the decay products of the L^0, there is also a non-negligible effect in the energy distribution. This distribution changes as a function of polarization. Figure 5 shows the energy distribution of the μ^- from the decay $L^0\to\mu^-e^+\nu_e$ for several helicities. The other decay modes show similar distributions. In addition, with the exception of decay processes where the two charged leptons are identical, there also exists an asymmetry between the charged particles that is dependent on the polarization of the neutral heavy lepton. An example of this asymmetry is shown in Fig. 6. Both the asymmetry, as well as the energy distribution of the decay products, could have significant effects in both event analysis and reconstruction of neutral heavy leptons.

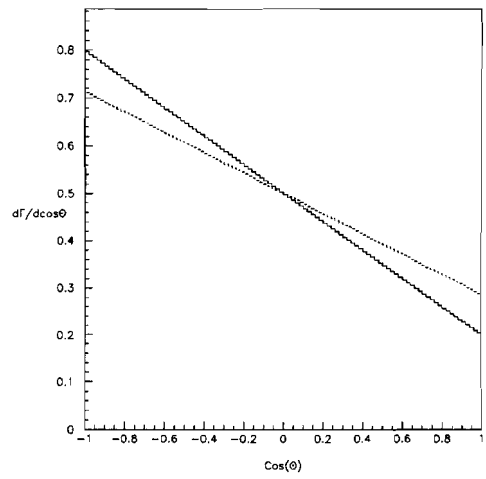

FIG. 3. Angular distribution of μ^- in fully polarized (helicity +1) decay of $L^0\to\mu^-e^+\nu_e$ for masses of 0.5 GeV (solid line) and 5 GeV (dashed line).

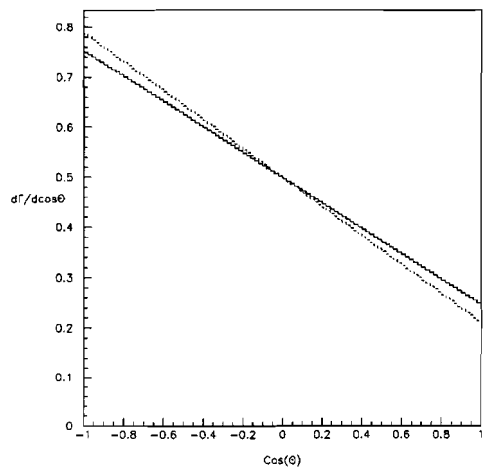

FIG. 4. Angular distribution of μ^- in fully polarized (helicity +1) decay of $L^0\to\mu^-\mu^+\nu_\mu$ for masses of 0.5 GeV (solid line) and 5 GeV (dashed line).

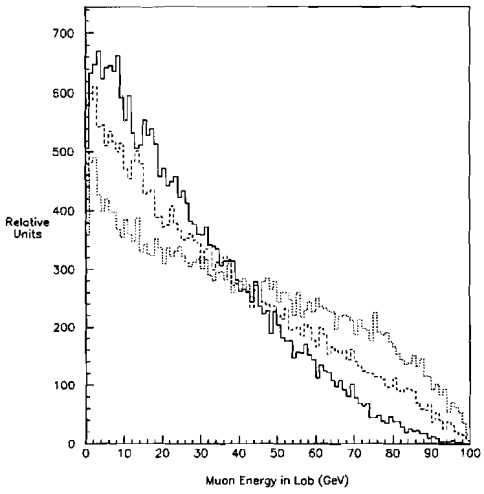

FIG. 5. Energy distribution of μ^- from $L^0 \to \mu^- e^+ \nu_e$ for helicity+1 (solid line), 0 (dashed line), and −1 (dotted line). The L^0 have a mass of 5 GeV/c^2 and energy of 100 GeV.

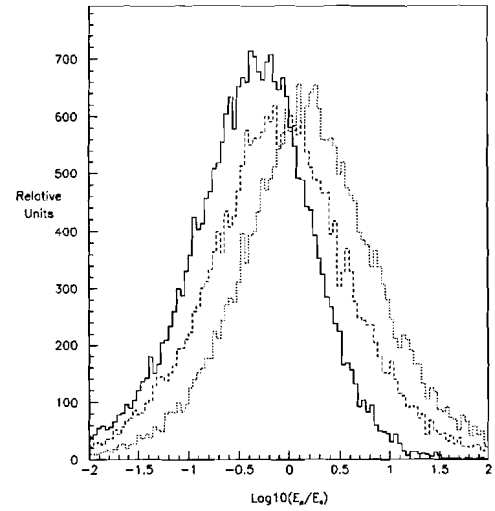

FIG. 6. Distribution for the $\log_{10}(E_{\mu^-}/E_{e^+})$ ratio in $L^0 \to \mu^- e^+ \nu_e$ decay for helicity +1 (solid line), 0 (dashed line) and −1 (dotted line). The L^0 have a mass of 5 GeV/c^2 and energy of 100 GeV.

CONCLUSION

We have calculated the helicity dependent distributions for the decay of neutral heavy leptons to mesons and/or leptons. Because of the non-zero mass of the neutral heavy leptons, polarization does affect both the angular and energy distribution of the decay products. These results are applicable to all neutral heavy lepton searches and, in particular, the ongoing NuTeV [7], NOMAD, CHORUS, and the previous CHARM [8] neutrino experiments.

[1] F. Boehm and P. Vogel, *Physics of Massive Neutrinos* (Cambridge University Press, Cambridge, England, 1992).

[2] M. Gronau, C.N. Leung, and J.L. Rosner, Phys. Rev. D **29**, 2539 (1984).

[3] R.E. Shrock, Phys. Rev. D **24**, 1232 (1981); **24**, 1275 (1981).

[4] T. Bolton, L. Johnson, and D. McKay, Phys. Rev. D **56**, 2970 (1997).

[5] L.M. Sehgal and P.M. Zerwas, Phys. Rev. D **16**, 2379 (1977).

[6] P. de Barbaro *et al.*, in *New and Exotic Phenomena '90: Proceedings*, edited by O. Fackler and J. Tran Thanh Van (Editions Frontières, Gif-sur-Yvette, France, 1990), p. 37.

[7] J. Conrad, NuTeV DET019 (1994).

[8] C. Santoni *et al.*, *Tignes 1986, Proceedings, '86 Massive Neutrinos*, edited by O. Fackler and J. Tran Thanh Van (Editions Frontières, Gif-sur-Yvette, France, 1986), pp. 229–240.

[9] A. Hsieh and E. Yehudai, SLAC PUB 5576 (1991).

```
coinc of counters: lfcbit, 6x(start, end, width) (timing from the coincidence module)

individual counters: ctr, 6x(start, end, width)
  12 | 662, 766, 104 | 794, 966, 172 |   0,   0,   0 |   0,   0,   0 |   0,   0,   0 |   0,   0,   0

Veto projection for track  1
x,y position at veto: -33.5055962  34.1560516
Projects to paddle(s):  7  8  9 10 13 14 17
Veto projection for track  2
x,y position at veto: -52.7395706 -38.6737518
Projects to paddle(s): 15 16 17 18

DID NOT have an in-time projection

*** Cal Counter information ***
ctr,tmaplo,tminlo,dvten,sbit1-6,                                    | mip range
   1      .70      .75      .78   946  1102     0     0     0     0 |      0.5-1.5
   2      .82      .87     1.07   942  1154     0     0     0     0 |      0.5-1.5
   3     1.19     1.34     1.31   942  1094     0     0     0     0 |      0.5-1.5
   4      .70      .76      .74   934  1142     0     0     0     0 |      0.5-1.5
   5      .77      .82      .80   934  1082     0     0     0     0 |      0.5-1.5
   6      .59      .59      .76   950  1098     0     0     0     0 |      0.5-1.5
   7      .58      .59      .61   946  1094     0     0     0     0 |      0.5-1.5
   8      .61      .67      .75   942  1086     0     0     0     0 |      0.5-1.5
   9     1.26     1.30     1.08   938  1130     0     0     0     0 |      0.5-1.5
  10      .86      .89      .97   938  1150     0     0     0     0 |      0.5-1.5
  11      .86      .89      .93   938  1174     0     0     0     0 |      0.5-1.5
  12      .74      .79      .80   946  1090     0     0     0     0 |      0.5-1.5
  13     7.39     7.83     7.52   930  1286     0     0     0     0 |                      >3.5
  14     2.93     3.04     3.07   934  1190     0     0     0     0 |              1.5-3.5
  15     1.74     1.95     1.73   934  1086     0     0     0     0 |              1.5-3.5
  16      .82      .83      .72   942  1114     0     0     0     0 |      0.5-1.5
  17     2.16     2.27     2.14   934  1178     0     0     0     0 |              1.5-3.5
  18      .59      .63      .60   942  1162     0     0     0     0 |      0.5-1.5
  19      .72      .79      .92   942  1162     0     0     0     0 |      0.5-1.5
  20     2.38     2.34     2.79   934  1082  1154  1310     0     0 |              1.5-3.5
  21    14.55    15.38    14.88   946  1098  1102  1274     0     0 |                      >3.5
  22     1.08     1.07      .76   938  1102     0     0     0     0 |      0.5-1.5
  23      .66      .64      .82   942  1102     0     0     0     0 |      0.5-1.5
  24     1.02      .97      .98   942  1146     0     0     0     0 |      0.5-1.5
  25      .65      .64      .43   942  1106     0     0     0     0 |      0.5-1.5
  26      .82      .71      .55   946  1154     0     0     0     0 |      0.5-1.5
  27      .81      .86      .90   942  1142     0     0     0     0 |      0.5-1.5
  28      .49      .40      .40   950  1102  2038  2042     0     0 | <0.5
  29      .82      .87      .94   942  1106     0     0     0     0 |      0.5-1.5
  30     1.76     1.89     1.81   942  1102     0     0     0     0 |              1.5-3.5
  31     1.00     1.05      .82   950  1158     0     0     0     0 |      0.5-1.5
  32     1.72     1.83     1.26   934  1150     0     0     0     0 |              1.5-3.5
  33     3.99     4.28     4.06   926  1078     0     0     0     0 |                      >3.5
  34     5.17     5.22     5.10   938  1086     0     0     0     0 |                      >3.5
  35      .99      .76      .96   946  1090  2022  2042     0     0 |      0.5-1.5
  36     1.51     1.63     1.66   942  1178     0     0     0     0 |              1.5-3.5
  37     2.74     2.85     2.88   934  1210     0     0     0     0 |              1.5-3.5
  38     1.06     1.08     1.13   934  1150     0     0     0     0 |      0.5-1.5
  39     1.02     1.09      .90   942  1154     0     0     0     0 |      0.5-1.5
  40     -.12     -.12      .00     0     0     0     0     0     0 | <0.5
  41     1.06     1.09     1.28   954  1106     0     0     0     0 |      0.5-1.5
  42     1.35     1.42     1.55   942  1158     0     0     0     0 |      0.5-1.5
  43      .67      .71      .73   946  1146     0     0     0     0 |      0.5-1.5
  44     1.43     1.50     1.63   942  1182     0     0     0     0 |      0.5-1.5
  45     2.52     2.58     2.77   938  1086     0     0     0     0 |              1.5-3.5
  46     1.09     1.13     1.26   942  1162     0     0     0     0 |      0.5-1.5
  47      .83      .88      .81   946  1098     0     0     0     0 |      0.5-1.5
  48      .89      .90      .92   950  1154     0     0     0     0 |      0.5-1.5
  49     1.06     1.09      .95   942  1090     0     0     0     0 |      0.5-1.5
  50      .06      .07     -.03     0     0     0     0     0     0 | <0.5
  51      .49      .46      .67   950  1098     0     0     0     0 | <0.5
  52      .93      .96     1.14   942  1086     0     0     0     0 |      0.5-1.5
  53     1.23     1.24      .94   938  1086     0     0     0     0 |      0.5-1.5
  54     1.81     1.76     1.57   938  1086     0     0     0     0 |              1.5-3.5
  55      .57      .59      .69   938  1146     0     0     0     0 |      0.5-1.5
  56      .64      .64      .94   942  1090     0     0     0     0 |      0.5-1.5
  57      .65      .62      .88   942  1090     0     0     0     0 |      0.5-1.5
  58      .92      .96      .99   942  1114     0     0     0     0 |      0.5-1.5
  59     2.49     2.55     2.41   938  1094     0     0     0     0 |              1.5-3.5
  60     2.16     2.18     2.01   934  1186     0     0     0     0 |              1.5-3.5
  61     3.81     3.93     3.81   930  1082     0     0     0     0 |                      >3.5
  62      .77      .79      .72   946  1094     0     0     0     0 |      0.5-1.5
  63      .58      .60      .64   946  1130     0     0     0     0 |      0.5-1.5
  64      .75      .76      .74   942  1094     0     0     0     0 |      0.5-1.5
  65     1.08     1.08     1.19   942  1094     0     0     0     0 |      0.5-1.5
  66     1.01     1.03     1.04   942  1090     0     0     0     0 |      0.5-1.5
  67      .60      .60      .68   946  1094     0     0     0     0 |      0.5-1.5
  68     1.36     1.39     1.78   938  1086  1170  1330     0     0 |      0.5-1.5
```

```
 69    1.74    1.80    1.97   938  1090    0    0    0    0 |              1.5-3.5
 70    1.96    2.02    2.31   934  1090    0    0    0    0 |              1.5-3.5
 71    3.26    3.22    3.57   934  1090    0    0    0    0 |              1.5-3.5
 72    1.75    1.74    2.06   938  1090    0    0    0    0 |              1.5-3.5
 73    2.04    2.11    2.19   938  1070    0    0    0    0 |              1.5-3.5
 74    2.67    2.70    2.65   930  1070    0    0    0    0 |              1.5-3.5
 75    2.68    2.72    2.83   934  1178    0    0    0    0 |              1.5-3.5
 76    1.17    1.21    1.34   934  1022 1026 1190    0    0 |     0.5-1.5
 77    3.35    3.66    3.30   934  1230    0    0    0    0 |              1.5-3.5
 78    3.01    2.90    3.10   934  1198    0    0    0    0 |              1.5-3.5
 79    1.54    1.56    1.62   930  1074    0    0    0    0 |              1.5-3.5
 80    1.95    1.96    2.07   938  1086    0    0    0    0 |              1.5-3.5
 81    1.49    1.49    1.55   942  1106    0    0    0    0 |     0.5-1.5
 82    1.19    1.25    1.51   942  1110    0    0    0    0 |     0.5-1.5
 83    1.82    1.77    1.94   942  1090    0    0    0    0 |              1.5-3.5
 84    1.86    1.97    1.89   938  1158    0    0    0    0 |              1.5-3.5

*** Chamber information ***
Cal ch, pl, nhit, 8 x (cell, tim*sns/wid)
 1 1 1 |12, -1068/ 84 | 0,     0/  0 | 0,     0/  0 | 0,     0/  0 | 0,     0/  0 | 0,     0/  0
 1 2 1 | 6, -1176/ 60 | 0,     0/  0 | 0,     0/  0 | 0,     0/  0 | 0,     0/  0 | 0,     0/  0
 2 1 1 |11,  1096/ 52 | 0,     0/  0 | 0,     0/  0 | 0,     0/  0 | 0,     0/  0 | 0,     0/  0
 2 2 2 | 6,  -616/ 68 | 6,  -720/ 16 | 0,     0/  0 | 0,     0/  0 | 0,     0/  0 | 0,     0/  0
 3 1 1 |11,  1648/ 48 | 0,     0/  0 | 0,     0/  0 | 0,     0/  0 | 0,     0/  0 | 0,     0/  0
 3 2 3 | 6,  -968/ 64 |19,  1996/ 48 |20, -2016/ 28 | 0,     0/  0 | 0,     0/  0 | 0,     0/  0
 4 1 1 |12, -1456/ 68 | 0,     0/  0 | 0,     0/  0 | 0,     0/  0 | 0,     0/  0 | 0,     0/  0
 4 2 1 | 6,  1088/ 60 | 0,     0/  0 | 0,     0/  0 | 0,     0/  0 | 0,     0/  0 | 0,     0/  0
 5 1 1 |11,  1328/ 68 | 0,     0/  0 | 0,     0/  0 | 0,     0/  0 | 0,     0/  0 | 0,     0/  0
 5 2 1 | 6,  -848/ 60 | 0,     0/  0 | 0,     0/  0 | 0,     0/  0 | 0,     0/  0 | 0,     0/  0
 6 1 1 |12, -1200/ 48 | 0,     0/  0 | 0,     0/  0 | 0,     0/  0 | 0,     0/  0 | 0,     0/  0
 6 2 1 | 6,   932/ 56 | 0,     0/  0 | 0,     0/  0 | 0,     0/  0 | 0,     0/  0 | 0,     0/  0
 7 1 3 |10,  1656/ 76 |11, -1652/ 76 |11,  1028/ 56 | 0,     0/  0 | 0,     0/  0 | 0,     0/  0
 7 2 1 | 6,  1424/ 76 | 0,     0/  0 | 0,     0/  0 | 0,     0/  0 | 0,     0/  0 | 0,     0/  0
 8 1 1 |12, -1352/ 80 | 0,     0/  0 | 0,     0/  0 | 0,     0/  0 | 0,     0/  0 | 0,     0/  0
 8 2 1 | 6,   980/ 64 | 0,     0/  0 | 0,     0/  0 | 0,     0/  0 | 0,     0/  0 | 0,     0/  0
 9 1 1 |12, -1264/ 68 | 0,     0/  0 | 0,     0/  0 | 0,     0/  0 | 0,     0/  0 | 0,     0/  0
 9 2 1 | 7, -1440/ 80 | 0,     0/  0 | 0,     0/  0 | 0,     0/  0 | 0,     0/  0 | 0,     0/  0
10 1 1 |11,  1232/ 64 | 0,     0/  0 | 0,     0/  0 | 0,     0/  0 | 0,     0/  0 | 0,     0/  0
10 2 1 | 6,  1068/ 60 | 0,     0/  0 | 0,     0/  0 | 0,     0/  0 | 0,     0/  0 | 0,     0/  0
11 1 4 |12,  -724/ 96 |12,  -864/112 |12, -1072/ 72 |12, -1316/ 84 | 0,     0/  0 | 0,     0/  0
11 2 3 | 7,   868/152 | 7,  1052/ 12 | 7, -1216/320 | 0,     0/  0 | 0,     0/  0 | 0,     0/  0
12 1 1 |11,   696/ 80 | 0,     0/  0 | 0,     0/  0 | 0,     0/  0 | 0,     0/  0 | 0,     0/  0
13 1 1 |11,  1024/ 64 | 0,     0/  0 | 0,     0/  0 | 0,     0/  0 | 0,     0/  0 | 0,     0/  0
13 2 1 | 7,  -712/ 72 | 0,     0/  0 | 0,     0/  0 | 0,     0/  0 | 0,     0/  0 | 0,     0/  0
14 2 1 | 7,  -928/ 68 | 0,     0/  0 | 0,     0/  0 | 0,     0/  0 | 0,     0/  0 | 0,     0/  0
15 1 1 |11,  1064/ 56 | 0,     0/  0 | 0,     0/  0 | 0,     0/  0 | 0,     0/  0 | 0,     0/  0
15 2 1 | 7, -1208/ 64 | 0,     0/  0 | 0,     0/  0 | 0,     0/  0 | 0,     0/  0 | 0,     0/  0
16 1 1 |12, -1412/ 64 | 0,     0/  0 | 0,     0/  0 | 0,     0/  0 | 0,     0/  0 | 0,     0/  0
16 2 1 | 7,  -424/148 | 0,     0/  0 | 0,     0/  0 | 0,     0/  0 | 0,     0/  0 | 0,     0/  0
17 1 2 |11,  -444/ 40 |11,  -536/ 12 | 0,     0/  0 | 0,     0/  0 | 0,     0/  0 | 0,     0/  0
17 2 1 | 7,   836/ 56 | 0,     0/  0 | 0,     0/  0 | 0,     0/  0 | 0,     0/  0 | 0,     0/  0
18 1 3 |11,   672/208 |11,   904/ 96 |12, -1524/ 60 | 0,     0/  0 | 0,     0/  0 | 0,     0/  0
18 2 7     -> too many hits to print
19 1 1 |11,   972/ 76 | 0,     0/  0 | 0,     0/  0 | 0,     0/  0 | 0,     0/  0 | 0,     0/  0
19 2 2 | 7,  1364/ 76 | 7,  1536/ 56 | 0,     0/  0 | 0,     0/  0 | 0,     0/  0 | 0,     0/  0
21 1 1 |11,   852/ 56 | 0,     0/  0 | 0,     0/  0 | 0,     0/  0 | 0,     0/  0 | 0,     0/  0
21 2 1 | 7,  1348/ 76 | 0,     0/  0 | 0,     0/  0 | 0,     0/  0 | 0,     0/  0 | 0,     0/  0
22 1 2 |11,  -384/ 76 |11,  -512/  8 | 0,     0/  0 | 0,     0/  0 | 0,     0/  0 | 0,     0/  0
22 2 1 | 8, -1100/ 76 | 0,     0/  0 | 0,     0/  0 | 0,     0/  0 | 0,     0/  0 | 0,     0/  0
23 1 1 |11,   540/ 64 | 0,     0/  0 | 0,     0/  0 | 0,     0/  0 | 0,     0/  0 | 0,     0/  0
23 2 4 | 7,  1456/ 56 | 8,  -836/128 | 8, -1124/ 56 | 8, -1376/ 44 | 0,     0/  0 | 0,     0/  0
24 1 1 |11,   652/ 60 | 0,     0/  0 | 0,     0/  0 | 0,     0/  0 | 0,     0/  0 | 0,     0/  0
24 2 1 | 8,  -456/ 96 | 0,     0/  0 | 0,     0/  0 | 0,     0/  0 | 0,     0/  0 | 0,     0/  0
25 1 1 |11,  -720/120 | 0,     0/  0 | 0,     0/  0 | 0,     0/  0 | 0,     0/  0 | 0,     0/  0
25 2 2 | 7,   768/ 48 | 8, -1436/ 56 | 0,     0/  0 | 0,     0/  0 | 0,     0/  0 | 0,     0/  0
26 1 1 |11,   656/ 60 | 0,     0/  0 | 0,     0/  0 | 0,     0/  0 | 0,     0/  0 | 0,     0/  0
26 2 2 | 8,  -376/  8 | 8,  -392/ 60 | 0,     0/  0 | 0,     0/  0 | 0,     0/  0 | 0,     0/  0
27 1 1 |11, -1344/ 56 | 0,     0/  0 | 0,     0/  0 | 0,     0/  0 | 0,     0/  0 | 0,     0/  0
27 2 1 | 8,  -376/ 76 | 0,     0/  0 | 0,     0/  0 | 0,     0/  0 | 0,     0/  0 | 0,     0/  0
28 1 1 |11,  -604/ 64 | 0,     0/  0 | 0,     0/  0 | 0,     0/  0 | 0,     0/  0 | 0,     0/  0
28 2 1 | 8,  -456/ 84 | 0,     0/  0 | 0,     0/  0 | 0,     0/  0 | 0,     0/  0 | 0,     0/  0
29 1 1 |11,  -904/ 56 | 0,     0/  0 | 0,     0/  0 | 0,     0/  0 | 0,     0/  0 | 0,     0/  0
29 2 1 | 8,  1200/ 64 | 0,     0/  0 | 0,     0/  0 | 0,     0/  0 | 0,     0/  0 | 0,     0/  0
30 1 1 |11,  -860/ 96 | 0,     0/  0 | 0,     0/  0 | 0,     0/  0 | 0,     0/  0 | 0,     0/  0
30 2 2 | 8,   356/112 | 8,  -420/ 28 | 0,     0/  0 | 0,     0/  0 | 0,     0/  0 | 0,     0/  0
31 2 5 | 5,  1392/ 68 | 8,   644/ 96 | 8,  1172/ 68 | 8,  1448/ 36 | 9, -1172/144 | 0,     0/  0
32 1 1 |10,  1412/ 80 | 0,     0/  0 | 0,     0/  0 | 0,     0/  0 | 0,     0/  0 | 0,     0/  0
32 2 1 | 9, -1220/ 56 | 0,     0/  0 | 0,     0/  0 | 0,     0/  0 | 0,     0/  0 | 0,     0/  0
34 1 1 |11,  -948/ 60 | 0,     0/  0 | 0,     0/  0 | 0,     0/  0 | 0,     0/  0 | 0,     0/  0
34 2 1 | 9, -1092/ 64 | 0,     0/  0 | 0,     0/  0 | 0,     0/  0 | 0,     0/  0 | 0,     0/  0
35 1 2 |10,  1172/ 64 |12,   504/128 | 0,     0/  0 | 0,     0/  0 | 0,     0/  0 | 0,     0/  0
35 2 2 | 8,  1408/ 64 |15,  1264/ 44 | 0,     0/  0 | 0,     0/  0 | 0,     0/  0 | 0,     0/  0
36 1 6 |12,   788/ 68 |12,  1112/ 60 |12,  1184/ 88 |13,  -936/ 28 |13, -1024/ 80 |13, -1336/ 20
36 2 2 | 9,   456/ 68 |17, -1128/ 72 | 0,     0/  0 | 0,     0/  0 | 0,     0/  0 | 0,     0/  0
```

```
 37 1 2 |10,   616/ 56 |12,  -420/ 68 | 0,     0/  0 | 0,     0/  0 | 0,     0/  0 | 0,     0/  0
 37 2 2 |17,  -304/ 44 |17,  -372/ 36 | 0,     0/  0 | 0,     0/  0 | 0,     0/  0 | 0,     0/  0
 38 1 2 |11, -1136/ 80 |12,  1280/ 56 | 0,     0/  0 | 0,     0/  0 | 0,     0/  0 | 0,     0/  0
 38 2 2 | 9,  -380/ 76 |17,  -736/ 64 | 0,     0/  0 | 0,     0/  0 | 0,     0/  0 | 0,     0/  0
 39 1 2 |10,  1256/136 |12,   736/ 60 | 0,     0/  0 | 0,     0/  0 | 0,     0/  0 | 0,     0/  0
 39 2 3 | 9,  1108/ 60 |17,   504/128 |17,   968/ 48 | 0,     0/  0 | 0,     0/  0 | 0,     0/  0
 40 1 2 |10,   468/ 60 |12,  -568/ 68 | 0,     0/  0 | 0,     0/  0 | 0,     0/  0 | 0,     0/  0
 40 2 2 | 9,  -252/164 |17, -1124/ 52 | 0,     0/  0 | 0,     0/  0 | 0,     0/  0 | 0,     0/  0
 42 1 2 |10,  -424/ 76 |12,  -940/ 84 | 0,     0/  0 | 0,     0/  0 | 0,     0/  0 | 0,     0/  0
 42 2 3 |10,  -532/212 |10, -1144/ 56 |17,  -748/ 72 | 0,     0/  0 | 0,     0/  0 | 0,     0/  0
 Tor ch, pl, nhit, 8 x (cell, tim/wid)
 44 1 1 |13,  1060/ 60 | 0,     0/  0 | 0,     0/  0 | 0,     0/  0 | 0,     0/  0 | 0,     0/  0
 44 2 1 | 5,  1456/ 64 | 0,     0/  0 | 0,     0/  0 | 0,     0/  0 | 0,     0/  0 | 0,     0/  0
 46 1 1 |12,  1000/ 56 | 0,     0/  0 | 0,     0/  0 | 0,     0/  0 | 0,     0/  0 | 0,     0/  0
 46 2 1 | 5,   832/ 56 | 0,     0/  0 | 0,     0/  0 | 0,     0/  0 | 0,     0/  0 | 0,     0/  0
 47 1 1 |12,  1492/ 52 | 0,     0/  0 | 0,     0/  0 | 0,     0/  0 | 0,     0/  0 | 0,     0/  0
 47 2 1 | 5,   708/ 76 | 0,     0/  0 | 0,     0/  0 | 0,     0/  0 | 0,     0/  0 | 0,     0/  0
 48 1 1 |12,   556/ 76 | 0,     0/  0 | 0,     0/  0 | 0,     0/  0 | 0,     0/  0 | 0,     0/  0
 48 2 1 | 5,  1192/ 32 | 0,     0/  0 | 0,     0/  0 | 0,     0/  0 | 0,     0/  0 | 0,     0/  0
 49 1 1 |12,   740/ 68 | 0,     0/  0 | 0,     0/  0 | 0,     0/  0 | 0,     0/  0 | 0,     0/  0
 49 2 1 | 5,  1388/ 72 | 0,     0/  0 | 0,     0/  0 | 0,     0/  0 | 0,     0/  0 | 0,     0/  0
 50 1 1 |12,   944/ 56 | 0,     0/  0 | 0,     0/  0 | 0,     0/  0 | 0,     0/  0 | 0,     0/  0
 50 2 1 | 5,   516/ 64 | 0,     0/  0 | 0,     0/  0 | 0,     0/  0 | 0,     0/  0 | 0,     0/  0
 51 1 1 |12,  1004/ 52 | 0,     0/  0 | 0,     0/  0 | 0,     0/  0 | 0,     0/  0 | 0,     0/  0
 51 2 1 | 5,  1328/ 72 | 0,     0/  0 | 0,     0/  0 | 0,     0/  0 | 0,     0/  0 | 0,     0/  0
 52 1 1 |12,   456/ 84 | 0,     0/  0 | 0,     0/  0 | 0,     0/  0 | 0,     0/  0 | 0,     0/  0
 52 2 1 | 5,   736/ 56 | 0,     0/  0 | 0,     0/  0 | 0,     0/  0 | 0,     0/  0 | 0,     0/  0
 54 1 1 |13,  1524/ 52 | 0,     0/  0 | 0,     0/  0 | 0,     0/  0 | 0,     0/  0 | 0,     0/  0
 54 2 1 | 6,  1336/ 72 | 0,     0/  0 | 0,     0/  0 | 0,     0/  0 | 0,     0/  0 | 0,     0/  0
 55 1 1 |12,   868/ 64 | 0,     0/  0 | 0,     0/  0 | 0,     0/  0 | 0,     0/  0 | 0,     0/  0
 55 2 1 | 5,   868/ 68 | 0,     0/  0 | 0,     0/  0 | 0,     0/  0 | 0,     0/  0 | 0,     0/  0
 56 1 1 |13,  1436/ 52 | 0,     0/  0 | 0,     0/  0 | 0,     0/  0 | 0,     0/  0 | 0,     0/  0
 56 2 1 | 6,   964/ 68 | 0,     0/  0 | 0,     0/  0 | 0,     0/  0 | 0,     0/  0 | 0,     0/  0
 57 1 1 |12,  1288/ 48 | 0,     0/  0 | 0,     0/  0 | 0,     0/  0 | 0,     0/  0 | 0,     0/  0
 57 2 1 | 6,  1480/ 40 | 0,     0/  0 | 0,     0/  0 | 0,     0/  0 | 0,     0/  0 | 0,     0/  0
 59 1 1 |13,   664/ 64 | 0,     0/  0 | 0,     0/  0 | 0,     0/  0 | 0,     0/  0 | 0,     0/  0
 59 2 1 | 6,   576/ 52 | 0,     0/  0 | 0,     0/  0 | 0,     0/  0 | 0,     0/  0 | 0,     0/  0
 60 1 1 |13,  1480/ 56 | 0,     0/  0 | 0,     0/  0 | 0,     0/  0 | 0,     0/  0 | 0,     0/  0
 60 2 1 | 6,  1096/ 72 | 0,     0/  0 | 0,     0/  0 | 0,     0/  0 | 0,     0/  0 | 0,     0/  0
 61 1 1 |14,   588/ 60 | 0,     0/  0 | 0,     0/  0 | 0,     0/  0 | 0,     0/  0 | 0,     0/  0
 61 2 1 | 6,   476/ 52 | 0,     0/  0 | 0,     0/  0 | 0,     0/  0 | 0,     0/  0 | 0,     0/  0
 62 1 1 |14,  1320/ 60 | 0,     0/  0 | 0,     0/  0 | 0,     0/  0 | 0,     0/  0 | 0,     0/  0
 62 2 1 | 6,  1392/ 68 | 0,     0/  0 | 0,     0/  0 | 0,     0/  0 | 0,     0/  0 | 0,     0/  0
 64 1 2 |11,  1548/108 |14,  1012/ 52 | 0,     0/  0 | 0,     0/  0 | 0,     0/  0 | 0,     0/  0
 64 2 1 | 6,  1224/ 28 | 0,     0/  0 | 0,     0/  0 | 0,     0/  0 | 0,     0/  0 | 0,     0/  0
 65 1 2 | 1,  1996/ 40 |15,  1428/ 60 | 0,     0/  0 | 0,     0/  0 | 0,     0/  0 | 0,     0/  0
 65 2 2 | 7,   472/ 76 |10,  1740/ 40 | 0,     0/  0 | 0,     0/  0 | 0,     0/  0 | 0,     0/  0
 67 1 2 | 3,  1652/ 76 |15,   796/ 60 | 0,     0/  0 | 0,     0/  0 | 0,     0/  0 | 0,     0/  0
 67 2 1 | 7,  1020/ 80 | 0,     0/  0 | 0,     0/  0 | 0,     0/  0 | 0,     0/  0 | 0,     0/  0
 69 1 1 |15,  1064/ 48 | 0,     0/  0 | 0,     0/  0 | 0,     0/  0 | 0,     0/  0 | 0,     0/  0
 69 2 1 | 7,   620/ 68 | 0,     0/  0 | 0,     0/  0 | 0,     0/  0 | 0,     0/  0 | 0,     0/  0
 DK ch, pl, nhit, 8 x (cell, tim/wid), sns not shown
 80 1 2 |10,  1284/168 |11,   224/ 72 | 0,     0/  0 | 0,     0/  0 | 0,     0/  0 | 0,     0/  0
 80 2 2 |10,   288/424 |15,   520/ 92 | 0,     0/  0 | 0,     0/  0 | 0,     0/  0 | 0,     0/  0
 81 1 2 |10,   612/ 64 |11,   340/ 64 | 0,     0/  0 | 0,     0/  0 | 0,     0/  0 | 0,     0/  0
 81 2 2 |11,   524/ 76 |16,   892/ 52 | 0,     0/  0 | 0,     0/  0 | 0,     0/  0 | 0,     0/  0
 82 1 2 |10,   268/100 |11,   244/100 | 0,     0/  0 | 0,     0/  0 | 0,     0/  0 | 0,     0/  0
 82 2 2 |11,   360/ 48 |15,   480/ 72 | 0,     0/  0 | 0,     0/  0 | 0,     0/  0 | 0,     0/  0

*****************************************************************************************************

 RUN6133:   TOROID FOCUSING MU-.

 WE HAVE AN EVENT! Number: 6133 3846
  The mode was: 1 --> mumu
  ************************************************
  * Passed all standard closed-box analysis cuts *
  ************************************************

npart,nx_extra,ny_extra:     2    0    0
vertex(x,y,z):      18.311   -15.245 -2041.164
error (x,y,z):        .037      .120     7.221
vert_chi2 =       .17E+03 for   17 dof

 Info on each vertex track
 itrk,p(1-5),pid#,flags(trk,pid,e),nx,ny,chi2(x,y)
  1     .134   -1.518   92.029   92.042   92.042  1  0  0  0  6  6    1.845    2.806
  2    -.099     .064    5.844    5.846    5.845  1  0  0  0  6  6    5.149    4.478

 cal_pos +/- ecal_pos (x,y,z)
  1    20.332      .022   -37.332      .022  -701.010      .000
  2   -11.628      .116    -6.771      .114  -701.010      .000

  Effective variables
```

```
eff_mass,q2,x,y,w:     .8851       2.501       .1906       .7061E-01   3.391
eff_p(1-5):       .035   -1.455   97.873   97.888   97.884

  Full variables
full_mass,q2,x,y,w:     17.90       316.6       1.741       .9837       .8851
full_p(1-5):       .000      .000   97.873   99.496   97.873
missing_pt,phi_misspt:     1.415       1.595
trans_mass:     3.084


  *****  6133 3846 ******
  upstream in cal: slope, incept, sigma
    view 1      .0004   20.5990     .0251 pos42=  20.3106
    view 1     -.0139  -21.2561     .0530 pos42= -11.5368
    view 2     -.0175  -49.5940     .0041 pos42= -37.3016
    view 2      .0041   -3.9053     .1817 pos42=  -6.7951

mutot,emu(1-mutot):   2    92.0     5.8

  tracks from decay channel:

     Explanation of t0 fit
     intime tracks have t0 w/i +/- 12
     t0=.0000 => all hits are on the same side.
                 In this case you cannot fit for a t0
                 because variations give you a shift
                 rather than a poor fit.  For lack of
                 any way to check, we assume t0 is ok.
  view 1: ntracks= 2
  seg     1: slp, int, t0, sig, nhit, pos      .0015    21.3960    -1.8162      .0180     6   20.3179
  seg     2: slp, int, t0, sig, nhit, pos     -.0246   -29.4225    -2.4512      .0928     6  -12.2055
  view 2: ntracks= 2
  seg     1: slp, int, t0, sig, nhit, pos     -.0164   -48.8447     2.1229      .0234     6  -37.3182
  seg     2: slp, int, t0, sig, nhit, pos      .0057    -1.8887      .5692      .1097     6   -5.9128

   trk     1 Hits:  2 -3 -3 -2  3  0  0  0 -2 Hituv:  -3
       hit pos:    20.17   20.03   19.95   19.31   18.75 9999.90 9999.90 9999.90   18.38    1.66
   trk     2 Hits:  1  2 -2 -1 -2  0  0  0 -1 Hituv:   1
       hit pos:    -8.79   -7.20   -5.89    3.59   13.07 9999.90 9999.90 9999.90   -7.78     .34

   trk     1 Hits:  2 -2 -2 -2 -3  0  0  0 -3 Hituv:  -2
       hit pos:   -35.42  -34.27  -33.39  -26.75  -20.43 9999.90 9999.90 9999.90  -35.34     .92
   trk     2 Hits:  1  1 -1  1  2  0  0  0  1 Hituv:  -1
       hit pos:    -7.20   -7.42   -7.70   -9.59  -11.81 9999.90 9999.90 9999.90   -7.01    -.36

 Energy estimates for tracks
ixy,itrk,dkp(ixy,itrk):     1   1   92.
ixy,itrk,dkp(ixy,itrk):     1   2   5.8
ixy,itrk,dkp(ixy,itrk):     2   1   92.
ixy,itrk,dkp(ixy,itrk):     2   2   5.8

 dkvertex.com information
Found     2 linked x/y pairs
match_views =     2
ilnk_trk,dkl_x,dkl_y:     1   1   1
ilnk_trk,dkl_x,dkl_y:     2   2   2
vert_lnk array:
   1   2
dclap=     2.865
(xclap,yclap,zclap):    18.292 -15.658 -2018.3
(xclap,yclap,zclap):    20.148 -13.476 -2018.3
xvert,yvert,zvert,vert_qual:
  18.311 -15.245 -2041.2   2.865

 Msfit results
View:  1
Track:     1
ityp     zfit      xfit                 sxfit              chisq/ndf      ptrk
  1     -701.0    20.332+/-    .022    .00157+/-  .00010     1.8    /  4   92.04
  2    -2041.2    18.257+/-    .037    .00154+/-  .00006     1.8    /  4   92.04
  3     -878.7    20.053+/-    .012    .00157+/-  .00008     1.8    /  4   92.04
Track:     2
ityp     zfit      xfit                 sxfit              chisq/ndf      ptrk
  1     -701.0   -11.628+/-    .116   -.02371+/-  .00087     5.1    /  4    5.85
  2    -2041.2    20.709+/-    .240   -.02456+/-  .00076     5.1    /  4    5.85
  3     -878.7    -7.414+/-    .015   -.02386+/-  .00047     5.3    /  4    5.85
View:  2
Track:     1
ityp     zfit      xfit                 sxfit              chisq/ndf      ptrk
  1     -701.0   -37.332+/-    .022   -.01648+/-  .00010     2.8    /  4   92.04
  2    -2041.2   -15.282+/-    .037   -.01644+/-  .00006     2.8    /  4   92.04
  3     -877.2   -34.428+/-    .012   -.01648+/-  .00008     2.8    /  4   92.04
Track:     2
ityp     zfit      xfit                 sxfit              chisq/ndf      ptrk
```

```
 1     -701.0    -6.771+/-    .114    .00354+/-  .00087     4.5    /  4    5.85
 2    -2041.2   -13.606+/-    .241    .00574+/-  .00076     4.5    /  4    5.85
 3     -877.2    -7.396+/-    .015    .00382+/-  .00047     4.9    /  4    5.85

 vert_fit_dk results
chifit_vert/ndf =    166.2    /  17
x0,y0,z0:  18.311+/-   .037-15.245+/-   .120-2041.2+/-    7.2
 ivtrk,itrkx,itrky,sx +/- dsx,sy +/- dsy
   1   1   1   .0015+/-   .0001  -.0165+/-   .0001
   2   2   2  -.0169+/-   .0004   .0109+/-   .0006


 Veto wall info:
 in time is between 225 and 295
 noisy counters have width lt 10

 coinc of counters: lfcbit, 6x(start, end, width) (timing from the coincidence module)

 individual counters: ctr, 6x(start, end, width)
   10 | 262, 366, 104 |   0,   0,   0 |   0,   0,   0 |   0,   0,   0 |   0,   0,   0 |   0,   0,   0

 Veto projection for track  1
 x,y position at veto:  17.6882057 -9.20188236
 Projects to paddle(s):  9 10 11 12
 Veto projection for track  2
 x,y position at veto:  29.7915249 -15.728797
 Projects to paddle(s):  3  4  5  6  9 10 11 12

 POINTED TO A VETO THAT FIRED INTIME=> 10

 *** Cal Counter information ***
 ctr,tmaplo,tminlo,dvten,sbit1-6,                                          | mip range
    1      .91     1.21      .98   938  1094     0     0     0     0 |      0.5-1.5
    2      .73      .82      .76   950  1106     0     0     0     0 |      0.5-1.5
    3     1.63     2.06     1.57   938  1090     0     0     0     0 |                  1.5-3.5
    4      .93     1.17     1.02   938  1086     0     0     0     0 |      0.5-1.5
    5     1.40     1.60     1.54   942  1094     0     0     0     0 |      0.5-1.5
    6     1.14     1.40     1.11   946  1094     0     0     0     0 |      0.5-1.5
    7      .75      .89      .80   946  1134     0     0     0     0 |      0.5-1.5
    8      .78     1.03      .94   938  1082     0     0     0     0 |      0.5-1.5
    9      .85     1.04      .86   938  1138     0     0     0     0 |      0.5-1.5
   10     1.14     1.43     1.10   938  1138     0     0     0     0 |      0.5-1.5
   11      .68      .74      .82   938  1106     0     0     0     0 |      0.5-1.5
   12     1.36     1.88     1.56   938  1106     0     0     0     0 |      0.5-1.5
   13      .69      .95      .81   942  1174     0     0     0     0 |      0.5-1.5
   14      .76      .83      .78   950  1150     0     0     0     0 |      0.5-1.5
   15      .81     1.03      .81   942  1094     0     0     0     0 |      0.5-1.5
   16     1.33     1.51     1.19   938  1146     0     0     0     0 |      0.5-1.5
   17      .69      .82      .74   946  1098     0     0     0     0 |      0.5-1.5
   18      .34      .43      .45   950  1150     0     0     0     0 | <0.5
   19     1.56     2.00     1.47   942  1170     0     0     0     0 |                  1.5-3.5
   20      .49      .50      .83   942  1166     0     0     0     0 | <0.5
   21      .87      .94      .94   958  1110     0     0     0     0 |      0.5-1.5
   22      .65      .75      .71   946  1170     0     0     0     0 |      0.5-1.5
   23      .85      .93      .73   958  1142     0     0     0     0 |      0.5-1.5
   24      .95     1.03      .83   954  1158     0     0     0     0 |      0.5-1.5
   25      .56      .56      .61   954  1118     0     0     0     0 |      0.5-1.5
   26     1.04      .94     1.03   942  1162     0     0     0     0 |      0.5-1.5
   27      .81     1.00      .87   946  1166     0     0     0     0 |      0.5-1.5
   28     1.22     1.05     1.30   938  1174     0     0     0     0 |      0.5-1.5
   29      .96     1.15     1.07   942  1106     0     0     0     0 |      0.5-1.5
   30     1.26     1.35     1.31   946  1110     0     0     0     0 |      0.5-1.5
   31     1.02     1.18      .90   950  1094     0     0     0     0 |      0.5-1.5
   32     1.44     1.49     1.18   942  1158     0     0     0     0 |      0.5-1.5
   33     1.00     1.28      .87   942  1162     0     0     0     0 |      0.5-1.5
   34     1.19     1.39     1.13   946  1174     0     0     0     0 |      0.5-1.5
   35     1.72      .73     1.38   942  1094     0     0     0     0 |                  1.5-3.5
   36     1.54     1.74     1.36   950  1106     0     0     0     0 |                  1.5-3.5
   37     1.50     1.80     1.44   942  1098     0     0     0     0 |      0.5-1.5
   38      .96     1.11     1.01   946  1094     0     0     0     0 |      0.5-1.5
   39     1.02     1.26      .99   950  1094     0     0     0     0 |      0.5-1.5
   40     1.51     1.84     1.57   946  1190     0     0     0     0 |                  1.5-3.5
   41     1.39     1.66     1.27   946  1098     0     0     0     0 |      0.5-1.5
   42     2.83     3.31     2.81   942  1094     0     0     0     0 |                  1.5-3.5
   43     1.07     1.15      .84   954  1158     0     0     0     0 |      0.5-1.5
   44      .61      .70      .84   946  1098     0     0     0     0 |      0.5-1.5
   45      .71      .76      .96   950  1102     0     0     0     0 |      0.5-1.5
   46      .50      .61      .59   946  1142     0     0     0     0 |      0.5-1.5
   47      .92     1.09      .91   946  1102     0     0     0     0 |      0.5-1.5
   48     1.43     1.85     1.19   950  1102     0     0     0     0 |      0.5-1.5
   49      .70      .85      .71   942  1170     0     0     0     0 |      0.5-1.5
   50     2.58     3.13     2.86   946  1090     0     0     0     0 |                  1.5-3.5
   51     2.22     2.18     2.61   946  1094     0     0     0     0 |                  1.5-3.5
   52     2.84     2.99     2.64   942  1090     0     0     0     0 |                  1.5-3.5
```

```
 53    1.55    1.82    1.53  946  1190    0    0    0    0 |                1.5-3.5
 54    1.60    1.47    1.59  946  1166    0    0    0    0 |                1.5-3.5
 55    1.53    1.67    1.67  942  1090    0    0    0    0 |                1.5-3.5
 56    2.65    2.88    2.69  942  1094    0    0    0    0 |                1.5-3.5
 57    5.03    4.74    5.43  942  1090    0    0    0    0 |                      >3.5
 58    4.05    4.24    4.22  938  1222    0    0    0    0 |                      >3.5
 59    1.32    1.41    1.29  946  1170    0    0    0    0 |      0.5-1.5
 60    1.47    1.62    1.40  942  1098    0    0    0    0 |      0.5-1.5
 61    2.51    2.74    2.20  942  1198    0    0    0    0 |                1.5-3.5
 62    2.64    2.95    2.58  942  1098    0    0    0    0 |                1.5-3.5
 63    1.76    1.94    1.52  950  1174    0    0    0    0 |                1.5-3.5
 64    2.13    2.33    2.14  946  1218    0    0    0    0 |                1.5-3.5
 65    6.36    7.00    6.81  942  1102    0    0    0    0 |                      >3.5
 66    1.90    2.18    1.93  942  1098    0    0    0    0 |                1.5-3.5
 67    1.72    1.88    1.72  938  1094    0    0    0    0 |                1.5-3.5
 68    1.43    1.56    1.62  942  1102    0    0    0    0 |      0.5-1.5
 69    3.02    3.49    3.60  938  1094 1370 1530    0    0 |                1.5-3.5
 70     .95    1.11    1.37  946  1102    0    0    0    0 |      0.5-1.5
 71    2.08    2.22    2.32  946  1202    0    0    0    0 |                1.5-3.5
 72    1.56    1.70    1.79  942  1094    0    0    0    0 |                1.5-3.5
 73    2.04    2.18    2.14  942  1078    0    0    0    0 |                1.5-3.5
 74    2.05    2.19    2.07  942  1078    0    0    0    0 |                1.5-3.5
 75    1.58    1.70    1.59  938  1186    0    0    0    0 |                1.5-3.5
 76    1.58    1.69    1.46  950  1086    0    0    0    0 |                1.5-3.5
 77    2.73    3.33    2.72  942  1078    0    0    0    0 |                1.5-3.5
 78    4.79    4.98    4.95  938  1070    0    0    0    0 |                      >3.5
 79    1.61    1.75    1.85  942  1082    0    0    0    0 |                1.5-3.5
 80    2.92    3.28    2.96  942  1190    0    0    0    0 |                1.5-3.5
 81    1.16    1.27    1.11  946  1110 1970 2042    0    0 |      0.5-1.5
 82    3.59    4.06    3.60  942  1110    0    0    0    0 |                      >3.5
 83    2.53    2.52    2.51  942  1094    0    0    0    0 |                1.5-3.5
 84    1.97    2.09    1.90  938  1094    0    0    0    0 |                1.5-3.5

*** Chamber information ***
Cal ch, pl, nhit, 8 x (cell, tim*sns/wid)
 1 1 1 |17, -1232/ 64 | 0,     0/  0 | 0,     0/  0 | 0,     0/  0 | 0,     0/  0 | 0,     0/  0
 1 2 1 | 2,  -636/100 | 0,     0/  0 | 0,     0/  0 | 0,     0/  0 | 0,     0/  0 | 0,     0/  0
 2 1 1 |16,   980/ 84 | 0,     0/  0 | 0,     0/  0 | 0,     0/  0 | 0,     0/  0 | 0,     0/  0
 2 2 1 | 2,   864/ 80 | 0,     0/  0 | 0,     0/  0 | 0,     0/  0 | 0,     0/  0 | 0,     0/  0
 3 1 2 |16,  1516/204 |17, -1620/ 60 | 0,     0/  0 | 0,     0/  0 | 0,     0/  0 | 0,     0/  0
 3 2 3 | 2,   616/ 80 | 2,  -552/112 | 2, -1248/ 48 | 0,     0/  0 | 0,     0/  0 | 0,     0/  0
 4 1 1 |17, -1540/ 72 | 0,     0/  0 | 0,     0/  0 | 0,     0/  0 | 0,     0/  0 | 0,     0/  0
 4 2 1 | 2,  1552/ 76 | 0,     0/  0 | 0,     0/  0 | 0,     0/  0 | 0,     0/  0 | 0,     0/  0
 5 1 1 |16,  1280/ 56 | 0,     0/  0 | 0,     0/  0 | 0,     0/  0 | 0,     0/  0 | 0,     0/  0
 5 2 1 | 2,   568/100 | 0,     0/  0 | 0,     0/  0 | 0,     0/  0 | 0,     0/  0 | 0,     0/  0
 6 1 1 |17, -1260/ 56 | 0,     0/  0 | 0,     0/  0 | 0,     0/  0 | 0,     0/  0 | 0,     0/  0
 6 2 1 | 2,  1388/ 48 | 0,     0/  0 | 0,     0/  0 | 0,     0/  0 | 0,     0/  0 | 0,     0/  0
 7 1 8     -> too many hits to print
 7 2 1 | 3, -1524/ 84 | 0,     0/  0 | 0,     0/  0 | 0,     0/  0 | 0,     0/  0 | 0,     0/  0
 8 1 1 |17, -1336/ 72 | 0,     0/  0 | 0,     0/  0 | 0,     0/  0 | 0,     0/  0 | 0,     0/  0
 8 2 1 | 2,  1412/ 56 | 0,     0/  0 | 0,     0/  0 | 0,     0/  0 | 0,     0/  0 | 0,     0/  0
 9 1 1 |17, -1224/ 68 | 0,     0/  0 | 0,     0/  0 | 0,     0/  0 | 0,     0/  0 | 0,     0/  0
 9 2 1 | 3, -1028/ 76 | 0,     0/  0 | 0,     0/  0 | 0,     0/  0 | 0,     0/  0 | 0,     0/  0
10 1 1 |16,  1340/ 68 | 0,     0/  0 | 0,     0/  0 | 0,     0/  0 | 0,     0/  0 | 0,     0/  0
10 2 1 | 2,  1504/ 64 | 0,     0/  0 | 0,     0/  0 | 0,     0/  0 | 0,     0/  0 | 0,     0/  0
11 1 1 |17, -1192/ 52 | 0,     0/  0 | 0,     0/  0 | 0,     0/  0 | 0,     0/  0 | 0,     0/  0
11 2 1 | 3,  -976/ 76 | 0,     0/  0 | 0,     0/  0 | 0,     0/  0 | 0,     0/  0 | 0,     0/  0
12 1 1 |16,   896/ 60 | 0,     0/  0 | 0,     0/  0 | 0,     0/  0 | 0,     0/  0 | 0,     0/  0
12 2 1 | 3, -1096/ 76 | 0,     0/  0 | 0,     0/  0 | 0,     0/  0 | 0,     0/  0 | 0,     0/  0
13 1 1 |16,  1284/ 68 | 0,     0/  0 | 0,     0/  0 | 0,     0/  0 | 0,     0/  0 | 0,     0/  0
13 2 1 | 3,   548/112 | 0,     0/  0 | 0,     0/  0 | 0,     0/  0 | 0,     0/  0 | 0,     0/  0
14 2 1 | 3,  -536/136 | 0,     0/  0 | 0,     0/  0 | 0,     0/  0 | 0,     0/  0 | 0,     0/  0
15 1 1 |16,  1480/ 56 | 0,     0/  0 | 0,     0/  0 | 0,     0/  0 | 0,     0/  0 | 0,     0/  0
15 2 1 | 3,  -836/ 60 | 0,     0/  0 | 0,     0/  0 | 0,     0/  0 | 0,     0/  0 | 0,     0/  0
16 1 1 |17,  -944/ 60 | 0,     0/  0 | 0,     0/  0 | 0,     0/  0 | 0,     0/  0 | 0,     0/  0
16 2 1 | 3,   692/ 80 | 0,     0/  0 | 0,     0/  0 | 0,     0/  0 | 0,     0/  0 | 0,     0/  0
17 1 1 |16,   936/ 72 | 0,     0/  0 | 0,     0/  0 | 0,     0/  0 | 0,     0/  0 | 0,     0/  0
17 2 1 | 3,  1168/ 76 | 0,     0/  0 | 0,     0/  0 | 0,     0/  0 | 0,     0/  0 | 0,     0/  0
18 111     -> too many hits to print
18 2 1 | 3,   456/100 | 0,     0/  0 | 0,     0/  0 | 0,     0/  0 | 0,     0/  0 | 0,     0/  0
19 1 1 |17, -1448/ 60 | 0,     0/  0 | 0,     0/  0 | 0,     0/  0 | 0,     0/  0 | 0,     0/  0
19 2 1 | 4, -1332/ 64 | 0,     0/  0 | 0,     0/  0 | 0,     0/  0 | 0,     0/  0 | 0,     0/  0
20 1 1 |16,   704/ 76 | 0,     0/  0 | 0,     0/  0 | 0,     0/  0 | 0,     0/  0 | 0,     0/  0
20 2 1 | 3,  1120/ 64 | 0,     0/  0 | 0,     0/  0 | 0,     0/  0 | 0,     0/  0 | 0,     0/  0
22 1 1 |16,  1272/ 64 | 0,     0/  0 | 0,     0/  0 | 0,     0/  0 | 0,     0/  0 | 0,     0/  0
22 2 1 | 4,  -920/ 72 | 0,     0/  0 | 0,     0/  0 | 0,     0/  0 | 0,     0/  0 | 0,     0/  0
23 1 1 |17, -1332/ 60 | 0,     0/  0 | 0,     0/  0 | 0,     0/  0 | 0,     0/  0 | 0,     0/  0
23 2 1 | 4, -1416/ 64 | 0,     0/  0 | 0,     0/  0 | 0,     0/  0 | 0,     0/  0 | 0,     0/  0
24 2 1 | 4,  -368/164 | 0,     0/  0 | 0,     0/  0 | 0,     0/  0 | 0,     0/  0 | 0,     0/  0
25 1 1 |16,  1300/ 36 | 0,     0/  0 | 0,     0/  0 | 0,     0/  0 | 0,     0/  0 | 0,     0/  0
25 2 1 | 4, -1408/ 52 | 0,     0/  0 | 0,     0/  0 | 0,     0/  0 | 0,     0/  0 | 0,     0/  0
26 1 2 |10,  1320/ 72 |17,  -904/ 64 | 0,     0/  0 | 0,     0/  0 | 0,     0/  0 | 0,     0/  0
26 2 3 | 4,  -364/ 60 | 4,  -444/  8 | 4,  -456/ 16 | 0,     0/  0 | 0,     0/  0 | 0,     0/  0
27 1 2 |10,   608/ 64 |16,   884/ 64 | 0,     0/  0 | 0,     0/  0 | 0,     0/  0 | 0,     0/  0
```

```
27 2 3 | 4,  -456/ 96 | 4,  -676/112 |12,  -508/ 60 | 0,     0/  0 | 0,     0/  0 | 0,     0/  0
28 1 2 |10,  1176/ 56 |17, -1336/ 60 | 0,     0/  0 | 0,     0/  0 | 0,     0/  0 | 0,     0/  0
28 2 2 | 4,  -592/ 84 |12,  -632/ 60 | 0,     0/  0 | 0,     0/  0 | 0,     0/  0 | 0,     0/  0
29 1 2 |10,   512/104 |16,  1372/160 | 0,     0/  0 | 0,     0/  0 | 0,     0/  0 | 0,     0/  0
29 2 2 | 4,   980/ 60 |12,   772/ 68 | 0,     0/  0 | 0,     0/  0 | 0,     0/  0 | 0,     0/  0
30 1 2 |10,   368/104 |17, -1412/ 68 | 0,     0/  0 | 0,     0/  0 | 0,     0/  0 | 0,     0/  0
30 2 2 | 4,  -436/ 76 |12,  -952/ 52 | 0,     0/  0 | 0,     0/  0 | 0,     0/  0 | 0,     0/  0
31 1 1 |17,  -544/ 64 | 0,     0/  0 | 0,     0/  0 | 0,     0/  0 | 0,     0/  0 | 0,     0/  0
31 2 2 | 4,   772/ 76 |12,  -512/ 80 | 0,     0/  0 | 0,     0/  0 | 0,     0/  0 | 0,     0/  0
32 1 2 |10,  -460/ 72 |16,  1112/ 68 | 0,     0/  0 | 0,     0/  0 | 0,     0/  0 | 0,     0/  0
32 2 2 | 4,  1204/124 |12,  -520/ 76 | 0,     0/  0 | 0,     0/  0 | 0,     0/  0 | 0,     0/  0
33 1 3 |10,   364/184 |10,   576/ 52 |17, -1300/ 56 | 0,     0/  0 | 0,     0/  0 | 0,     0/  0
33 2 2 | 4,   740/ 52 |11,  1232/120 | 0,     0/  0 | 0,     0/  0 | 0,     0/  0 | 0,     0/  0
34 1 3 |10,   760/ 56 |16,  1144/124 |17, -1068/ 76 | 0,     0/  0 | 0,     0/  0 | 0,     0/  0
34 2 3 | 4,   588/ 96 | 4,  1184/ 64 |11,  1232/ 64 | 0,     0/  0 | 0,     0/  0 | 0,     0/  0
36 1 2 |10,  -252/184 |17, -1312/ 60 | 0,     0/  0 | 0,     0/  0 | 0,     0/  0 | 0,     0/  0
36 2 3 | 5,  -696/ 72 |11,  1132/ 48 |11,  1216/ 72 | 0,     0/  0 | 0,     0/  0 | 0,     0/  0
37 1 2 |10, -1004/ 64 |16,   840/ 56 | 0,     0/  0 | 0,     0/  0 | 0,     0/  0 | 0,     0/  0
37 2 2 | 5,  -852/ 52 |11,   640/ 96 | 0,     0/  0 | 0,     0/  0 | 0,     0/  0 | 0,     0/  0
38 1 2 |10,   624/ 64 |17,  -852/ 56 | 0,     0/  0 | 0,     0/  0 | 0,     0/  0 | 0,     0/  0
38 2 9     -> too many hits to print
39 1 2 |10,   412/116 |17, -1184/ 72 | 0,     0/  0 | 0,     0/  0 | 0,     0/  0 | 0,     0/  0
39 2 4 | 5,  -324/ 60 | 5,  -408/ 52 |11,   736/ 80 |11,   836/ 44 | 0,     0/  0 | 0,     0/  0
40 1 2 |10,  -592/ 64 |16,   964/ 48 | 0,     0/  0 | 0,     0/  0 | 0,     0/  0 | 0,     0/  0
40 2 2 | 5, -1380/ 80 |11,  -720/ 80 | 0,     0/  0 | 0,     0/  0 | 0,     0/  0 | 0,     0/  0
41 1 2 |10,   856/ 80 |17,  -964/ 84 | 0,     0/  0 | 0,     0/  0 | 0,     0/  0 | 0,     0/  0
41 2 3 | 5,  -628/100 |11,   260/ 68 |11,   336/ 36 | 0,     0/  0 | 0,     0/  0 | 0,     0/  0
42 1 2 |10,  -604/ 60 |16,   656/ 76 | 0,     0/  0 | 0,     0/  0 | 0,     0/  0 | 0,     0/  0
42 2 2 | 5,   368/ 84 |11,   592/128 | 0,     0/  0 | 0,     0/  0 | 0,     0/  0 | 0,     0/  0
Tor ch, pl, nhit, 8 x (cell, tim/wid)
44 1 1 |18,   548/112 | 0,     0/  0 | 0,     0/  0 | 0,     0/  0 | 0,     0/  0 | 0,     0/  0
44 2 2 | 2,   536/ 72 | 2,   652/ 28 | 0,     0/  0 | 0,     0/  0 | 0,     0/  0 | 0,     0/  0
46 1 2 |17,  1088/ 56 |17,  1508/ 36 | 0,     0/  0 | 0,     0/  0 | 0,     0/  0 | 0,     0/  0
46 2 1 | 1,  1264/ 64 | 0,     0/  0 | 0,     0/  0 | 0,     0/  0 | 0,     0/  0 | 0,     0/  0
47 1 1 |16,  1368/ 60 | 0,     0/  0 | 0,     0/  0 | 0,     0/  0 | 0,     0/  0 | 0,     0/  0
47 2 1 | 1,   636/ 76 | 0,     0/  0 | 0,     0/  0 | 0,     0/  0 | 0,     0/  0 | 0,     0/  0
48 1 1 |17,  1080/140 | 0,     0/  0 | 0,     0/  0 | 0,     0/  0 | 0,     0/  0 | 0,     0/  0
48 2 1 | 1,  1536/100 | 0,     0/  0 | 0,     0/  0 | 0,     0/  0 | 0,     0/  0 | 0,     0/  0
49 1 1 |17,   740/ 52 | 0,     0/  0 | 0,     0/  0 | 0,     0/  0 | 0,     0/  0 | 0,     0/  0
49 2 1 | 2,  1540/ 48 | 0,     0/  0 | 0,     0/  0 | 0,     0/  0 | 0,     0/  0 | 0,     0/  0
50 1 1 |17,  1492/ 44 | 0,     0/  0 | 0,     0/  0 | 0,     0/  0 | 0,     0/  0 | 0,     0/  0
50 2 1 | 1,   816/ 96 | 0,     0/  0 | 0,     0/  0 | 0,     0/  0 | 0,     0/  0 | 0,     0/  0
51 1 1 |17,  1092/136 | 0,     0/  0 | 0,     0/  0 | 0,     0/  0 | 0,     0/  0 | 0,     0/  0
51 2 1 | 1,  1208/ 88 | 0,     0/  0 | 0,     0/  0 | 0,     0/  0 | 0,     0/  0 | 0,     0/  0
52 1 1 |16,  1520/ 60 | 0,     0/  0 | 0,     0/  0 | 0,     0/  0 | 0,     0/  0 | 0,     0/  0
52 2 2 | 1,   480/ 80 | 1,   584/ 64 | 0,     0/  0 | 0,     0/  0 | 0,     0/  0 | 0,     0/  0
54 1 1 |17,   520/ 76 | 0,     0/  0 | 0,     0/  0 | 0,     0/  0 | 0,     0/  0 | 0,     0/  0
54 2 1 | 2,  1524/ 80 | 0,     0/  0 | 0,     0/  0 | 0,     0/  0 | 0,     0/  0 | 0,     0/  0
55 1 1 |17,  1392/ 60 | 0,     0/  0 | 0,     0/  0 | 0,     0/  0 | 0,     0/  0 | 0,     0/  0
55 2 1 | 1,   672/ 64 | 0,     0/  0 | 0,     0/  0 | 0,     0/  0 | 0,     0/  0 | 0,     0/  0
56 1 1 |17,  1604/ 24 | 0,     0/  0 | 0,     0/  0 | 0,     0/  0 | 0,     0/  0 | 0,     0/  0
56 2 1 | 1,  1228/ 84 | 0,     0/  0 | 0,     0/  0 | 0,     0/  0 | 0,     0/  0 | 0,     0/  0
57 1 1 |16,  1100/ 48 | 0,     0/  0 | 0,     0/  0 | 0,     0/  0 | 0,     0/  0 | 0,     0/  0
57 2 1 | 1,   696/ 56 | 0,     0/  0 | 0,     0/  0 | 0,     0/  0 | 0,     0/  0 | 0,     0/  0
59 2 1 | 2,  1376/ 68 | 0,     0/  0 | 0,     0/  0 | 0,     0/  0 | 0,     0/  0 | 0,     0/  0
60 1 1 |16,  1484/ 56 | 0,     0/  0 | 0,     0/  0 | 0,     0/  0 | 0,     0/  0 | 0,     0/  0
60 2 1 | 1,   996/ 68 | 0,     0/  0 | 0,     0/  0 | 0,     0/  0 | 0,     0/  0 | 0,     0/  0
61 1 1 |17,  1064/ 56 | 0,     0/  0 | 0,     0/  0 | 0,     0/  0 | 0,     0/  0 | 0,     0/  0
61 2 1 | 1,   736/ 64 | 0,     0/  0 | 0,     0/  0 | 0,     0/  0 | 0,     0/  0 | 0,     0/  0
62 1 1 |18,   892/ 60 | 0,     0/  0 | 0,     0/  0 | 0,     0/  0 | 0,     0/  0 | 0,     0/  0
62 2 1 | 2,  1176/ 88 | 0,     0/  0 | 0,     0/  0 | 0,     0/  0 | 0,     0/  0 | 0,     0/  0
64 1 1 |18,  1004/300 | 0,     0/  0 | 0,     0/  0 | 0,     0/  0 | 0,     0/  0 | 0,     0/  0
64 2 1 | 2,  1404/ 52 | 0,     0/  0 | 0,     0/  0 | 0,     0/  0 | 0,     0/  0 | 0,     0/  0
65 1 1 |17,   840/ 48 | 0,     0/  0 | 0,     0/  0 | 0,     0/  0 | 0,     0/  0 | 0,     0/  0
65 2 1 | 2,  1132/ 48 | 0,     0/  0 | 0,     0/  0 | 0,     0/  0 | 0,     0/  0 | 0,     0/  0
67 1 1 |17,  1396/ 64 | 0,     0/  0 | 0,     0/  0 | 0,     0/  0 | 0,     0/  0 | 0,     0/  0
67 2 2 | 1,  1412/ 36 |14,  1708/ 92 | 0,     0/  0 | 0,     0/  0 | 0,     0/  0 | 0,     0/  0
69 1 1 |17,  1060/ 68 | 0,     0/  0 | 0,     0/  0 | 0,     0/  0 | 0,     0/  0 | 0,     0/  0
69 2 1 | 2,  1368/ 72 | 0,     0/  0 | 0,     0/  0 | 0,     0/  0 | 0,     0/  0 | 0,     0/  0
DK ch, pl, nhit, 8 x (cell, tim/wid), sns not shown
80 1 2 |11,   816/ 56 |16,   256/108 | 0,     0/  0 | 0,     0/  0 | 0,     0/  0 | 0,     0/  0
80 2 3 | 5,   820/ 60 | 5,   912/ 84 |10,  1144/ 68 | 0,     0/  0 | 0,     0/  0 | 0,     0/  0
81 1 3 |10,  1916/128 |11,   480/ 60 |17,  1360/ 52 | 0,     0/  0 | 0,     0/  0 | 0,     0/  0
81 2 2 | 6,   448/ 64 |11,   968/ 52 | 0,     0/  0 | 0,     0/  0 | 0,     0/  0 | 0,     0/  0
82 1 3 | 4,     4/220 |12,  1120/ 80 |17,   716/ 68 | 0,     0/  0 | 0,     0/  0 | 0,     0/  0
82 2 2 | 6,   580/ 52 |11,   240/ 52 | 0,     0/  0 | 0,     0/  0 | 0,     0/  0 | 0,     0/  0
83 1 2 |14,  1156/ 68 |17,   808/ 76 | 0,     0/  0 | 0,     0/  0 | 0,     0/  0 | 0,     0/  0
83 2 2 | 7,   260/ 88 |10,   992/136 | 0,     0/  0 | 0,     0/  0 | 0,     0/  0 | 0,     0/  0
84 1 3 | 8,   776/ 64 |15,   176/ 56 |16,   488/ 64 | 0,     0/  0 | 0,     0/  0 | 0,     0/  0
84 2 3 | 9,  1008/ 80 |10,  1008/ 80 |22,  1080/ 80 | 0,     0/  0 | 0,     0/  0 | 0,     0/  0

*****************************************************************************************************

RUN6013:   TOROID FOCUSING MU-.
```

```
 WE HAVE AN EVENT! Number: 6013 219863
  The mode was: 1 --> mumu
  ***********************************************
  * Passed all standard closed-box analysis cuts *
  ***********************************************

npart,nx_extra,ny_extra:     2    0    0
vertex(x,y,z):     -23.250     5.831 -1416.680
error (x,y,z):        .178      .236     5.275
vert_chi2 =      23.     for   10 dof

 Info on each vertex track
 itrk,p(1-5),pid#,flags(trk,pid,e),nx,ny,chi2(x,y)
  1     .526    2.142   47.932   47.982   47.982  1  0  0  0  4  5    2.454    5.231
  2     .236    -.224    4.331    4.344    4.343  1  0  0  0  4  4   12.708     .658

 cal_pos +/- ecal_pos (x,y,z)
  1   -15.363      .056    37.783      .032  -701.010      .000
  2    15.584      .143   -31.585      .141  -701.010      .000

  Effective variables
eff_mass,q2,x,y,w:    1.573       5.555       .4366       .1239       2.837
eff_p(1-5):      .762    1.917   52.262   52.327   52.303

  Full variables
full_mass,q2,x,y,w:    11.31       119.3       1.237       .9471       1.573
full_p(1-5):      .000     .000   54.028   55.200   54.028
missing_pt,phi_misspt:    2.068      -1.949
trans_mass:    4.665


  *****  6013 219863 ******
  upstream in cal: slope, incept, sigma
    view 1      .0131   -6.0641     .0285 pos42= -15.2750
    view 1      .0243   32.3313     .1530 pos42=  15.2767
    view 2      .0456   69.7389     .0297 pos42=  37.7444
    view 2     -.0515  -67.3633     .0727 pos42= -31.2705

mutot,emu(1-mutot):   2     9.8     5.2

  tracks from decay channel:

     Explanation of t0 fit
     intime tracks have t0 w/i +/- 12
     t0=.0000 => all hits are on the same side.
                 In this case you cannot fit for a t0
                 because variations give you a shift
                 rather than a poor fit.  For lack of
                 any way to check, we assume t0 is ok.
  view 1: ntracks= 3
  seg     1: slp, int, t0, sig, nhit, pos      .0588    54.5829    -3.7324      .0246     4   13.3845
  seg     2: slp, int, t0, sig, nhit, pos      .0111    -7.5893      .0000      .0245     4  -15.3576
  seg     3: slp, int, t0, sig, nhit, pos      .0531    52.7162     1.0827      .0367     4   15.4656
  view 2: ntracks= 3
  seg     1: slp, int, t0, sig, nhit, pos      .0447    69.1302     4.1881      .0400     5   37.8078
  seg     2: slp, int, t0, sig, nhit, pos     -.0524   -68.1948    -2.6909      .0244     4  -31.4302
  seg     3: slp, int, t0, sig, nhit, pos     -.0361   -38.4200    -2.6153      .0225     4  -13.1467

   trk     1 Hits:  3  2 -2  0  0  0  0  0  3 Hituv:  -1
       hit pos:     6.31    2.40    -.69 9999.90 9999.90 9999.90 9999.90 9999.90    4.42   -1.47
   trk     2 Hits:  2  1  1  0  0  0  0  0  1 Hituv:  -1
       hit pos:   -16.70  -17.41  -18.03 9999.90 9999.90 9999.90 9999.90 9999.90  -15.86   -1.44
   trk     3 Hits:  4 -3  2  0  0  0  0  0  4 Hituv:   3
       hit pos:     9.17    5.59    2.74 9999.90 9999.90 9999.90 9999.90 9999.90    4.90    1.06

   trk     1 Hits:  1 -1 -1  1  0  0  0  0 -1 Hituv:   1
       hit pos:    32.49   29.53   27.21    9.12 9999.90 9999.90 9999.90 9999.90   30.72    -.79
   trk     2 Hits:  3  3 -4  0  0  0  0  0  3 Hituv:   4
       hit pos:   -25.30  -21.69  -18.96 9999.90 9999.90 9999.90 9999.90 9999.90  -22.46     .27
   trk     3 Hits:  2  2 -2  0  0  0  0  0  2 Hituv:  -5
       hit pos:    -8.93   -6.44   -4.58     .00 9999.90 9999.90 9999.90 9999.90   -6.90     .09

 Energy estimates for tracks
ixy,itrk,dkp(ixy,itrk):    1   1   .10E+05
ixy,itrk,dkp(ixy,itrk):    1   2   48.
ixy,itrk,dkp(ixy,itrk):    1   3   4.3
ixy,itrk,dkp(ixy,itrk):    2   1   48.
ixy,itrk,dkp(ixy,itrk):    2   2   4.3
ixy,itrk,dkp(ixy,itrk):    2   3   .10E+05

 dkvertex.com information
Found    3 linked x/y pairs
match_views =    2
```

```
ilnk_trk,dkl_x,dkl_y:    1   1   3
ilnk_trk,dkl_x,dkl_y:    2   2   1
ilnk_trk,dkl_x,dkl_y:    3   3   2
vert_lnk array:
   2   3
dclap=      .773
(xclap,yclap,zclap):  -23.292   5.815 -1417.0
(xclap,yclap,zclap):  -22.583   6.122 -1417.0
xvert,yvert,zvert,vert_qual:
 -23.250   5.831 -1416.7   .7728

 Msfit results
View:  1
Track:    1
ityp     zfit      xfit                 sxfit              chisq/ndf      ptrk
  1     -701.0    13.239+/-    .129    .05797+/-  .00099     .75    /  2    5.00
  2    -1416.7   -28.675+/-    .495    .05877+/-  .00134     .75    /  2    5.00
  3     -878.7     2.935+/-    .016    .05816+/-  .00052     .90    /  2    5.00
Track:    2
ityp     zfit      xfit                 sxfit              chisq/ndf      ptrk
  1     -701.0   -15.363+/-    .056    .01105+/-  .00031    2.4    /  2   47.98
  2    -1416.7   -23.288+/-    .167    .01108+/-  .00033    2.5    /  2   47.98
  3     -878.7   -17.327+/-    .013    .01106+/-  .00030    2.4    /  2   47.98
Track:    3
ityp     zfit      xfit                 sxfit              chisq/ndf      ptrk
  1     -701.0    15.584+/-    .143    .05381+/-  .00112    13.    /  2    4.34
  2    -1416.7   -22.564+/-    .554    .05314+/-  .00152    13.    /  2    4.34
  3     -878.7     6.025+/-    .016    .05349+/-  .00056    13.    /  2    4.34
View:  2
Track:    1
ityp     zfit      xfit                 sxfit              chisq/ndf      ptrk
  1     -701.0    37.783+/-    .032    .04456+/-  .00018    5.2    /  3   47.98
  2    -1416.7     5.830+/-    .029    .04468+/-  .00011    5.2    /  3   47.98
  3     -877.2    29.931+/-    .013    .04458+/-  .00013    5.3    /  3   47.98
Track:    2
ityp     zfit      xfit                 sxfit              chisq/ndf      ptrk
  1     -701.0   -31.585+/-    .141   -.05330+/-  .00112     .66    /  2    4.34
  2    -1416.7     6.103+/-    .556   -.05245+/-  .00152     .66    /  2    4.34
  3     -877.2   -22.195+/-    .016   -.05314+/-  .00056     .74    /  2    4.34
Track:    3
ityp     zfit      xfit                 sxfit              chisq/ndf      ptrk
  1     -701.0   -13.233+/-    .127   -.03653+/-  .00099    1.2    /  2    5.00
  2    -1416.7    12.655+/-    .497   -.03605+/-  .00134    1.2    /  2    5.00
  3     -877.2    -6.797+/-    .016   -.03646+/-  .00052    1.2    /  2    5.00

 vert_fit_dk results
chifit_vert/ndf =    22.59    /  10
x0,y0,z0: -23.250+/-    .178  5.831+/-    .236-1416.7+/-    5.3
 ivtrk,itrkx,itrky,sx +/- dsx,sy +/- dsy
   1   2   1   .0110+/-    .0003   .0447+/-    .0001
   2   3   2   .0545+/-    .0010  -.0518+/-    .0014


  Veto wall info:
  in time is between 225 and 295
  noisy counters have width lt 10

  coinc of counters: lfcbit, 6x(start, end, width) (timing from the coincidence module)
     4 |   0,   0,   0 | 582, 682, 100 |   0,   0,   0 |   0,   0,   0 |   0,   0,   0 |   0,   0,   0

  individual counters: ctr, 6x(start, end, width)
     7 | 578, 710, 132 |   0,   0,   0 |   0,   0,   0 |   0,   0,   0 |   0,   0,   0 |   0,   0,   0
     8 | 578, 714, 136 |   0,   0,   0 |   0,   0,   0 |   0,   0,   0 |   0,   0,   0 |   0,   0,   0
    11 |1450,1558, 108 |1806,1918, 112 |   0,   0,   0 |   0,   0,   0 |   0,   0,   0 |   0,   0,   0
    14 |   2,  42,  40 |1806,1918, 112 |   0,   0,   0 |   0,   0,   0 |   0,   0,   0 |   0,   0,   0

  Veto projection for track  1
  x,y position at veto: -34.3064995 -38.5963516
  Projects to paddle(s): 11 12 15 16 17
  Veto projection for track  2
  x,y position at veto: -75.3988266  58.2488708
  Projects to paddle(s): 13 14

  DID NOT have an in-time projection

  *** Cal Counter information ***
  ctr,tmaplo,tminlo,dvten,sbit1-6,                                  | mip range
     1     -.10     -.10      .03     0     0     0     0     0     0 | <0.5
     2      .03      .03      .00     0     0     0     0     0     0 | <0.5
     3      .01      .01     -.06     0     0     0     0     0     0 | <0.5
     4     -.02     -.02     -.01     0     0     0     0     0     0 | <0.5
     5      .03      .03     -.01     0     0     0     0     0     0 | <0.5
     6      .02      .02     -.01     0     0     0     0     0     0 | <0.5
     7     -.10     -.10     -.04     0     0     0     0     0     0 | <0.5
```

8	.01	.01	.03	0	0	0	0	0	0	<0.5			
9	.04	.04	-.02	0	0	0	0	0	0	<0.5			
10	.01	.01	.05	0	0	0	0	0	0	<0.5			
11	.01	.01	-.05	0	0	0	0	0	0	<0.5			
12	.25	.25	.11	0	0	0	0	0	0	<0.5			
13	.17	.17	-.03	0	0	0	0	0	0	<0.5			
14	.05	.05	-.01	0	0	0	0	0	0	<0.5			
15	.04	.04	-.01	0	0	0	0	0	0	<0.5			
16	.05	.05	-.01	0	0	0	0	0	0	<0.5			
17	.11	.11	.02	0	0	0	0	0	0	<0.5			
18	.05	.05	.03	0	0	0	0	0	0	<0.5			
19	.11	.11	.05	0	0	0	0	0	0	<0.5			
20	-.01	-.01	.02	0	0	0	0	0	0	<0.5			
21	-.14	-.14	-.05	0	0	0	0	0	0	<0.5			
22	.00	.00	.36	950	1110	0	0	0	0	<0.5			
23	-.15	-.15	.01	0	0	0	0	0	0	<0.5			
24	-.20	-.20	.00	0	0	0	0	0	0	<0.5			
25	-.03	-.03	.02	0	0	0	0	0	0	<0.5			
26	.19	.19	.05	0	0	0	0	0	0	<0.5			
27	2.83	2.83	2.68	934	1086	0	0	0	0			1.5-3.5	
28	.68	.68	.83	934	1146	0	0	0	0		0.5-1.5		
29	.62	.85	.81	938	1102	0	0	0	0		0.5-1.5		
30	.96	1.42	.96	942	1098	0	0	0	0		0.5-1.5		
31	7.35	9.09	7.19	934	1078	0	0	0	0				>3.5
32	1.06	1.23	.94	934	1102	0	0	0	0		0.5-1.5		
33	.95	1.46	.80	938	1158	0	0	0	0		0.5-1.5		
34	1.09	1.35	1.12	938	1158	0	0	0	0		0.5-1.5		
35	.81	1.31	.73	942	1086	0	0	0	0		0.5-1.5		
36	.87	1.06	.85	942	1094	0	0	0	0		0.5-1.5		
37	.62	.78	.61	942	1094	0	0	0	0		0.5-1.5		
38	1.19	1.53	1.27	946	1094	0	0	0	0		0.5-1.5		
39	1.17	1.56	1.17	942	1086	0	0	0	0		0.5-1.5		
40	.78	1.05	1.00	942	1090	0	0	0	0		0.5-1.5		
41	.82	1.09	.80	942	1118	1538	1686	0	0		0.5-1.5		
42	1.15	1.38	1.13	938	1086	0	0	0	0		0.5-1.5		
43	.99	1.29	1.08	938	1114	0	0	0	0		0.5-1.5		
44	-.02	-.03	.00	0	0	0	0	0	0	<0.5			
45	.56	.70	.59	942	1090	0	0	0	0		0.5-1.5		
46	.71	.96	.72	942	1098	0	0	0	0		0.5-1.5		
47	.90	1.20	1.01	942	1098	0	0	0	0		0.5-1.5		
48	.73	1.01	.78	942	1170	0	0	0	0		0.5-1.5		
49	.76	.91	.64	946	1094	0	0	0	0		0.5-1.5		
50	1.21	1.68	1.22	946	1090	0	0	0	0		0.5-1.5		
51	.83	1.09	.95	950	1094	0	0	0	0		0.5-1.5		
52	1.03	1.43	1.05	942	1090	0	0	0	0		0.5-1.5		
53	.82	1.05	.80	942	1094	0	0	0	0		0.5-1.5		
54	1.22	1.80	1.34	938	1198	0	0	0	0		0.5-1.5		
55	1.92	2.36	1.89	938	1086	0	0	0	0			1.5-3.5	
56	2.35	2.93	2.46	926	1078	0	0	0	0			1.5-3.5	
57	1.48	1.56	1.57	942	1090	0	0	0	0		0.5-1.5		
58	2.03	2.26	2.05	942	1222	0	0	0	0			1.5-3.5	
59	2.22	2.70	2.33	938	1094	0	0	0	0			1.5-3.5	
60	2.24	2.84	2.40	934	1090	0	0	0	0			1.5-3.5	
61	1.87	2.46	1.81	938	1178	0	0	0	0			1.5-3.5	
62	2.67	3.37	2.83	930	1090	0	0	0	0			1.5-3.5	
63	1.71	2.19	1.66	934	1186	0	0	0	0			1.5-3.5	
64	3.80	4.60	3.91	934	1250	0	0	0	0				>3.5
65	1.92	2.37	1.92	942	1198	0	0	0	0			1.5-3.5	
66	2.55	3.19	2.81	938	1094	1906	2042	0	0			1.5-3.5	
67	.70	.82	.88	942	1098	0	0	0	0		0.5-1.5		
68	1.93	2.19	2.22	942	1102	0	0	0	0			1.5-3.5	
69	1.79	2.26	1.98	930	1086	0	0	0	0			1.5-3.5	
70	2.19	2.72	2.55	938	1094	0	0	0	0			1.5-3.5	
71	1.46	1.79	1.61	942	1098	0	0	0	0		0.5-1.5		
72	2.07	2.51	2.28	934	1086	0	0	0	0			1.5-3.5	
73	4.65	5.41	4.69	938	1070	0	0	0	0				>3.5
74	2.06	2.44	2.00	934	1174	0	0	0	0			1.5-3.5	
75	2.01	2.32	1.94	938	1078	0	0	0	0			1.5-3.5	
76	1.81	2.02	1.75	938	1190	0	0	0	0			1.5-3.5	
77	3.16	3.73	3.12	934	1214	0	0	0	0			1.5-3.5	
78	1.37	1.56	1.46	942	1074	0	0	0	0		0.5-1.5		
79	6.40	6.64	6.73	930	1074	0	0	0	0				>3.5
80	2.72	3.00	2.69	938	1082	0	0	0	0			1.5-3.5	
81	2.77	3.07	2.86	930	1094	0	0	0	0			1.5-3.5	
82	1.94	2.32	2.06	946	1110	0	0	0	0			1.5-3.5	
83	6.10	6.19	6.17	938	1222	0	0	0	0				>3.5
84	4.87	4.99	5.01	930	1082	1090	1246	0	0				>3.5

```
*** Chamber information ***
Cal ch, pl, nhit, 8 x (cell, tim*sns/wid)
15 1 3 |10,  1420/ 68 |11,  -656/ 96 |11,  -760/ 68 | 0,     0/  0 | 0,     0/  0 | 0,     0/  0
15 2 2 |24,   704/ 84 |24, -1216/112 | 0,     0/  0 | 0,     0/  0 | 0,     0/  0 | 0,     0/  0
16 1 2 |11, -1056/188 |11, -1300/ 76 | 0,     0/  0 | 0,     0/  0 | 0,     0/  0 | 0,     0/  0
16 2 1 |24,   736/ 76 | 0,     0/  0 | 0,     0/  0 | 0,     0/  0 | 0,     0/  0 | 0,     0/  0
```

```
17 1 1 |10,   756/ 68 | 0,     0/  0 | 0,     0/  0 | 0,     0/  0 | 0,     0/  0 | 0,     0/  0
17 2 1 |24,   640/ 64 | 0,     0/  0 | 0,     0/  0 | 0,     0/  0 | 0,     0/  0 | 0,     0/  0
18 1 1 |10,  1240/ 76 | 0,     0/  0 | 0,     0/  0 | 0,     0/  0 | 0,     0/  0 | 0,     0/  0
18 2 1 |24, -1364/ 60 | 0,     0/  0 | 0,     0/  0 | 0,     0/  0 | 0,     0/  0 | 0,     0/  0
19 1 1 |10,  1404/ 72 | 0,     0/  0 | 0,     0/  0 | 0,     0/  0 | 0,     0/  0 | 0,     0/  0
19 2 1 |24,  -560/ 80 | 0,     0/  0 | 0,     0/  0 | 0,     0/  0 | 0,     0/  0 | 0,     0/  0
20 1 1 |10,   455/100 | 0,     0/  0 | 0,     0/  0 | 0,     0/  0 | 0,     0/  0 | 0,     0/  0
21 1 1 |10,  1392/ 72 | 0,     0/  0 | 0,     0/  0 | 0,     0/  0 | 0,     0/  0 | 0,     0/  0
21 2 1 |23,  1184/ 68 | 0,     0/  0 | 0,     0/  0 | 0,     0/  0 | 0,     0/  0 | 0,     0/  0
22 1 3 |10,   792/ 60 |10,  1496/ 48 |11, -1460/ 76 | 0,     0/  0 | 0,     0/  0 | 0,     0/  0
22 2 1 |23,  1136/ 76 | 0,     0/  0 | 0,     0/  0 | 0,     0/  0 | 0,     0/  0 | 0,     0/  0
23 1 1 |10,  1136/ 60 | 0,     0/  0 | 0,     0/  0 | 0,     0/  0 | 0,     0/  0 | 0,     0/  0
23 2 1 |23,  -568/ 64 | 0,     0/  0 | 0,     0/  0 | 0,     0/  0 | 0,     0/  0 | 0,     0/  0
24 1 1 |10,  1252/ 72 | 0,     0/  0 | 0,     0/  0 | 0,     0/  0 | 0,     0/  0 | 0,     0/  0
24 2 1 |23,   528/ 56 | 0,     0/  0 | 0,     0/  0 | 0,     0/  0 | 0,     0/  0 | 0,     0/  0
25 1 1 |10,   508/ 76 | 0,     0/  0 | 0,     0/  0 | 0,     0/  0 | 0,     0/  0 | 0,     0/  0
25 2 1 |22,  1376/ 52 | 0,     0/  0 | 0,     0/  0 | 0,     0/  0 | 0,     0/  0 | 0,     0/  0
26 1 4 |10,   652/156 |10,   848/ 76 |10,  1172/ 52 |10,  1264/ 60 | 0,     0/  0 | 0,     0/  0
26 2 4 |23,   560/ 60 |23,   648/ 48 |23,   824/ 12 |23, -1124/ 60 | 0,     0/  0 | 0,     0/  0
27 1 1 |10,  -724/ 68 | 0,     0/  0 | 0,     0/  0 | 0,     0/  0 | 0,     0/  0 | 0,     0/  0
27 2 1 |22,  1208/ 68 | 0,     0/  0 | 0,     0/  0 | 0,     0/  0 | 0,     0/  0 | 0,     0/  0
28 1 3 |10,   600/100 |10,   768/192 |16,  1248/ 64 | 0,     0/  0 | 0,     0/  0 | 0,     0/  0
28 2 2 | 3, -1268/ 76 |22,   484/ 68 | 0,     0/  0 | 0,     0/  0 | 0,     0/  0 | 0,     0/  0
29 1 3 |10,  -360/ 72 |10,  -468/ 20 |16,   500/ 88 | 0,     0/  0 | 0,     0/  0 | 0,     0/  0
30 1 2 |10,  -328/ 68 |16,   596/ 84 | 0,     0/  0 | 0,     0/  0 | 0,     0/  0 | 0,     0/  0
30 2 2 | 4,  -888/ 68 |22, -1132/ 72 | 0,     0/  0 | 0,     0/  0 | 0,     0/  0 | 0,     0/  0
31 1 1 |16,  1144/ 68 | 0,     0/  0 | 0,     0/  0 | 0,     0/  0 | 0,     0/  0 | 0,     0/  0
31 2 2 | 4,   556/ 92 |22,  -972/ 60 | 0,     0/  0 | 0,     0/  0 | 0,     0/  0 | 0,     0/  0
32 1 2 |10, -1000/ 72 |16,  -688/ 64 | 0,     0/  0 | 0,     0/  0 | 0,     0/  0 | 0,     0/  0
32 2 3 | 4,  1152/ 76 |22,  1108/ 24 |22, -1108/ 24 | 0,     0/  0 | 0,     0/  0 | 0,     0/  0
33 2 2 | 4,   912/ 52 |21,   752/ 64 | 0,     0/  0 | 0,     0/  0 | 0,     0/  0 | 0,     0/  0
34 1 2 |10,  -492/ 68 |16,   680/ 72 | 0,     0/  0 | 0,     0/  0 | 0,     0/  0 | 0,     0/  0
34 2 2 | 5, -1048/ 80 |21,   632/ 68 | 0,     0/  0 | 0,     0/  0 | 0,     0/  0 | 0,     0/  0
35 1 2 |10, -1276/ 72 |16,  -560/ 80 | 0,     0/  0 | 0,     0/  0 | 0,     0/  0 | 0,     0/  0
35 2 1 | 5, -1052/ 68 | 0,     0/  0 | 0,     0/  0 | 0,     0/  0 | 0,     0/  0 | 0,     0/  0
36 1 5 |10,  -872/160 |16,  -296/124 |16,   372/124 |16,   540/ 48 |16,   596/ 44 | 0,     0/  0
36 2 6 | 5,   908/ 72 | 5,  1060/ 56 | 5,  -512/108 | 5,  -632/112 | 5,  -856/ 72 |21,   408/ 64
37 1 2 |16,  -640/ 84 |16, -1140/ 52 | 0,     0/  0 | 0,     0/  0 | 0,     0/  0 | 0,     0/  0
37 2 2 | 5,  1152/ 72 |21,  -672/ 80 | 0,     0/  0 | 0,     0/  0 | 0,     0/  0 | 0,     0/  0
38 1 3 |10,  -728/ 72 |16,   264/ 84 |16,   396/ 32 | 0,     0/  0 | 0,     0/  0 | 0,     0/  0
38 2 2 | 5,   864/ 60 |20,  1116/ 72 | 0,     0/  0 | 0,     0/  0 | 0,     0/  0 | 0,     0/  0
39 1 2 |10, -1156/ 72 |16,  -592/ 68 | 0,     0/  0 | 0,     0/  0 | 0,     0/  0 | 0,     0/  0
39 2 2 | 6,  -664/ 72 |21, -1176/ 52 | 0,     0/  0 | 0,     0/  0 | 0,     0/  0 | 0,     0/  0
40 1 1 | 9,   852/ 96 | 0,     0/  0 | 0,     0/  0 | 0,     0/  0 | 0,     0/  0 | 0,     0/  0
40 2 3 | 5,  1364/ 88 |20,  -320/ 88 |20,  -760/ 88 | 0,     0/  0 | 0,     0/  0 | 0,     0/  0
41 1 2 |10, -1160/ 84 |16,  -776/ 88 | 0,     0/  0 | 0,     0/  0 | 0,     0/  0 | 0,     0/  0
41 2 2 | 6,  -368/ 84 |20,   296/ 88 | 0,     0/  0 | 0,     0/  0 | 0,     0/  0 | 0,     0/  0
42 1 8     -> too many hits to print
42 2 2 | 6,   864/ 72 |20,   384/ 76 | 0,     0/  0 | 0,     0/  0 | 0,     0/  0 | 0,     0/  0
Tor ch, pl, nhit, 8 x (cell, tim/wid)
DK ch, pl, nhit, 8 x (cell, tim/wid), sns not shown
80 1 5 | 9,   504/104 |13,   216/344 |13,   640/128 |13,   872/ 64 |13,   944/ 80 | 0,     0/  0
80 2 3 | 7,   924/ 68 |10,  1192/ 64 |18,   380/ 52 | 0,     0/  0 | 0,     0/  0 | 0,     0/  0
81 1 3 | 9,   368/ 64 |13,   280/104 |14,  1084/ 44 | 0,     0/  0 | 0,     0/  0 | 0,     0/  0
81 2 3 | 8,  1320/ 40 |11,  1440/ 64 |19,  1012/ 52 | 0,     0/  0 | 0,     0/  0 | 0,     0/  0
82 1 2 | 9,   636/140 |13,  1016/ 96 | 0,     0/  0 | 0,     0/  0 | 0,     0/  0 | 0,     0/  0
82 2 4 | 9,   848/ 64 |12,  1144/ 80 |12,  1276/ 72 |18,   272/ 88 | 0,     0/  0 | 0,     0/  0
83 2 1 |14,   364/176 | 0,     0/  0 | 0,     0/  0 | 0,     0/  0 | 0,     0/  0 | 0,     0/  0
```

Appendix D

FORTRAN Code for Helicity Decay Elements

The following code was used for calculating secondary-particle decay distributions for decays of neutral heavy leptons. The code takes into account mass and helicity effects in the matrix calculations.

```
      SUBROUTINE DECAY3(M,MD,IMODE,POLAR,PCM,
     +     decay_wt,set_maxwt,MU_TYPE,CHARGE)
c
c     This routine unweights itself, since its weight should not
c     be in the event weight calculation.  decay_wt is always 1.0.
c     Should be called a few thousand times with set_maxwt = .true.
c     in order to find a good maximum weight.
c
C     This routine now distinguishes kinematically between muon and
C     electron type neutral heavy leptons
C*************************************************************************
C   SIMULATE THREE BODY DECAY PROCESS WITH HELICITY TAKEN INTO ACCOUNT
C   INPUTS:
C           M = The mass of the decay product
C           MD(3) = The masses of the three decay products
C           IMODE = Type of decay:
C                                 0 - Isotropic
C                                 1 - u u v  (masses overwritten)
```

```
C                                   2 - e u v  (masses overwritten)
C                                   3 - e e v  (masses overwritten)
C           POLAR = Polarization of particle
c           set_maxwt = If .true. just trying to find maximum weight
C   OUTPUTS:
C           PCM(4,3) = The 4-momenta (px,py,pz,E) of each particle in CM frame
C*************************************************************************
C Set all Variables
      implicit none
      REAL M,MD(3),PCM(4,3),decay_wt
      logical set_maxwt
      REAL XM12LO,XM12HI,XM12
      REAL E3,P3,P1,E1
      REAL COSTH,SINTH,PHI,PI
      REAL WT,PROB,WT_POL
      REAL NHL_UUV,NHL_EEV,NHL_UEV,NHL_TAULEPV
      REAL PR1(4),PR2(4),PR3(4),PR4(4)
      REAL PR,POLAR,cosph,sinph
      real ng_ran
      REAL*8 P(4),PB(4)
      INTEGER I,J,IMODE,Q,POL,CHARGE
      LOGICAL MU_TYPE
      real rtemp
      real wt_max(10)
      data wt_max /10*0.0/
      save
      DATA PI/3.141593/
C Set Variables
      Q = 0
      WT = 1.
      PROB = 0.
c initialize weight and check if decay is kinematically allowed
      decay_wt = 0.
      if(md(1)+md(2)+md(3).gt.m) return
      DO Q=1,100000
C Distribute first particle in CMS123
       XM12LO = MD(1)+MD(2)
       XM12HI = M - MD(3)
       XM12 = XM12LO + ng_ran()*(XM12HI-XM12LO)
       E3 = (M**2 + MD(3)**2 - XM12**2)/(2.*M)
       P3 = SQRT(E3**2 - MD(3)**2)
```

```
      COSTH = 2.*ng_ran() - 1.
      IF(ABS(COSTH).GT.1.0) COSTH=SIGN(1.,COSTH)
      SINTH = SQRT(max(0.0,1. - COSTH**2))
      PHI = 2.*PI*ng_ran()
      COSPH = COS(PHI)
      SINPH = SIN(PHI)
      PCM(1,3) = P3*SINTH*COSPH
      PCM(2,3) = P3*SINTH*SINPH
      PCM(3,3) = P3*COSTH
      PCM(4,3) = E3
C Distribute next two particles in CMS12
      E1 = (XM12**2 + MD(1)**2 - MD(2)**2)/(2.*XM12)
      P1 = SQRT(ABS(E1**2 - MD(1)**2))
      COSTH = 2.*ng_ran() - 1.
      IF(ABS(COSTH).GT.1.0) COSTH=SIGN(1.,COSTH)
      SINTH = SQRT(max(0.0,1. - COSTH**2))
      PHI = 2.*PI*ng_ran()
      COSPH = COS(PHI)
      SINPH = SIN(PHI)
      PCM(1,1) = P1*SINTH*COSPH
      PCM(2,1) = P1*SINTH*SINPH
      PCM(3,1) = P1*COSTH
      PCM(4,1) = E1
      PCM(1,2) = -PCM(1,1)
      PCM(2,2) = -PCM(2,1)
      PCM(3,2) = -PCM(3,1)
      PCM(4,2) = PCM(1,2)**2 + PCM(2,2)**2 + PCM(3,2)**2 + MD(2)**2
      PCM(4,2) = SQRT(max(0.0,PCM(4,2)))
C Boost the two particles into CMS123
      rtemp = DSQRT(max(0.0d0,DBLE(P3**2) + DBLE(XM12**2)))
      DO I = 1,2
       DO J = 1,4
         P(J) = DBLE(PCM(J,I))
         PB(J) =DBLE(-PCM(J,3))
       ENDDO
       PB(4)=rtemp
       CALL LORENTZ4(P,PB,dble(xm12),1)
       DO J = 1,4
         PCM(J,I) = SNGL(P(J))
       ENDDO
      ENDDO
```

```
C Setup four vectors
      DO I = 1,4
        PR1(I) = 0.
        PR2(I) = PCM(I,1)
        PR3(I) = PCM(I,2)
        PR4(I) = PCM(I,3)
      ENDDO
      PR1(4) = M
C Determine left or right handedness
      WT_POL = ng_ran()
      PR = (1. + POLAR)/2.
      IF (WT_POL.LT.PR) THEN
        POL = 1
      ELSE
        POL = -1
      ENDIF
C Mode Isotropic
      IF (IMODE.EQ.0) THEN
       PROB=1.
      ENDIF
C Mode u u v
      IF (IMODE.EQ.1) THEN
       PROB = NHL_UUV(PR1,PR2,PR3,PR4,POL,MU_TYPE,CHARGE)
      ENDIF
C Mode u e v
      IF (IMODE.EQ.2) THEN
       PROB = NHL_UEV(PR1,PR2,PR3,PR4,POL,MU_TYPE,CHARGE)
      ENDIF
C Mode e e v
      IF (IMODE.EQ.3) THEN
       PROB = NHL_EEV(PR1,PR2,PR3,PR4,POL,MU_TYPE,CHARGE)
      ENDIF
C Mode v mu tau or v e tau
      IF ((IMODE.EQ.9).OR.(IMODE.EQ.10)) THEN
         PROB = NHL_TAULEPV(PR1,PR2,PR3,PR4,POL,MU_TYPE,CHARGE)
      ENDIF
C Keep a running maximum weight.  I try on the first attempt to choose
c a weight that is high enough to never be hit, but it may in some new
c running conditions.
      IF (IMODE.NE.0) THEN
        if (set_maxwt) wt_max(imode) = max(wt_max(imode),prob*1.3)
```

```
          IF (PROB .GT. wt_MAX(imode)) then
            write(*,*)
            write(*,*) 'decay3: Internal max wt increased by factor ',
     $                 prob/wt_max(imode) * 1.1
            write(*,*) '        Could be a problem if >> 1 or frequent.'
            write(*,*)
            call flush(6)
            wt_MAX(imode) = PROB * 1.1
          endif
          PROB = PROB / wt_MAX(imode)
        ENDIF
C End routine
        WT = ng_ran()
        IF (WT.LE.PROB) GOTO 100
      ENDDO
      write(*,*) 'decay3: Maximum number of unweighting trys reached.'
      call flush(6)
 100  CONTINUE ! Jump here if event passes unweighting
      decay_wt = 1.0
      RETURN
      END
C Calculates NHL --> uuv decay
      real FUNCTION NHL_UUV(P1,P2,P3,P4,POL,MU_TYPE,CHARGE)
      implicit none
      REAL P1(4),P2(4),P3(4),P4(4)
      REAL DotProduct,ThetaW,MU
      REAL A1,A2,A3,P(4)
      INTEGER POL,I,CHARGE
      LOGICAL MU_TYPE
      MU = 0.1056
      ThetaW = 0.4925
C Add spin factor (p1 -> p1 - m1*s) and calculate M matrix
      DO I=1,4
        P(I) = P1(I)
      ENDDO
      P(3) = P1(3) - CHARGE*POL*P1(4)
      IF (MU_TYPE) THEN
         A1 = 8*SIN(ThetaW)**4
         A2 = 2*(2 + Cos(2*ThetaW))**2
         A3 = 4*(2 + Cos(2*ThetaW))*Sin(ThetaW)**2
      ELSE
```

```
         A1 = 8*SIN(ThetaW)**4
         A2 = 2*(Cos(2*ThetaW)**2)
         A3 = 4*Cos(2*ThetaW)*Sin(ThetaW)**2
      ENDIF
      NHL_UUV = A1*DotProduct(p,p3)*DotProduct(p2,p4)
      NHL_UUV = NHL_UUV + A2*DotProduct(p,p2)*DotProduct(p3,p4)
      NHL_UUV = NHL_UUV - A3*DotProduct(p,p4)*MU**2
      RETURN
      END
C Calculates NHL --> uev decay
      real FUNCTION NHL_UEV(P1,P2,P3,P4,POL,MU_TYPE,CHARGE)
      implicit none
      REAL DotProduct
      REAL P1(4),P2(4),P3(4),P4(4),P(4)
      INTEGER POL,I,CHARGE
      LOGICAL MU_TYPE
C Add spin factor (p1 -> p1 - m1*s) and calculate M matrix
      DO I=1,4
        P(I) = P1(I)
      ENDDO
      P(3) = P1(3) - CHARGE*POL*P1(4)
      IF (MU_TYPE) THEN
         NHL_UEV = DotProduct(P2,P4)*DotProduct(P,P3)
      ELSE
         NHL_UEV = DotProduct(P3,P4)*DotProduct(P,P2)
      ENDIF
      RETURN
      END
C Calculates NHL -->eev decay
      real FUNCTION NHL_EEV(P1,P2,P3,P4,POL,MU_TYPE,CHARGE)
      implicit none
      REAL DotProduct,ThetaW,ME
      REAL P1(4),P2(4),P3(4),P4(4)
      REAL A1,A2,A3,P(4)
      INTEGER POL,I,CHARGE
      LOGICAL MU_TYPE
      ME = 0.0005
      ThetaW = 0.4925
C Add spin factor (p1 -> p1 - m1*s) and calculate M matrix
      DO I=1,4
        P(I) = P1(I)
```

```
      ENDDO
      P(3) = P1(3) - CHARGE*POL*P1(4)
      IF (MU_TYPE) THEN
         A1 = 8*SIN(ThetaW)**4
         A2 = 2*(Cos(2*ThetaW)**2)
         A3 = 4*Cos(2*ThetaW)*Sin(ThetaW)**2
      ELSE
         A1 = 8*SIN(ThetaW)**4
         A2 = 2*(2 + Cos(2*ThetaW))**2
         A3 = 4*(2 + Cos(2*ThetaW))*Sin(ThetaW)**2
      ENDIF
      NHL_EEV = A1*DotProduct(p,p3)*DotProduct(p2,p4)
      NHL_EEV = NHL_EEV + A2*DotProduct(p,p2)*DotProduct(p3,p4)
      NHL_EEV = NHL_EEV - A3*DotProduct(p,p4)*ME**2
      RETURN
      END
C Calculates NHL --> tau lep v decay
      real FUNCTION NHL_TAULEPV(P1,P2,P3,P4,POL,MU_TYPE,CHARGE)
      implicit none
      REAL DotProduct
      REAL P1(4),P2(4),P3(4),P4(4),P(4)
      INTEGER POL,I,CHARGE
      LOGICAL MU_TYPE
C Add spin factor (p1 -> p1 - m1*s) and calculate M matrix
      DO I=1,4
        P(I) = P1(I)
      ENDDO
      P(3) = P1(3) - CHARGE*POL*P1(4)
      NHL_TAULEPV = DotProduct(P2,P4)*DotProduct(P,P3)
      RETURN
      END
C     Compute dot product of four-vectors
      real FUNCTION DotProduct(P1,P2)
      implicit none
      REAL p1(4),p2(4)
      DotProduct = P1(4)*P2(4) - P1(1)*P2(1) - P1(2)*P2(2) - P1(3)*P2(3)
      RETURN
      END
```

Appendix E

Convoluted Poisson Probabilities

The probability of seeing N events where μ events were expected is given by the simple Poisson distribution:

$$P(N, \mu) = \frac{\mu^N e^{-\mu}}{N!}, \tag{E.1}$$

Consider the case now where two measurements are made on two separate samples, with N_1 events seen in first sample (with a background μ_1) and N_2 events seen in the second sample (with a background μ_2). Given the observation in the first set, what is the probability of seeing N_2 events in the second set? To solve this problem, one must integrate over all possible values of μ_1:

$$P(N_1, \mu_1, N_2, \mu_2) = \int_0^\infty \frac{\mu_1^{N_1} e^{-\mu_1}}{N_1!} \cdot \frac{\mu_2^{N_2} e^{-\mu_1}}{N_2!} d\mu_1, \tag{E.2}$$

Let $\mu = \mu_1$, $R = \mu_2/\mu_1$, $N = N_1 + N_2$, and $m = N_1$. If one treats R as a constant, then it is possible to use following substitution:

$$P(N, m, R) = \int_0^\infty \frac{\mu^N e^{-\mu(1+R)} R^{(N-m)}}{m!(N-m)!} d\mu, \tag{E.3}$$

Now let $s = \mu(1+R)$ and use s as the integration variable:

$$P(N,m,R) = \int_0^\infty s^N e^{-s} ds \frac{R^{(N-m)}}{(1+R)^{N+1} m!(N-m)!}, \tag{E.4}$$

Using the relation $\int_0^\infty s^N e^{-s} ds = N!$, we can express P as an analytical function:

$$P(N,m,R) = C(N,m) \cdot \frac{R^{(N-m)}}{(1+R)^{N+1}}, \tag{E.5}$$

where $C(N,n) = N!/[(N-m)!\ m!]$. This relation only works for constant values of R.

Appendix F

Search for Lepton Family Number Violation

If I stop, will you?

- Trucker wisdom

Both inverse muon decay (IMD) and lepton number violation (LNV) measurements provide a direct window into the structure of the weak interaction. The fact that each process is a purely leptonic interaction assures that there is no complications from strong coupling terms. This allows us to directly probe the nature of the weak interaction.

Inverse muon decay is a purely leptonic interaction between muon neutrinos and electrons:

$$\nu_\mu + e^- \rightarrow \nu_e + \mu^-. \tag{F.1}$$

By measuring the rate of inverse muon decays, one is able to make an accurate determination of the vector/axial-vector (V−A) nature of the weak interaction [87].

This can be compared with theoretical predictions stemming from muon decay. In addition, because IMD events have such a direct window into the nature of the weak interaction, this measurement is sensitive to non-Standard Model phenomena, including:

- V+A coupling
- lepton compositeness
- right-handed neutrinos

In addition to being a solid measurement on its own, the inverse muon decay measurement also provides a platform into studying lepton number violating processes:

$$\overline{\nu}_\mu + e^- \rightarrow \overline{\nu}_e + \mu^-. \tag{F.2}$$

This interaction is forbidden by the Standard Model since it violates lepton number ($\Delta L = 2$). One can search for such a process by looking for IMD-like events in the anti-neutrino beam. Because there are no positrons in the target, the allowed $\bar{\nu}_\mu e^+ \rightarrow \mu^+ \bar{\nu}_e$ interaction is not present. In addition, because of the purity of our neutrino/anti-neutrino beam, all backgrounds for the process are highly suppressed. As a result, any events seen in the data may be evidence for new physics. Some topics that could be addressed by this measurement include (but are not limited to) the following:

- Multiplicative lepton number conservation [88].
- Left-right symmetry [89].
- Existence of dileptons [90].

Multiplicative lepton number conservation is an empirical law used to explain why certain processes, such as $\mu \to e\gamma$ and $\mu \to 3\gamma$, are not observed. Left-right symmetry is an attractive extension of the Standard Model that attempts to explain parity violation in weak interactions by invoking the lepton as a fourth color. Left-right symmetric models are usually based on $SU(2)_L \times SU(2)_R \times U_{B-L}$ gauge symmetries. Dileptons are bosons introduced by extensions to the Standard Model which carry lepton number. All three theoretical models predict that lepton number is *not* conserved. The observation of the forbidden process $\bar{\nu}_\mu e^- \to \mu^- \bar{\nu}_e$ would be a clear signature for these models.

Thus, both IMD and LNV provide platforms to both measure and validate the standard model's predictions for weak interactions. This is ample reason to pursue these two measurements, which are described in our article in Appendix G.

Appendix G

Paper on Lepton Number Violation

The following Appendix consists of the article submitted to *Physical Review Letters* on the NuTeV search for the family lepton number violating process $\bar{\nu}_\mu e^- \to \mu^- \bar{\nu}_e$. The article was published in Phys. Rev. Lett. **87**, 071803 (2001).

arXiv:hep-ex/0104029 16 Apr 2001

Search for the Lepton Number Violating Process $\overline{\nu}_\mu e^- \to \mu^- \overline{\nu}_e$

J. A. Formaggio[2], J. Yu[3], T. Adams[4], A. Alton[4], S. Avvakumov[8], L. de Barbaro[5], P. de Barbaro[8], R. H. Bernstein[3], A. Bodek[8], T. Bolton[4], J. Brau[6], D. Buchholz[5], H. Budd[8], L. Bugel[3], J. M. Conrad[2], R. B. Drucker[6], B. T. Fleming[2], J. Foster[4], R. Frey[6], J. Goldman[4], M. Goncharov[4], D. A. Harris[3], R. A. Johnson[1], J. H. Kim[2], S. Koutsoliotas[2], M. J. Lamm[3], W. Marsh[3], D. Mason[6], J. McDonald[7], K. S. McFarland[8], C. McNulty[2], D. Naples[7], P. Nienaber[3], A. Romosan[2], W. K. Sakumoto[8], H. M. Schellman[5], M. H. Shaevitz[2], P. Spentzouris[3], E. G. Stern[2], N. Suwonjandee[1], M. Vakili[1], A. Vaitaitis[2], U. K. Yang[8], G .P. Zeller[5], and E. D. Zimmerman[2]

[1] *University of Cincinnati, Cincinnati, OH 45221*
[2] *Columbia University, New York, NY 10027*
[3] *Fermi National Accelerator Laboratory, Batavia, IL 60510*
[4] *Kansas State University, Manhattan, KS 66506*
[5] *Northwestern University, Evanston, IL 97403*
[6] *University of Oregon, Eugene, OR 97403*
[7] *University of Pittsburgh, Pittsburgh, PA 15260*
[8] *University of Rochester, Rochester, NY 14627*

(April 16, 2001)

The NuTeV experiment at Fermilab has used a sign-selected neutrino beam to perform a search for the lepton number violating process $\overline{\nu}_\mu e^- \to \mu^- \overline{\nu}_e$, and to measure the cross-section of the Standard Model inverse muon decay process $\nu_\mu e^- \to \mu^- \nu_e$. NuTeV measures the inverse muon decay asymptotic cross-section σ/E to be $(13.8 \pm 1.2 \pm 1.4) \times 10^{-42}$ cm^2/GeV. The experiment also observes no evidence for lepton number violation and places one of the most restrictive limits on the cross-section ratio $\sigma(\overline{\nu}_\mu e^- \to \mu^- \overline{\nu}_e)/\sigma(\nu_\mu e^- \to \mu^- \nu_e) \leq 1.7\%$ at 90% C.L. for V−A couplings and $\leq 0.6\%$ for scalar couplings.

Neutrino-lepton interactions provide an excellent tool to study the properties of the weak interaction. Such purely leptonic processes experience no interference from strong coupling terms, and thus provide a direct channel to investigate the nature of the weak force. The inverse muon decay (IMD) process:

$$\nu_\mu + e^- \to \mu^- + \nu_e \tag{1}$$

allows one to make an accurate determination of the vector/axial-vector (V−A) nature of the weak interaction [1]. This process is also sensitive to scalar couplings and right-handed currents.

An experiment with separate neutrino and anti-neutrino beams can search for the process:

$$\overline{\nu}_\mu + e^- \to \mu^- + \overline{\nu}_e \tag{2}$$

Such an interaction is forbidden by the Standard Model, since it violates lepton family number conservation ($\Delta L_e = -\Delta L_\mu = 2$). Theories which incorporate multiplicative lepton number conservation [2], left-right symmetry [3], or the existence of bileptons [4] allow for such processes to occur.

The NuTeV neutrino experiment at Fermilab has investigated these processes in its high-energy, sign-selected neutrino beamline. Although the NuTeV inverse muon decay measurement is dominated by systematic uncertainties, the search for lepton number violation (LNV) processes is very sensitive because the relevant backgrounds are highly suppressed.

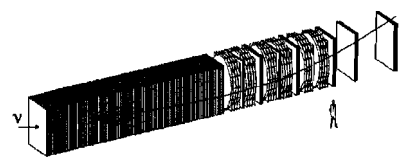

FIG. 1. Schematic of the NuTeV detector, showing the calorimeter and the toroid spectrometer.

The experiment collected data during the 1996-1997 fixed target run, receiving a total of 2.9×10^{18} 800 GeV protons striking a BeO target. Pions and kaons produced in the interaction were focused using the Sign-Selected Quadrupole Train (SSQT) [5] and aimed toward the NuTeV detector at a 7.8 mrad angle relative to the primary proton beam direction. The SSQT enabled the detector to be exposed to either pure neutrino or pure anti-neutrino beams. NuTeV received 1.3×10^{18} and 1.6×10^{18} protons on target for neutrino and anti-neutrino running modes, respectively. The fractional contamination from wrong-sign meson decays was below 5×10^{-3} [6]. Pions and kaons decay to neutrinos as they travel through a 440 m vacuum pipe; undecayed hadrons are

filtered out in a beam dump at the end of the pipe. The neutrinos pass through about 900 m of earth berm shielding before reaching the NuTeV neutrino detector.

The NuTeV detector [7], located 1.4 km downstream of the primary target, consists of a segmented iron-scintillator sampling calorimeter, followed by a toroid spectrometer (see Fig. 1). The calorimeter is composed of 42 segments, each segment consisting of four 2 inch thick steel plates, two liquid scintillator counters, and one drift chamber. The calorimeter serves as a neutrino target with a fiducial mass of 350 tons. The scintillation counters measure the deposited hadronic energy and the drift chamber determine the position and direction of the outgoing muon. The toroid spectrometer uses a 15 kG toroid magnetic field to measure the charge and energy of muons exiting from the calorimeter. The toroid magnetic field is configured so as to always focus muons coming from the selected neutrino beam (μ^- for neutrinos, μ^+ for anti-neutrinos). The energy resolution and response of the detector is measured directly using a separate beam of hadrons, muons, and electrons at varying energies. The hadronic energy resolution of the calorimeter is $\sigma/E = (0.024 \pm 0.001) \oplus (0.874 \pm 0.003)/\sqrt{E}$, and the electromagnetic energy resolution is $\sigma/E = (0.04 \pm 0.001) \oplus (0.52 \pm 0.01)/\sqrt{E}$ [8]. The resolution of the muon energy as determined by the toroid spectrometer is $\Delta p/p = 11\%$, limited predominantly by multiple scattering.

The selection criteria for the inverse muon decay measurement and the lepton number violation search were similar, since the characteristic signatures of the processes are nearly identical. Candidate events were selected based on the following criteria: the event occurred during the beam gate, had its interaction vertex within the fiducial volume, and had a single μ^- reaching the toroid spectrometer. The muon was required to be well contained within the toroid and to have an energy between 15 and 600 GeV. The muon angle was also required to be less than 150 mrad with respect to the beam axis. To reduce the number of cosmic ray muons entering the selection sample, events which contained significant activity upstream of the reconstructed vertex were removed. The hadronic energy of the interaction was required to be less than 3 GeV. Finally, the neutrino beam running mode determined the sample into which the events were placed. For IMD, we required a μ^- in neutrino mode; for LNV candidates, a μ^- in anti-neutrino mode. For the LNV sample, we also placed an additional requirement on the χ^2 of the muon track within the toroid, in order to minimize events where the charge of the muon was misidentified.

Because both IMD and LNV events involve neutrino scattering from an electron, there exists a kinematic limit on the transverse momentum of the muon: $p_t^2 \leq 2m_e E_\nu$, where m_e is the mass of the electron and E_ν is the neutrino energy. We therefore apply an energy-dependent

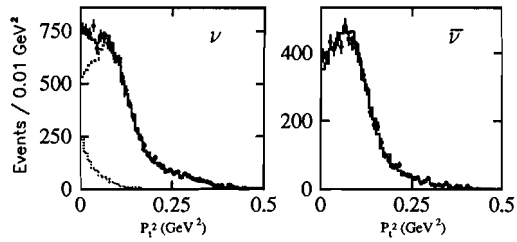

FIG. 2. Transverse momentum distributions for data (crosses) and Monte Carlo (solid) for right-sign neutrino events (left) and right-sign anti-neutrino events (right). The plot on the left is broken down into background only (dashed) and IMD signal (dotted). The plot on the right shows Monte Carlo background only.

requirement on the transverse momentum of the event in order to further isolate signal events. The cut requires $p_t^2 \leq p_t^{2\,max}$, where $p_t^{2\,max} \equiv (0.059 + E_\mu/671)$ GeV^2. This cut, which is based on Monte Carlo signal studies, was designed to retain 90% of the signal. The efficiency after all cuts for IMD events was 79.6%. The final efficiency for LNV events was 89.8% for V−A couplings and 79.9% for scalar couplings. Figures 2 and 3 show the p_t^2 distributions for right-sign and wrong-sign events respectively. Right-sign events are neutrino (anti-neutrino) events with an outgoing μ^- (μ^+); wrong-sign events are the opposite: neutrino (anti-neutrino) events with a outgoing μ^+ (μ^-).

For right-sign events, the primary backgrounds that enter the IMD sample come from low hadronic energy neutrino charged-current interactions in the detector. These include quasi-elastic events, resonance events, and some small fraction of deep-inelastic scattering (DIS) events with a very small momentum transfer [9,10]. Understanding the background levels is essential for the IMD measurement, since the signal to background ratio for these events is one to eight. To accomplish this, we perform a full Monte Carlo simulation of low hadronic energy neutrino processes. To simulate neutrino resonance production, we used a low-Q^2 higher-twist approximation [11]. We found this method more accurate in averaging over all low-multiplicity states than the single-pion production model from Rein and Sehgal [12]. Nuclear effects such as Fermi motion [13] and Pauli suppression [9,14] were also applied to the Monte Carlo simulations. The Monte Carlo was absolutely normalized to data DIS events with hadronic energies above 30 GeV for each running mode. The normalization sample contained 0.83(0.25) million neutrino (anti-neutrino) interactions with a mean energy of 140(120) GeV.

The dominant systematic uncertainties for the right-sign events are related to the modeling of these low hadronic energy processes. Systematic errors include ef-

TABLE I. Errors on IMD expected signal and LNV expected background. Total statistical and systematic errors reflect errors from full parameter fit, which take into account correlations between errors.

Category	IMD (%)	LNV (%)
Statistical Error	±6.7	±13.0
Muon Energy Scale	±1.0	±2.2
Hadron Energy Scale	±0.3	±0.7
Angle Smearing	±0.6	±1.4
Normalization	±6.4	±2.6
Quasi-Elastic Cross-Section	±1.0	±0.6
Pauli Suppression	±8.5	±2.2
Beam Impurities	N/A	±0.7
Charge Identity	$\ll 0.1$	±1.5
Radiative Corrections	±1.0	±1.0
Total Systematics (fit)	±8.2	±4.4

fects from muon energy and angular resolution, background cross-section uncertainties, Pauli suppression, and MC normalization. In addition, we take into account radiative correction errors which affect the IMD cross-section. A complete list of systematic errors is shown in Table I.

The validity of the background modeling was checked directly against the data by looking at the right-sign, anti-neutrino process $\overline{\nu}_\mu + N \rightarrow \mu^+ + N'$. This particular configuration selects only background events, and thus is an ideal platform to test the data to Monte Carlo agreement and systematics. A fit to the anti-neutrino p_t^2 distribution (Fig. 2) is performed where the backgrounds are allowed to vary within the uncertainties shown in the first column of Table I. The fit gives an excellent χ^2/d.o.f. of 44.9/50, indicating that the background estimate agrees well with the anti-neutrino data within the systematic uncertainties.

Having verified the size and spectrum of the background, a fit to the neutrino data is performed to extract the IMD signal. The fit includes the previously mentioned backgrounds plus an IMD signal contribution with the proper p_t^2 distribution. As before, the backgrounds are allowed to vary within the uncertainties shown in the first column of Table I. As shown in Fig. 2, the data are well described by the combination of an IMD signal at low p_t^2 plus the background. From the fit, we extract a total of 1050 ± 139 IMD events, where 1311 events were expected based on Standard Model predictions, taking into account radiative corrections [15] (see Table II).

The differential cross-section for IMD can be written as:

$$\frac{d\sigma}{dy} = \sigma_0 \cdot E_\nu \cdot (1 - r) \qquad (3)$$

where $y = E_\mu/E_\nu$, $r = m_\mu^2/s$, $\sigma_0 = \frac{2m_e G_F^2}{\pi}$, and s is the center-of-mass energy of the interaction. For inverse muon decay, the NuTeV measurement for the IMD asymptotic cross-section ($E_\nu \gg m_\mu$) is:

$$\sigma_0 = (13.8 \pm 1.2 \pm 1.4) \times 10^{-42}\ \mathrm{cm}^2/\mathrm{GeV} \qquad (4)$$

where the first error is statistical, and the second is systematic. The average neutrino energy for the IMD events sampled in the NuTeV experiment is 130 GeV. This measurement is in agreement with the theoretically predicted value of 17.2×10^{-42} cm^2/GeV and is also consistent with the CHARM II measurement of $(16.5 \pm 0.9) \times 10^{-42}$ cm^2/GeV [16].

By requiring that the muon charge not match the neutrino running mode (wrong-sign events), the analysis immediately becomes sensitive to lepton number violation. The dominant backgrounds in this case arise from beam impurities and muon charge mis-identification. Beam impurities come mainly from charmed meson decays and decays of wrong-sign hadrons produced in secondary interactions [17]. Beam impurities constitute about 72% of the total LNV background. Charge mis-identification backgrounds are often associated with δ-ray production or multiple scattering of the muon in the toroid spectrometer. These backgrounds can be greatly reduced by imposing quality cuts on the muon track in the toroid spectrometer. The total fraction of charge mis-identification is 0.06% for anti-neutrino running mode. This source contributes 14% of the LNV background. Finally, there exists an irreducible background from $\overline{\nu}_e e^- \rightarrow \mu^- \overline{\nu}_\mu$, which contributes about 14% of the LNV background.

TABLE II. Signal extraction from Monte Carlo background.

Type	ν Mode / μ Charge	Data	Fit Results
IMD Signal	ν / μ^-	11792	1050 ± 139
LNV Signal (V−A)	$\overline{\nu}$ / μ^-	24	0.6 ± 3.3
LNV Signal (scalar)	$\overline{\nu}$ / μ^-	24	-0.6 ± 3.3

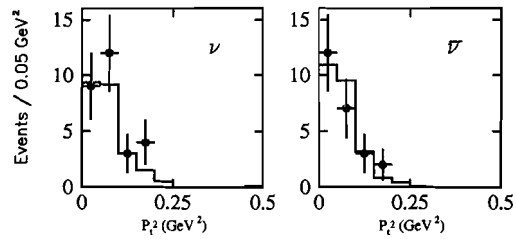

FIG. 3. Transverse momentum distributions for data (crosses) and Monte Carlo (solid) for neutrino events (left) and anti-neutrino events (right) with a wrong-sign muon. A LNV signal would appear as an excess of events in anti-neutrino mode.

The generic expression for the differential LNV cross-section is given by:

$$\frac{d\sigma}{dy} = \lambda \frac{G_F^2 s}{\pi}[A_V \cdot y(y-r) + A_S \cdot (1-r)] \qquad (5)$$

where λ represents the strength of the interaction and A_V and A_S determine whether the reaction is V−A or scalar. Integrating over all allowed values of y, and normalizing to the Standard Model IMD cross-section, allows the LNV cross-section to be written as:

$$\frac{\sigma(\overline{\nu}_\mu e^- \to \mu^- \overline{\nu}_e)}{\sigma(\nu_\mu e^- \to \mu^- \nu_e)} = \lambda \cdot [A_V \cdot (\frac{1+r/2}{3}) + A_S] \qquad (6)$$

We can make a consistency check on the background estimation by looking at the neutrino process $\nu_\mu + N \to \mu^+ + N'$. Momentum distributions of these events are shown in Fig. 3. A total of 28 data events were seen in this sample where 23.5±3.7 (stat. + sys.) were expected, consistent with the background estimate.

Looking in the LNV signal channel $\overline{\nu}_\mu + e^- \to \mu^- + \overline{\nu}_e$ yields a total of 24 data events. A fit of the p_t^2 distribution to only background sources yields an acceptable χ^2/d.o.f. of 2.5/5, showing no indication of a LNV signal. Including a possible LNV signal in the fit yields a total LNV contribution of 0.6±3.1±1.1 events for a V−A coupling and −0.6±3.1±1.1 events for a scalar coupling. As shown in Table I, the LNV analysis is dominated by statistical uncertainty. These fit results can be recast in the form of 90% C.L. limits on the LNV cross-section as a function of $(A_V - A_S)/(A_V + A_S)$, as shown in Figure 4. If we assume a pure V−A coupling, this yields $\lambda \leq 1.7\%$ while a scalar coupling yields a limit of $\lambda \leq 0.6\%$.

This limit is currently the most stringent limit obtained directly from neutrino-electron scattering. Previous results limited the pure V−A coupling to below 5% [18]. The LAMPF experiment has set an earlier limit from muon decay rates at $\leq$ 1.2% [19] for pure V−A couplings.

In conclusion, NuTeV has performed a measurement of the inverse muon decay cross-section and a direct search for lepton number violation. The IMD asymptotic cross-section is measured to be $(13.8 \pm 1.2 \pm 1.4) \times 10^{-42}$ cm^2/GeV. The LNV search limits the strength of the interaction to be $\leq$ 1.7% for V−A and $\leq$ 0.6% for scalar couplings.

This research was supported by the U.S. Department of Energy and the National Science Foundation. We thank the staff of FNAL for their contributions to the construction and support of this experiment during the 1996-1997 fixed target run.

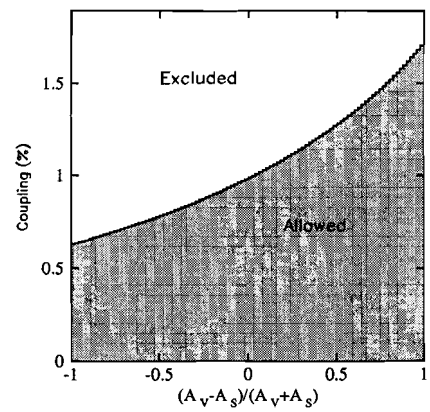

FIG. 4. Limit on the lepton number violation process $\overline{\nu}_\mu e^- \to \mu^- \overline{\nu}_e$ as a function of the scalar and vector couplings $(A_V - A_S)/(A_V + A_S)$. The non-shaded region is excluded by this result.

[1] W. Fetscher, H. J. Gerber, and K. F. Johnson, Phys. Lett. **B173**, 102 (1986).
[2] N. Cabbibo and R. Gatto, Phys. Rev. Lett. **6**, 381 (1961).
[3] P. Herczeg and R. N. Mohapatra, Phys. Rev. Lett. **69**, 2475 (1992).
[4] F. Cuypers and S. Davidson, Eur. Phys. Jour. **C2**, 503 (1998).
[5] J. Yu *et al.*, "Technical Memorandum: NuTeV SSQT performance," Report No. FERMILAB-TM-2040, 1998.
[6] A. Alton *et al.*, Phys. Rev. **D63**, 012001 (2001).
[7] W. Sakumoto *et al.*, Nucl. Instr. Meth. **A294**, 179 (1990). B. King *et al.*, Nucl. Instr. Meth. **A302**, 254 (1991).
[8] D. A. Harris, J. Yu, *et al.*, Nucl. Instr. Meth. **A447**, 373 (2000).
[9] C.H. Llewellyn Smith, Phys. Rep. **3C**, 261 (1971).
[10] R. Belusevic and D. Rein, Phys. Rev. **D46**, 3747 (1992).
[11] U. K. Yang and A. Bodek, Phys. Rev. Lett. **82**, 2467 (1999).
[12] D. Rein and L. M. Sehgal, Annals of Phys. **133**, 79 (1981).
[13] A. Bodek and J. L. Ritchie, Phys. Rev. **D23**, 1070 (1981).
[14] E. A. Paschos, L. Pasquali, and J. Y. Yu, Phys. Rev. **B588**, 263 (2000).
[15] D. Yu. Bardin and V. A. Dokuchaeva, Nucl. Phys. **B287**, 839 (1987).
[16] P. Vilain *et al.*, Phys. Lett. **B364**, 121 (1995).
[17] A. Alton, Ph.D. thesis, Kansas State University, (2001); A. Alton *et al.*, "Observation of Neutral Current Charm Production in ν_μFe Scattering at the Tevatron," to be published in Phys. Rev. D (hep-ex/0008068).
[18] F. Bergsma *et al.*, Phys. Lett. **122B**, 465 (1983).
[19] S. J. Freedman *et al.*, Phys. Rev. **D47**, 811 (1993).

Bibliography

[1] W. Pauli, "Letter to the Physical Society of Tubingen", reproduced in C. E. Lane and R. I. Steinberg, *Discovery of the Neutrino*, World Scientific, (1993).

[2] E. Fermi, *Richerca Scient.*, **2**, 12 (1933).

[3] R. G. H. Robertson,"Neutrino Mass," *Discovery of the Neutrino*, World Scientific, (1993).

[4] E. Fermi, *Z. Physik.*, **88**, 161 (1934).

[5] H. A. Bethe and R. Peierls, *Nature*, **133**, 532 (1934).

[6] F. Reines and C. L. Cowan,Jr., Phys. Rev. **92**, 830 (1953).

[7] G. Danby *et al.*, Phys. Rev. Lett. **9**, 36 (1962).

[8] M. Schwartz, Phys. Rev. Lett. **4**, 306 (1960).

[9] B. Pontecorvo, *J. Exptl. Theoret. Phys.*, **37**, 1751 (1959).

[10] M. Perl *et al.*, Phys. Rev. Lett. **35**, 1489 (1975).

[11] K. Kodama *et al.*, Phys. Lett. **B504**, 218 (2001).

[12] M. Acciarri *et al.*, Phys. Lett. **B431**, 199 (1998).

[13] P. D. B. Collins, A. D. Martin, and E. J. Squires, *Particle Physics and Cosmology* John Wiley & Sons, (1989).

[14] C. S. Wu, *et al.* Phys. Rev. **105**, 1413, (1957).

[15] F. Boehm and P. Vogel,*Physics of Massive Neutrinos*, Cambridge University Press, (1992).

[16] C. W. Kim and A. Pevsner, *Neutrinos in Physics and Astrophysics*, Harwood Academics, (1993).

[17] D. Griffiths, *Introduction to Elementary Particles*, John Wiley & Sons (1987).

[18] B. Kayser, F. Gibrat-Debu, and F. Perrier, *The Physics of Massive Neutrinos*, World Scientific, (1989).

[19] J. C. Pati, "Discovery of Proton Decay: A Must for Theory, a Challenge for Experiment", hep-ph/005095 (2000).

[20] M. Gronau, C. N. Leung, and J. L. Rosner, Phys. Rev. **D29**, 2539 (1984).

[21] R. E. Shrock, Phys. Rev. **D24**, 1232 (1981).

[22] L. M. Johnson, D. W. McKay, and T. Bolton, Phys. Rev. **D56**, 2970 (1997).

[23] J. A. Formaggio *et al.*, Phys. Rev. **D57**, 7037 (1998).

[24] L. Borissov *et al.*, Phys. Rev. Lett. **83**, 4943 (1999).

[25] M. H. Shaevitz *et al*,"Fermilab Proposed Experiment 815", FNAL-P-815 (1990).

[26] J. Conrad, "The Search for Neutral Heavy Leptons with a New Decay Channel," NuTeV Detector Memo, DET020 (1995).

[27] A. Vaitaitis *et al.*, Phys. Rev. Lett. **83**, 4943 (1999).

[28] J. Yu *et al.*, "Technical Memorandum: NuTeV SSQT performance," Report No. FERMILAB-TM-2040, 1998.

[29] W. Sakumoto *et al.*, Nucl. Instr. Meth. **A294**, 179 (1990).

[30] B. King *et al.*, Nucl. Instr. Meth. **A302**, 254 (1991).

[31] G. Zeller, *et al.* hep-ex/0010007; K. S. McFarland, *et al.* hep-ex/9806013.

[32] B. T. Fleming *et al.*, "A First Measurment of Low-x, Low-Q^2 Structure Function in Neutrino Scattering", to be published in Phys. Rev. Lett. (hep-ex/0011094).

[33] T. Adams *et al.*, Phys. Rev. **D61**, 092001 (2000).

[34] J. A. Formaggio *et al.*, Phys. Rev. Lett. **87**, 071803 (2001).

[35] J. Goldman, Ph. D. thesis, Kansas State University, (2001).

[36] D. A. Harris, J. Yu, *et al.*, Nucl. Instr. Meth. **A447**, 373 (2000).

[37] D. E. Groom *et al.*, Eur. Phys. J. **C 15** (2000).

[38] SLAC-246, March 1982.

[39] A. Alton *et al.*, Phys. Rev. **D63**, 012001 (2001).

[40] G. Ingelman *et al.*, Proc. 'Physics at HERA', (1992).

[41] W. G. Seligman *et al.*, Phys. Rev. Lett. **79**, 1213 (1997).

[42] K. J. Eskola *et al.*, Eur. Phys. Jour. C **9** 61 (1999).

[43] M. Arneodo *et al.*, Phys. Lett. **150B**, 458 (1985).

[44] J. J. Aubert *et al.*, Phys. Lett. **100B**, 433 (1981).

[45] G. T. Jones *et al.*, Z. Phys. **C25**, 121 (1985).

[46] C. H. Llewellyn Smith, Phys. Rep. **3C**, 261 (1971).

[47] L. A. Ahrens *et al.*, Phys. Rev. **D35**, 785 (1987).

[48] U. K. Yang and A. Bodek, Phys. Rev. Lett. **82**, 2467 (1999).

[49] R. Belusevic and D. Rein, Phys. Rev. D **38**, 2753 (1988).

[50] D. Rein and L. M. Sehgal, Annals of Phys. **133**, 79 (1981).

[51] R. P. Feynman, M. Kislinger, and F. Ravndal, Phys. Rev. **D3**, 2706 (1971).

[52] A. Bodek and J. L. Ritchie, Phys. Rev. **D23**, 1070 (1981).

[53] E. A. Paschos, L. Pasquali, and J. Y. Yu, Phys. Rev. **B588**, 263 (2000).

[54] CERN CN/ASD, GEANT detector description and simulation library (1998).

[55] G. Zeller, private communication.

[56] T. Adams *et al.*, Phys. Rev. D **61**, 092001 (2000).

[57] B. Armbruster *at al.*, Phys. Lett. **B348**, 19 (1995).

[58] T. E. Jannakos *et al.*, Nucl. Phys. B, Proc. Suppl. **85**, 101 (2000).

[59] C. Oehler, in Proc. Sixth Topical Seminar on Neutrino and Astroparticle Physics (1999).

[60] M. Daum *et al.*, Phys. Rev. Lett. **85**, 1815 (2000).

[61] M. Daum *et al.*, Phys. Lett. **B361**, 179 (1995).

[62] N. de Leener-Rosier *et al.*, Phys. Lett. **D43**, 3611 (1991).

[63] R. Barate *et al.*, Eur. Phys. Jour. **C2**, 395 (1998).

[64] J. Govaerts, J. Deutsch, and P.M. Van Hove, Phys. Lett. **B389**, 700 (1996).

[65] V. Barger, R. J. N. Phillips, and S. Sarkar, Phys. Lett. **B352**, 365 (1995). and *erratum* Phys. Lett. **B356**, 617 (1995).

[66] D. Choudhury *et al.*, hep-ph/9911365.

[67] G. Feldman and R. Cousins, Phys. Rev. D **57**, 3873 (1998).

[68] R. Ammar *et al.*, Phys. Rev. Lett. **61**, 2185 (1988); K. Kodoma *et al.*, Phys. Lett. B **263**, 573 (1991). (Also, see S. Frixione *et al.*, Nucl. Phys. B **431**, 453 (1994)).

[69] T. Alexopoulos *et al.*, Phys. Rev. Lett. **82**, 41 (1999).

[70] C. H. Albright, Phys. Rev. **D12**, 1319 (1975).

[71] C. Y. Pang *et al*, Phys. Rev. **D8**, 1989 (1973).

[72] S. R. Mishra *et al*, Phys. Rev. Lett. **59**, 1397 (1987).

[73] J. Dorenbosch *et al.*, Phys. Lett. **B166**, 473 (1986).

[74] A. M. Cooper-Sarkar *et al.*, Phys. Lett. **B160**, 207 (1985).

[75] A. Soni, Phys. Rev. **D11**, 624 (1975).

[76] L. Montanet et al , Phys. Rev. **D54**, 1 (1996).

[77] K. Eitel *et al.*, Nucl. Phys. B, Proc. Suppl. **91**, 191 (2001).

[78] E. Church *et al.*, "A Proposal for an Experiment to Measure $\nu_\mu \to \nu_e$ Oscillations and ν_μ Disappearence at the Fermilab Booster: BooNE", FERMILAB-P-0898 (1997).

[79] S. Case *et al.*, "Future limits on the KARMEN timing anomaly at MiniBooNE", to be submitted to Phys. Rev. D.

[80] C. Athanassppoulos *et al.*, Phys. Rev. Lett. **81**, 1774 (1998).

[81] C. Oehler, private communication.

[82] J. Altegoer *et al.*, Nucl. Instr. Meth. **A404**, 96 (1998).

[83] L. Camilleri, private communication.

[84] I. Bigi *et al.*, hep-ph/0106177 (2001).

[85] V. Barger, S. Geer, and K. Whisnant, Phys. Rev. **D61**, 053004 (2000).

[86] R. Shrock, Phys. Rev. **D24**, 1232 (1981).

[87] W. Fetscher, H. J. Gerber, and K. F. Johnson, Phys. Lett. **B173**, 102 (1986).

[88] G. Feinberg and S. Weinberg, Phys. Rev. Lett. **6**, 381 (1961).

[89] P. Herczeg and R. N. Mohapatra, Phys. Rev. Lett. **69**, 2475 (1992).

[90] F. Cuypers and S. Davidson, Eur. Phys. Jour. **C2**, 503 (1998).